DYNAMIC DOMAIN OBSERVATION IN GRAIN-ORIENTED ELECTRICAL STEEL USING MAGNETO-OPTICAL TECHNIQUES

by

OLEKSANDR HOSHTANAR

A thesis submitted to Cardiff University in candidature for the Degree of Doctor of Philosophy.

Wolfson Centre for Magnetics,
School of Engineering, Cardiff University

2006

UMI Number: U585555

All rights reserved

INFORMATION TO ALL USERS
The quality of this reproduction is dependent upon the quality of the copy submitted.

In the unlikely event that the author did not send a complete manuscript
and there are missing pages, these will be noted. Also, if material had to be removed,
a note will indicate the deletion.

UMI U585555
Published by ProQuest LLC 2013. Copyright in the Dissertation held by the Author.
Microform Edition © ProQuest LLC.
All rights reserved. This work is protected against
unauthorized copying under Title 17, United States Code.

ProQuest LLC
789 East Eisenhower Parkway
P.O. Box 1346
Ann Arbor, MI 48106-1346

TO MY PARENTS

ACKNOWLEDGEMENT

Most of the work described in this thesis was performed at the Wolfson Centre for Magnetics, School of Engineering, Cardiff University. The author would like to thank all of whom showed me great courtesy and helped throughout my work.

I would especially like to thank to my supervisor Professor Anthony J. Moses for his help and guidance during the course of this project.

Also, I would like to greatly thank Dr. Paul I. Williams for his valid advice and support and for his time and patience in the proof reading of the original manuscript and ensuing recommendations.

I am also grateful to Professor Philip Beckley for his helpful advice.

I would also wish to thank Dr. Stan Zurek for his help.

I would also like to extend my thanks to Professor Bruce Batchelor for his advice in image processing.

An indicating garnet film used within the project was provided by the Scientific Research Company "Carat" (Ukraine), and non-oriented steel samples were provided by Cogent Power Ltd.

Thanks also go to Mr. Alan Griffiths for his cooperation and help in building the system parts.

I am indebted to Cardiff University and the EPSRC for the financial support during the course of this project.

Finally, I would like to extend my thanks to all the people at the Teaching Office and Registry of the University for administrative help and particularly for arranging my attendance at courses and seminars which I found to be very interesting and beneficial.

SUMMARY

Direct, real time domain observations in electrical steel during its magnetisation at 50 Hz and 75 Hz was limited due to low the limited sensitivity and frame sampling rate of the camera systems available.

In this work, a high efficiency Kerr magneto-optic microscope was coupled to a recent commercially available high speed intensified camera. The superior efficiency of the developed system enabled domain dynamics measurement to be made at magnetisation frequencies up to 100 Hz in the real time mode and up to 1.8 kHz in stroboscopic mode.

The application of the system was focussed on the study of grain-oriented electrical steel. Observations in this work revealed that the behaviour of the domain walls under sinusoidal excitation is far from being ideal sinusoidal motion. The deviations from the ideal behaviour can be summarised as non-sinusoidal, non-uniform and non-repetitive domain wall motion. The dependence of the non-uniformity of wall motion and cycle-to-cycle non-repeatability on magnetisation conditions studied by direct real-time observation revealed that under certain conditions the non-uniformity and non-repeatability is much higher. Recommendations have been made on how to reduce losses by adjusting the magnetisation conditions and "magnetic history" of the steel core. The observations confirmed previous researchers' suggestions that the perfection of grain-to-grain orientation and grain size uniformity would improve wall motion uniformity, hence reducing power loss in the material.

In addition to Kerr-microscopy observations, the application of a magnetic indicator imaging technique was demonstrated. Moving domains under the insulating, opaque coating on commercial grain-oriented electrical steel were observed using this method. The influence of surface roughness and the effect of coating tension on the domain structure and distortion of bar domains under dynamic magnetisation was observed.

New experimental techniques and image processing programs have been developed such as the first attempt of automatic domain wall recognition and analysis by computer vision methods.

It was demonstrated that the system and software tools were flexible for use with other materials such as steel, NiFe and CoFe alloys, amorphous ribbons and wires, ferrites and magnetic films.

CONTENTS

CHAPTER 1 INTRODUCTION TO MAGNETIC THEORY AND MAGNETIC DOMAIN FORMATION IN FERROMAGNETIC MATERIALS

1.1 Historical overview of magnetism

This chapter covers some basic theory with an historical overview and the physics of magnetic domain formation.

Lodestone was known to be a natural magnet, several centuries before Christ. It was quarried in Asia Minor, in Magnesia, on the Aegean coast. Hence the rock was given the name `magnetite', and its peculiar properties came to be known as `magnetism' (cited in [1]). Since then it was studied in alchemy and witch-craft. By the 13th century the only proven application was in compasses.

The first scientific treatment of magnetism was by William Gilbert in the 16th century. His treatise is entitled *De Magnete (On the Magnet)* [2], published in 1600. Among Gilbert's scientific contributions was the study of terrestrial magnetism, and the discovery that a magnet loses its magnetism at high temperatures. Gilbert's work brought the study of magnetism out of the realm of witch-craft, and into the realm of an accepted academic field of study.

The renaissance era saw further works on magnetism. One of these was the second paper in *Two Tracts on Electricity and Magnetism*, by Robert Boyle, in 1676 [3]. Electricity and magnetism remained as separate natural phenomena. The union of the two was not seen until the 19th century.

At the beginning of the 19th century, John Christian Oersted discovered that a magnetic field was generated by an electric current in a wire [4]. Further work carried out by Ampere [5], and Biot and Savart resulted in Ampere's circuital law, and the Biot-Savart law, as they are known today. Later that century, Michael Faraday discovered the reverse effect, magnetic induction, in which an electric current was generated by a changing magnetic field [6].

At the end of the 19th century, James Clerk Maxwell, in his famous *A Treatise on Electricity and Magnetism*, 1892 [7], expressed the laws of electromagnetism as they are known today. The Gaussian laws for the electric and magnetic fields, the Ampere circuital law and the Faraday law of induction were combined mathematically to form the four Maxwell equations [8]. The natural phenomena of electricity and magnetism were at long last united into the one natural phenomenon of electromagnetism.

1.2 Magnetic field in a medium

Maxwell's equations as they stood described admirably the behaviour of electric and magnetic fields in a vacuum or in homogeneous, isotropic, linear, and stationary materials. However, magnetic materials are not necessarily as such.

When a magnetic field **H** has been generated in a medium by a current loop, in accordance with Ampere's law, the response of the medium is its magnetic induction **B**, also called the flux density. Magnetic flux in this case is $\Phi = \mathbf{B} *$ Area of current loop. In general the relation between B and H is given by the $\mathbf{B} = \mu H$, where μ is the permeability of the medium.

In this work, the SI system of units is used with the following definitions:

Magnetic flux Φ is measured in Weber [Wb], 1Wb is the amount of flux which when reduced uniformly to zero in one second produces an e.m.f of one volt in a one-turn coil of conductor through which the flux passes.

B – measured in Tesla [T], $1T = 1Wb/m^2$,

H – measured in A/m. More detailed explanation may be found in Jiles [9] and Grant and Phillips [10].

In a vacuum $\mathbf{B}_0 = \mu_0 \mathbf{H}$ where $\mu_0 = 4\pi \times 10^{-7} H/m$ is the magnetic permeability of free space (In SI units). B_0 – is the magnetic induction in free space.

In a medium, usually $\mathbf{B} = \mu H = \mu_0 \mu_r \mathbf{H}$ where μ_r is the relative permeability of the medium. The term 'permeability' usually refers to relative permeability and is most commonly used by engineers.

If a piece of material exhibits magnetism without any applied external field it can be considered as having a permanent dipole moment. The atomic magnetic dipole moments **m** (amp·metre^2) of a specimen can be considered analogous to current loops and rotate (i.e. experience torque) in an external magnetic field.

The magnetic moment per unit volume $\mathbf{M} = \mathbf{m}/V$ is called the magnetisation and is expressed in [A/m]. Magnetisation represents the net magnetic state of the material.

If no external field is present the induction inside the specimen is $\mathbf{B} = \mu_0 \mathbf{M}$. And therefore the magnetisation **M** and magnetic field **H** contribute to the magnetic induction in a similar way. If both magnetisation and magnetic field are present then their contribution can be summed (as vectors).

$$\mathbf{B} = \mu_0(\mathbf{H} + \mathbf{M}) \qquad (1.1)$$

In describing the magnetic behaviour of materials, the `magnetic susceptibility' χ, is sometimes more convenient to use than the magnetic permeability μ. The magnetic susceptibility is defined as the ratio between the material magnetization **M** and the external applied field **H**:

$$\mathbf{M} = \chi \mathbf{H} \qquad (1.2)$$

The relation between the permeability and the susceptibility is therefore:

$$\mu = \mu_0 (\chi + 1) \qquad (1.3)$$

The value $\chi + 1$ is equal to the relative permeability μ_r. χ and μ_r represents the response of the material to externally applied magnetic fields and in the most general form must be a 3 ×3 tensors that takes into account nonlinear and nonisotropic response of the material. It is also know that the magnetic behaviour of the material is dependent on its magnetic history. Therefore χ and μ_r must be history dependent but they can be treated as simple scalars for simplified models in many cases.

Materials may be classified by their response to externally applied magnetic fields as diamagnetic, paramagnetic, or ferromagnetic. The following definitions from [10] are most common:

Materials for which χ is small and negative ($\sim 10^{-5}$) are **diamagnetic**. Magnetisation here is opposite to the applied field. The orbital motion of electrons creates tiny atomic current loops, which produce magnetic fields. When an external magnetic field is applied to a material, these current loops will tend to align in such a way as to oppose the applied field. All materials are inherently diamagnetic, but if the atoms have some net magnetic moment as in paramagnetic materials, or if there is long-range ordering of atomic magnetic moments as in ferromagnetic materials, these stronger effects are always dominant. Examples of diamagnets are bismuth, graphite and inert gases.

Any conductor will show a strong diamagnetic effect in the presence of changing magnetic fields because circulating currents will be generated in the conductor to oppose the magnetic field changes. A superconductor will be a perfect diamagnet since there is no resistance to the forming of the current loops ($\chi = -1$).

A material is said to be **paramagnetic** if it exhibits a magnetization which is proportional to the applied magnetic field in which the material is placed. It happens if the material contains microscopic magnetic moments, such as electron spin or orbital

moments. When an external magnetic field is applied, their orientations tend to rotate slightly toward the direction of the applied field, resulting in a slight net material magnetization. Susceptibility of paramagnets is small and positive (typically 10^{-5} to 10^{-3}). Examples of paramagnets are aluminium, platinum, copper sulphate and oxygen.

A rigorous theory of diamagnetism and paramagnetism is presented in [11], [12].

1.3 Ferromagnetism

Iron, nickel, cobalt and some of the rare earths (e.g. gadolinium, dysprosium) exhibit a unique magnetic behaviour, which is called **ferromagnetism** because iron is the most common and most dramatic example. In an external magnetic field ferromagnets reveal strong net material magnetization toward the direction of the applied field. Susceptibility is positive and can reach a giant value of 10^6 (for supermalloy). Ferromagnets also stay magnetised to some extent after the external magnetic field is removed.

Ewing [13] first attempted to explain the phenomena of **ferromagnetism** from the atomistic point of view. He constructed a physical model of a ferromagnetic material consisting of an array of magnetic compass needles. He then tried to explain hysteresis in ferromagnetic materials in terms of magnetic interaction between microscopic or `molecular' magnets in the magnetic material.

The idea of the existence of permanent areas of spontaneous magnetisation was first proposed by Weiss with his postulation of the existence of magnetic domains in 1907 [14]. His theory helped to account for the experimental observations that had previously been made showing that it is possible to saturate a ferromagnetic specimen in a weak magnetic field. Weiss gave the correct interpretation of ferromagnetism but he couldn't explain the reasons for the existence of magnetic domains.

The existence of ferromagnetism can be explained in terms of quantum mechanics.

1.4 Existence of ferromagnetism as a result of quantum mechanics long-range ordering interaction

In an individual atom there are a number of magnetic moments including orbital angular moments of electrons and spin angular moments of electrons, protons and neutrons, their combination into a total magnetic moment of individual atom was explained by Russell and Saunders [15] theory, based on the `Pauli Exclusion Principle'.

In 1928 Heisenberg [16] published the first fully-fledged quantum theory of ferromagnetism, which was meant to replace the Weiss theory. In this theory, the Weiss molecular field was replaced by an exchange of one magnetic moment with all other moments in the medium. For ordered moments in the crystal it became possible to write an interaction integral equation. That long-range interaction happens to be high for atoms with an incomplete 3d electron shell.

Using that theory, Slater in [17] found a dependence of the interaction integral on the distance between atoms. The results are presented in the form of the `Bethe - Slater curve', shown in figure 1.1. It explains why the ferromagnetic state is so strong for iron, nickel and cobalt. Moreover, it gives an idea how to make other materials ferromagnetic by changing the interatomic spacing. For example manganese and copper are both paramagnetic, but can form ferromagnetic alloys such as the Heusler alloy containing 61% Cu, 26% Mn and 13% Al. Other examples are MnSb, MnBi, CrO_2 and $ZnZr_2$ below 28.5 K

In 2004, it was reported [18] that a certain allotrope of carbon nanofoam, exhibited ferromagnetism. It is thought that other similarly-formed materials, such as isoelectronic compounds of boron and nitrogen, may also be ferromagnetic.

Further developments in the quantum theory of ferromagnetism were made, and that branch of science grew into the field of solid-state physics. However, the many theories that were conceived and continue to be postulated, are mainly suitable for describing the extremely idealised case of a single magnetic domain, in a single crystal. The discoveries of complicated magnetic domain patterns, as well as complicated polycrystalline structures, brought with them the need for more practicable, and less idealized theories of ferromagnetism. The study of ferromagnetism was to move to a more macroscopic scale, and a return to the methods of Weiss molecular field theory was to be made (classical physics).

1.5 Magnetic domains and their internal energies

Landau and Lifshitz (cited in [19]) proposed theoretical domain structures based on a minimum energy concept, which forms the basis for modern domain theory. The primary reason for the existence of domains within a crystal is that their formation reduces the magnetic free energy. In the simplest case for such a crystal, the energy, E, is the sum of several free energy terms [20]:

$$E = (E_{ex}+E_k)+E_\lambda+E_D+E_H \qquad (1.5)$$

where E_{ex} is the exchange energy, E_k is the magnetocrystalline anisotropy energy, E_λ is the magnetoelastic energy, E_D is the magneto-static energy, and E_H is the energy of the domains in the presence of an applied field. There is also a wall energy E_w which is examined in detail in section 1.5.4. However, since E_w comprises E_{ex} and E_k, it is not necessary to include E_w as a separate term in equation 1.5.

1.5.1 Exchange energy E_{ex}

As mentioned in section 1.4 the magnetic moments of neighbouring atoms are coupled via exchange long range interactions which tend to align them so that the energy of parallel moments is minimal, and the energy of anti-parallel pairs is maximum.

The energy of two neighbouring magnetic moments in the domain wall may be represented as, [9]

$$E_{ex}^{\text{per moment}} = -\mu_0 z\beta \boldsymbol{m}_i\cdot\boldsymbol{m}_j = -\mu_0 z\beta \boldsymbol{m}^2\cos\varphi \qquad (1.6)$$

Where β is the analogous interaction, z is the number of nearest neighbours and magnetic moments $\boldsymbol{m}_i$ and $\boldsymbol{m}_j$ are in units of Am^2. For small angle φ, (see figure 1.2) the above equation becomes

$$E_{ex}^{\text{per moment}} = -\mu_0 z\beta \boldsymbol{m}^2(\varphi^2-2) \qquad (1.7)$$

For a 180° (see figure 1.2) wall of thickness n lattice parameters, each of size a, $\varphi = \pi/n$, the energy per unit area is then

$$E_{ex} = \frac{\mu_0 \beta m^2 \pi^2}{na^2} \qquad (1.8)$$

From this equation it is clear that the exchange energy is minimised when φ is very small, corresponding to a very wide domain wall (as in amorphous ribbons for example).

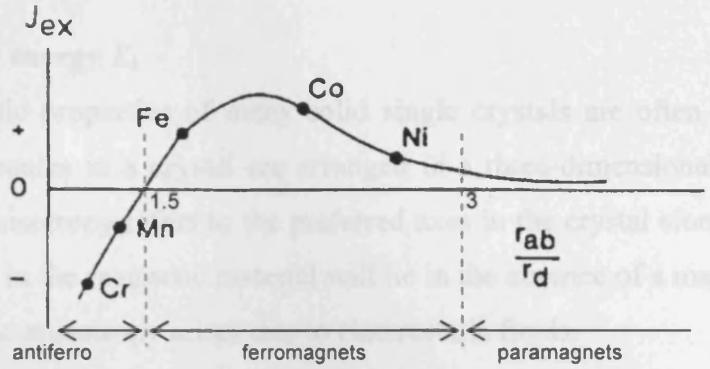

Fig. 1.1 The Bethe-Slater curve representing the variation of the exchange integral J with interatomic spacing r_{ab} and radius of unfilled d shell r_d. The rare earth elements lie to the right of nickel on the curve, (after [1]).

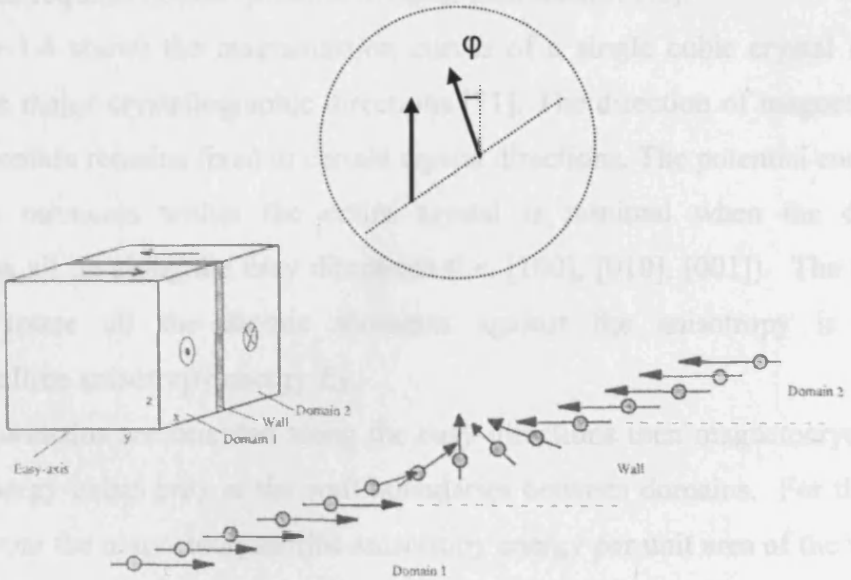

Fig. 1.2 Schematic structure of 180° Bloch wall showing rotation of spins, (after [8]).

1.5.2 Anisotropy energy E_k

The magnetic properties of many solid single crystals are often anisotropic. The atoms or molecules in a crystal are arranged in a three-dimensional, geometric lattice. Magnetic anisotropy refers to the preferred axes in the crystal along which the magnetic moments in the magnetic material will lie in the absence of a magnetic field, figure 1.3. Magnetic anisotropy arises due to electrostatic fields.

The magnetisation M versus applied field H curve depends on the crystal orientation relative to the field. For an iron cubic crystal, M reaches its saturation level more easily in the [100] directions compared to any other direction as H increases (see figure 1.4). The [100] direction is called the easy direction of magnetisation in iron because a lower field is required to attain the saturation magnetisation along this direction.

The [111] direction in iron is the hard magnetisation direction and is the most difficult to saturate. Magnetisations for [110] and [111] directions require a large magnetic field to attain the saturation magnetisation. The magnetisation process for these directions requires domain rotation to occur (see section 1.6).

Figure 1.4 shows the magnetisation curves of a single cubic crystal of iron along its three major crystallographic directions [21]. The direction of magnetisation within each domain remains fixed to certain crystal directions. The potential energy of the magnetic moments within the entire crystal is minimal when the domain magnetisations all lie along the easy directions (i.e. [100], [010], [001]). The energy required to rotate all the atomic moments against the anisotropy is called magnetocrystalline anisotropy energy E_K.

If all domains are oriented along the easy directions then magnetocrystalline anisotropy energy exists only at the wall boundaries between domains. For the wall thickness $l_d = na$ the magnetocrystalline anisotropy energy per unit area of the wall is, [21]

$$E_k = K_1 l_d \qquad (1.9)$$

Where K_1 is the anisotropy constant of [100] direction. This energy is minimal for a very thin wall.

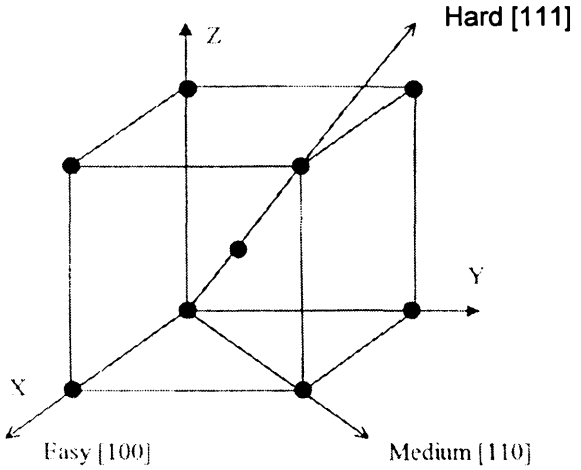

Fig. 1.3 Cubic crystal structure of iron showing principal crystallographic axes.

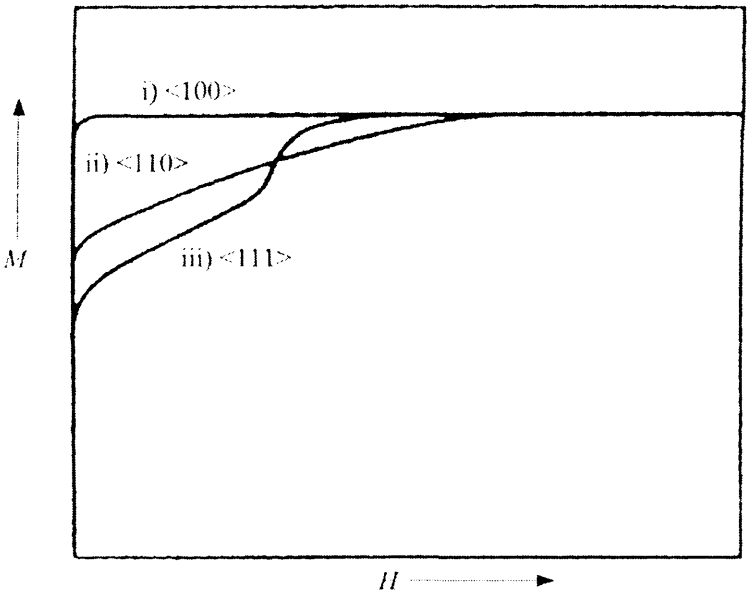

Fig. 1.4 Typical magnetisation curves for a single cubic crystal of iron along a cube edge [100], ii) a cube-face diagonal [110], iii) a cube-body diagonal [111], (reproduced from [9]).

1.5.4 Total domain wall energy E_w

Domains are separated from each other by walls. The walls are not so much walls but rather transition layers between the domains where spins within the lattice rotate to accommodate the different direction of spontaneous magnetisation in an adjacent domain. The domain wall structures were first investigated by Bloch (cited in [19] and a wall such as that illustrated in figure 1.2 is called a 180° Bloch wall. The energy associated with the strong interaction acting between the neighbouring spins to align the spins parallel to each other is exchange energy. An abrupt change of spin direction does not occur because otherwise the exchange energy contribution to the system energy would be very large as a result of the spins adjacent to the wall being anti-parallel. The exchange energy can be reduced if the 180° change in spin direction takes place gradually over n atoms.

The exchange energy stored in the domain wall decreases with an increase in the number of transition layers. Therefore, the exchange energy tends to increase the wall thickness. On the other hand the magnetocrystalline anisotropy energy increases as the spins in the wall rotate away from the easy magnetisation direction thus tending to restrict the width of the boundary. The wall energy can be expressed as

$$E_w = E_{ex} + E_k = \frac{\mu_0 \beta m^2 \pi^2}{a l_d} + K_1 l_d \qquad (1.10)$$

A stable thickness of wall is obtained when the sum of the exchange energy and the anisotropy energy is a minimum. The width of the (100) domain wall can be found by differentiating equation 1.10 with respect to l_d. For instance the domain wall thickness in iron is 3.95 x 10^{-8}m or 160 lattice parameters [1].

1.5.5 Magnetoelastic energy E_λ

The change in the dimensions of a ferromagnetic material as a result of being subjected to a magnetic field is called magnetostriction. Like magnetic anisotropy, magnetostriction originates from the interactions between atomic magnetic moments, and as such may be regarded as representing the strain dependence of anisotropy energy.

Figure 1.5 shows idealised domain structures and magnetostriction effects for different domain configurations. When applying a magnetic field parallel to the easy axis of a material with uniaxial anisotropy there is no magnetostriction (figure 1.5a).

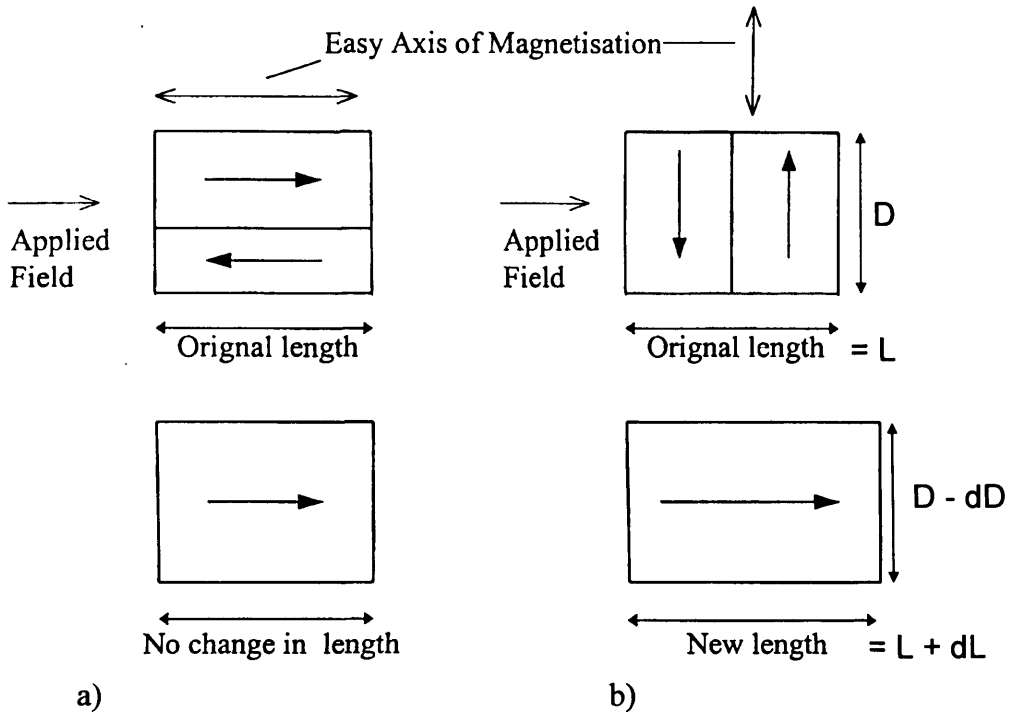

Fig. 1.5 Domain structures and magnetostriction: a) Domain growth when applying field parallel to the easy axis. b) Domain rotation and resulting magnetostriction when field is applied perpendicular to the easy axis.

However, magnetostriction does occur when the magnetic field is applied perpendicular to the easy axis due to magnetisation rotation (figure 1.5b). For materials with cubic anisotropy, the magnetisation changes from one easy axis to another by domain wall motion when a magnetic field is applied. The rotation of the moments into a new alignment cause the length of the bonds between the atoms to change. As such, the dimensions of the crystal change. If a ferromagnetic crystal experiences a change of dimensions when placed in a magnetic field, a state of strain may be created if the crystal is not allowed to expand freely. This contributes a further free energy of the crystal called magnetoelastic energy E_λ.

1.5.6 Magnetostatic energy E_D

Magnetostatic energy E_D is the energy associated with the existence of a demagnetising field induced on the surface of the material caused by free magnetic poles when the domain magnetisation is directed out of the material. The free magnetic poles are a result of surface charges. The effect of magnetostatic energy is to encourage the formation of a domain structure which would produce an internal field opposite in direction to the magnetisation field. Its effect is to eliminate the emergence of stray field from the surface of the material.

This is achieved when the direction of domain magnetisation adjacent to the surface lies in a plane parallel to the surface. Formation of such domains provides a closed path for the magnetisation in the underlying domains. The emergence of this magnetisation field from the surface is thus avoided.

Figure 1.6a shows a schematic diagram of a single iron crystal containing just one domain spontaneously magnetised parallel to an easy axis. As such there is no domain wall present and therefore the domain wall energy is zero. Likewise the magnetocrystalline anisotropy energy of this structure is zero. The large magnetostatic energy resulting from the free poles at the ends of the domains may be halved if the crystal is divided into two domains of opposite magnetisations (see figure 1.6b).

Magnetostatic energy can be reduced considerably by further division of the ideal single domain (see figure 1.6c). The energy is always proportional to the width of the domain. The energy is decreased as the width of the domain decreases. However, the total energy associated with domain walls increases because the number of walls increases with domain division. As the energy associated with the formation

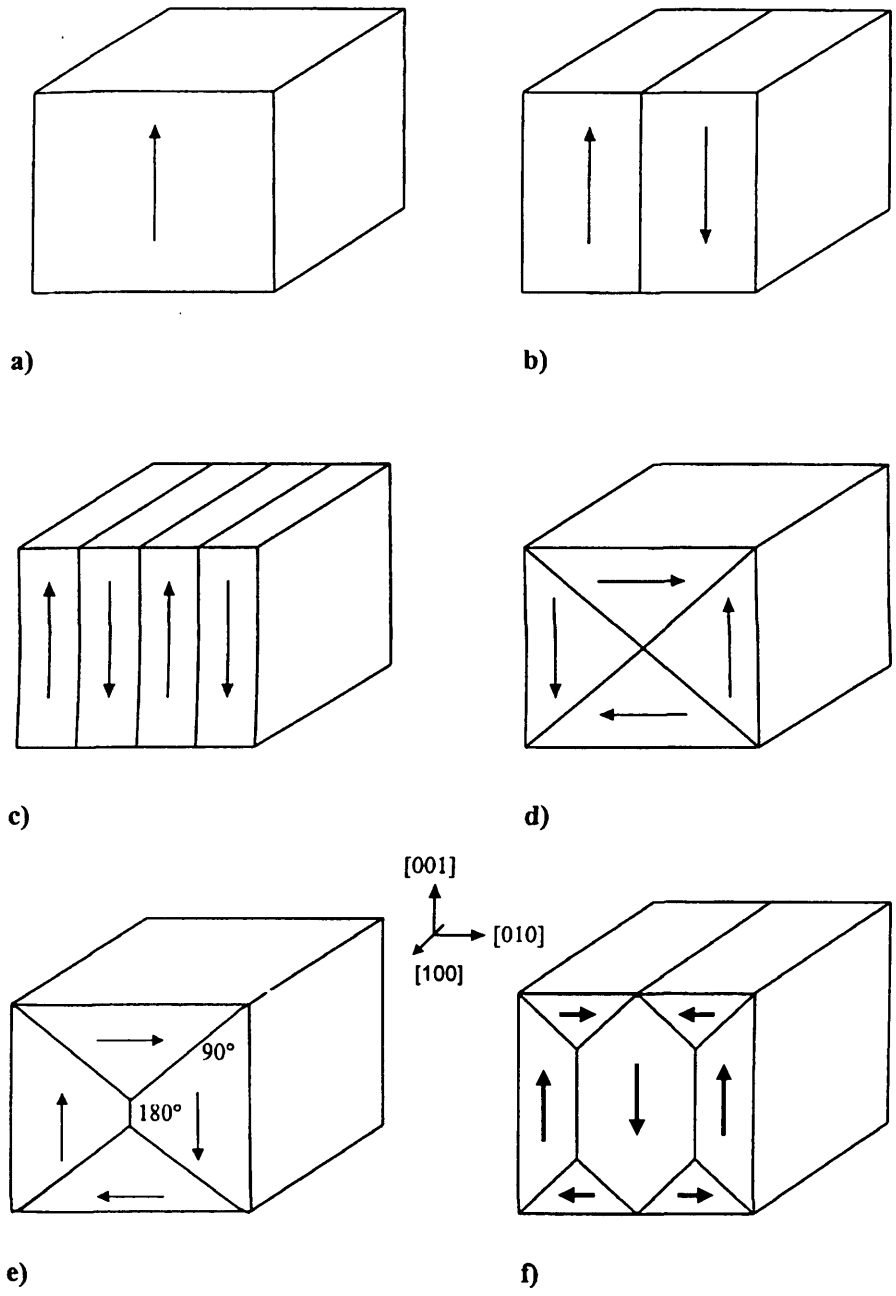

Fig. 1.6 Schematic representation of domains in a single crystal of iron a). Single domain, b) Domain split into two domains, c) Division into multiple domains to reduce magnetostatic energy. d) Hypothetically large closure domains. e) Actual combination of 180° and 90° closure domains, f) Typical domain formation found in (100)[001] iron, (after [21]).

of the additional domain walls becomes greater than the subsequent reduction in the magnetostatic energy, equilibrium is achieved and no further division occurs.

Iron crystals have three easy directions of magnetisation, and magnetostatic energy can be eliminated by the appearance of closure domains (with 90° domain walls) (see figure 1.6d). The easy directions of magnetisation allow the flux to follow a closed path within the material, avoiding free poles and the need to store magnetostatic energy.

One might assume that since the only obvious form of energy is wall energy that the closure domains could be very large. This can be true in small samples where the effect of magnetoelastic energy is not significant. However, in large samples domains have a tendency to change shape, either to elongate (Figure 1.6e) or shrink along the direction of magnetisation, depending on the sign of the magnetostriction coefficient along that direction. The domains change shape because the crystal lattice within each domain is deformed in the directions parallel and perpendicular to the domain magnetisation, and if, for instance, the deformation along [100] direction is smaller than in [010] direction, the elongation of [100] domains will be predominant. Magnetoelastic compatibility of domains is predominant factor for domain arrangement in large bulk samples [20].

If the crystal has a finite magnetostriction, the closure domains, which tend to deform in the direction of domain magnetisation, are squeezed into a space which is deformed to fit in with the magnetostriction of the underlying basic domain. As a result the closure domain stores magnetoelastic energy. For this reason the structure such as that shown in figure 1.6f is more often seen rather than the structure in figure 1.6e.

1.6 Ferromagnetic materials in an external magnetic field

When an external magnetic field is applied to a ferromagnetic material the domain structure changes so as to increase the resultant component of magnetisation parallel to that field. The effect of an external field is shown by the magnetisation curve in figure 1.7 [22]. When the magnetic material is in a demagnetised condition, its magnetisation is zero (the point **O** on the curve) due to the spontaneous magnetisation of the domains cancelling each other out. When a field is applied, domains with magnetisation directions that lie close to the direction of the applied field direction grow in volume at the expense of the other domains that are

magnetised in the opposite directions. The net magnetisation in the field direction (M_H) increases as shown by the curve **OAB**.

When the magnetic field is applied parallel to the anisotropy easy axis, domain wall motion is the primary mechanism that occurs [20]. This is because domains are *fixed* to the crystallographic directions.

If the applied field is removed the walls from the **OA** region return to their initial positions and the wall motion is said to be reversible. If the applied field is increased to a point between points **A** and **B** on the magnetisation curve, larger movements of domain walls occur. If the field is then reduced to zero, much of the wall motion is said to be *irreversible* due to the walls being displaced beyond internal energy barriers that arise from non-magnetic inclusions and residual stress. Since all of the walls do not return to their original position there is said to be a remanent magnetisation present in the material. It is necessary to apply a field in the opposite direction to completely reverse the wall motion to its original position.

Increasing the applied field further towards point C will result in the gradual disappearance of domain walls. For fields applied at some angle to the easy axis, the volume of the domains which have their magnetisation direction closest to the field direction, increase until they cover the whole volume of the specimen. Then by means of *domain rotation* (see figure 1.8b) the magnetisation direction of the domains is gradually rotated away from the easy axis to finally reach magnetic saturation (see figure 1.7). At point **C** (magnetic saturation) the specimen is a single domain with the magnetisation direction parallel to the field H. As H is reduced so the magnetisation decreases. Domain walls reappear, and the domain magnetisations may rotate away from the original field direction. However, the magnetisation does not decrease at the same rate as it increased along the initial magnetisation curve. The loop **JCDEFGJ** shown in figure 1.7 is called an **M-H** *hysteresis loop*. It represents the relation between **M** and alternating field **H**.

In materials such as iron or 3% Si-Fe, domain rearrangements occur largely by movement of walls between domains. Domain rotation in these materials occurs only in large applied fields ($H > 800$ A/m) [20].

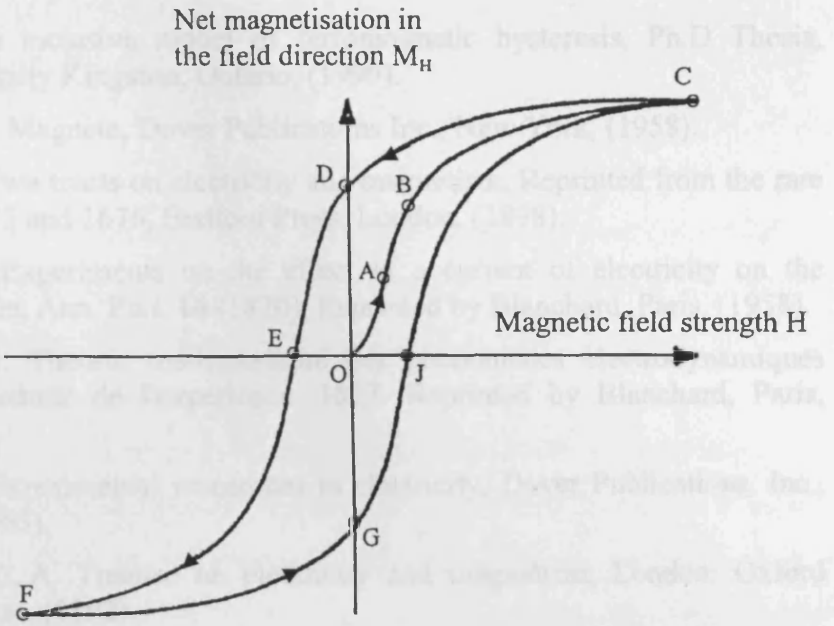

Fig. 1.7 Initial magnetisation curve OABC and Hysteresis loop JCDEFGJ for a typical ferromagnetic material (after [21]).

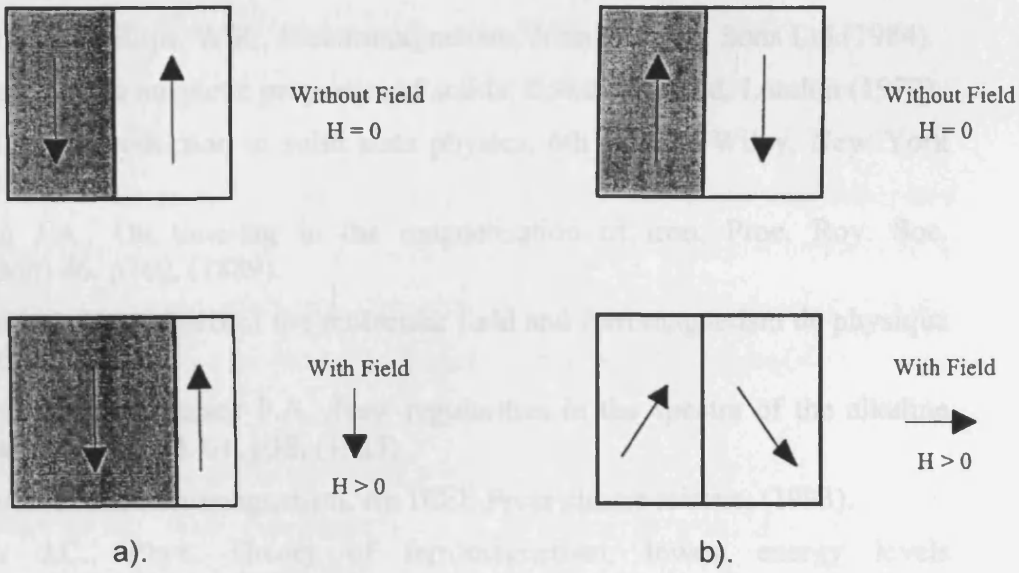

Fig. 1.8 Domain motion by displacement (a), and rotation (b).

1.7 References of chapter1

1. Phelps F., An inclusive model of ferromagnetic hysteresis, Ph.D Thesis, Queen's University Kingston, Ontario, (1999).
2. Gilbert W., De Magnete, Dover Publications Inc., New York, (1958).
3. Boyle H. R., Two tracts on electricity and magnetism, Reprinted from the rare editions of 1675 and 1676, Bedford Press, London, (1898).
4. Oersted J.C., Experiments on the effect of a current of electricity on the magnetic needle, Ann. Phil. **16** (1820), Reprinted by Blanchard, Paris, (1958).
5. Ampere, A.M. Theorie mathematique des phenomenes electrodynamiques uniquement deduite de l'experience. 1827. Reprinted by Blanchard, Paris, (1958).
6. Faraday M., Experimental researches in electricity, Dover Publications, Inc., New York (1965).
7. Maxwell J. C., A Treatise on electricity and magnetism, London: Oxford University Press, (1892).
8. Lorrain P., Corson D.P., Electromagnetic fields and waves, W.H. Freeman and Co., New York (1988).
9. Jiles D., Introduction to magnetism and magnetic materials, Chapman and Hall, New York (1991).
10. Grant, I.S., Phillips, W.R., Electromagnetism, John Wiley & Sons Ltd.(1984).
11. Crangle J., The magnetic properties of solids, Edward Arnold, London (1977).
12. Kittel, C., Introduction to solid state physics, 6th Edition Wiley, New York (1986).
13. Ewing J.A., On time-lag in the magnetisation of iron, Proc. Roy. Soc. (London) 46, p269, (1889).
14. Weiss P.J., Hypothesis of the molecular field and ferromagnetism de physique 6, p661, (1907).
15. Russell H.N., Saunders F.A., New regularities in the spectra of the alkaline earths, Astrophys. J. 61, p38, (1925).
16. Bozorth, R.M., Ferromagnetism, An IEEE Press classic reissue, (1993).
17. Slater J.C., Phys. Theory of ferromagnetism, lowest energy levels Phys. Rev. 52, p198, (1937).
18. Rode A.V., Gamaly E.G., Christy A.G., Unconventional magnetism in all-carbon nanofoam, Phys. Rev. B 70, 054407, (2004).
19. Carey R., Isaac E.D., Magnetic domains and techniques for their observation, The English University Press Ltd, London, (1966).
20. Shilling J.W., Houze J.R., Magnetic properties and domain structure in Grain-oriented Si-Fe, IEEE Trans. Magn. 10, 2, p195, (1974).
21. Chikazumi S., Physics of magnetism –2nd Edition, Malabar, (1978).
22. Goldman A., Handbook of modern ferromagnetic materials, Kluwer Academic Publishers, (2002).

CHAPTER 2 MAGNETIC DOMAINS IN COMMERCIAL MAGNETIC MATERIALS

2.1 Introduction

Magnetic materials are conveniently classified as 'soft' or 'hard' according to their coercivity. The major application of soft ferromagnetic materials is in electrical circuits in which amplification of the flux is required [1]. Some industrial grades of soft magnetic alloys are listed in Appendix 2.1.

The form of manufacturing is defined by the mode of operation. DC applications may employ solid cores. AC applications often need lamination to reduce eddy current energy loss. Also, soft magnetic metallic alloys can be produced in a form of powder cores with insulated particles in order to restrict eddy currents. Soft ferrites are insulators so they are normally used in bulk form.

Electrical steels form the largest group of soft magnetic materials. They are produced in sheet form suitable for use in AC applications, mainly in motors and transformers. Non-oriented steels contain 0 - 3% silicon normally and have isotropic magnetic properties, so they are used in motor cores and where cost is more important than efficiency.

Grain-oriented (or textured) 2 - 6% silicon steel is a highly sophisticated product with an easy direction of magnetisation in each grain oriented along sheet's rolling direction. Textured steel usually has large grains with regular domain structure, so that the quantitative analysis of domain images is often possible.

2.2 The basic features of textured Si-Fe steel

Throughout this section mention is made of grains. A grain is an individual crystal. In a polycrystalline material such as electrical steel the domain magnetisations tends to aligned along the easy axis of each grain (in a demagnetised state).

The development of Si-Fe alloys started with Hadfield's discovery in 1900 that the addition of silicon as an alloying element to low carbon steels, improved the performance of magnetic cores [2]. The addition of silicon to iron decreases the magnetocrystalline anisotropy causing increased permeability, also it increases electric resistively, hence reducing eddy current power loss.

If the rolling and annealing of Si-Fe sheet is carefully controlled, preferred crystal orientation can be induced. Goss in 1934 produced the first polycrystalline

Si-Fe sheet which had a high degree of anisotropic properties comparable with a single crystal (Goss (1935) cited in [3]).

A Goss textured material is one where the crystals in a sheet tend be arranged with their [001] directions close to the rolling direction (RD) and the (110) planes parallel to the surface of the sheet (see figure 2.1a). It is therefore easier to magnetise such a textured sheet along the rolling direction compared to a sheet with randomly oriented grains. The Goss textured steel is the most widely used form of electrical steel for transformers and is the material most focused in this investigation.

2.3 Domain patterns in polycrystalline Goss textured 3% Si-Fe sheet

In each grain of the sheet illustrated in figure 2.1a there is only one easy axis in the plane of the surface, and since the anisotropy constant K_1 is larger than K_2 and K_3, then structures with closure domains of the type shown in figures 1.6d,e are not likely to exist. Instead the reduction of the magnetostatic energy is achieved by subdivision of the domain structure into a system of antiparallel bar domains, as shown in figure 1.6f.

Provided that the grains are not too small, the domain structures in each grain are similar to those in a single crystal. Parallel 180° walls are often seen to run continuously along a sample stretching over many grains [4]. When two neighbouring grains are perfectly oriented along RD, bar domains extend uniformly across the grain boundary and closure domains, such as those in figure 1.6f are not seen. However, misalignment of neighbouring grains means that there is a certain amount of magnetostatic energy associated with the grain boundaries. This can result in the formation of closure domains of reverse magnetisation (spike domains) nucleating at the grain boundaries in order to reduce the demagnetizing field associated with the magnetostatic energy, see figure 2.2 [5], [6].

A grain can be oriented with its [001] direction out of the sheet plane, termed the angle of tilt θ, and about the sheet normal, termed the angle of yaw α, as shown in figure 2.3. Typically, the average tilt angle in conventional grain oriented materials is $\pm 7^{\circ}$ [8] and $\pm 4^{\circ}$ in high permeability materials [7].

The variation of domain structures with grain miss-orientation was first studied by Paxton and Nilan [8]. Using the Bitter colloid technique (see chapter 3)

a).

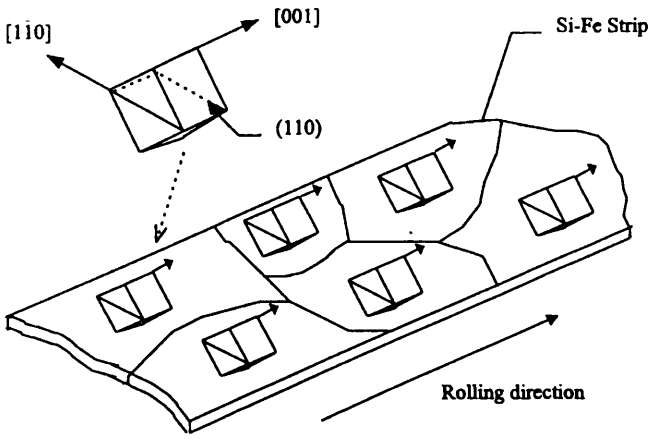

b).

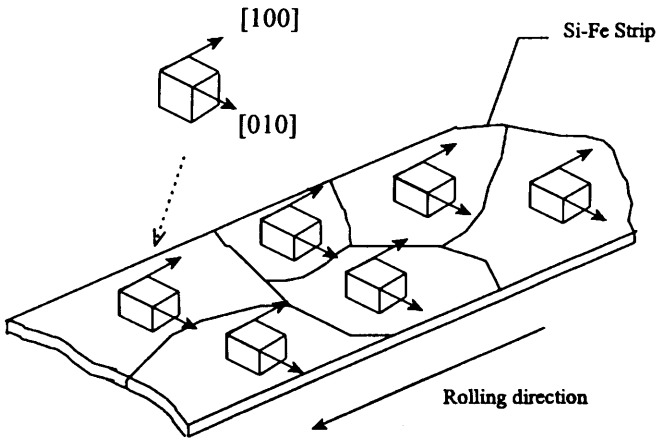

Fig. 2.1 Schematic diagrams showing (a) Goss oriented texture (110)[001] and (b) double oriented "cube" texture. The small cubes indicate the orientation of each grain. (after [7])

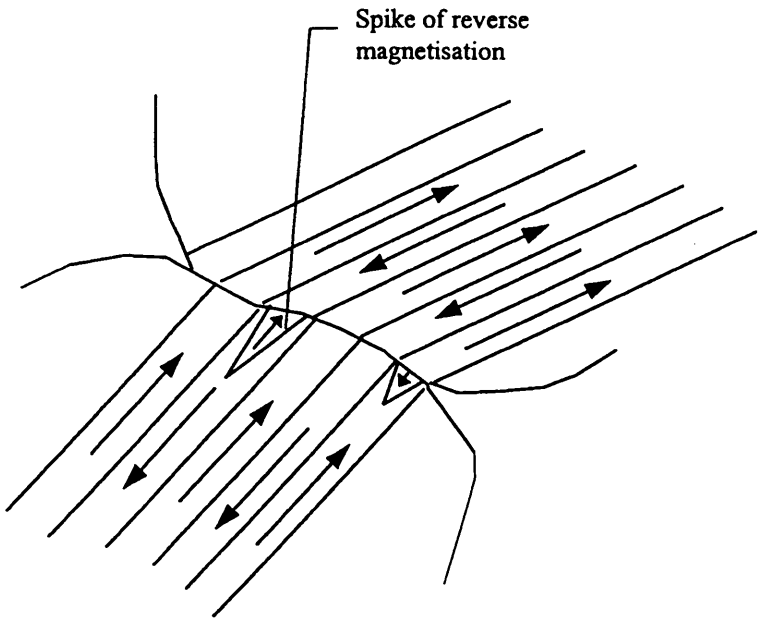

Fig. 2.2 Simplest domain closure structure on surface of polycrystalline SiFe steel at a grain boundary. Domain walls lie parallel to the easy axis in each grain (after [8])

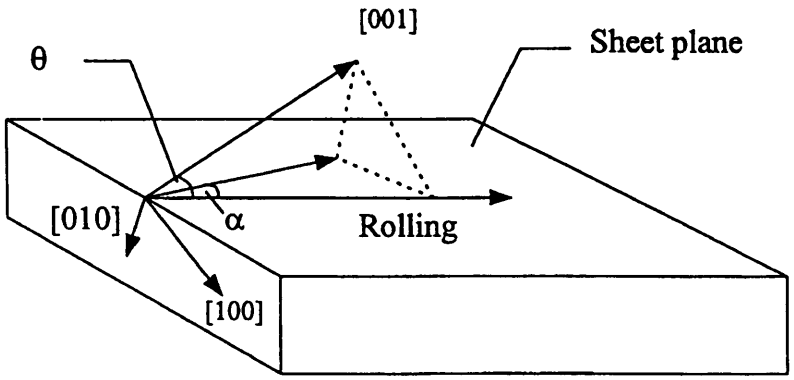

Fig. 2.3 Crystallographic orientation of the SiFe lattice showing tilt angle θ and yaw angle α relative to the sheet plane and rolling direction (after [18])

they found a semi-quantitative relationship between the domain patterns and the crystal orientation. The patterns revealed that as a tilt angle θ increased, supplementary closure domains on the surface appears as a result of the free magnetic poles that are induced on the sheet surface as shown in figure 2.4.

When $\theta = 0^{o}$ only a simple 180^{o} wall structure is observed, and this is maintained until θ becomes greater than 2^{o} when a lancet structure is produced. All lancet domains point along the [001] direction and are connected through the sample thickness by transverse domains. Figure 2.4d shows a typical transverse domain structure throgh the sample thickness. This structure avoids demagnetising fields such that the net magnetisation lies parallel to the sheet plane.

As θ approaches 4^{o}, the lancet domains become reduced in size and increased in number. Additionally, the volume of transverse domains also increases within the material, in order to keep the net flux parallel to the surface of the sample. At $\theta = 4^{o}$, lancets are observed to align in combs in order to use a common transverse domain roughly directed in the [0,1,-1] direction as shown in figure 2.4f. This has been termed an *aligned lancet comb structure* [9].

When $\theta > 8^{o}$ the volume of the transverse domains increases even more and a very fine lancet pattern is formed. For $\theta > 13^{o}$ a fine closure domain pattern is observed (not shown), and these patterns do not exhibit any identifiable basic regularity.

During remagnetisation the supplementary domains are completely destroyed and then rebuild. The energy bound in the supplementary domains is dissipate in every cycle of magnetisation, thus forming an important part of hysteresis losses [10]. Secondary, the system of supplementary domains effects the eddy current distribution in the vicinity of a moving wall of the basic bar domain, and this either increases or decreases the dynamic losses. The changing volume of transverse domains is also responsible for magnetostrictive noise.

Another kind of steel has a (100)[001] texture shown in figure 2.1b and is referred to as cube oriented. Such steel has two easy axes in its plane, parallel and perpendicular to the rolling direction. If a grain is slightly misoriented fir tree supplementary domains form on the surface, as in figure 2.5.

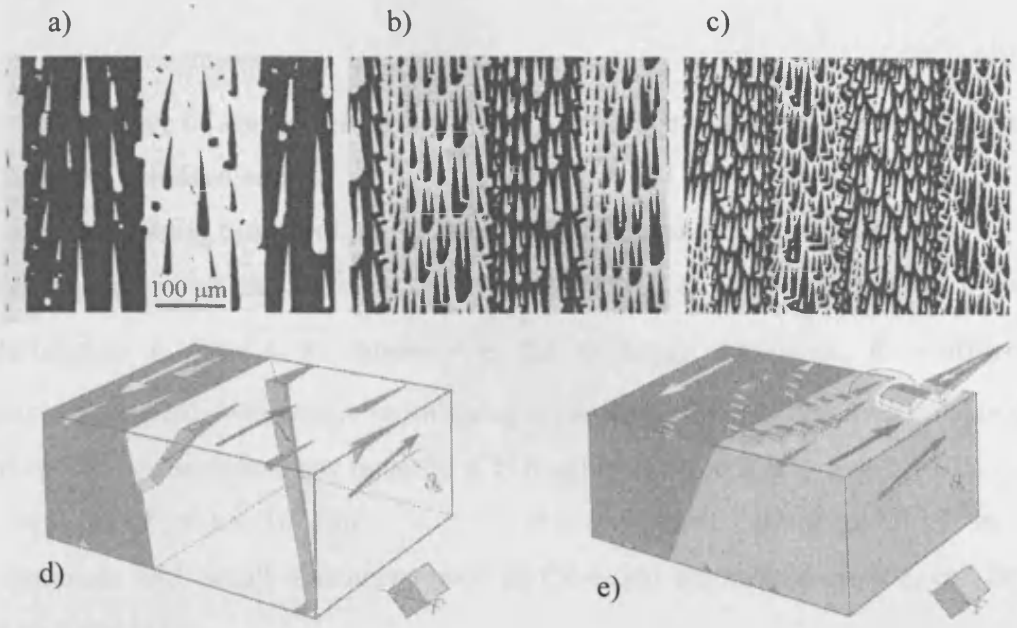

Fig. 2.4 Lancet patterns on (110) surfaces of Goss textured steel with a) 2°, b) 4°, and c) 8° misorientation. 3D model (d) and more complex patterns (e, f). (reproduced from [6]).

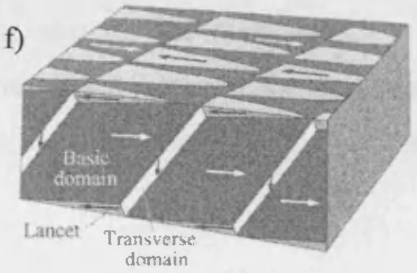

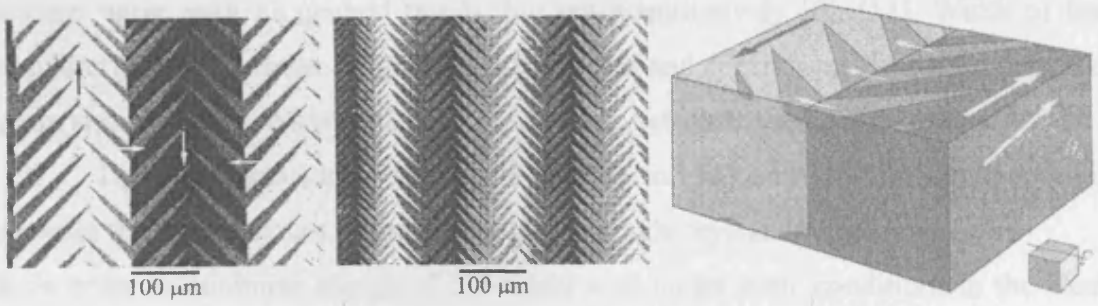

Fig. 2.5 Fir tree patterns on 3° and 4° misoriented surfaces with respect to (100) and a 3D interpretation (reproduced from [6]).

2.4 Summary of static domains geometry and its relation to the properties of grain oriented steel

Summarising information in Chapter 1 and Section 2.2, it is known that

1. Domain wall width can be found by differentiating (1.10) with respect to l_d, it gives a relationship $l_d = \pi\sqrt{A/K}$ where A-is the exchange parameter, K – effective constant of magnetic anisotropy (combining crystalline, strain or any over anisotropy, for unstressed cube-anisotropy material K is roughly equal to K_1).

For 3%Si-Fe $K_1 = 3.5 \cdot 10^4$ J/m^2, $A = 2 \cdot 10^{-11}$ J/m, hence $l_d = 7.5 \cdot 10^{-8}$ m

For materials with small anisotropy such as Co-based amorphous alloy l_d can be as large as 3 μm [11].

A – might be estimated from the Curie temperature of the material [3].

2. Bar-domain spacing in GO steel is more relevant value for this investigation.

By considering that the observed structures are those which minimise the total energy, Spacek [12] obtained the relationship between domain spacing, 2L, and grain diameter, D,

$$2L = \left(\frac{12\pi D}{4M_s^{\,2} + K_1} \right) \frac{1}{\theta} \qquad (2.1)$$

where M_s is in Tesla and θ is in radians. The equation is controversial and more resent authors agree with its general trends, but not quantitatively [6], [13]. Width of bar domains usually lie in the range from 0.2 to 5 mm and depends on sheet thickness and grain size [14] and weakly depends on alignment between neighboring grains.

There are also idealised domain models in [15] and [16] for single crystal samples that take account of the geometry of a single crystal.

3. In order to minimise energy of individual wall under static conditions in the ideal Goss textured steel, domain walls are inclined at 32° to the surface [4], [19], as shown in figure 2.4e. Sometimes they fold, forming a bracket or zigzag walls.

In ideal cube oriented steel the domain wall are perpendicular to the surface.

4. Lancet domains size:

A quantitative theory for lancet domains is discussed in [17]. The width W_o and the length L_o of lancet domain on the surface tilted at θ angle to the [001] direction is given as

$$W = \frac{1}{\theta}\left(\frac{\sqrt{8}\gamma_{180}\gamma_{90}d}{C_s^2}\right)^{1/3}, \qquad L = \frac{1}{\theta}\left(\frac{8\gamma_{90}{}^2 d^2}{C_s\gamma_{180}}\right)^{1/3} \tag{2.2}$$

were γ_{180} and γ_{90} are wall energies of 180° and 90° domain walls, d is the sheet thickness. The closure coefficient C_s is proportional to K_1 for large anisotropy crystals such as GO steel. For 0.3 mm thick steel sheet with misorientation θ = 3°, and parameters from [6]: K_1= 3.5 ·10^4 J/m^2, γ_{180} = 2.76, $\gamma_{90} = 1.42\sqrt{AK_1} = 1.2\cdot 10^{-3}$, the width of lancet is 0.01 mm.

5. Lancet combs appear at critical values of sheet thickness and angles of tilt θ and transverse tilt as explained in [6].

2.5 Phosphate coating and its effect on domain structure and magnetic properties of grain oriented Si-Fe sheet

Grain oriented Si-Fe laminations as used in transformers are coated with an insulating layer in order to limit a current flowing from one sheet to another and thereby reduce eddy current losses. The coating insulation is provided by two different coatings laid during the final steps of the production process.

A silicon dioxide (SiO_2) coating is the primary surface layer formed in Si-Fe production during oxidising de-carburisation annealing. A second coating is applied comprising aqueous magnesium oxide (MgO) slurry. The Si-Fe is purified and recrystalised into its final (110)[001] texture by a further annealing process. The MgO coating is applied mainly to serve as an annealing separator to prevent sticking of adjacent coil wraps [21]. As a side effect, the MgO reacts with the SiO_2 and forms a forsterite ($MgSiO_4$) coating (often termed mill glass base coating [22]). A final insulating phosphate coating is applied which in addition to giving good dielectric properties applies a planar tensile stress dominantly along the rolling direction [22]. The tensile stress occurs because the thermal coefficient of expansion is less than that of the steel, when it cools down to room temperature after coating application.

Power loss and stress sensitivity (particularly magnetostriction) of electrical steel have been shown to be reduced upon application of a uniaxial tensile stress parallel to the rolling direction [23], [24]. The imparted stress dictates the domain configurations that occur, which in turn reduce power loss and magnetostriction.

It has been shown in application of a uniaxial stress parallel to the rolling direction of 3% Si-Fe substantially removes the density of lancet supplementary

domain structures [25], [26]. The tensile stress also results in a refinement of the main 180° wall spacing. This in turn dictates the total core loss, as the eddy current component is dependent on the spacing of the 180° walls [22], [27]. This is explained in section 2.6.

In conventional grain oriented SiFe, the reduction in total core loss is small because of the relatively poor (110)[001] texture (i.e. with average grain misorientation $\pm$ 7°). The reduction in loss is much higher in high permeability grain oriented Si-Fe because of its improved (110)[001] texture (i.e. tilt missorientation <4°). Shilling and Foster [28] showed that a tensile stress of 6.9 MPa resulted in core loss reduction of 10 – 14 % at 1.7 T, 50 Hz, as opposed to less than 3 % reduction in conventional steel under the same conditions. The coating holds steel in a state of tension at about 1.2 MPa along the rolling direction [29], so that the proportional decrease in loss is anticipated about 2%.

Losses can be further affected by applying lines of stress on the steel surface. Mechanical scribing [30] and laser scribing [31], [32] transverse to the sheet rolling direction are methods that have been found to be effective in reducing the domain spacing and lowering the losses. Surface grooving creates artificial grain boundaries which cause *domain refinement*. Similarly, surface deformation by spark ablation [33], [34] can be used to reduce wall spacing. In grain oriented Si-Fe material with almost ideal Goss texture, it has been shown that the number of active domain walls increases by about three times after laser scribing and thereby reduces the distance which individual domain walls travel during a magnetisation cycle, so mean speed and thereby dynamic loss are also reduces [35].

2.6 Domain wall motion due to an external field

Dynamic processes during magnetisation are determinated by motion of domain walls. During this motion some dissipation of energy takes place, so it is necessary to consider the various forces acting upon the boundaries, and how each force influences the wall motion. The general equation of motion for a wall moving a distance, x, is [4]

$$2\mu_0 \mathbf{M}_s \cdot \mathbf{H} = m\ddot{x} + \beta\dot{x} + ax + T \qquad (2.3)$$

where the term on the left hand side is the magnetic force due to the applied field, H, as discussed in Section 4.4.1. The terms on the right hand side are:

1. An inertial force, $m\ddot{x}$, where m is the virtual mass of the wall as a measure of inertion of spins. This term is negligible below frequencies of 10 MHz.[3];
2. A damping force, $\beta\dot{x}$, where β is a viscous damping factor that consist of two terms $\beta = \beta_r + \beta_e$. β_r – is the spin relaxation damping factor that has to be taken into account only in the GHz range. β_e - is the damping factor due to eddy currents which is relevant at power frequencies and is explained in details in Section 2.6.3.
3. A restoring force, ax similar to that of a stretched spring causing it to revert to its original position. It is believed to originate from fluctuations in energy due to internal stress as discussed in Section 2.6.2.
4. A surface tension force, T, due to the wall surface energy. It is introduced because of domain wall bowing, where the walls become curved by moving more quickly at the sample surface than at the centre of a sample. This effect was first observed by Williams et al [37] and recently by other workers [18], [38]. In GO steel at high rates of magnetisation the walls are considered to be infinitely flexible, bowing being restrained only by a surface tension force, T [4].

Only the second, third and fourth terms are relevant for steel at 50 Hz magnetisation. The idealised one dimension model of single domain wall moving across symmetrical endless slab is discussed in the next sections.

2.6.1 Motion of planar rigid wall at low speed in an ideal nonconductive medium

If the magnetic field H is applied to a material the energy per unit volume is

$$E_H = -\mu_o M_s \cdot H \qquad (2.4)$$

Consequently the energy change caused by displacement of a 180° domain wall by a distance x is

$$\Delta E = -2\mu_o A\, \mathbf{M_s} \cdot \mathbf{H}\, x \qquad (2.4)$$

where A is the area of the wall. Therefore the force per unit area on such a wall is

$$F = -\frac{1}{A}\left(\frac{dE}{dx}\right) = 2\mu_0 \mathbf{M_s} \cdot \mathbf{H} \qquad (2.5)$$

From this equation the initial susceptibility of an idealized specimen with a rigid wall can be calculated, see [1].

When a domain wall moves in a potential field and does not experience any dissipation of energy its motion is completely reversible. When the external field is removed, the domain wall returns to its previous position of magnetostatic equilibrium defined by the solution of Brown's equation [38]. The magnetisation returns to point **O** following initial curve in figure 1.7.

At larger applied field magnetisation exhibit some hysteresis. It can be imaged that the domain walls are impeded in their movements by regions of strains and/or point defects which both provide local energy barriers which the domain wall needs to overcome, as illustrated in figure 2.6a.

2.6.2 Critical field when a planar domain wall is impeded by an imperfection

There are two approaches that originate from interpretation of pinning regions as impurities or strains, i.e.:

1. Inclusion domain wall pinning (on nonmagnetic inclusions, voids and cracks) – postulated by Kersten [39], see figure 2.6c;
2. Disperse field theory - proposed by Neel [40], where non uniformity is presented as a smoothly varying potential energy due to local strains as illustrated in figure 2.6b.

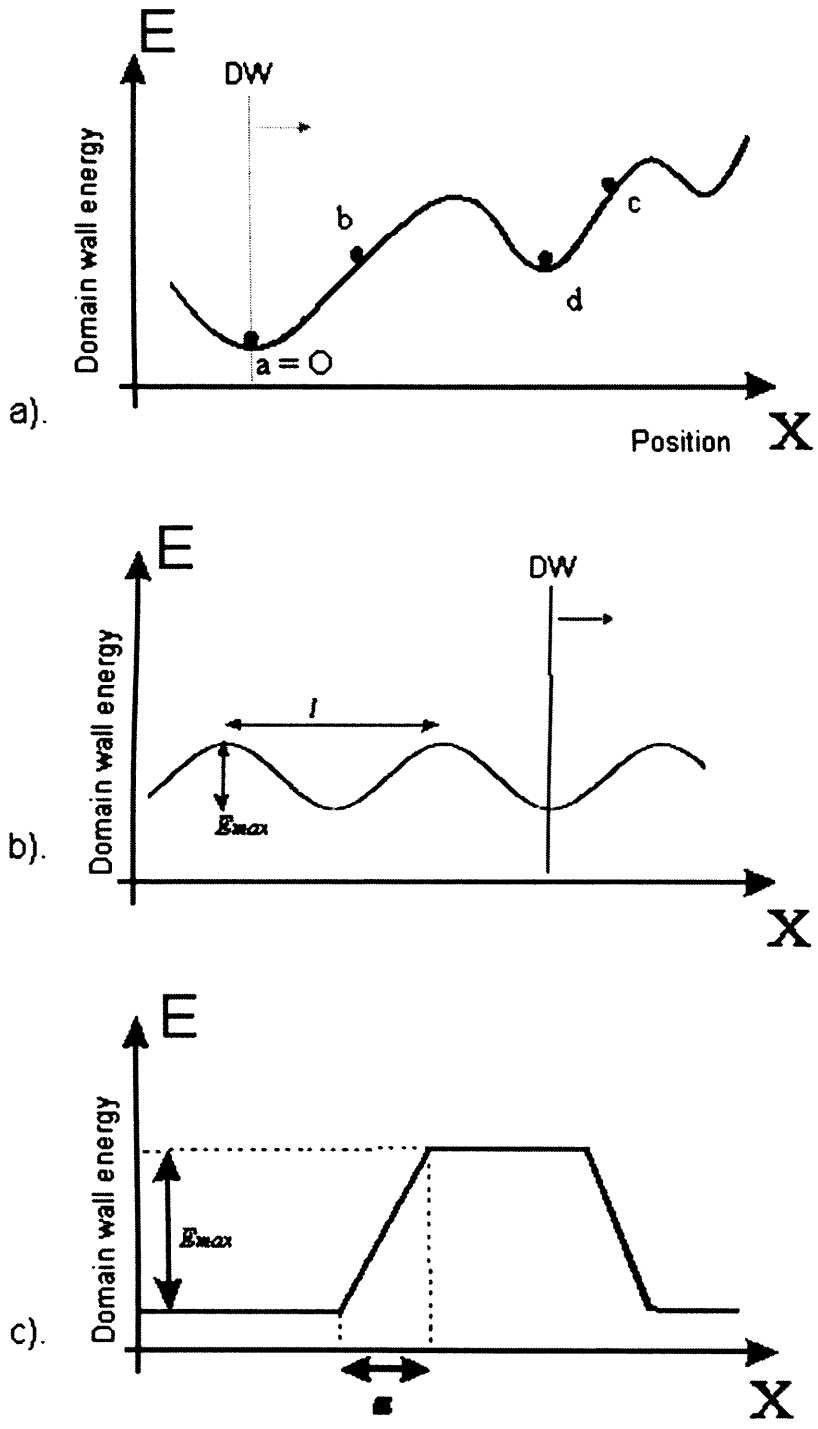

Fig. 2.6 Schematic of variation of total wall energy potential with position X (a) –random, (b) –sinusoidal "washboard", (c) – trapezoidal. (after [1]).

Both these models are correct under certain conditions and give good agreement with experiments [41].

In this work a very simplified model of pining mechanism taken from [1] is used. If the potential energy is given by $E_p = E_p(x)$ and the maximum slope of this is $\left[\frac{dE_p(x)}{dx}\right]_{max}$ then at the critical field the force per unit area must be exerted on the wall

$$F_{max} = \left[\frac{dE_p(x)}{dx}\right]_{max} \qquad (2.6)$$

So the critical field, above which the wall breaks away from its pinning site can be found from equation 2.5

$$H_{crit} = \frac{F_{max}}{2\mu_0 \mathbf{M}_s \cos\alpha} = \frac{1}{2\mu_0 \mathbf{M}_s \cos\alpha}\left[\frac{dE_p(x)}{dx}\right]_{max} \qquad (2.7)$$

Partial cases of potential field illustrated in figures 2.6b and 2.6c can be considered with analytical equation for $E_p(x)$. These are sinusoidal and trapezoid examples of Neel's *disperse field theory,* which assume that wall is rigid.

Step like potential barrier (what is a trapezoid with a limit value $a \rightarrow 0$) is an example of strong pinning. A bowing of the domain wall occurs due to the strong pinning, so that a different model must be used.

The flexible wall model for a nonconductive medium was developed by Globus [43] and helped to derive an initial susceptibility of ferrites. The domain wall is imaged like a flexible membrane, and analysed by the analogue with a liquid surface. With such a model it is easy give an interpretation of reversible and non-reversible wall motion. Modern use of this model can be found in [38], [44].

Hysteresis of the material can be explained as domain walls hung up on non-magnetic inclusions, grain boundaries, stress regions and rough surfaces. A domain wall pinned to an inclusion rests in a small energy well and snaps away if the applied field excides a barrier. When this happens the domain wall accelerates suddenly. In a conductive material micro eddy currents arise from the motion and energy is wasted, which is realised as heat. If magnetisation is performed at a low rate (slower than 1Hz) the obtained B-H loop is called a "*DC loop*" and the related power loss is called "*static*" or "*hysteresis*" loss.

2.6.3 Eddy current damping of moving domain wall and power loss

According to Faraday's law, current is generated in the sample's perimeter proportionally to rate of magnetic flux that passes through its cross-section. If only one 180° moving wall is present, as in figure 2.7, the whole flux change is due to this wall and all eddy currents are circulating in the vicinity of this wall. The damping force emerging from the induced eddy current is dominant in a conductive material such as electrical steel.

Eddy currents are responsible for most of energy loss when a material is AC magnetised. For loss estimation let's consider a low speed limit.

Assuming that the wall is a two-dimensional surface, as shown in figure 2.7, the internal wall structure and wall thickness are neglected. The magnetisation flux Φ linked to each limb cross-section is proportional to the domain wall position along the x direction. If d is the sheet thickness, we can write

$$\frac{\partial \Phi}{\partial t} = 2\mu_0 M_s v d \qquad (2.9)$$

where $v = dx/dt$ is the domain wall velocity.

The eddy current distribution around a domain wall can be derived from Maxwell's equations. Making some simplification for a single domain wall the solution of the problem is presented in [44].

At any point inside a sheet the eddy current density j is presented by orthogonal components j_x and j_y given by

$$j_x = \frac{2\sigma}{d}\frac{\partial \Phi}{\partial t}\sum_{odd\_n}\frac{(-1)^{(n-1)/2}}{n\pi}\sin\frac{n\pi y}{d}\exp\left(\frac{-n\pi|x|}{d}\right) \qquad (2.10)$$

$$j_y = \pm\frac{2\sigma}{d}\frac{\partial \Phi}{\partial t}\sum_{odd\_n}\frac{(-1)^{(n-1)/2}}{n\pi}\cos\frac{n\pi y}{d}\exp\left(\frac{-n\pi|x|}{d}\right) \qquad (2.11)$$

where σ is the electric conductivity, x and y are the coordinates of the point relatively to the wall centre ($x = 0, y = 0$). The two signs refer to the $x > 0$ and $x < 0$ regions, respectively. The behaviour of the eddy-current density is represented in figure 2.8. The eddy-current density is concentrated in a region of width ~ d around the domain

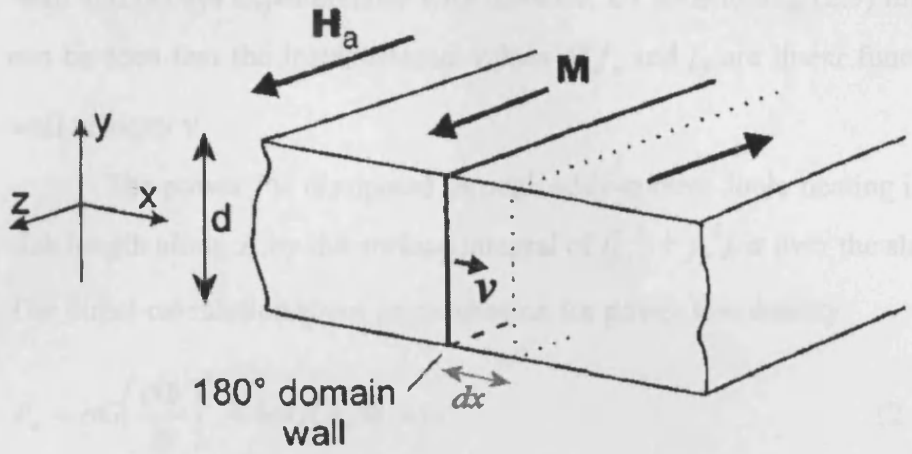

Fig. 2.7 Moving 180° domain wall geometry in an infinite slab.

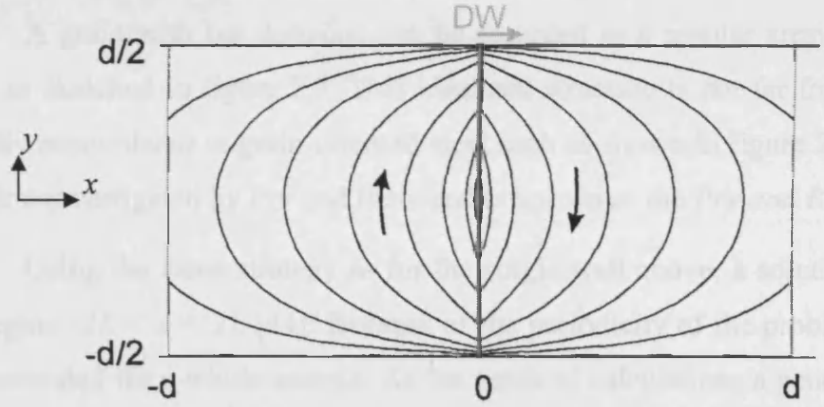

Fig. 2.8 Eddy-current flow contours calculated from equations 2.10, 2.11 around a 180° domain wall located at $x = 0$ and moving to the right of the figure. The magnetisation in the two domains is oriented as in Fig. 2.7. (modified after [44]).

wall and decays exponentially with distance. By substituting (2.9) into (2.10, 2.11) it can be seen that the instantaneous values of j_x and j_y are linear functions of domain wall velocity v.

The power Pw dissipated through eddy-current Joule heating is given, per unit slab length along z, by the surface integral of $(j_x^2 + j_y^2)/\sigma$ over the slab cross-section. The direct calculation gives an expression for power loss density

$$P_w = \sigma G\left(\frac{\partial \Phi}{\partial t}\right)^2 = 4\sigma G(\mu_0 M_s v d)^2 \qquad (2.12)$$

where geometry constant G for GO steel is equal to 0.1356 [44]. This equation shows that power loss is proportional to v^2.

2.6.4 Dynamics of a bar-like domain structure

A grain with bar domains can be regarded as a regular array of 180° domain walls as sketched in figure 2.9. This idealized structure is not far from the structures actually encountered in grain-oriented steel such as shown in figure 2.2. This problem was first investigated by Pry and Bean and is known as the *Pry and Bean model* [45].

Using the same strategy as for the single wall above, a solution was found in the region $-2L < x < 2L$ [44]. Because of the periodicity of the problem, the solution was extended for a whole sample. As the result of calculations a general formula was found for instantaneous loss per unit volume $P_{PB}(t)$ in a slab portion $0 < x < 2L$ and is given by

$$P_{PB}(t) = \frac{\sigma}{2Ld}\left(\frac{\partial \Phi}{\partial t}\right)^2 \frac{2}{\pi^3} \sum_{odd\_n} \frac{1}{n^3}\left[cth(n\pi \frac{L+x}{d}) + cth(n\pi \frac{L-x}{d})\right] \qquad (2.13)$$

where the time dependence is in x and $d\Phi/dt$.

For the case of magnetisation well below saturation, i.e., $x << L$, x can be neglected in comparison to L, which gives

$$P_{PB}(t) \cong \frac{\sigma}{2Ld}\left(\frac{\partial \Phi}{\partial t}\right)^2 \frac{4}{\pi^3} \sum_{odd\_n} \frac{1}{n^3} cth(\frac{n\pi L}{d}) \qquad (2.14)$$

Two extreme limits can be considered using this equation:

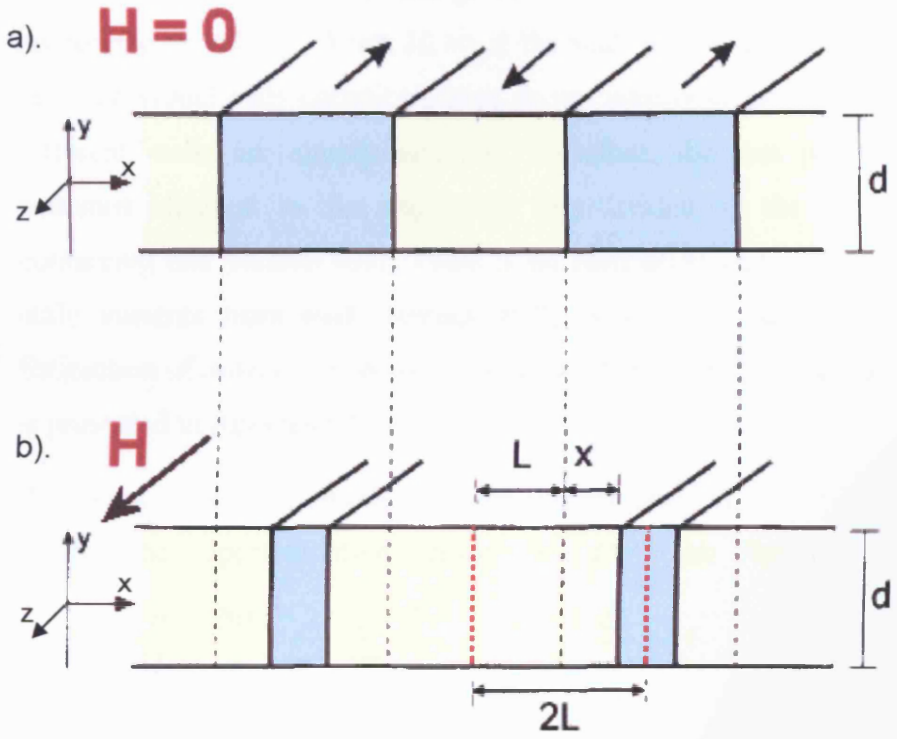

Fig. 2.9 Periodic array of bar-like domains of spacing 2L. a) demagnetised, b) instantaneous displacement x due to magnetisation in the z direction (modified after [44]).

1. If the domains are much wider than a slab thickness $2L >> d$, as in figure 2.10a. than the *coth* terms of equation 2.13 are all close to unity, so that

$$P_{PB}(t) \cong \frac{\sigma}{2Ld}\left(\frac{\partial \Phi}{\partial t}\right)^2 \frac{4}{\pi^3} \sum_{odd\_n} \frac{1}{n^3} = \frac{\sigma G}{2Ld}\left(\frac{\partial \Phi}{\partial t}\right)^2 = \frac{1}{2Ld} P_w(t) \qquad (2.15)$$

where *Pw* is the single-wall loss given by Eq. (2.12). Equation (2.15) can be interpreted as follows. When $2L >> d$, the walls are far apart from each other, their individual eddy-current patterns do not superpose, and the losses due to different walls are simply additive. Therefore, the loss per unit volume becomes identical to the single-wall loss divided by the slab area, $2Ld$, containing one domain wall. There is no correlation and cross-cancelling of eddy currents from each domain wall, as can be seen in figure 2.10a. Estimation of power loss for single and two domain walls in the same volume is presented in Appendix 5.1.

2. If the domain width is smaller than the slab thickness (i.e., $2L < d$) as in figure 2.10b, the approximation $cth(x) = 1/x$, can be used to give

$$P_{PB}(t) \cong \frac{\sigma}{2Ld}\left(\frac{\partial \Phi}{\partial t}\right)^2 \frac{2}{\pi^4} \sum_{odd\_n} \frac{1}{n^4}, \qquad \frac{2L}{d} << 1 \qquad (2.16)$$

The average induction rate in the slab can be presented as $\frac{\partial B}{\partial t} = \frac{1}{2Ld}\frac{\partial \Phi}{\partial t}$, hence

$$P_{PB}(t) = \frac{\sigma d^2}{12}\left(\frac{dB}{dt}\right)^2 = P_{cl}(t) \qquad (2.17)$$

This is an expression for so called *classical losses* [2] for uniform 'domainless' material. In other words the wall generated eddy currents are so finely distributed that they cancel each other but only at the surface. According to equations 2.15 and 2.17, the influence of magnetic domains on eddy-current loss is measured by the ratio, $2L/d$. Only when the domain size exceeds the slab thickness does the dynamic loss become definitely larger than the "classical loss". The analysis above is limited to the low-amplitude approximation, $x << L$. However Bertotti [44] postulated that the conclusions reached above for $x << L$ are nearly true for higher amplitude $x \sim L$.

The generalised power loss estimation using Pry and Bean model can be found in [46]

The **mobility** of the wall β_e can be calculated from Eq. 2.3.

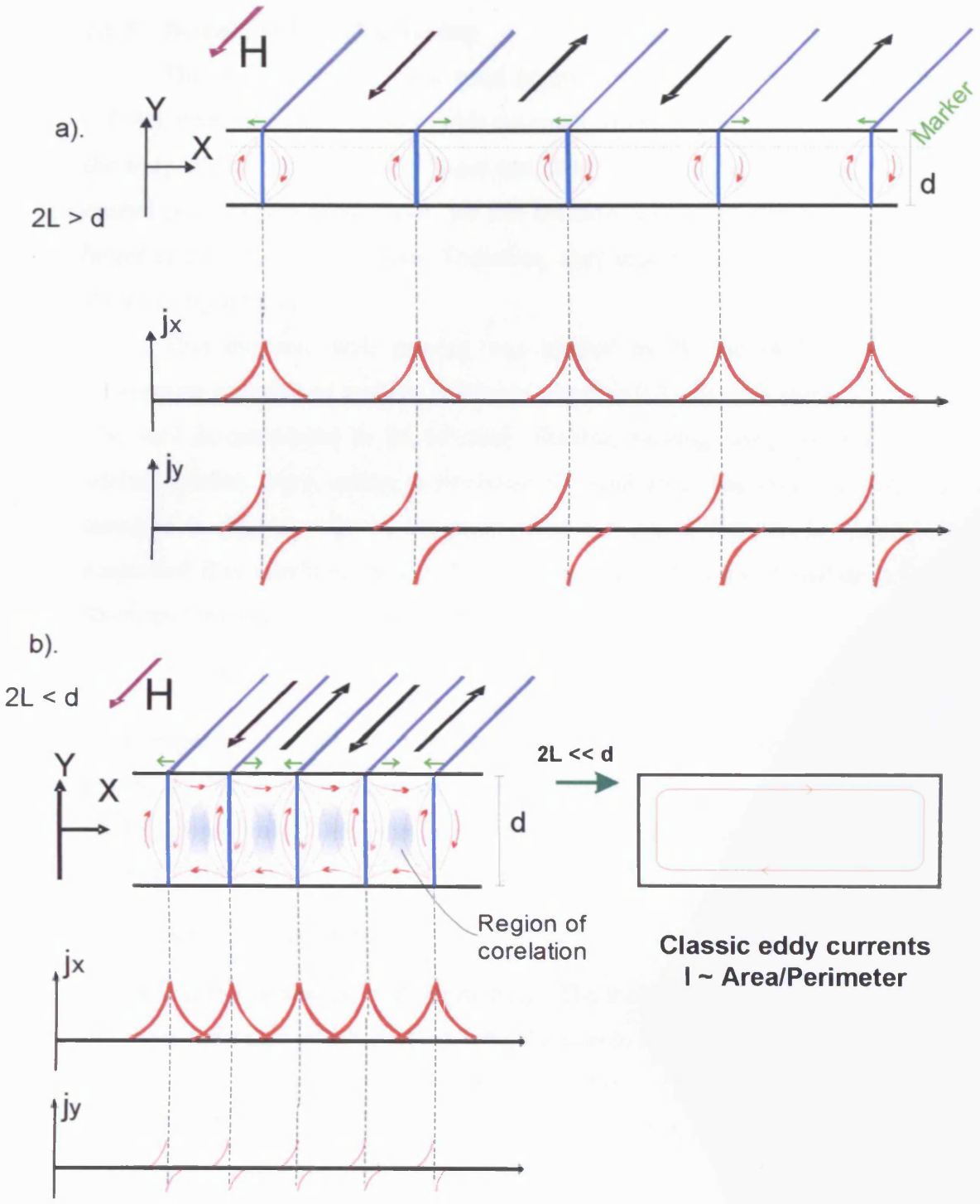

Fig. 2.10 Pry & Bean model of periodic bar-like domains with (a) 2L > d, (b) 2L < d. The lower plots give a schematic representation of single wall eddy-current components encountered when moving across the slab along the **Marker** (modified after [44]).

2.6.5 Domain wall profile bowing

The rigid plane wall is a good approximation at low rate of magnetisation ($\sim f \cdot H$), where the eddy-current fields are small. However, as the frequency increases, the eddy-current fields become larger and exert a pressure on the domain walls. The crucial point is that these fields are not uniform across the slab thickness, but are larger at the centre of the slab. Therefore, they tend to distort the wall surface, as shown in figure 2.11a.

This dynamic wall bowing was studied by Bishop [47], who solved an appropriate equation of motion, similar to equation 2.3, for each segment of the wall. The wall is considered to be infinitely flexible, bowing being restrained only by surface tension force, acting to minimise the wall area. The restoring force, ax, is assumed to depend only on the mean displacement, x, that can be ignored under controlled flux condition as it will not affect the wall shape. Equation 2.3 can be rewritten for motion of each segment, i, of the wall

$$2\mu_0 \mathbf{M} \cdot \mathbf{H} = (\beta_e)_i v_i + T_i \qquad (2.18)$$

In experiments conducted within this investigation it was possible to measure the speed of the segment close to the sample surface

Bishop [47] also found that planar walls stay undistorted below the mobility limit of

$$\beta_e = 7.73/(2\mu_o \mathbf{M}_s \sigma d) \qquad (2.19)$$

Where σ is the conductivity of the material. The mobility is inversely proportional to the sheet thickness which demonstrates the non-local character of the eddy current effect. For 0.3 mm thick steel sheet this value is about 3 cm/sec. Bishop also presented theoretically the reduction in eddy current loss per cycle compared to a rigid wall model. Severe bowing leads to a relative reduction in loss roughly proportional to the cube root of the frequency and the square root of the flux amplitude.

a).

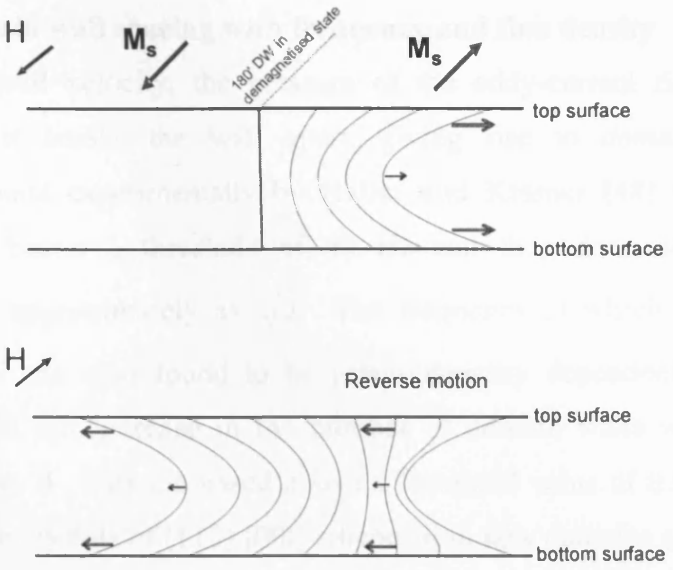

b).

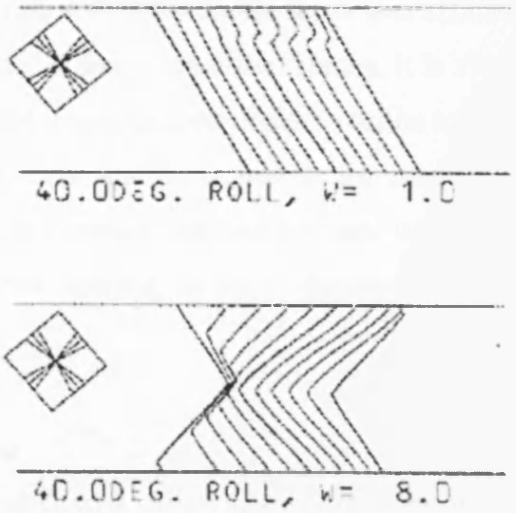

Fig. 2.11 (a) Idealised profile of eddy-current bowing of a perpendicular 180° domain wall. (b) Examples of domain wall profiles in (011) oriented steel during a half period of motion from left to right with various frequencies W. (copied from [19]).

2.6.6 Variation of domain wall spacing with frequency and flux density

With increasing wall velocity, the pressure of the eddy-current field can become so large that it breaks the wall apart, giving rise to *domain wall multiplication.* It was found experimentally by Haller and Kramer [48] that the domain width is static below a threshold of 40 Hz and then decreases with increasing frequency, f, approximately as $\sqrt{f}$. The frequency at which domain width starts to decrease was also found to be grain-geometry dependent, being usually about tens of Hz. An increase in the number of domain walls was also found as the flux density, B , was increased above a threshold value of 0.6 of the saturation value. In single crystals of (110) [00l] silicon-iron, new domains appeared near the side surfaces of the specimen. It was found that domain width varies inversely with peak induction as B_{max}.

The increase in the number of domain walls and decrease in spacing leads to nonlinear dependence of power loss per cycle on frequency, as illustrated in [49]. The condition of narrow domains (2L < d) is favorable for power efficiency, but a narrow domain structure is unstable under static condition. Hence, it is vital to get a material where at 50 Hz, 1.7 T sinusoidal magnetisation domains refine to the 2L < d state.

When a new wall nucleates and takes part in the magnetisation process, its existence might be unstable. This creates a discontinuous variation in the number of domain walls and therefore the spacing, at some frequencies was investigated by Wadekar and Kramer in [50].

2.6.7 Irregular wall motion

All domain theories discussed earlier assume that the walls move smoothly and, for sinusoidal time varying induction, in a sinusoidal manner. In practice, however, domain walls have been shown to move in a jerky fashion [49] and that, especially at very low frequencies, there is a wide variation of wall velocities. Since the eddy current power loss is dependent upon the square of the wall velocity, any irregularities in the velocity will have a significant effect upon the power loss.

Boon and Robey [51], measuring hysteresis loops of individual walls in grain-oriented Goss textured silicon-iron observed the walls to move in a series of jerks during cyclic excitation. Moreover the walls moved in a different manner

when they traversed the sample in one direction than when they returned during the second half of the cycle.

Houze [25] recorded wall positions as a function of time by taking high speed movie pictures of domain structure during magnetisation. He noted that individual domain walls were arrested several times during their movements. It was also observed that any given wall did not move as an entity, but segments of the wall moved more or less independently. When segmented wall motion occurred, a portion of the wall was arrested while the remainder moved. In some instances the arrested portion of the wall appeared to be pinned at an inclusion, but in the majority of cases the pinning defect was either not on the surface of the specimen or could not be resolved. Houze concluded that the most likely cause of the observed arrests was the interaction of the walls with defects such as non-magnetic inclusions, voids and surface irregularities. This intermittent pinning of walls leads to high instantaneous wall velocities making the mean square wall velocity over a complete magnetizing cycle greater than the squared mean velocity, and therefore a proportionately higher power loss occurs. This effect of loss increase with irregular wall motion compared to the smooth wall motion is illustrated in a simplified model in Appendix 5.2.

In an array of walls, pinning of one wall has an effect on the motion of the other walls. If the induction, B, is constrained to be sinusoidal then the instantaneous wall velocity averaged over all walls, $v_{av}(t)$, must also be sinusoidal. Thus if the motion of an individual wall is interrupted by pinning, then it will move slower than $v_{av}(t)$ while it is pinned and faster than $v_{av}(t)$ for a short time after it becomes unpinned. In order for $v_{av}(t)$ to remain sinusoidal, the velocities of other walls must adjust accordingly. This process also results in an increase in losses compared to uniform wall motion since the losses are proportional to the square of the wall velocity as shown previously in section 2.6.4.

2.7 Classical method of power loss separation

A general engineering approach to the calculation of iron losses in soft magnetic materials is based on the separation of losses into hysteresis losses, classical eddy current loss and excess loss components:

Static hysteresis loss – is the energy required to magnetise a sample at a very slow rate over a full magnetisation curve as shown in figure 1.7, and is spent to overcome the pinning sites. Hysteresis loss over one period, E_h, is equal to the area inside the original B-H loop and is frequency independent. E_h depends on inclusions, grain boundaries, stress regions, surface roughness and anything else that obstructs the easy motion of domain wall. Power loss per unit time, P_h, is equal to E_h multiplied by the number of cycles passed during unit time, i.e., $E_h \cdot f$.

Classical eddy current losses – is Joule heating, $J^2 \cdot \rho$, produced by the classical eddy currents of density j. The eddy-current density is obtained from Maxwell's equations when the presence of domains is neglected, with the assumption that the electrical resistively, ρ, and magnetic permeability, μ, are constant in space and time. The loss are calculated by volume integration, and for the low frequency limit [44] is

$$P_{cl}(t) = \frac{d^2}{12\rho}\left(\frac{dB}{dt}\right)^2 \qquad (2.20)$$

The time average of equation 2.20 in the case of triangular wave of peak induction B_{max} and magnetisation frequency f, gives the average power loss

$$P^{TRI}{}_{lcl} = \frac{3}{4\rho} d^2 B_{\max}^2 f^2 \qquad (2.21)$$

Under sinusoidal induction, where $B(t) = B_{max}\sin(2\pi ft)$, a simple calculation gives

$$P^{\sin}{}_{lcl} = \frac{\pi^2}{12\rho} d^2 B_{\max}^2 f^2 \qquad (2.22)$$

Classically the total power loss is the sum of static hysteresis loss and the eddy current loss. The static hysteresis loss is proportional to the frequency and is equal to $E_h \cdot f$, whilst reference to equations 2.21 and 2.22 shows that the eddy current loss is proportional to the square of the frequency and can be expressed as $E_{cl} \cdot f^2$. Thus the total frequency dependent power loss is

$$P = E_h \cdot f + E_{cl} \cdot f^2 \qquad (2.23)$$

or in terms of power loss per cycle

$$\frac{P}{f} = E_h + E_{cl} \cdot f \qquad (2.24)$$

Thus a plot P/*f* versus *f* should produce a linear relationship of gradient E_{cl} , and intercept on the P/*f* axis equal to the static hysteresis loss E_h. The measurements always give much higher values of loss with nonlinear frequency dependence, as shown in figure 2.12. The difference between classical and experimental loss is called the *excess current loss*. There are phenomenological theories [2], [44], [46], [52], [53] that try to explain this difference. For example Bertotti in [44] consider the domain structure of the material and introduced excess loss as an extra term in equation 2.24. This third term is roughly proportional to a square root of frequency, resulting in

$$\frac{P}{f} = E_h + E_{cl} \cdot f + E_{ex} \cdot \sqrt{f} \qquad (2.25)$$

Bertotti's and other phenomenological models do not consider the real structure of the material, thus often they appear to be limited in use to one material and give large errors if the material is changed.

A more likely error in the classical theory assumptions (and its modifications) lies in the supposition that the magnetisation changes by isotropic rotation of the magnetisation vector. The existence of domains is now well established, and it is known that magnetisation changes are due firstly to the movement of domains walls, and only after this motion is complete does magnetisation rotation take place. The existence of domain structures results in non-uniform permeability since all the magnetisation changes take place at the walls, leading to a high permeability being associated with the walls whilst elsewhere in the saturated domains the permeability is unity. Thus any power loss theory should be based upon a domain structure and the motion of domain walls.

Nevertheless, equation 2.25 is a good engineering approximation for practical tasks without any attempt to explain detail of behavior on a fundamental basis.

Summarising the above, the loss separation models are suitable for core design and loss prediction in applications. However the domain structure has to be considered at the material development stage and verified on small samples of the material where domain observation is possible.

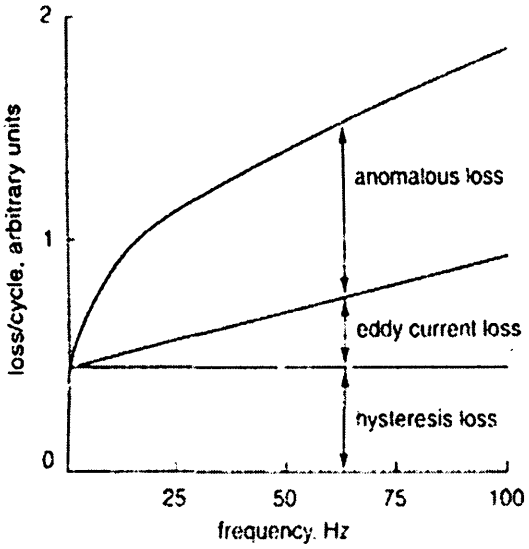

Fig. 2.12 Components of loss for grain-oriented steel (reprinted from [2])

2.8 References of chapter 2

1. Jiles D., Introduction to magnetism and magnetic materials, Chapman and Hall, New York (1991).
2. Fiorillo F., Power losses in soft magnetic laminations, Metallurgy and Magnetism Workshop, V7, (2004).
3. Chikazumi S., Physics of magnetism –2nd Edition, Malabar (1978).
4. Morgan J.V.S., Losses in 3.25 per cent grain-oriented silicon-iron, PhD. Thesis, University of Wales (1980).
5. Sharp M.R.G., Phillips R., Overshott K.J., The variation of domain wall motion throughout the magnetization cycle in grain-oriented silicon-iron, Proc. IEE, 120, p822, (1973).
6. Hubert A. and Schafer R., Magnetic domains, Springer, Berlin (1998).
7. Kawalla R., Schneider J., Hensel A., Workshop Metallurgy and Magnetism, V11, (2004).
8. Paxton W.S., Nilan T.G., Domain configurations and crystallographic orientation in grain oriented silicon steel, J. Appl. Phys., 26, p994, (1955).
9. Rose R.M., Shepard L.A. and Wulff J., The structure and properties of materials, IV, New York, John Wiley & Sons, Inc (1966).
10. Kuppers D., Kranz J., Hubert A. Coercivity and domain structure of silicon-iron crystals. J. Appl. Phys.,39, p608, (1968).
11. Zubov V. Kudakov A., Giant domain wall in Co-based amorphous alloy. SMM 16 V2. p749, (2003).
12. S'pac'ek, L., The domain configuration on polycrystalline material, Czech. J. Phys.,6, 3, p256, (1956).
13. Nozawa T., Misogami M., Mogi H., and Matsuo Y., Domain structures and magnetic properties of advanced grain-oriented silicon steel, J. Magn. Magn. Mat., 133, p115, (1994).
14. Phylipov B.N., Tankeev A.P., Dynamic effects in ferromagnetics, Nauka, Moscow, (1987).
15. Usov N.A., Peschany S.E., Modeling of equilibrium magnetisation structures in fine ferromagnetic particles with uniaxial anisotropy, J. Magn. Magn. Mat., 110, L1-6, (1992).
16. Sakaki, Y., An approach estimating the number of domain walls and eddy current losses in grain-oriented 3% Si-Fe tape wound cores, IEEE Trans. Magn., 16, 4, (1980).
17. Arai S., Hubert A., The profiles of lancet-shaped surface domains in iron, Phys. Status Solidi A, 147, p563, (1995).
18. Mohd Ali B.B., Computer mapping of grain structures in grain-oriented Silicon-Iron, PhD Thesis, University of Wales (1985).

19. Bishop J. E. L., Threapleton M. J., An analysis of domain wall ruckling initiated at the points of maximum shear-stress on a bracket wall in (110)[001] SiFe, J. Magn. Magn. Mat., 40, 3, p293, (1984).
20. Sharp M.R., Horner J.T. A theoretical analysis of the frequency dependence of domain wall spacing in a ferromagnetic sheet, J. Phys. D: Appl. Phys. 6, 15, p1835, (1973).
21. Morris W.G and Shilling J.W. Effect of Forsterite coatings on the domain structure of grain oriented 3% Si-Fe, IEEE Trans. Magn, 14, 1, p14, (1978).
22. Fortunati S., Grain Oriented Electrical Steels: Status and Trends, Workshop Metallurgy and Magnetism Proceedings, V15, (2004).
23. Taguchi S. and Sakakura A. Characteristics of magnetic properties of grain oriented Silicon Iron with high permeability, J. Appl. Phys, 40, p1539, (1969).
24. Soinski M. and Moses A.J., Anisotropy in iron-based soft magnetic materials, in Handbook of Magnetic Materials, ed. By Buschow K.H.J., Elsevier, (1995).
25. Houze Jr.G.L. Effect of longitudinal tensile stress on the static and 60 Hz domain structures of grain oriented silicon steel, J. Appl. Phys., 40, 3, p1090, (1969).
26. Werner F.E., Electrical steels 1970-1990, in Energy Efficient Electrical Steel, conf. proc. 1980 AIME, ed. by Marder A.R.
27. Masui H., Influence of stress condition on initiation of magnetostriction in grain oriented silicon steel, IEEE Trans. Magn., 31, (2), p930, (1995).
28. Shilling J.W., Foster K., Effect of tensile stress on domain structure and magnetic properties of oriented 3% Si-Fe, European Physical Society Conf. Proc.: Soft Mag. Matls. Cardiff, Wales, p13, (1975).
29. Moses A.J., Meydan, T.; Lau, H.F., Domain structures in silicon-iron in the stress transition stage, IEEE Trans. Magn., 31, (6), p4166, (1995).
30. Yamamoto T., Taguchi S., Tanaka O. and Nayama H., The effect of tensile stress on core loss of grain oriented 3% silicon iron, European Physical Society Conf. Proc.: 15th Soft Mag. Matls. Cardiff (1975).
31. Krause R.F., Rauch G.C., Kasner W.H., Effect of laser scribing on the magnetic properties and domain structure of high permeability 3% Si-Fe, J.Appl. Phys., 55, 6, p2121, (1984).
32. Weidenfeller B., Rieheman W., Domain refinement and domain wall activation of surface treated Fe-Si sheets, J. Magn. Magn. Mat., 160, p136, (1996).
33. Beckley P., Snell D. and Lockhart C., Domain control by spark ablation, J. Appl. Phys., 57, 1, p2412, (1985).
34. Taylor R., New techniques for practical quality assessments in grain oriented silicon steel, PhD Thesis, University of Wales (2002).
35. Yamaguchi S., Ichiyama T., Laser processing for reducing core loss of grain oriented silicon steel, J. Appl. Phys., 53, 3, p2410, (1982).

36. Walker L.R., report in J.F Dillon Jr., Domains and domain walls, in: magnetism, Vol. 3, ed. by G.T. Rado, Academic Press, New York, (1963).

37. Williams H.J., Shockley, W., Kittel, C., Studies of the Propagation Velocity of a Ferromagnetic Domain Boundary Phys. Rev., 80, pl090, (1950).

38. Yoon S.S., Kwon S.D., Kim C.G., Effect of ion-implantation on magnetization processes of 3% SiFe determined by susceptibility spectrum, J. Magn. Magn. Mat., 239, p513, (2002).

39. Dragoshanskiy, Y..N,. Zaykova, V.A., Tiunov, V.F., Phys. Met. Metal, 39, p61, (1975).

40. Kersten, M., Grundlagen einer Theorie der ferromagnetischen Hysterese und der Koerzitivktraft, S. Hirzel, Liepzig, reprinted by J.W. Edomain wallards, Ann. Arbor., (1943).

41. Neel L., Ferromagnetismus, Ann. Univ. Grenoble, v22, p299, (1946).

42. Bozorth R. M., Ferromagnetism, An IEEE Press classic reissue, (1993).

43. Globus A., Influence des dimensions des parois sur la permabilite initiale, C.R. Acad. Sci., 255, pl709, (1962).

44. Bertotti G., Hysteresis in magnetism, Academic press, San Diego (1998).

45. Pry R. H. and Bean C. P., Calculation of the energy loss in magnetic sheet materials using a domain model, J. Appl. Phys., 29, p532, (1958).

46. Matsuo T., Shimasaki, M. Simple modeling of the AC hysteretic property of a grain-oriented silicon steel sheet, IEEE Trans. Magn., 42, 4, (2006).

47. Bishop J. E.L., Eddy current dominated magnetisation processes in grain oriented silicon iron, IEEE Trans. Magn., 20, 5, pl527, (1984).

48. Haller T.R and Kramer J.J., Observation of Dynamic Domain Size Variation in a Silicon-Iron Alloy, J. Appl. Phys. 41, pl034, (1970)

49. Bishop, J.E.L., Pfutzner H., Domain wall bowing and dynamic domain width in grain oriented SiFe, IEEE Trans. Magn., 30, 1 , p46, (1994).

50. Wadekar S. and Kramer J.J., Reproducibility of domain wall motion in Metglas 2826, J. Appl. Phys. 61, p4225, (1987).

51. Boon C.R., Robey J.A., The hysteresis loops of individual domain walls and domain-wall motion in grain-oriented 3% Si-Fe, J. Phys. D: Appl. Phys., 3, p327, (1970).

52. Zirka S.E., Moroz Y.I., Marketos P. and Moses A..J., Viscosity-based magnetodynamic model of soft magnetic materials, IEEE Trans. Magn., 42, 5, (2006).

53. Winner H., Naber W., Sander R., and Grosse-Nobis W., Dynamic and hysteresis losses, Phys. Scripta 39, (1989).

CHAPTER 3 REVIEW OF DOMAIN IMAGING TECHNIQUES

3.1 Historical introduction

In this chapter methods of observing magnetic domain structures are briefly reviewed and compared and the potential use of dynamic observation is examined.

The first idea for observing magnetic domains belongs to Bitter (cited in [1]) who attempted the first direct observation of static magnetic domain structures with fine magnetic powder. Bitter observed irregular patterns due to stresses in the surface of the samples. At the time however, a theoretical understanding of magnetic domains did not exist and therefore what the pattern should look like was not known.

The first correct theoretical prediction of ferromagnetic domain structures was made by Landau and Lifshitz (cited in [1]). They predicted the structure of domains separated by 180° walls, with the 90° walls separating the closure domains at each end of a sample. They also calculated the width of the domains and the effect of an external applied field on the structure.

In 1949, Williams, Bozorth, and Shockley, [2], completed the long-awaited task of providing photographs of well-defined domain structures. The observations were in agreement with the predictions of Landau and Lifshitz (see section 1.5).
This method, known as the Bitter technique, is based on the phenomenon of attraction of fine particles to magnetic poles at the surface of ferromagnetic material. These stray field regions are typically formed by the intersection of domain walls at the surface. Colloid particles suspended in liquid are stirred by Brownian motion and settle more smoothly than dry powder. Another enhancement modification of the Bitter method is seen in the "*Orb viewer*" described in [3]. Normally, colloid particles are attracted mainly to regions of maximum gradient of the stray field H_s generated by Bloch walls. However, by applying a field (H_e) normal to the sample surface Bitter patterns are often seen to consist of alternate bands corresponding to anti-parallel domains.

Despite the simplicity and wide application of the Bitter method it is very limited with regards to dynamic domain observation. By stirring a suspension after each picture is taken, it is possible to record a quasi static movie with approximately 1 frame per second. Also the Bitter pattern method is indirect by its nature because it senses stray field and not the magnetisation vector in the domain structure.

3.2 Overview of dynamic observation methods

The demand for direct, dynamic domain observation during the magnetisation process was a key reason in the development of other methods for domain observation. A detailed overview of methods developed to date can be found elsewhere [4], [5], [6]. Some methods have high sensitivity to the magnetisation vector, hence they are direct methods. This includes all magneto-optic (MO) methods (based on Kerr, Faraday, second harmonics generation (SHG) and Voigt effects), X-ray dichroism, transmission electron microscopy (TEM) and neutron topography.

Most other methods which are in use today are indirect by measuring surface stray fields. Stray magnetic fields emergence as a consequence of the existence of magnetic domains and also as a result of the presence of grain boundaries and cracks. Apart from the Bitter pattern method and the similar magnetotactic bacteria technique field mapping techniques also include magnetic force microscopy (MFM), Hall Effect, magneto-resistive (MR) and giant magneto-resistive (GMR) sensor scanners, various electron microscopy methods, X-ray topography and Magneto-optic (MO) indicating film techniques.

In this work the interest is in dynamic *wide field* domain observation, meaning the simultaneous acquisition of information from each point in the area of interest. A key parameter for dynamic observation is the *Recording Time* ($\mathbf{t_{exp}}$) necessary for a sensor to acquire a clear enough image. Another important parameter for real time observation is the *Read Out* ($\mathbf{t_{readout}}$) time necessary for transferring the image from the sensor to the storage device.

Domain imaging techniques are classified below by the physical principle of their operation. Usage or possible usage for dynamic domain observation is examined with respect to limitations on $\mathbf{t_{exp}}$ and $\mathbf{t_{readout}}$ and the extent of the area of view.

3.3 Magneto-optical methods

The Kerr effect and microscopy equipment are explained in detail in chapters 4 and 5 respectively. The Faraday effect, which is similar in nature to the Kerr effect, is utilized in the imaging technique outlined in chapter 9. Details of the SHG effect are described in [7]. MO Kerr microscopy was the first wide-field, dynamic method of observation [8], and it remains the best in many respects. The measurement is direct, i.e. the light beam interacts with spin-oriented electrons inside a domain. Wide-field observation with spatial resolution of about 0.8μm is possible (0.4μm is

the highest theoretical resolution that can be reached with conventional microscope, 0.2μm with oil immersion objectives).

The limit of recording time is reported to be of the order of picoseconds [9], and read out time is limited by the electronics interface to units of milliseconds so that high speed observations are usually stroboscopic [10]. The fastest real time imaging reported in [11] had been carried out with t_{exp} = 40 μs and $t_{readout}$ = 0.3 ms using a mechanical film camera. Real time observation with a fast CCD camera such as the Kodak EctaPro which was tried in this investigation, was quite poor because of limited light sensitivity. The intensified camera used in this work has a minimum $t_{readout}$ = 0.55 ms and a minimum t_{exp} = 40 ns.

Second Harmonics Generation (SHG) is another MO method that allows examination of sub-surface domains. Some achievements are reported in [12].
The biggest drawback of the MO method is that the sample under investigation must be prepared so that its surface has a high degree of optical flatness.

3.4 Domain observations using a Magneto-optic indicator film

A magnetic indicator is a thin film of soft magnetic material deposited onto a transparent substrate. Fine magnetic domains on the indicatior film respond to the stray fields from the bulk sample placed underneath. It works on a Double Reflected Faraday effect and often a mirror layer is incorporated to improve light sensitivity, as shown in figure 9.1a. More details can be found in Chapter 9. The indicator film method offers high speed recording time (the same as all MO methods) and can be used in wide-field real time observations. However, the spatial resolution is limited to the size of the domains in the indicatior film itself.

3.5 Transmission Electron Microscopy (TEM)

Only thin film samples (<0.5 μm thick) are suitable for magnetic domain observation by TEM technique. A beam of electrons accelerated above 100keV energy is directed perpendicular to the sample surface (see figure 3.1). If there is a magnetic domain with its magnetisation component perpendicular to the electron beam, the electrons are deflected by the Lorentz force. Antiparallel domains will deflect electrons in opposite directions. The Lorentz force undergoes integration over the whole electron path, not only over a trajectory through a sample. Stray fields outside the sample contribute to the contrast as well. If a scintillation screen or

photographic film is placed behind the sample the electron shadow will delineate the boundaries of any domains. Because this method is based on the Lorentz force, it is called *defocused mode Lorentz Microscopy* [13]. The technique is direct and wide field*. If the picture is sufficiently bright, the dynamic processes may be recorded. The dynamics of Bloch lines has been observed stroboscopically at frequencies up to 100 MHz [14]. Other TEM techniques include: (i) Focused TEM, (ii) Differential Phase TEM, a scanning technique that offers high sensitivity and outstanding spatial resolution down to a 10 nm limit [13] that can observe directly the interaction between domain walls and lattice defects, and (iii) Differential Holography [15]. For all cases the external magnetising field can interfere with the acquistion equipment leading to a drastic effect on imaging performance. External field is limited to 3000 A/m.

Sample preparation is particularly important in TEM. Bulk material has to be thinned and surfaces must be smoother than for MO observation. The method requires high speed electrons (100 – 500keV, and up to 1000keV) which require ultra high vacuum conditions and therefore high investment costs.

3.6 Electron Reflection and Scattering Methods

These methods are appropriate for bulk samples. These techniques are extensions of SEM in which the surface is scanned by a fine electron beam. The scattered or re-emitted electrons are collected, their intensity is processed electronically and raster scanned images are stored. Depending on how reflected electrons are analysed there are a few variations of the method:

- Type 1 or Secondary Electron Contrast [16] – is sensitive to the stray field above a surface (see figure 3.2).
- Type 2 or Backscattering Contrast [17] is sensitive to the magnetisation vector and provides good contrast images on grain oriented steel (see figure 3.3). Domains down to a depth of 20μm can be viewed.
- Electron Polarisation Analysis [18] - Secondary electrons emitted from the surface are spin-polarised in the direction of magnetisation. The electrons can be accelerated and separated and the amount of s↑ and s↓ can be measured.

* *wide field* here means the ability of the apparatus to image a whole area of interest and simultaneous acquisition of information from each point in the area. Don't get confused with *field of view* definition in photography.

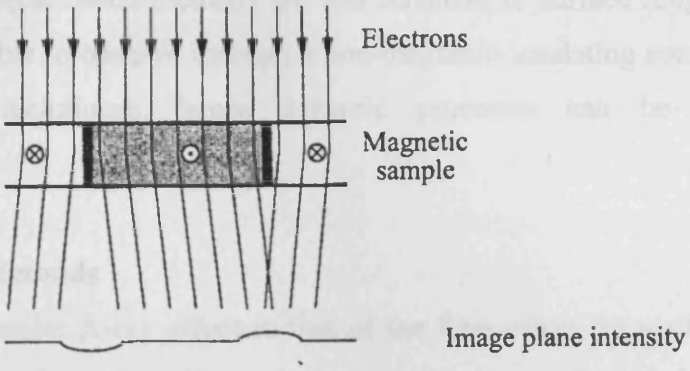

Fig. 3.1 Electron deflection and domain image formation in Lorentz TEM (reproduced from [5]).

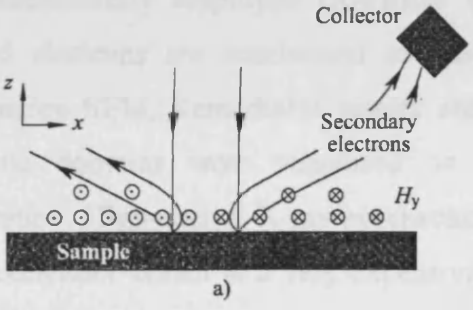

Fig. 3.2 Schematic of Secondary Electron Contrast. Electrons are deflected in the different direction due to the presence of stray field (reproduced from [5]).

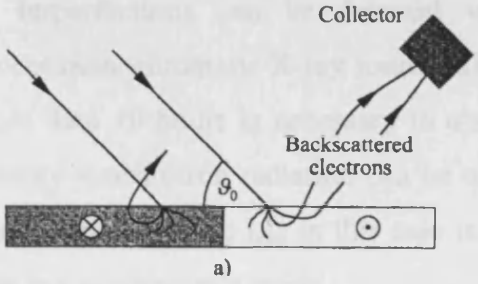

Fig. 3.3 Backscattering contrast in SEM (reproduced from [5]).

In general the SEM based methods are less sensitive to surface roughness. In some cases it is possible to observe through a non-magnetic insulating coating [19]. These are scanning techniques, hence dynamic processes can be observed only stroboscopically.

3.7 X-ray Methods

1. There is a similar X-ray effect to that of the Kerr effect for visible light. X-rays undergo changes in polarisation when transmitted or reflected from a magnetic surface, this effect is called X-ray circular dichroism and potentially can be used for domain imaging. As analysers for X-ray's polarisation are not available yet, the observation similar to Kerr microscopy is a mater of future progress.
2. The effect on the generation of secondary electrons with high-energy X-rays has been successfully employed (X-PEEM method) to study domains. X-ray photo emitted electrons are accelerated and analysed in a similar way as in Electron Polarisation SEM. Remarkable results are reported in [20] where the dynamics of magnetic domains were visualised on the nanosecond scale by stroboscopic observation. High-energy X-ray synchrotron radiation can be delivered by a storage ring accelerator which is a very expensive large science facility such as the one in Grenoble.
3. The X-ray diffraction method is used for measuring crystal spacing parameters and orientation. If a crystalline magnetic material has some magnetostrictive properties small changes in lattice distance exist between 90^{o} domains. These domain-induced crystal imperfections can be detected with Lang's scanning method using a convenient monochromatic X-ray source. The time of exposure of the method is long and more than 10 hours is necessary to obtain a scanned image [21]. Alternatively, high energy synchrotron radiation can be used in double reflected mode [22] with a wide-field exposure. The $\mathbf{t_{exp}}$ in this case is short enough for dynamic observation of domains in a stroboscopic mode.

3.8 Neutron Topography and Tomography

A neutron beam has an ability to pass through many materials in the same way as a light beam passes through glass. If polarised neutrons pass through a magnetic sample their spins interact with the spins of the electrons and nuclei. After analysing the transmitted beam it is possible to obtain an image analogous to polarised light

images, with black and white contrast between domains. In the case of unpolarised neutrons only domain walls become visible as black lines [23]. This method allows a wide field observation. There is no reported information on recording speed, so dynamic observation with this method is unknown. Taking projections at different angles it is possible to calculate a 3D image of the domain structure, similar to that in X-ray tomography but the spatial resolution is low. Finally the biggest disadvantage is that the method is very expensive and needs access to a nuclear reactor.

3.9 Stray field scanners

Stray field scanning is a technique that utilizes various types of magnetic field sensors to resolve stray magnetic fields above the surface of a material. These include:

- Hall Effect probe field scanners
- MR and GMR sensors [24]
- Vibrating pickup coil field scanning techniques
- Magnetic Force Microscopy (MFM) [25]
- Hybrid Near-Field Optical Scanning Microscopy

The main advantage of field scanners is that the field can be sensed at some distance above a sample surface, so that the mapping of the domains under a non-magnetic coating is possible. A remarkable spatial resolution down to 10 nm and good sensitivity has been reported with the MFM method [25]. A summary of field scanning methods is given in table 3.1.

Techniques	Vibrating Probe[5]	Hall Probe [5]	MR Probe [26]	GMR [24]	MFM [25]
Sensor resolution	10 μm	15-200 μm	100 μm - 2 mm	Down to 0.1 μm	10nm
Effective distance from sample surface	1 μm	13-100 μm	Up to 300 μm	Up to 300 μm	10nm
Material Application	Silicon Iron sheet	Cobalt film	Silicon Iron sheet	Silicon Iron sheet	
Imaged feature	Main domains (blurred)	Main domains	Stray field distribution only		Stray field distribution
Image quality	Very poor	Poor	Colour topogram		
Relative speed of mapping	Very Slow	Slow	Fast ~ 20,000 samples in 5 minutes	Very fast	Very Slow

Table 3.1 Features of field probe scanning techniques.

The methods listed in this table perform single point field measurements and scan the area of view point by point. This is why they are not suitable for dynamic wide field observation. Those, which have fast recording times such as MR or GMR sensors, can be used for point-by-point stroboscopic measurements of dynamic processes. For instance a sample can be embedded in a fast spinning disk and a GMR sensor in the form of a reading head can travel along a radius (as in a computer hard drive), both high spatial resolution and fast sampling may be achieved.

Recent developments in GMR sensor arrays offer better opportunities for wide-field real-time imaging. In [24] an array of 16 GMR sensors is described. The array is manufactured as an IC on a silicon substrate with a spacing of 5 μm between the sensors. Such an array enables a spatial resolution of a few microns. Also an impressive sensitivity (0.1 A/m) has been reported. Hopefully in the near future big arrays in the form of a matrix similar to CCD chips will be developed. Such a device will be very helpful for the observation of domains under the coatings of electrical steel. Smaller sensors, higher resolutions and faster signal processing may lead to such methods replacing KMO techniques for real-time observations [27].

3.10 Magnetoactic bacteria

The use of magnetoactic bacteria is an exotic method which has not been used widely. Certain bacteria use the earth's magnetic field for navigation. In the water where they live they act like small self-propelling compasses that travel to areas with maximum flux density. Placed on a magnetic sample, they move along the lines of the stray field until they reach – within a few seconds – the northern end of a field line at the sample surface. The method of static domain observation, similar to the Bitter method, is described in [28]. The ability of motion of the bacteria [29] can be used for slow (0.1mm/s) dynamic observation of the moving domain wall.

3.11 Summary of the domain observation techniques

In summary the best wide field real-time imaging techniques existing today are based on magneto optic effects. These methods are also not responsible to the stray field in the air around the sample, therefore any value and direction of field can be applied during observation. In addition MO microscopy is relatively easy to use and cheap compared to many other domain imaging techniques.

3.12 References of chapter 3

1. Carey R. and Isaac E.D., Magnetic domains and techniques for their observation, The English University Press Ltd, London (1966).
2. Williams H.J., Bozorth R.M., and W. Shockley, Magnetic domain patterns on single crystals of silicon iron, Phys. Rev. 75, p155, (1949).
3. Beckley P. and Taylor R., A commercial device for simple domain observations in electrotechnical steels, Proc. EPS Conf. Soft Magn. Mat. 9. (1989).
4. Celotta R.J., Unguris J., Kelley M.H., Pierce D.T., Techniques to measure magnetic domain structures, in: Methods in Materials Research: A Current Protocols Publication, Wiley, New York, (1999).
5. Hubert A., and Schafer R., Magnetic domains, Springer, Berlin (1998).
6. Moses A.J., Williams P.I, Hoshtanar O.A., Real time dynamic domain observation in bulk materials, J. Magn. Magn. Mater., 304, p150, (2006).
7. Kirilyuk A. and Rasing Th., Second harmonic generation in anisotropic magnetic films, Phys. Rev. B 63, 184407, (2001).
8. Green, A., Prutton, M., Magneto-optic detection of ferromagnetic domains using vertical illumination, J. Sci. Instrum. 39, p244, (1962).
9. Kimel A.V., Astakhov G.V., Schott G.M,. Kirilyuk A., Picosecond Dynamics of the Photoinduced Spin Polarization in Epitaxial (Ga,Mn)As Films, Phys. Rev. 92, 23, 237203, (2004).
10. Neudert A., McCord J., Schafer R., Schultz L., Sub-nanosecond vortex transformation in ferromagnetic film elements observed by stroboscopic wide-field Kerr microscopy, J. Appl. Phys. 97, 10E701, (2005).
11. Tiumov V.F., Zaykova B.A., Physics of Metals and Metallography (USSR), 59, 6, (1985).
12. Mewes T., Nembach H., Rickart M., Hillebrands B., Separation of the first- and second-order contributions in magneto-optic Kerr effect magnetometry of epitaxial FeMn/NiFe bilayers, J. Appl. Phys. 95, 5324 (2004).
13. Jakubovics J.P.: Lorentz microscopy, in: Handbook of Microscopy, Vol. 1, ed. by Amelinchx, VCH, New York, (1997).
14. Bostanjoglo O., Rosin T., Stroboscopic Lorentz TEM at 100 keV up to 100 MHz. Electron Microscopy 1, p88, (1980).
15. Mankos M., Cowley J.M., Scheinfein M.R., Quantitative micromagnetics at high spatial resolution using far-out-of-focus STEM electron holography. Phys. Status Solidi A 154, p469, (1996).
16. Wardly G.A., Magnetic contrast in the scanning electron microscope. J. Appl. Phys. 42, p376, (1971).
17. Ferrier R.P., McVitie S., The depth sensitivity of type II magnetic contrast. 49th Annual Meeting Electron Microscopy Society of America, San. Francisco

Press, P. p766, (1991).

18. Koike K., Matsuyama H., Hayakawa K., Spin-polarized scanning electron microscopy for micromagnetic structure observation, Scanning Microscopy Suppl. 1, p241, (1987).
19. Mivehchi E., Horrocks D.H. and Beckley P. Image processing application in measurements of features in SEM magnetic domain imaging, cited in Moses A. J., Basak A., Nonlinear Electromagnetic Systems, IOS Press, (1996).
20. Kuksov A., Schneider C.M., Oelsner A., Krasyuk A., Neeb D., Schönhense G., De Nadaï C. and Brookes N.B., Investigating magnetization dynamics in permalloy microstructures using time-resolved x-ray photoemission electron microscope, J. Appl. Phys. 95, 11, p6530, (2004).
21. Chrobok G., Hofmann M., Electron spin polarization of secondary electrons ejected from magnetized europium oxide. Phys. Lett. 57A, p257, (1976).
22. Scheinfein M.R., Celotta R.J., Unguris J., Pierce D.T., The influence of the surface on magnetic domain wall microstructure. Phys.Rev.Lett. 65, p668, (1989).
23. Kohashi T., Matsuyama H., Koike K., A spin rotator for detecting all three magnetization vector components by spin-polarized scanning electron microscopy. Rev. Sci. Instrum.66, 55-37-5543 (1995).
24. Smith C.H. and Schneider R.W., Very dense magnetic sensor arrays for precision measurement and detection, Presented at Sensors EXPO Chicago June 3, 2003
25. Rheem Y., Saito H., Ishio S., Fabrication of FePt/FeCo/FePt exchange-spring trilayer with very thin FeCo layer for high-resolution MFM tips, IEEE Trans. Magn.41, 10, p3793, (2005).
26. Tumanski S. and Stabrowski M., The magnetovision method as a tool for investigations of electrical steel quality, J. Meas. Sci. Tech., 9, 3, p488, (1998),
27. So M.H., Nicholson P.I., Meydan T., Moses A.J., Magnetic domain imaging in coated silicon-iron using magnetoresistive sensors, IEEE Trans. Mag. 31, 6, p3370, (1995).
28. Harasko G., Pfutzner H., Futschik K., On the effectiveness of magnetoactic bacteria for visualisations of magnetic domains. J. Magn. Magn. Mat. 133, p409, (1994).
29. Nogueira F.S. and Lins de Barros H.G.P., Study of the motion of magnetotactic bacteria. European Biophysics Journal. EBJ. 24, no. 1: p13, (1995).
30. Elsbrock E.B., Schroeder W., Kubalek E., Evalution of 3-dimentional micromagnetic stray fields by means of electron-beam tomography, IEEE Trans. Magn. 21, p1593, (1985).

CHAPTER 4 THEORY OF THE KERR EFFECT FOR DOMAIN OBSERVATION

4.1 Introduction

The physical origins of Magneto Optical effects are described in this chapter. As background information the basic properties of polarised light and its reflection from various types of surface are also detailed here. The theory of the Magneto Optical Kerr effect is described in relation to optimising image contrast for ferromagnetic domain observation.

4.2 Polarised light

In this work a simplified theoretical model from [1] is used to describe properties of light. This model is precise enough for tasks within the project, however, a comprehensive physical theory can be found elsewhere [2].

Coherent monochromatic light is an electromagnetic wave with a single frequency *w,* where electric, **E**, and magnetic, **B,** vectors are perpendicular to the wave direction represented by vector **k**. Such waves are said to be transverse and exhibit the property of *polarisation*. Any transverse monochromatic electromagnetic wave can be represented in *xyz* coordinates as a superposition of independent (orthogonal) *x* and *y* waves as shown in figure 4.1a. The electric vector of the wave can be presented by its orthogonal components as

$$\mathbf{E}(z,t) = (E_{0x}, E_{0y}e^{i\delta})e^{i(kz-wt)} \qquad (4.1)$$

where z is propagation axis, E_{0x} is the *x* amplitude of **E**, E_{0y} is *y* amplitude of **E**, and δ is the relative phase of $\mathbf{E}_y$ with respect to $\mathbf{E}_x$

The above equation presents the most general case of *elliptically polarised* light, as illustrated in figure 4.1b. The polarisation angle α can be found using the following equation:

$$\tan 2\alpha = \frac{2E_{0x}E_{0y}}{E_{ox}^2 - E_{oy}^2}\cos\delta \qquad (4.2)$$

If light is composed of only one electromagnetic wave it said to be *linearly polarised*, and can be represented in XY coordinates by $\mathbf{E}_x$ and $\mathbf{E}_y$ without a phase shift. The angle of polarisation is simply given by *atan*(E_{0y} /E_{0x}). The transverse electric field wave is accompanied by a magnetic field wave, as illustrated in figure 4.1c.

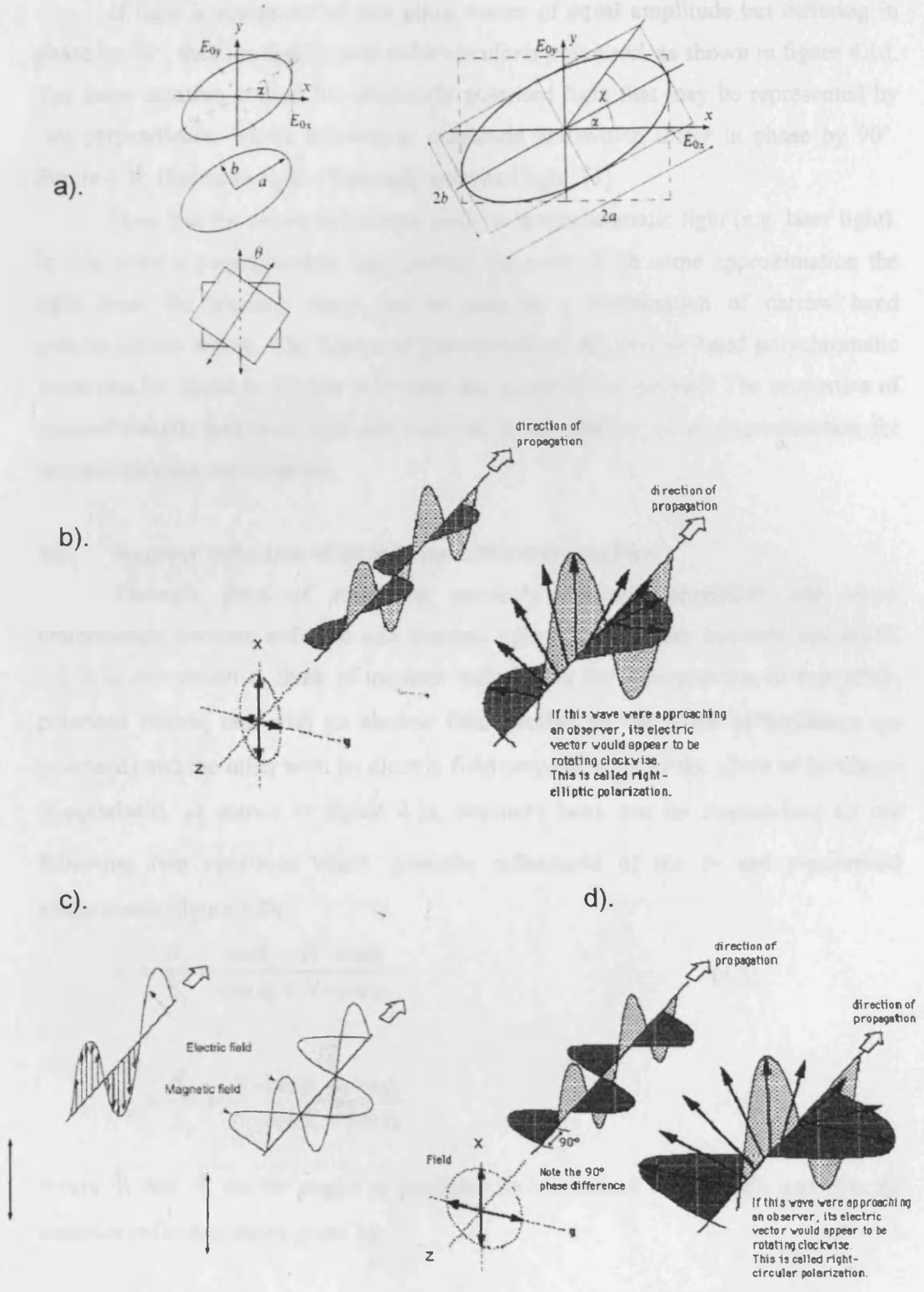

Fig.4.1 (a) Representation of polarised light. (b) Rotation of a vector of elliptically polarised light. (c) Linear polarisation. (d) Circular polarised light [10].

If light is composed of two plane waves of equal amplitude but differing in phase by 90°, then the light is said to be *circularly polarised,* as shown in figure 4.1d. The same notation is used for elliptically polarised light that may be represented by two perpendicular waves of unequal amplitude and which differ in phase by 90°. Figure 4.1b illustrates right-elliptically polarised light, [7].

Note that the above definitions apply to monochromatic light (e.g. laser light). In this work a polychromatic light source was used. With some approximation the light from the mercury lamp can be seen as a combination of narrow band polychromatic waves. The theory of polarisation of the narrow band polychromatic wave can be found in [2] but is beyond the scope of this project. The properties of monochromatic polarised light are analysed in this chapter as an approximation for domain viewing experiments.

4.3 Regular reflection of light from a dielectric surface

Fresnel's laws of reflection precisely describe amplitude and phase relationships between reflected and incident light at a boundary between two media [1]. It is convenient to think of incident radiation as the superposition of two plane-polarised beams, one with its electric field parallel to the plane of incidence (*p*-polarised) and the other with its electric field perpendicular to the plane of incidence (*s*-polarised), as shown in figure 4.2a. Fresnel's laws can be summarised by the following two equations which give the reflectance of the *s*- and *p*-polarised components (figure 4.2b):

$$r_s = \frac{R_s}{E_s} = \frac{\cos\phi_i - N \cdot \cos\phi_t}{\cos\phi_i + N \cdot \cos\phi_t} \qquad (4.3)$$

$$r_p = \frac{R_p}{E_p} = \frac{N \cdot \cos\phi_i - \cos\phi_t}{N \cdot \cos\phi_i + \cos\phi_t} \qquad (4.4)$$

where ϕ_i and ϕ_t are the angles of incidence and refraction respectively and N is the complex reflective index given by:

$$N = n(1 - ik) \qquad (4.5)$$

where n and k are ordinary refractive and absorption indices.

a).

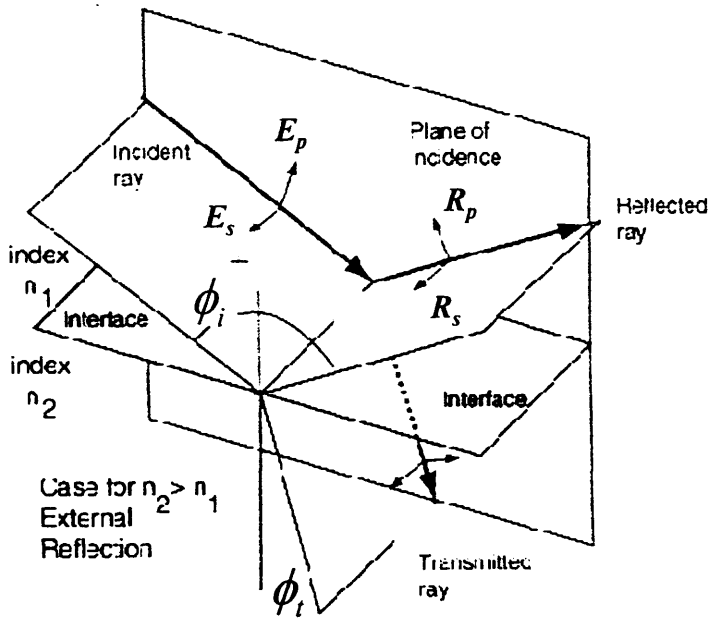

b).

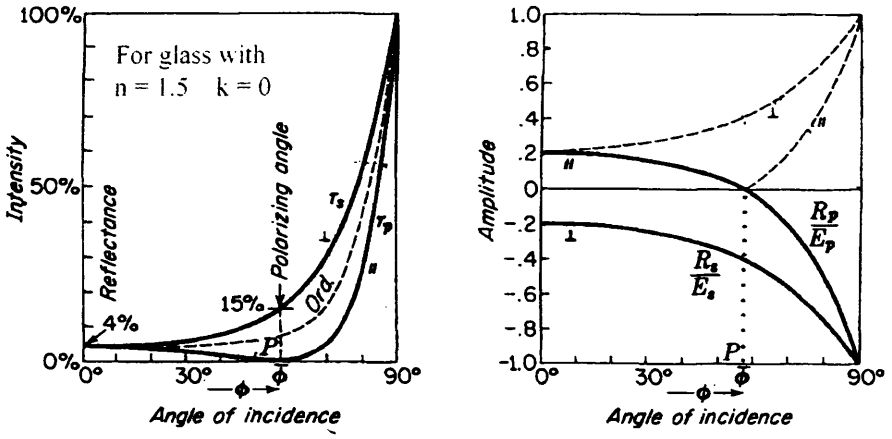

c).

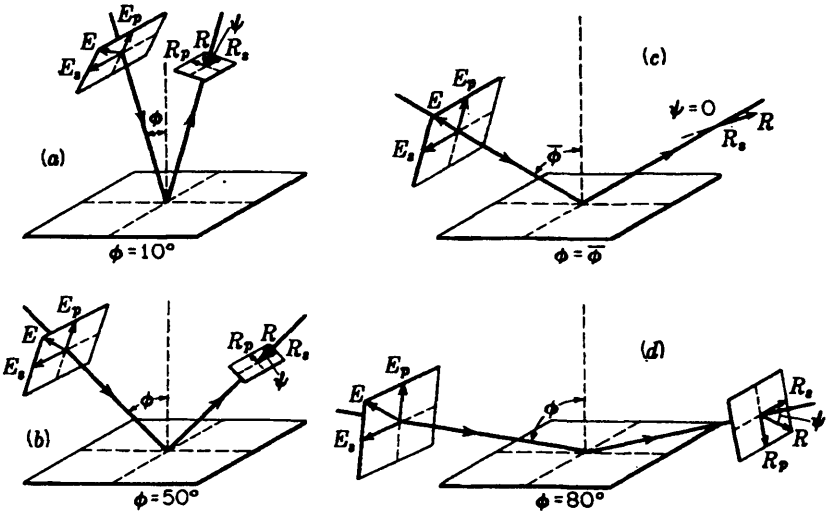

Fig.4.2 (a) Geometry of reflection from the dielectric surface, (b) reflection coefficients, (c) change of phase as a function of angle of incidence. Reproduced from [1].

It is generally assumed [4] that for an angle of incidence less than 65°, $cos\phi_t \approx 0$, thus equations 4.3 and 4.4 become:

$$r_s = \frac{\cos\phi_i - N}{\cos\phi_i + N} \tag{4.6}$$

$$r_p = \frac{N \cdot \cos\phi_i - 1}{N \cdot \cos\phi_i + 1} \tag{4.7}$$

For dielectric materials such as garnets, oxides and ferrites the absorption index k is close to zero, and equations 4.6 and 4.7 reduce to

$$r_s = \frac{\cos\phi_i - n}{\cos\phi_i + n} \tag{4.8}$$

$$r_p = \frac{n \cdot \cos\phi_i - 1}{n \cdot \cos\phi_i + 1} \tag{4.9}$$

In figure 4.2b the variation of reflectance with angle of incidence for both *s*- and *p*-components is plotted using the above formulae, for glass with $n = 1.5$. Note that light detecting equipment usually records intensity (power) of the light, so experimentally we can measure intensity reflectance [1], given by

$$p_s = \frac{(R_s)^2}{(E_s)^2} \tag{4.10}$$

$$p_p = \frac{(R_p)^2}{(E_p)^2} \tag{4.11}$$

At normal incidence, i.e. $\phi_i = 0$, the *s*- and *p*- components are equally reflected and from eq. 4.9 the intensity reflectance reduces to the following simple equation:

$$p = \frac{(n-1)^2}{(n+1)^2} \tag{4.12}$$

With increasing ϕ_i, p_p drops to a minimum at around 60° and the reflected light consists of only the *s*- component, which is linearly polarised as illustrated in figure

4.2c (c). This angle is called the Brewster angle. With further increases of ϕ_i, reflectance increases and at the grazing incidence both components are totally reflected.

Note that the value of r_s in equation 4.8 is always negative which means that the amplitude R_s is exactly 180° out of phase with E_s. On the other hand equation 4.9 shows that the phase of R_p switches from 0° to 180° at the Brewster angle. Vector R, as a superposition of R_s and R_p has a different plane of polarisation compared to E as represented in figure 4.2c, but remains linearly polarised.

4.4 Reflection from a metallic surface

Reflection from a metallic surface is far more complicated than that from a dielectric surface. Due to the presence of free electrons, metals have very high absorption k, hence equations 4.6 and 4.7 are not reduced to 4.8 and 4.9 respectively and the reflection coefficients become more complex. Phase shifts appear to be different from 180° and ellipticity of the reflected light becomes almost unavoidable [1], [2]. Many magnetic materials are metals, so the more complicated regular reflection interferes with the Kerr effect application. To reduce the ellipticity of regular reflection special angles of illumination and ¼ wave plates for ellipticity compensation are used.

4.5 Physical origins of magneto optical effects

In general, when plane polarised light interacts with electrons, it causes them to vibrate and emit own radiation. This process is described by the Zeeman theory of dispersion [2] and is based on the classical Lorentz theory. If we consider a system of harmonically bound electrons in an oscillating electric field with a static magnetic field along the z axis, then according to [3] the equation of motion of each electron is

$$m_e\ddot{r} + b_e\dot{r} + k_e r = -eE_0 e^{jwt} - e\mu_0 \dot{r} \times H \qquad (4.13)$$

Where m_e is an electron mass, b_e is a damping coefficient and $(k_e/m_e)^{1/2} = w_0$ is the eigenfrequency of the electron oscillation (where k_e is a 'spring' constant). The last term is the Lorentz force. The substitution of $r = r_0 e^{jwt}$ yields a pair of equations for x and y components of r_0, these equations being coupled by the term that arises from the Lorentz force. An electric field along the x axis produces motion along the x axis which in the presence of a magnetic field gives rise to a force and subsequent motion

along the y axis. Owing to this secondary motion of light-agitated electrons in the solid state additional terms in reflected and transmitted light appears.

If, however, the electrons at the reflecting surface are ordered, such as in magnetic domains, the secondary motion of light-agitated electrons adds up and a change in the ellipticity of the reflected light is produced [5]. These changes are known as Magneto Optical (MO) effects. The most common MO effects are the Faraday effect in transmission and the Kerr effect in reflection. All these effects can be represented by a generalised dielectric permittivity tensor [6] and Voigt material constant Q_v.

4.6 Description of the Kerr effect

There are three Kerr effects: polar, longitudinal and transverse, which depend upon the orientation of magnetisation relative to the plane of the reflecting surface and the plane of incidence as illustrated in figure 4.3.

The microscope used in this investigation had only *longitudinal* and *polar* effect configurations available. For the longitudinal effect the light beam has to be inclined relative to the surface and the magnetisation lies parallel to the plane of incidence. The *longitudinal* effect occurs separately as a perpendicular mode and a parallel mode as illustrated in figure 4.3a and 4.3b respectively. In the case of the polar Kerr effect the magnetisation is perpendicular to the surface as shown in figure 4.3c.

The angle of light polarisation rotation is proportional to the Lorentz force $\boldsymbol{\nu}_{lor} = -\mathbf{m} \times \mathbf{E}$, and therefore depends on the angle between the magnetisation vector and the **E** vector of light. The general theory for the magnitude of the incident and reflected light rays was developed by Voigt. For longitudinal and polar effects, the equations may be written as:

$$\mathbf{R_s} = r_s \mathbf{E_s} + r_{sp} \mathbf{E_p} \qquad (4.14)$$

$$\mathbf{R_p} = r_p \mathbf{E_p} + r_{ps} \mathbf{E_s} \qquad (4.15)$$

Where $\mathbf{R_s}$ and $\mathbf{R_p}$ are the amplitudes of the reflected electric vectors perpendicular and parallel to the plane of incidence respectively. $\mathbf{E_s}$ and $\mathbf{E_p}$ are the associated incident vectors. r_s and r_p are the ordinary metallic coefficients of reflection (given

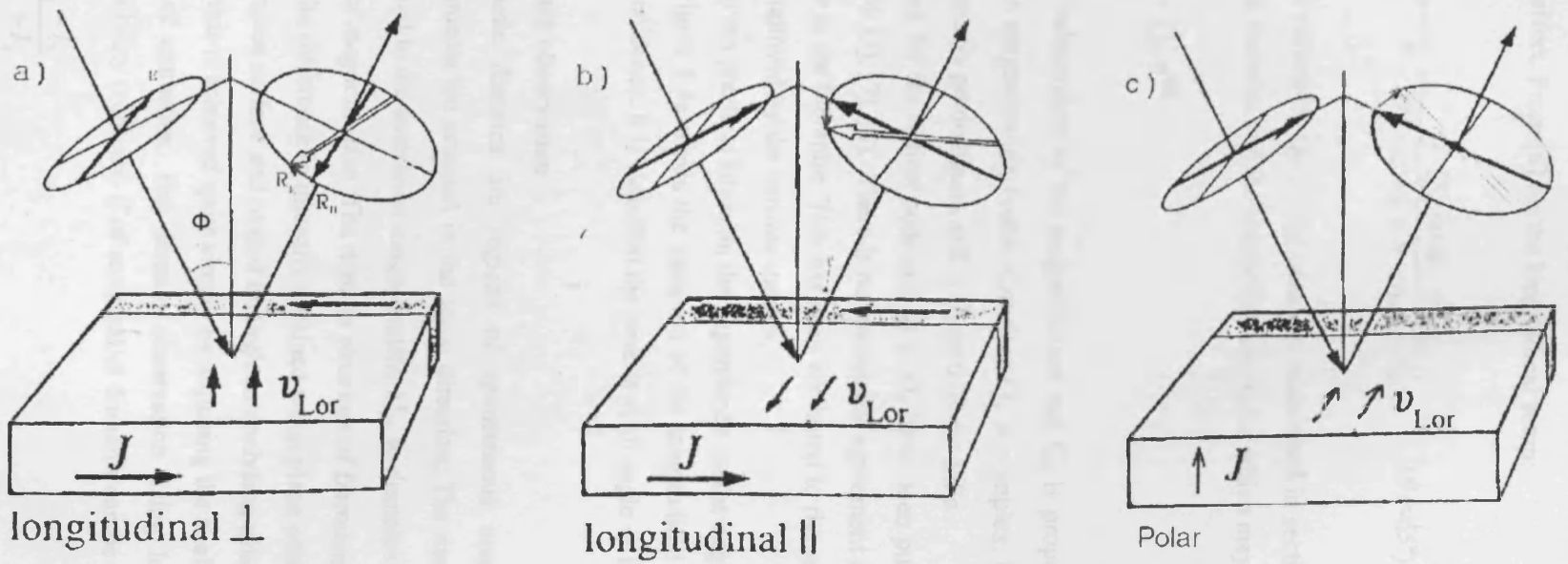

Fig 4.3. The geometry of the magneto optical rotation for (a,b) longitudinal and (c) polar setup.

by equations 4.3, 4.4). $r_{s\,p}$ and $r_{p\,s}$ are the coefficients of reflections which give rise to the Kerr effect. From [6] for the longitudinal setup:

$$r_{sp} = -r_{ps} = \frac{-i \cdot Q_v \cdot \cos\phi_i \cdot \sin\phi_i}{(N + \cos\phi_i)(N \cdot \cos\phi_i + 1)} \qquad (\phi_i < 65^\circ) \qquad (4.16)$$

the complex parameter $\mathbf{Q_v}$ (Voigt constant, mentioned in section 4.5) is a property of the reflecting material and the magnetisation vector which may be written as:

$$Q_v = Q_0\, e^{-iq} \qquad (4.17)$$

Where q is independent of the magnetisation and Q_0 is proportional to and changes sign with the magnetisation vector. Constant Q_v is complex, but according to [6] the real part is usually predominant and is about 0.03 for SiFe.

Values for the optical constants n, k, Q_o have been published for iron, nickel and permalloy [3], [7], [8]. There is no reasonable agreement on the value of q which varies widely in the literature. This has been attributed to the surface conditions of the specimens employed by the various authors.

In a given practical situation the dependence on the angle of incidence is more significant. Figure 4.4a shows the variation of the longitudinal effect as a function of the angle of incidence. It is clear that the peak is at an angle of incidence of 60°.

4.7 Domain observation

Magnetic domains are regions of spontaneous magnetisation where all magnetic moments are oriented in the same direction. The magnetisation inside any domain is equal to the saturation magnetisation M_s, so domains are characterised only by *direction of magnetisation*. The domain structure of ferromagnetic materials can be observed by the difference in intensity obtained when plane polarised light is reflected from the specimen surface and passed through an analysing prism. In longitudinal and polar effects, this is achieved quite simply by adjusting the analysing prism to be near the position of extinction. For domain observation using longitudinal and polar effects, the visibility (contrast) C of antiparallel domains can be written as:

$$C = \frac{I_1 - I_2}{I_1 + I_2} \qquad (4.18)$$

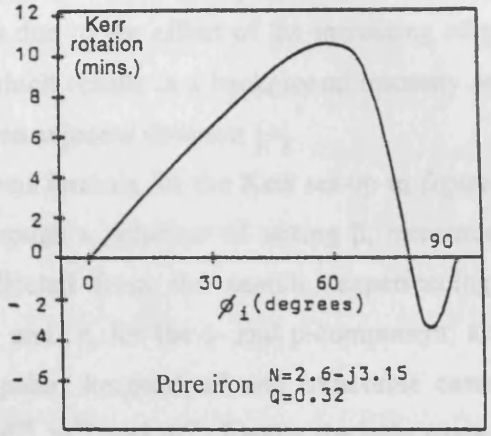

Fig.4.4 a Longitudinal Kerr rotation as a function of angle of incidence

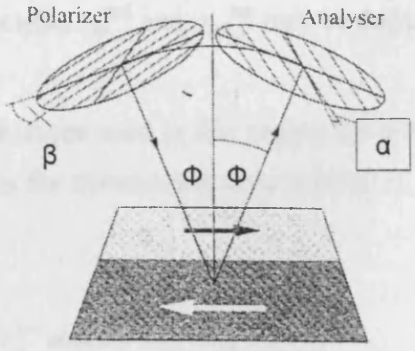

Fig.4.4 b. Polariser and analyser in a Kerr setup with definition of the respective angles

Where I_1 and I_2 are the light intensities of antiparallel domains. Visibility for the polar effect (figure 4.3c) is maximal at perpendicular incidence. For the longitudinal Kerr effect, although the peak of the modulation occurs at an angle of incidence of 60°, the optimum visibility occurs at the angle of incidence close to 40° (for iron and Ni-Fe alloys). This is due to the effect of the increasing ellipticity with angle of incidence close to 60°, which results in a background intensity and consequent reduction of the contrast between adjacent domains [4].

A general formula for the Kerr set-up in figure 4.4b is given in [8]. The light passes first through a polariser of setting β, measured from the plane of incidence, then it is reflected from the sample, experiencing regular amplitude reflection coefficients r_s and r_p for the s- and p-component, and Kerr amplitudes r_{sp}^{pol}, r_{sp}^{lon}, r_{sp}^{tan} for the polar, longitudinal and transverse cases related to the magnetisation components m^{pol}, m^{lon} and m^{tra}. Finally the light passes through an analyser (with the setting α, measured from the plane of incidence), leading to the total relative to E amplitude:

$$A_{tot} = -r_p \cos\beta \sin\alpha + r_s \sin\beta \cos\alpha + r_{sp}^{pol} \cos(\alpha-\beta)\cdot m_{pol} + r_{sp}^{lon} \cos(\alpha+\beta)\cdot m_{lon} - r_{sp}^{tra} \sin\alpha \cos\beta \cdot m_{lon} \quad (4.19)$$

The first line in Eq 4.19 represents a regular reflection, the second gives the Kerr components. Coefficients r_{sp}^{pol} and r_{sp}^{tan} may be defined by similar expressions as for r_{sp}^{lon}, r_s and r_p;

For the microscope used in this project the polariser was permanently fixed at β = 0 position, hence the above expression reduces to

$$A_{tot} = -r_p \sin\alpha + r_{sp}^{pol} \cos(\alpha)\cdot m_{pol} + r_{sp}^{lon} \cos(\alpha)\cdot m_{lon} - r_{sp}^{tra} \sin\alpha \cdot m_{lon} \quad (4.20)$$

When only in-plane magnetisation is considered, the above expression reduces to

$$A_{tot} = -r_p \sin\alpha + r_{sp}^{lon} \cos(\alpha)\cdot m_{lon} \quad (4.21)$$

For two domains with opposite magnetisation, the Kerr amplitudes differ only in sign.

Writing eq. 4.21 in the form $A_{tot} = A_N \pm A_K$, where A_N represents the regular part, and A_K is the effective Kerr amplitude, the Kerr rotation can be defined as the small angle $\varphi_k = A_K / A_N$. It is recommended in [9] to begin from analyser $\alpha = \varphi_k$ setting, which extinguishes the light coming from one of the domains. But this setting may not be the best one for optimal contrast in certain imaging systems (with a specific dynamic range). In [6] a method of obtaining the best contrast C for visual observation is presented by optimising Eq. 4.18 with respect to the angle α:

$$\tan \alpha_{opt} = \sqrt{\frac{A_K^2 + I_0}{A_N^2 + I_0}}, \qquad C_{opt} = \frac{A_K A_N}{\sqrt{(A_N^2 + I_0)(A_K^2 + I_0)}} \tag{4.22}$$

where I_0 is a background intensity due to imperfections with the system and the surface.

When using electronic video systems contrast optimisation needs to take into account the noise and dynamic range of the image sensor. Optimal conditions for electronic imaging sensors may differ from those required for human visual observation.

4.8 Dielectric coatings for contrast enhancement

The technique of coating the sample surface with a thin dielectric layer of Zinc Sulphide (ZnS) to enhance contrast of the magnetic domains by reducing the amount of regular reflected light is called blooming. Reduction in amplitude of the reflected light results from destructive interference between light rays reflected directly from the ZnS film (R_N^1), as shown in figure 4.5, and light rays undergoing reflection from the metal surface (R_N^2). This occurs if two light rays have equal amplitudes and are π or an odd multiple of π out of phase. In this case the difference in optical path lengths ((AB+BC)n – AD) should equal $\lambda/2$.

Note that in figure 4.5 $AB = BC = d/\cos\phi_t$ and $AD = AC \sin\phi_i = 2d \operatorname{tg}\phi_t \sin\phi_i$

Where ϕ_i is the angle of illumination and n is the refractive index of the dielectric material. Taking into account that $\frac{1}{n} = \frac{\sin\phi_t}{\sin\phi_i}$

it is possible to find an expression for the required thickness of the dielectric coating as follows:

$$d = \frac{\lambda}{4\sqrt{n^2 - \sin^2\phi_i}} \tag{4.23}$$

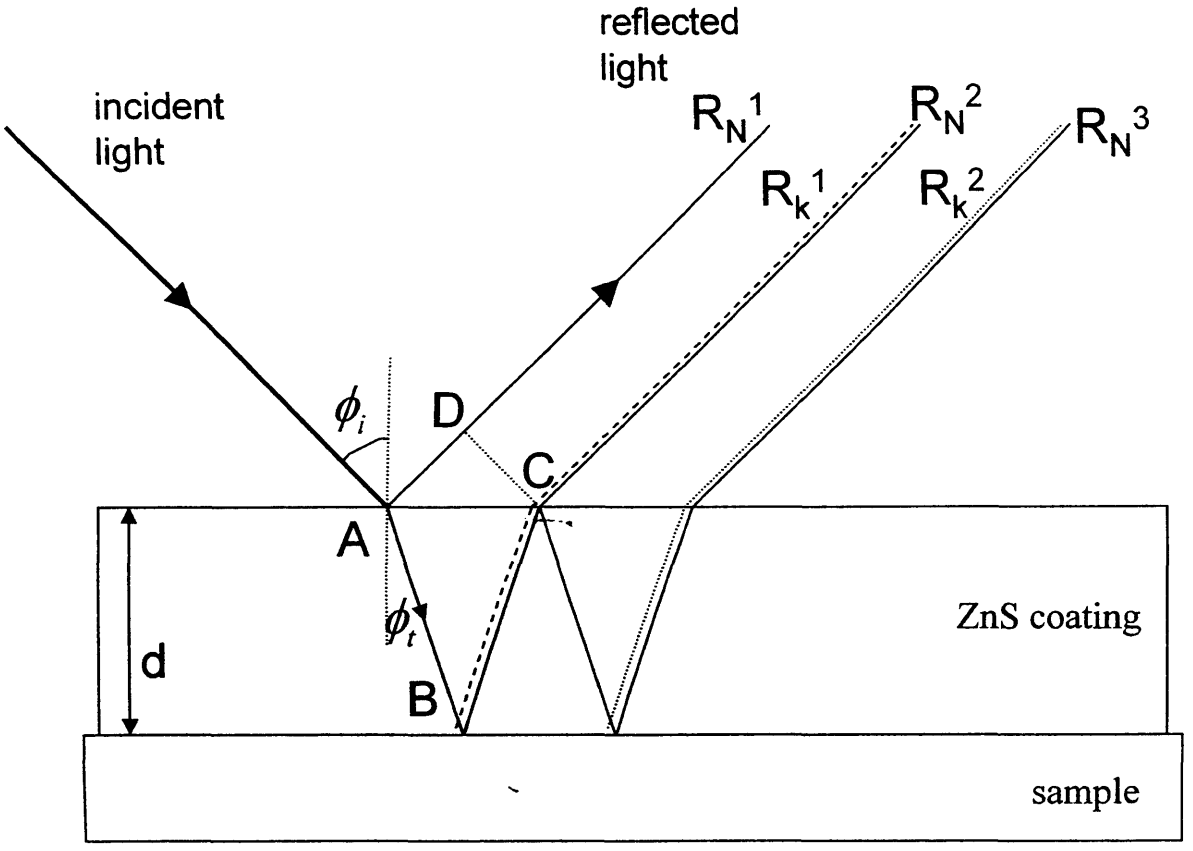

Fig.4.5 Light reflection paths from top and bottom of dielectric coating on a magnetic sample.

The dielectric coating thickness is therefore determined by the light source wavelength, the refractive index of dielectric material and the angle of illumination.

In this project λ = 550 nm (green line of Hg discharge), n = 2.25 and ϕ_i = 45° giving a value of 64 nm for d.

In addition to the destructive interference the Kerr components R_k^1 and R_k^2 undergo constructive interference (dashed line in figure 4.5), because of a 180° phase shift for the reflection inside the dielectric layer [6]). The Kerr component in the reflected light increases resulting in the reflected light from antiparallel domains providing greater contrast [11].

4.9 Summary of optimal conditions for image contrast

- Good Kerr contrast critically depends on the angles between the plane of polarisation and the magnetisation vector.
- Optimal conditions can be predicted for dielectric materials and can be estimated for metallic materials.
- Background intensity should be reduced by accurate alignment of the system, perfect sample surface conditions and using a ¼ wave plate.
- Significant contrast enhancement can be achieved by deposition of a ZnS coating with suitable thickness.
- Depth sensitivity of the Kerr effect in iron is limited to about 30nm below the surface [5], [6], [12].

4.10 References of chapter 4

1. Jenkins F.A., White H.E., Fundamentals of Optics, McGraw-Hill Book Co., New York (1957).
2. Stone J.M., Radiation and optics, Tosho printing CO., Tokyo, (1963).
3. Freiser M. J., A Survey of Magnetooptic Effects. IEEE Trans. Magn., Vol. Mag-4, 2, (1968).
4. Husni M.R.A., Applications of high resolution magneto-optics : (investigation of bubble overlay elements), Ph.D. Thesis, University of Wales, (1980).
5. Kolk A.J., Orlovic M., Increasing the Kerr magneto-optic effect in thin films, J. Appl. Phys., 34, p1060, (1963).
6. Hubert A., Schafer R., Magnetic Domains, Springer, Berlin (1998).
7. Robinson C. J., Optical Soc., Am., 53, 6, p681, (1963).
8. Rave W., Schafer R., Hubert A., Quantitative observation of magnetic domains with the magneto-optical Kerr effect. J. Magn. Magn. Mater. 65, p7, (1987).
9. Hubert A., Traeger G., Magnetooptical sensitivity functions of thin film systems. J. Magn. Mat. 124, p185, (1993).
10. Woan G., The Cambridge handbook of physics formulas, Cambridge University Press, (2000).
11. Qureshi N., Schmidt H., Cavity-enhanced Kerr effect for magneto-optic spectroscopy of nanostructures, Third IEEE Conference on Nanotechnology, Proc. 1, (2003).
12. Wenzel L., Kambersky V., Hubert A., A systematic first-order theory of magnetooptic defraction in magnetic multilayers. Phys. Status Solidi A, 151, p449, (1995).
13. Greiner J., Fan G., Longitudinal Magneto-optical Kerr Effect in EuO and EuS, Applied Physics Letter, 9, p27, (1966).

CHAPTER 5 OPTICAL MICROSCOPY FOR MAGNETIC DOMAIN OBSERVATION

5.1 Introduction

In this chapter magnetic domain optical microscopes from [1], [2], [3], [4] are briefly described before explaining in greater detail the configuration of the microscope system used in this work. The chapter is focused on achieving of the best visibility of the domain structures.

Three most common Kerr microscopes are sketched in figures 5.1 and 5.2.

5.2 High contrast, low magnification microscopy

When viewing relatively large domains with in-plane magnetisation a low magnification system similar to that in figure 5.1 can be used which provides high image contrast. It employs a separate illumination collimator and lens objective inclined at the optimum angle of incidence. With such an arrangement it is easy to illuminate the sample at wide angles (i.e. from 40° to 80°) in order to get the best Kerr contrast as described in detail in section 4.6. Its second advantage is that no optical elements other than the sample exist between polariser and analyser, so that there is no depolarisation of the light beam. Adjustment of the angle of incidence is also much simpler in this type of set-up. The high image contrast achievable often eliminates the need for image processing. This type of system however suffers from two major disadvantages [2]. Firstly, in order to obtain greater resolution a shorter working distance objective must be used with its associated mechanical deficiencies. Secondly, only a small fraction of the field of view can be focused due to a limited depth of focus. Both of these difficulties are overcome if a single lens could be used as both condenser and objective similar to those used in conventional microscopes with vertical illumination.

5.3 High magnification microscopy

Observations down to the limiting resolution of optical microscopy (i.e. 0.4μm) are possible with the set-up shown in figure 5.2a. Such a set-up can be a purpose built microscope like the one used in this project, or a system based on a conventional polarising microscope as reported in [1], [3], [5].

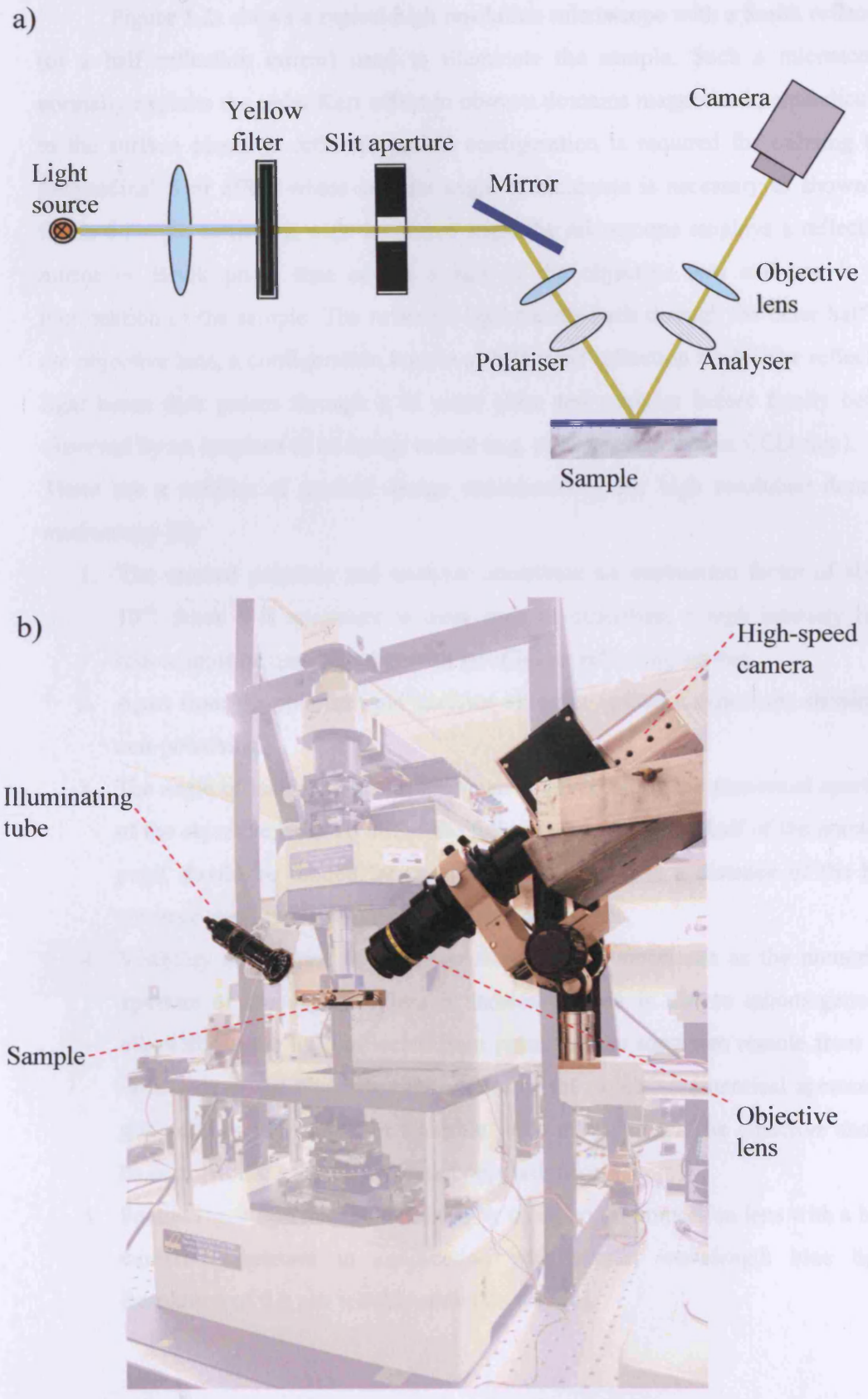

Fig.5.1 (a) Schematic of the low magnification V – shaped microscope.
(b) Photograph of the low magnification part of the system.

Figure 5.2a shows a typical high resolution microscope with a Smith reflector (or a half reflection mirror) used to illuminate the sample. Such a microscope normally exploits the polar Kerr effect to observe domains magnetised perpendicular to the surface plane. A different optical configuration is required for utilising the longitudinal Kerr effect where a wider angle of incidence is necessary as shown in figure 5.2b. To achieve a wide incidence angle the microscope employs a reflective mirror or Berek prism that covers a half of the objective lens and use it for illumination of the sample. The reflected light travels back through the other half of the objective lens, a configuration known as half pupil reflection mode. The reflected light beam then passes through a ¼ wave plate and analyser before finally being observed by an eyepiece or an image sensor (e.g. photographic film or CCD chip).
There are a number of general design considerations for high resolution domain microscopy [2]:

1. The crossed polariser and analyser contribute an attenuation factor of about 10^{-6}. Since it is necessary to work near to extinction, a high intensity light source must be used together with an efficient reflecting system.
2. Apart from the polariser and analyser all other optical components should be non-polarising.
3. The angle of incidence of the specimen is governed by the numerical aperture of the objective lens. To utilise the full semi-aperture, one half of the entrance pupil should be limited by an aperture positioned at a distance of the half entrance pupil radius from the optic axis of the lens.
4. Visibility or contrast of magnetic domains may decreases as the numerical aperture of the objective lens is increased. This is due to inhomogeneous ellipticity in the light reflected from points on the specimen remote from the optic axis of the objective. The choice of the objective numerical aperture is governed by the minimum tolerable value of visibility. The objective should be of a specific geometry to avoid depolarisation.
5. Spatial resolution may be extended by using an oil immersion lens with a high numerical aperture in conjunction with shorter wavelength blue light. Resolution of 0.3 μm is achievable this way [6].

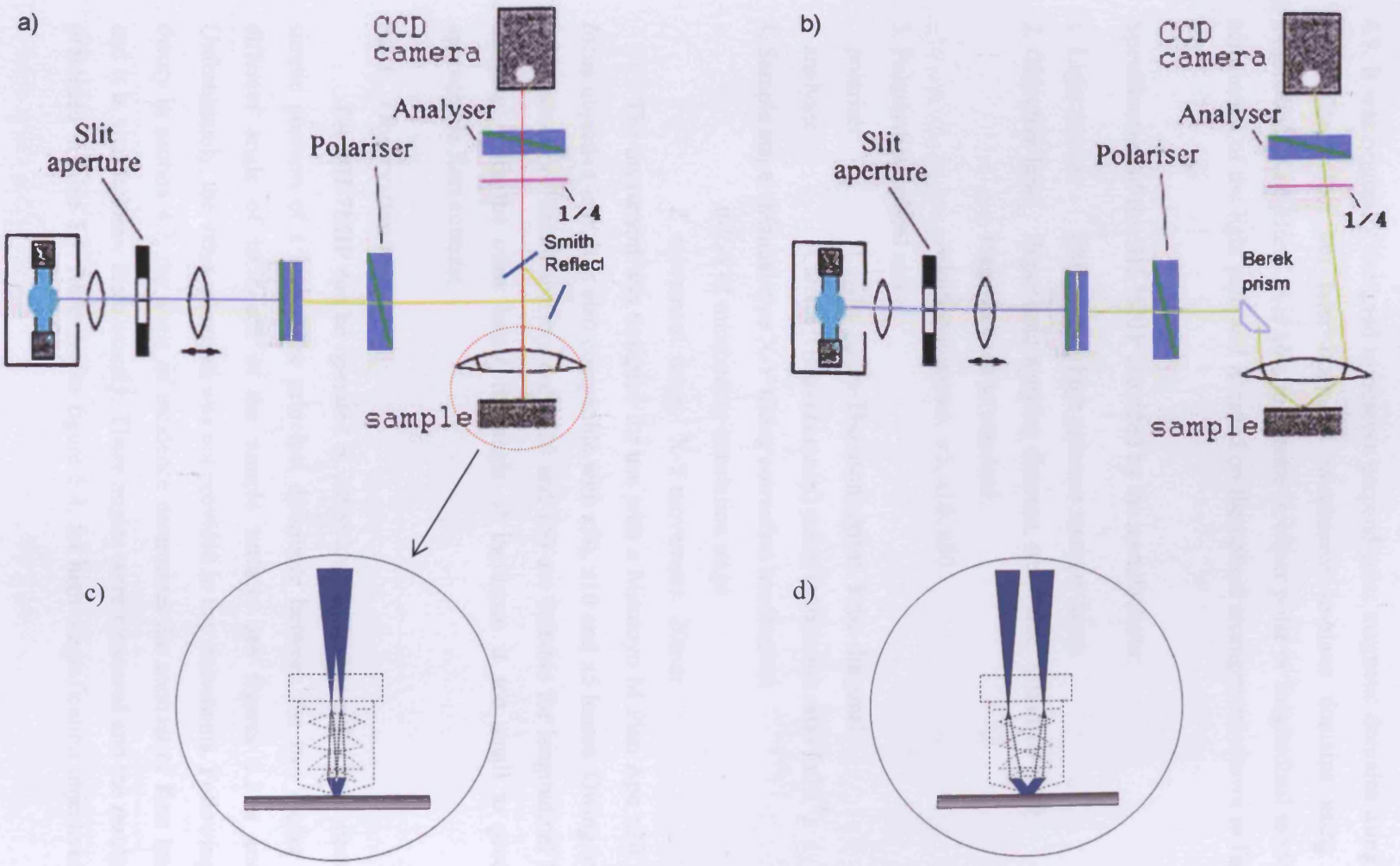

Fig.5.2 a). Microscope in 'Polar' mode, b). – 'In-plane' mode. c) Illumination of the sample through the objective lens in the polar geometry, d) in the longitudinal geometry.

5.3 The Neoark BH-785IP high magnification polarising microscope

The commercial system used in this work was designed specifically for magnetic domain observation and it meets most of the requirements listed in section 4.9. It was originally designed to observe perpendicular magnetic domains using the polar Kerr effect but later upgraded to observe in-plane domains using the longitudinal Kerr effect. It is able to operate in either polar or longitudinal mode by adjustment of the light path and is based on the optical arrangement shown in figure 5.2.

Specification of the BH-785IP provided by the manufacturer:

1. Light source: 100W Super high pressure mercury lamp.
2. Objective lens: Super long working distance, strain free 'Mitutoyo' x20 magnification as standard.
   Additional lenses: x5, x10, x50
3. Polarisation optical unit
   polariser: Calcite (Glan-Thomson) prism, 8mm diagonal
   analyser: Calcite (Glan-Thomson) prism (extinction ratio $5x10^{-5}$)
4. Sample stage: Manual type X-Y tilting correction mechanism
   θ-X-Y-Z micrometer translation stage
   Z movement: 6mm, X-Y movement: 20mm

The instrument was designed for use with a Mitutoyo M Plan Apo x20 long focus objective lens, it is also compatible with x50, x10 and x5 lenses. Owing to the long focus and limited aperture only x20 and x50 are suitable for longitudinal Kerr imaging. With the other lenses the angle of incidence is too small to produce appreciable Kerr contrast.

5.3.1 Observation mode

The **BH-785IP** can be operated in either longitudinal or polar Kerr mode by simple position of a lever. The principal difference between the two modes is a different angle of incidence at the sample surface, see figures 5.3 a and b. Unfortunately, the value of angles was not provided in any documents. Following the theory in section 4.7, the angle of incidence determines the contrast of Kerr images and it is vital to know them exactly. These angles were measured and the results are presented in table 5.1. Referring to figure 5.4, for high magnification objectives i.e.

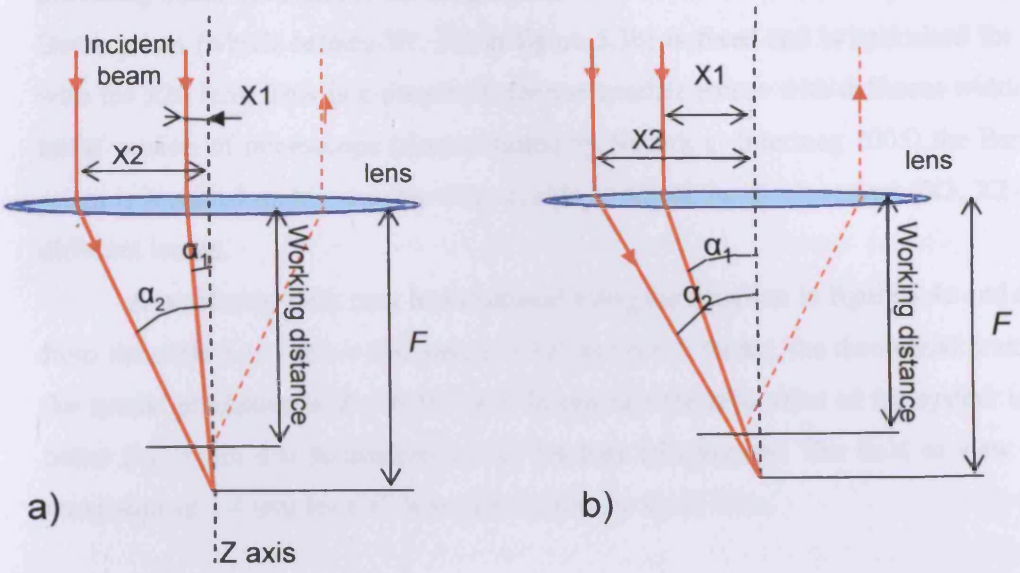

Fig.5.3 Light path through the lens (a) in 'polar' mode and (b) in longitudinal mode.

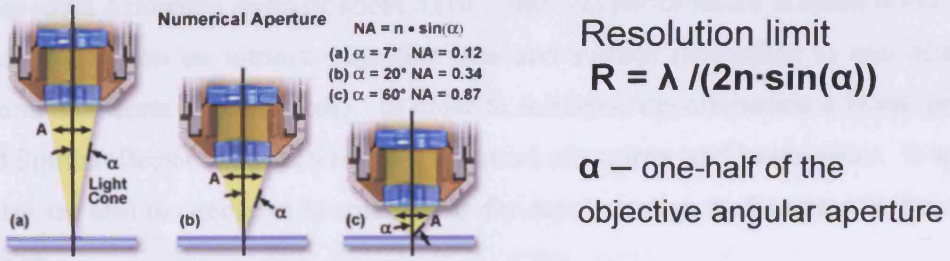

Fig.5.4 Illustration of light path for x10, x20 and x50 times lenses and relation between Numerical Aperture and working distance. (reprinted from Olympus web site)

Table 5.1. Lens's parameters

Objective	*Working distance* *	*F*** (mm)	NA*	Angles α_1,α_2 (deg) **		Diameter of lens
				In plane	Polar	
5x	34	40	0.14	0 - 4	0 - 4.3	20
10x	33.5	35	0.28	3.3 – 8.7	0 - 5	20
20x	20	22	0.42	5.2 – 15.3	0 – 23.4	18
50x	13	14	0.55	12.1 – 32.7	0 - 30	18

* Data from specification sheet, ** Measured data, the tolerance is ~ 0.5mm, 2°

x20 and x50, the working distance is short resulting in wider angles α_1, α_2 and providing better contrast for the longitudinal Kerr mode. Note that the position of the Berek prism (which defines X1, X2 in figure 5.3b) is fixed and is optimised for use with the x20 lens. This is a drawback for use another lenses with different width. In latest version of microscope (demonstrated by Neoark at Intermag 2005) the Bereck prism is installed on micrometer what enable to adjust the displacement (X1, X2) for different lenses.

A resolution limit may be calculated using the equation in figure 5.4c and data from the table 5.1. For λ = 590 nm, α = 32° and n = 1 for air, the theoretical limit for the spatial resolution is R = 0.557 μm. In practice the resolution of the system is no better that 1 μm due to intolerences of the lens components. The field of view is a maximum of 1.4 mm for a x5 lens and 140μm for a x50 lens.

5.3.2 Polarising prisms

The Glan-Thomson prisms used for both polariser and analyser exhibit a cross-nicol *Extinction Ratio* of about $5x10^{-5}$. But real performance is much lower due to depolarisation on mirrors, objective lens and surface (according to non official information from manufactures). In order to minimise depolarisation a Berek prism and Smith reflector have been employed instead of a mirror and beamspliter. ¼ wave plates are also incorporated to compensate for depolarisation as discussed in the next section.

The rotation of the analyser and ¼ wave plate is possible with an angular tolerance of 0.5°. The polariser is rigidly fixed to provide light polarised parallel to the plane of incidence i.e. parallel longitudinal Kerr effect and therefore it was not possible to adjust the system to operate in perpendicular longitudinal Kerr mode.

5.3.3 ¼ wave length plate compensator

Retardation plates (also called *waveplates*) are used to change the state of polarisation of the incident light by unequal phase-shifting of its orthogonal components. The operation is based on the linear birefringent effect i.e. difference in the refractive indices for the beams with parallel and normal polarisation towards the optical axis of the crystalline quartz material being within the plate [7]. While inside the material, the faster component has a longer wavelength. After a certain distance the two waves will have travelled a different number of wavelengths. The faster wave

may lead for ¼ of period. Upon exiting the material, both waves regain their original wavelengths, but they are now out of phase by ¼ of a wave length, see figure 5.5. Slabs of birefringent material that retard the phase of one component with respect to the other are called **retardation plates**. The example given is called a ¼ λ plate for a specific λ, other values include ½ λ and ¾ λ plates.

Quarter-waveplates are used for conversion of linearly polarised radiation into circularly polarised radiation when the input polarisation is oriented at an angle of 45° to the waveplate optical axis, see figure 5.5. At angles other than 45°, the ¼ λ plate transforms linearly polarised light into elliptically polarised light. The reverse of this process is also possible i.e. a ¼ λ plate can change elliptically polarised light into linearly polarised light. This phenomenon is employed in the Neoark microscope for correction of elliptical light back to the linearly polarised light. In the Neoark system the ¼ wave length plate is optimised for use with green light with $\lambda = 540$ nm. (as for green laser, but makers said that its OK for mercury lamp as well, unofficially).

5.3.4 Light source

Traditionally a short-arc mercury lamp is used as a point light source with sufficient brightness in Kerr microscopes. It has a spectrum with narrow lines at 440, 540 and 590 nm and around 55% of the light's power is emitted at these wavelengths [8]. More luminous power may be produced by a point arc source operating at a higher vapour pressure but that the subsequent spectral lines become wider as explained in [7]. Spectral filters are applied when only green or yellow light is used. If a continuous spectrum is required then a xenon-arc discharge or tungsten-halogen lamp can be used. The main disadvantage of arc lamps is their instability which is a critical concern when real-time images are acquired using fast shuttering speeds i.e. exposure times of 1 ms or less. In the Neoark microscope a HBO 103 W/2 mercury lamp is used (2550 Lm /100 W) containing a noble gas for flickering suppression. The lamp is powered by an Olympus BH2-RTL-T3 power supply with a sophisticated ballasting circuit.

The Neoark BH-785IP microscope is equipped with the mercury ark lamp, thought the manufacturers didn't suppose it will be used for a high-speed observations. A laser illumination is a good alternative to arc lamp that can be used in future.

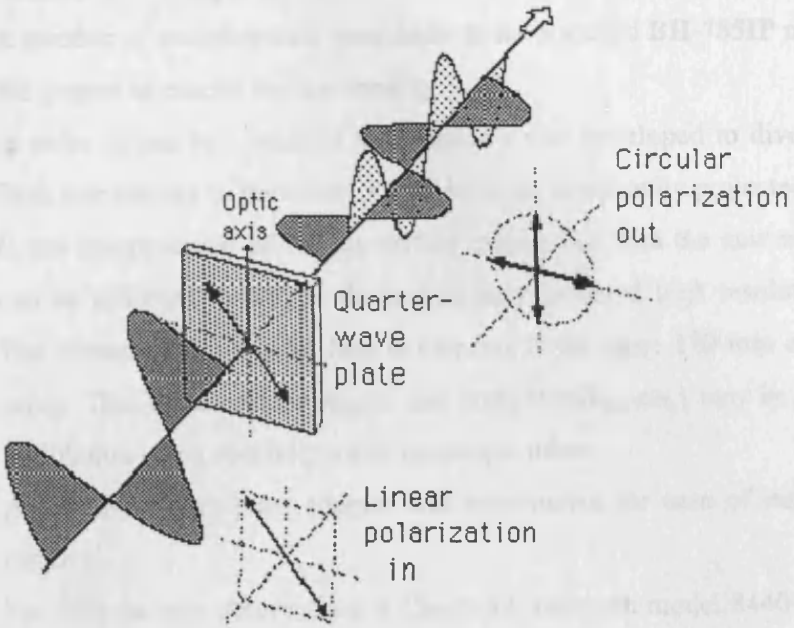

Fig.5.5. Linear polarised light passing through ¼ wave plate at 45° changes to the circular polarised light. Reprinted from [10].

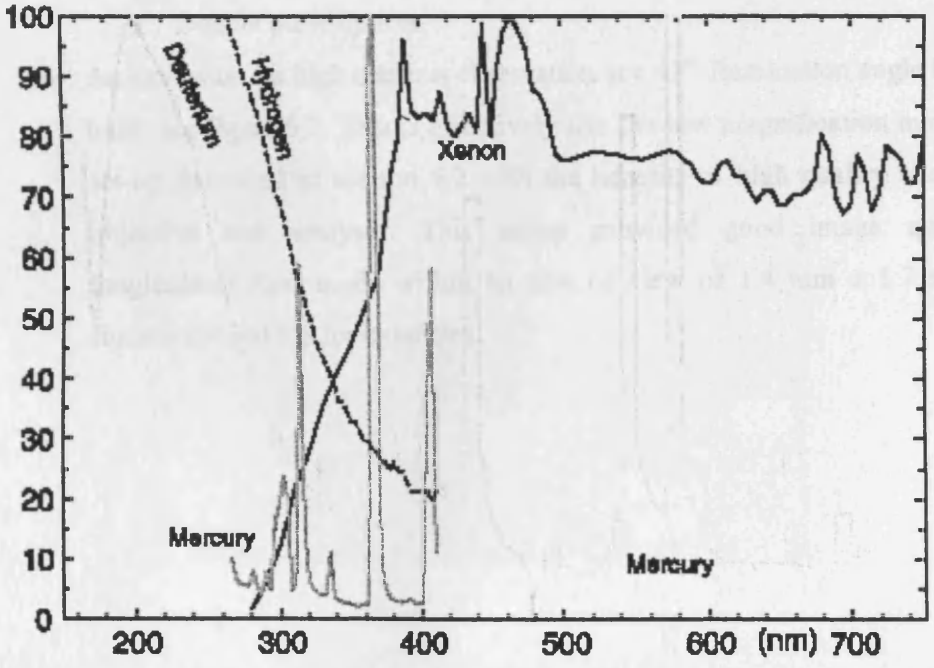

Fig.5.6 Power spectrums of light sources. Reprinted from [8].

5.4 Neoark microscope modifications

A number of modifications were made to the standard **BH-785IP** microscope during this project to extend its functionality.

1. In order to use two cameras a mechanism was developed to divert the beam from one camera to the other. The light beam is normally projected directly on to the image sensor of the intensified camera but with the new mechanism it can be reflected by 90° to the horisontally mounted high resolution camera. The distance form erector lens to cameras is the same 180 mm as in original setup. That distance {for sensor size compatibility, ets,} may be extended up to 500 mm using specially made telescopic tubes.
2. A ¼ wave length plate adaptor was constructed for ease of installation and removal.
3. For stroboscopic observations a Chadwick Helmuth model 8440-6 Pulse light source was adopted in this system via specially made adaptors. The light source has the following specifications:
    - 0.1ms light pulse.
    - Frequency of pulses 0.1 Hz – 3000 Hz.
    - External synchronisation and triggering option.
    - Double pulse option.
4. An extension for high contrast observation at a 45° illumination angle has been built, see figure 5.7. This is effectively like the low magnification microscope set-up described in section 5.2 with the benefits of high quality microscope objective and analyser. This set-up provided good image quality in longitudinal Kerr mode within an area of view of 1.4 mm x 1.7 mm (see figures 8.7 and 8.8 for example).

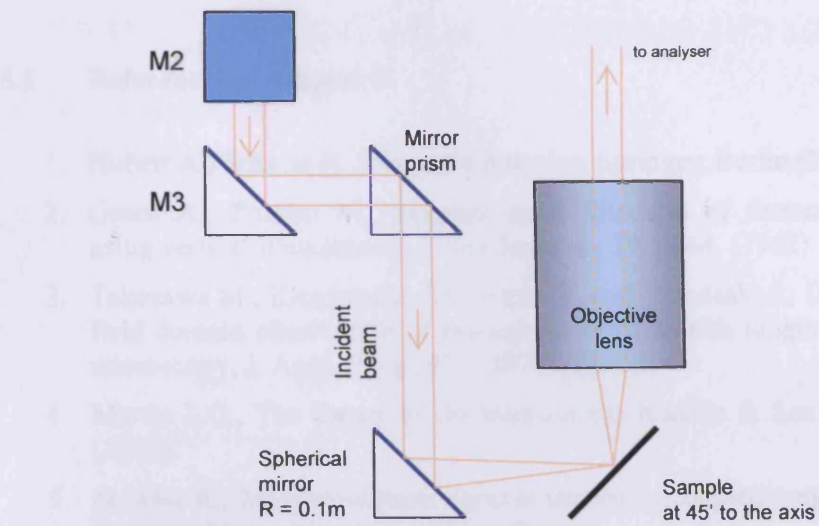

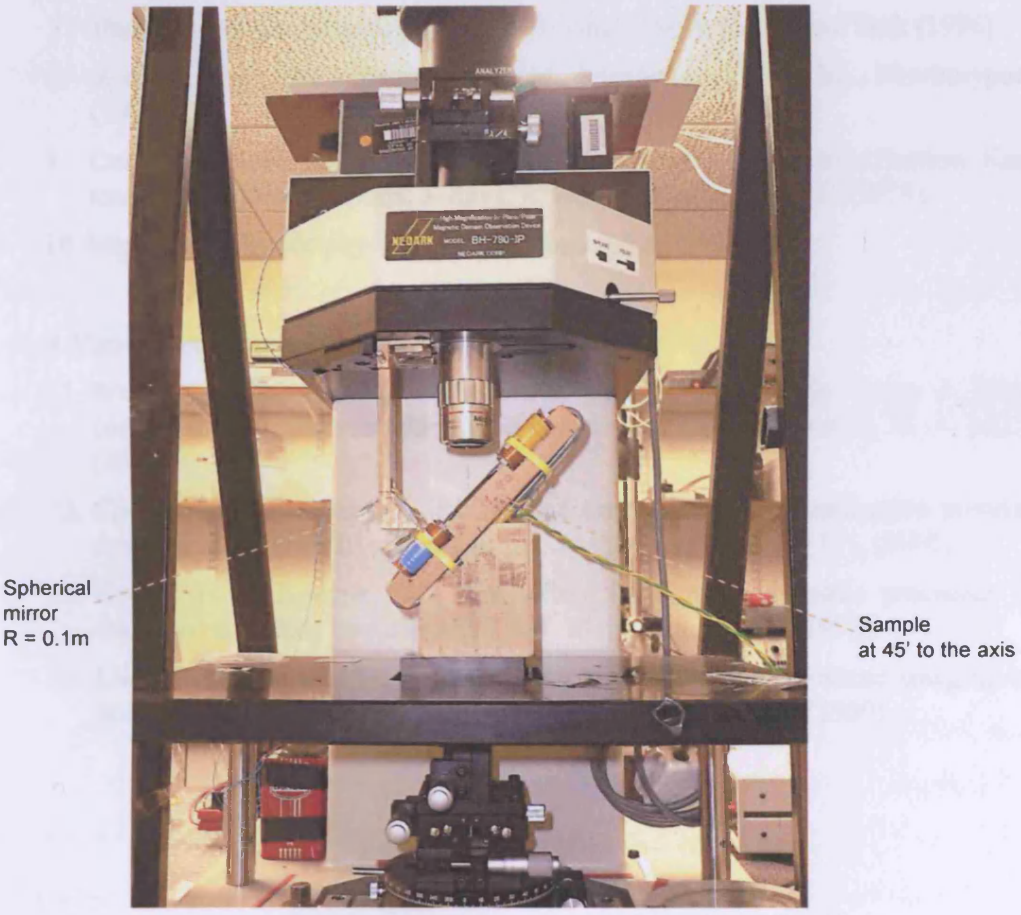

Fig. 5.7 Attachment for high contrast longitudinal observation at 45° illumination with x5 lens

5.5 References of chapter 5

1. Hubert A., Schafer R., Magnetic domains, Springer, Berlin (1998).
2. Green A., Prutton M., Magneto-optic detection of ferromagnetic domains using vertical illumination, J. Sci. Instrum., 39, p244, (1962).
3. Takezawa M., Kitajima K., Morimoto Y. and Yamasaki J., Dynamic and wide field domain observation of amorphous ribbons with longitudinal Kerr effect microscopy, J. Appl. Phys., 97, 10F701, (2005).
4. Martin L.C., The theory of the microscope, Blackie & Son Limited, London (1966).
5. Schafer R., Magneto-optical domain studies in coupled magnetic multilayers, J. Magn. Magn. Mat. 148, p226, (1995).
6. Schmidt F., Hubert, A., Domain observation on CoCr layers with a digitally enhanced Kerr microscope, J. Magn. Magn. Mat. 61, p307 (1986).
7. Burke M.W., Image acquisition, Vol.1, Chapman & Hall, New York (1996).
8. Ryer A., Light measurement handbook, International Light Inc., Newburyport (1998).
9. Collins A.J., Husni M., Jones R.M., A versatile high-magnification Kerr magneto-optic microscope, J. Phys. E: Sci. Instrum., 11, p547, (1978).
10. http://hyperphysics.phy-astr.gsu.edu/hbase/hframe.html

Additional recommended literature

11. Wang Q., Thomas X., Achromatic polarization switch using a film-compensated twisted nematic liquid crystal cell, Lyquid Crystals, 31, 4, p535, (2004).
12. Choi B.C., Ballentine G.E, Picosecond time-resolved magnetisation reversal dynamics in Ni80Fe20 microstructure, J. Appl. Phys., 89, p7171, (2001).
13. Kryder M.H., Koeppe P.V., Kerr effect imaging of dynamic processes in magnetic recording heads, IEEE Trans. Magn., 26, p2995, (1990).
14. Liu F.H., Schultz M.D., Kryder M.H., High frequency dynamic imaging of domains in thin film heads, IEEE Trans. Magn., 26, p1340, (1990).

CHAPTER 6 EXPERIMENTAL PROCEDURES AND METHODS

6.1 Introduction

The details of sample preparation, magnetising and imaging equipment, and image processing methods are presented in this chapter. The understanding of these details helps to develop the most appropriate conditions for domain imaging experiments. Knowing the tolerance of the equipment and effects on domain structure introduced by the sample preparation procedures is important for correct interpretation of the imaging results presented in chapters 7 and 8.

6.2 Magnetisation apparatus

6.2.1 Magnetising devices

A number of magnetising devices were built to energise various samples. Helmholtz coils were used for magnetising thin film samples, amorphous ribbons and amorphous wires. They were designed using an analytical equation from [1]. To fit the system, coils with a radius of 7.5 cm were used consisting of 103 turns of 0.7 mm^2 wire which could carry a continuous current of 4 Amps (10 Amp for short periods). A maximum continuous field of about 4000 A/m (10000 A/m for short duration) was possible with this configuration. The resistance of each coil was 3.4 Ohms.

A U-yoke, made of laminated steel, was used with specially shaped brackets designed to magnetise 30x30 mm square samples of GO and NO steel and Ni-Fe alloys. It was important to achieve high uniformity of the field in the sample under test, so optimisation of the geometry with the help of FEM modelling was carried out.

The OPERA-2d software package was used for DC and AC modelling of the yokes. A finite element mesh and the calculated magnetic flux distribution for 50 Hz magnetisation is presented in figure 6.1a. The sample was held at both sides in the slots forming a close loop. It was found that the flux density through a sample did not depend much on the lap distance Δx in the slot when it was more that 1.5 mm. Fixing the distance at 3 ± 0.5 mm it was found that a maximum flux change of up to 8% was possible in low permeability materials. In such cases, when uniformity of the flux density along a sample is still important, an additional correction winding shown in figure 6.3 was used. In general, the U-yoke was used when high field strength was required; the low-reluctance yoke (figure 6.1b) was used when high accuracy was required over a wide range of frequencies of magnetisation.

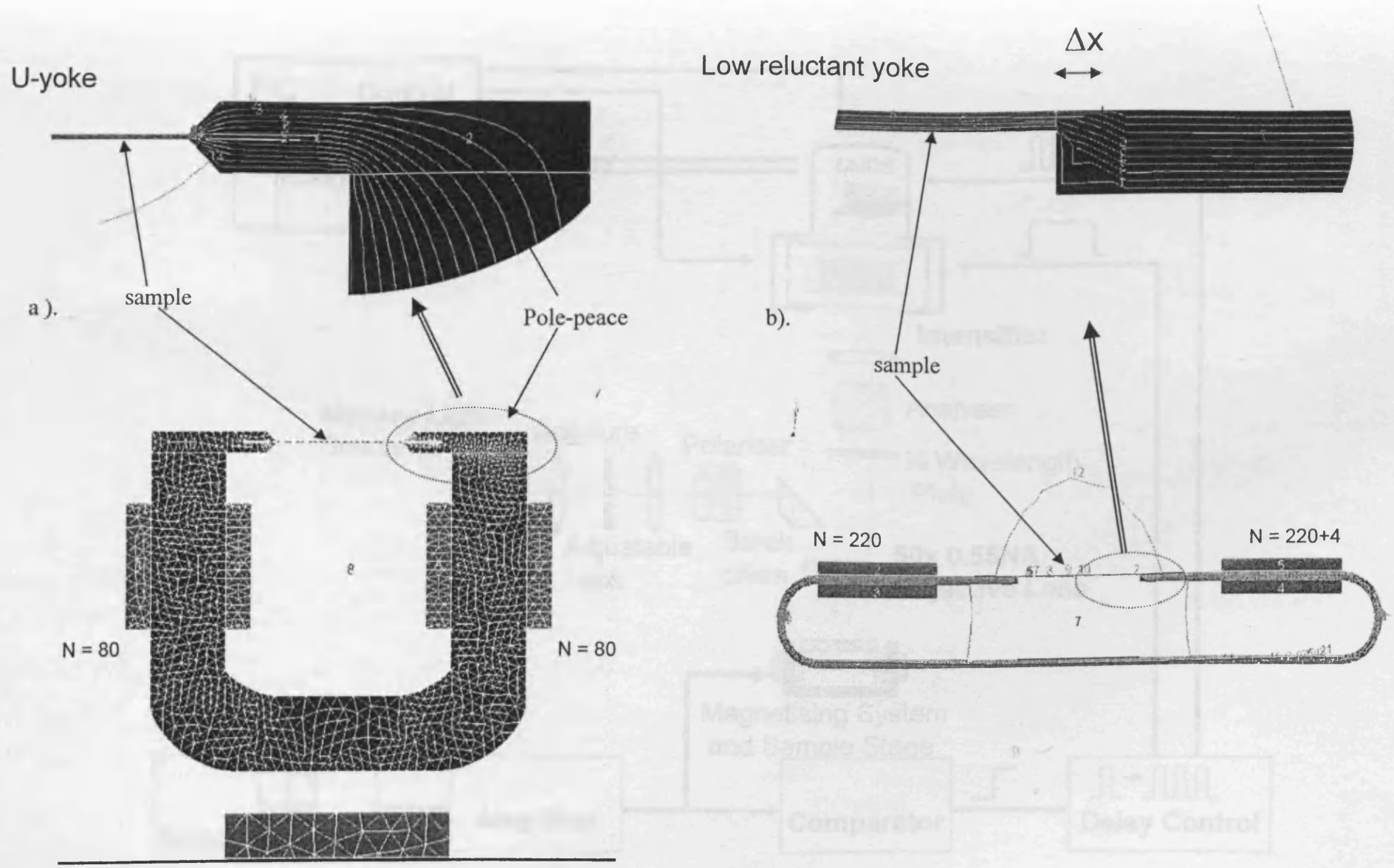

Fig. 6.1 FEM modelling and derived flux density lines in the pole-peaces of U-yoke (a) and low-reluctant yoke (b) used in the experiments.

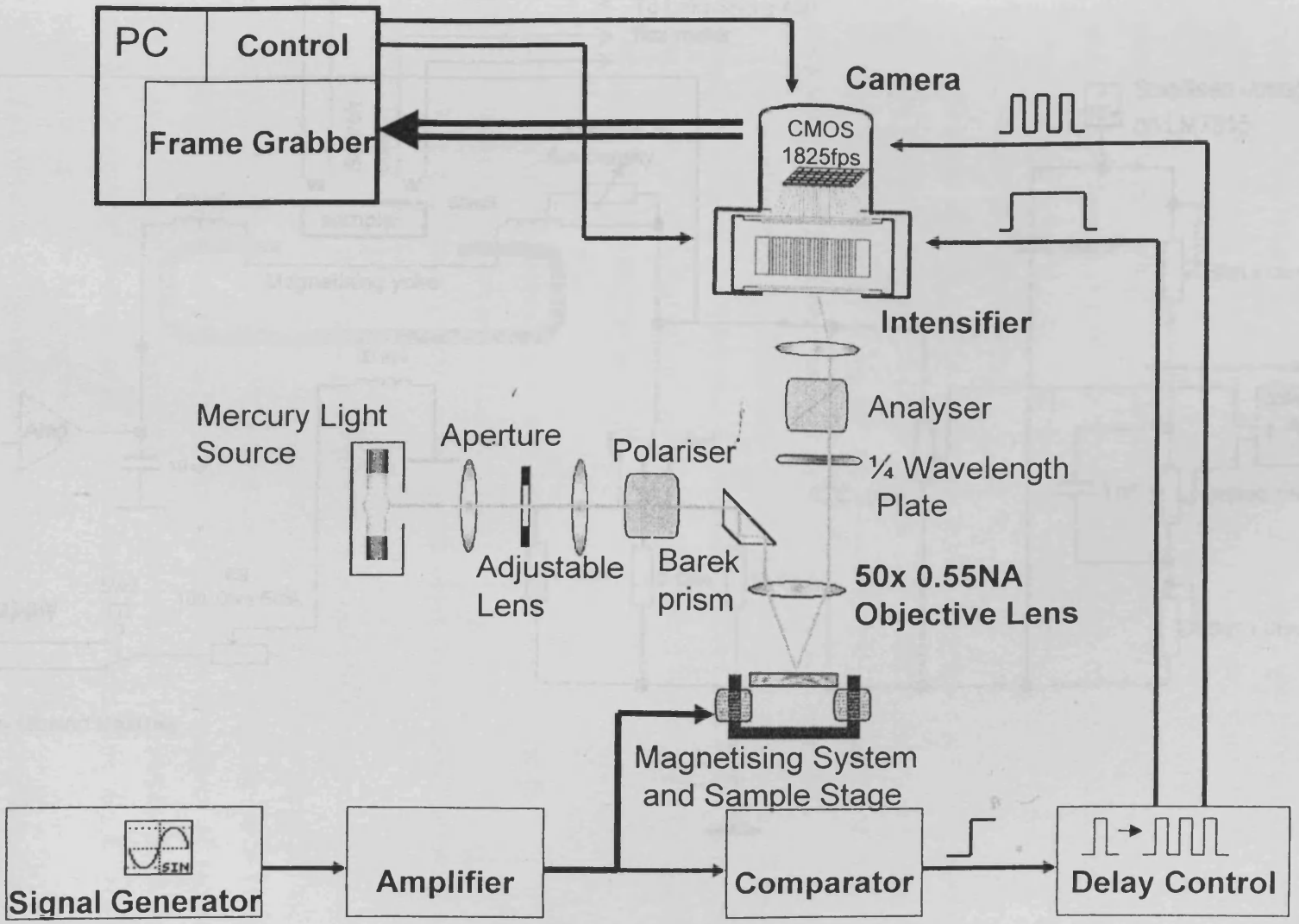

Fig. 6.2 Schematic diagram of the experimental system featuring a sweep generator as a master clocking device.

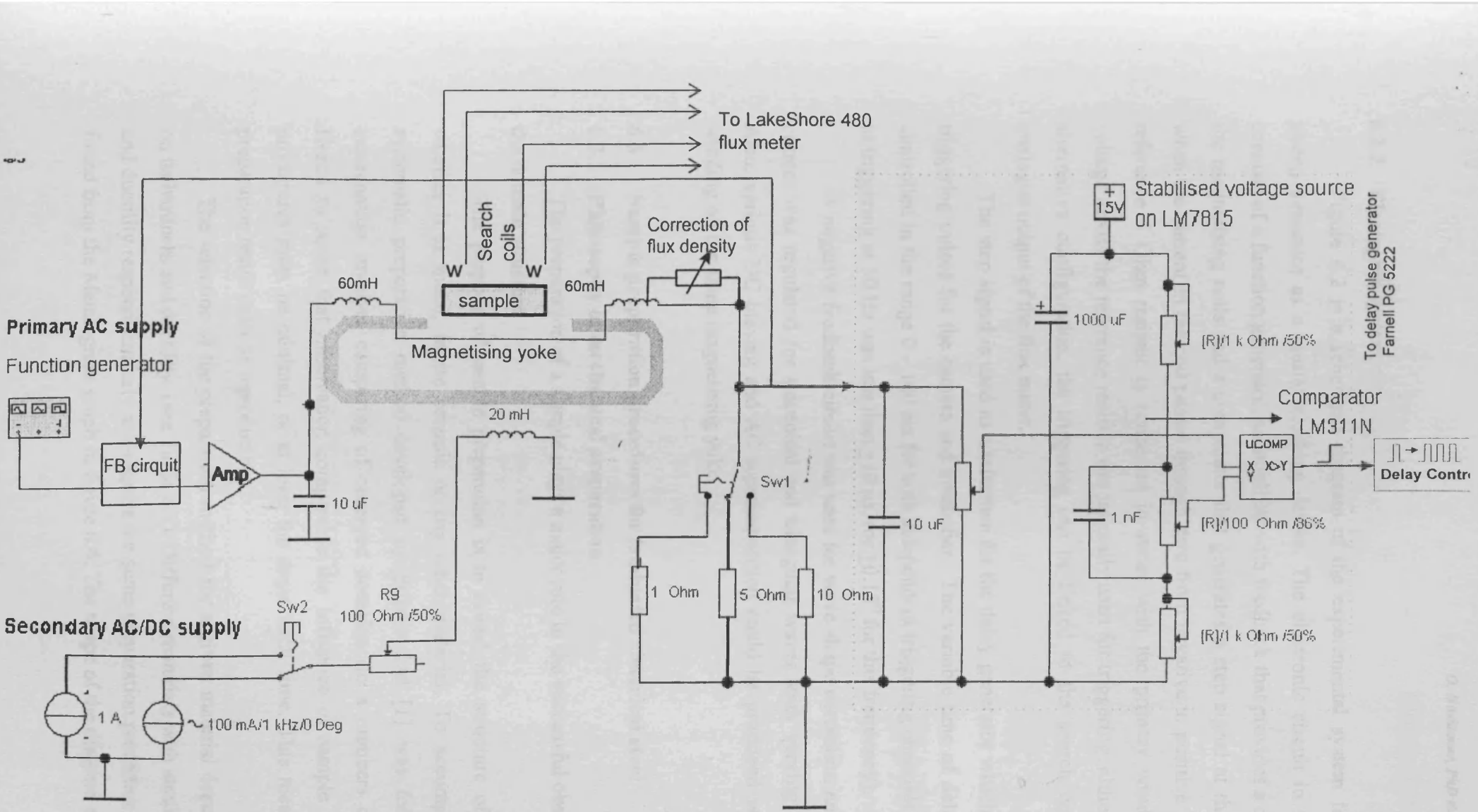

Fig. 6.3 Magnetising circuit, yoke and triggering circuit used for dynamic observation on sheet samples

6.2.2 Electronic system

Figure 6.2 is a schematic diagram of the experimental system featuring a sweep generator as a master clocking device. The electronic circuit in figure 6.3 consists of a function generator, an amplifier with feedback that provides a current for the magnetising coils and a comparator that generates a step signal at the moment when the current in the coil passes through zero from negative to positive current. A reference 5 Ohm resistor is connected in series with the primary windings. The voltage across the reference resistor was normally used for triggering, although in the alternative configuration, the triggering can be linked to the search coils or the analogue output of the flux meter.

The step signal is used as a reference for the delay generator which generates triggering pulses for the camera and intensifier. The variable time of delay may be controlled in the range 0 – 100 ms for both independent triggering channels. The error in triggering at 50 Hz was less than ± 10 μs, (or $\pm 0.18^{\circ}$ for this frequency).

A negative feedback circuit was used for wave shape correction and the peak current was regulated for sinusoidal and triangular waves with varying frequency. Also, various DC biasing and AC superimposition could be produced with second winding on the same magnetising yoke.

6.3 Sample preparation procedures for laminated electrical steel

6.3.1 Philosophy of mechanical preparation

The preparation of a sample plays a major role in the successful observation of the domain structure.

The purpose of sample preparation is to reveal the structure of a sample, whether it is metal, ferrite ceramic or any other material. To accomplish this a systematic preparation method developed by Struers Ltd [1] was followed. An examination involves comparing of observed domains on a numbers of samples. Hence to make that observation comparable the influence of sample preparation procedures must be minimal, or at least the same each time. This means that the preparation result must be reproducible.

The selection of the preparation method for a given material depends mainly on its hardness and ductility, (see Table 6.1). Different materials with similar hardness and ductility respond similarly and require the same preparation procedure that can be found from the Metalogram graph in figure 6.4. The shape of the diagram results from

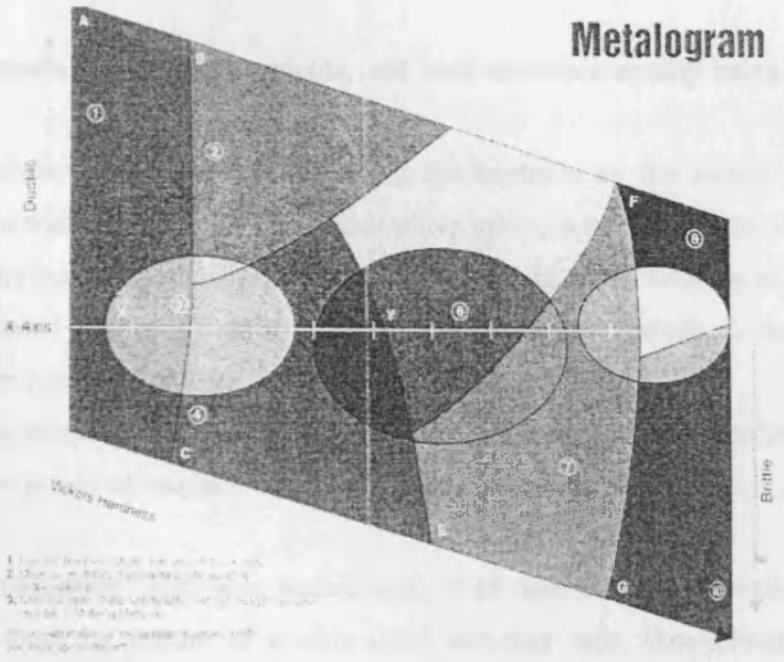

Fig.6.4 HV graph of materials taken from the Struers guidance ©, groups of materials are referred in the table below.

Material	Condition	Hardness Vickers (Kg/mm^2)	Region on the graph
Cobalt	Annealed	48 [7]	A
	Drawn	140	
Iron, pure	Annealed	70	A
	Worked	200	
Nickel	Grey	150-240	
	Annealed	70-80	
	Electroplated	200-420	
Ni36Fe 64 (Invar)	Rolled	160	
Ni43Fe57	Rolled	200	
Steel			
Low carbon (C 0.2-0.3)	Annealed	110	C
	Worked	200	D
High carbon (C 0.5)	Annealed	140	
	Worked	300-420	Y
Ball bearing steel		1300	Z
Diamond	(knoob)	6500	
Silicon Carbide		2100	F
Steels GOSI, (Si <3%)	Like	120	
NOSI,	annealed	200 [2]	B
Cubic oriented	Like worked	200 ?	
	Like worked		
2. Cobalt Iron	Rotalloy T	200-400 ?	
5. Co ferrite		1270 [6]	
6. Films, evaporated epitaxelly grown on garnet	Like plated metals	300-500 ? Up to 5000	

Table 6.1 Hardness of some industrial materials [37].

soft materials generally being more ductile, and hard materials usually being more brittle.

The selection of the method begins by finding the hardness on the x-axis. Then, depending on the material's ductility, we either move upwards or downwards. Unlike hardness, ductility is not easily defined in precise numbers. In most cases, the point on the y-axis was found by trial and error. This section is focused on electrical steel, the methods for other material are often the same, exceptions are noted.

Basically, the sample preparation consists of three stages: polishing, annealing and blooming. The sequence of mechanical polishing steps is as follows:

1 **Sample mounting:** 30x30mm square samples of sheet material were mounted on tufnol blocks by means of double-sided adhesive tape. Amorphous wire specimens were encapsulated in castable epoxy resin, or by hot compression with thermoplastic stage. The purpose of mounting is for convenient handling of the specimens in the polishing machine and to preserve microstructure of the specimen from mechanical and heating injurious [2], [3].

2 **Grinding** is the first step of mechanical preparation. Proper grinding removes damage, uneven or deformed surface material, while introducing only limited amount of new deformation. Grinding was carried out on the Struers Rotopol35 machine with automatic control of applied pressure, rotation speed, cooling and time of procedure. Abrasive silicon carbide discs of 200, 600 and 1200 grade were used until the sample surface become plane and smooth.

3 **Polishing** was performed using the same machine as for grinding plus the automatic multidoser. Diamond disk MD-Largo and cloth disks MD-Mol and MD-Nap were used with appropriate abrasives. The final polishing with ¼ μm diamond abrasive and/or oxide suspension OP-U involved careful manual operation.

6.3.2 Reproducibility, true structure and acceptable results of polishing

Once a preparation method has been developed and adjusted, it should produce exactly the same results for the same material, every time it is applied. This requires consumables of a uniform quality and precise control of parameters such as:

- Rotational speed,
- Force on the specimens,
- Preparation time,
- Amount and type of abrasive and lubricant.

The best way of adjustment and control of these parameters is by automatic equipment. The ideally prepared sample should have:

- No deformation
- No introduced stresses
- No scratches
- No pull-outs
- No smearing
- No thermal damage

Using mechanical preparation, however, it is almost impossible to achieve all of the above conditions. There will be limited damage to the structure invisible with optical microscope but this means that the size of non uniformities has gone below the optical resolution (<0.8μm). If this minimal damage does not influence the examination results, this nearly perfect condition is commonly called the **true structure**.

It was difficult to achieve the **true structure**, but for most examinations a few scratches does not matter. As long the surface is good enough it is called the **acceptable preparation result** [4].

Another concern is about strain induced on the surface during mechanical preparation. Stresses are very harmful for magnetic microstructure because they cause a distortion of magnetic anisotropy. Hence observed on the surface magnetic domains can be very different from the true structure (as illustrated in section 8.4.3). With the aim to avoid mechanical stresses and destruction of a crystalline lattice, no more than 50N force per 30 x 30 mm sample, was used. Special care in lubrication and cooling of the sample was taken. The residual strains were relieved during **annealing** in a vacuum furnace.

6.3.3 Strain-Relief Annealing

The grain-oriented silicon steel samples were annealed for two hours at 800 °C in a vacuum tube furnace. The furnace was pumped to a pressure of 10^{-6} torr, as recommended in [5], before the temperature was raised. The samples were allowed to cool to room temperature whilst still under vacuum before removal from the furnace. The vacuum is essential to prevent oxidation of the polished surface. The heating and cooling rate was adjusted to 1 °C/min to ensure uniform temperature and avoid to possible distortions of the samples.

6.3.4 The influence of the preparation on the surface microstructure of GO steel and its connection with bulk magnetic properties

Commercial steel sheets have rough surfaces because they are manufactured by rolling. During the manufacturing process an interfacial structure forms between the metallic surface and the insulating coating [6]. This physical region is a site of a complex arrangement of closure magnetic domains due to the presence of fine oxide and forsterite layer (Mg_2SiO_4, see section 2.5) resulting from the industrial annealing treatments. The penetration of the oxide layer produces a local stress distribution on the metallic surface, which in turn tends to create a higher coercive layer of a few microns on both sides. In thin sheet <0.2mm, such a 'disturbed layer' can represent up to 5 – 10% of the strip volume [7].

The change of the surface condition due to the polishing leads to the change of the average permeability and coercivity of the steel lamination. Figure 6.5 shows how the polishing preparation changes the surface. A 30x30 mm square sample of 0.27 mm thick MOH grade steel was polished at a small angle to its surface. Only a few tens of μm were removed and a surface with gradually thinning coating was obtained as illustrated in figure 6.5. It can be seen that on one side of the sample the surface is polished and on the other side the coating remains almost untouched. Between these two sites there is a transient region where roughness of the surface and surface phases can be observed. Reduced surface roughness results in the reduction of tension force, T, in equation 2.3, hence the dynamics of the basic domain walls in polished laminations is different than in unpolished one. Reduced surface roughness should be taken into account than domain observations are used to explain the properties of the material [8].

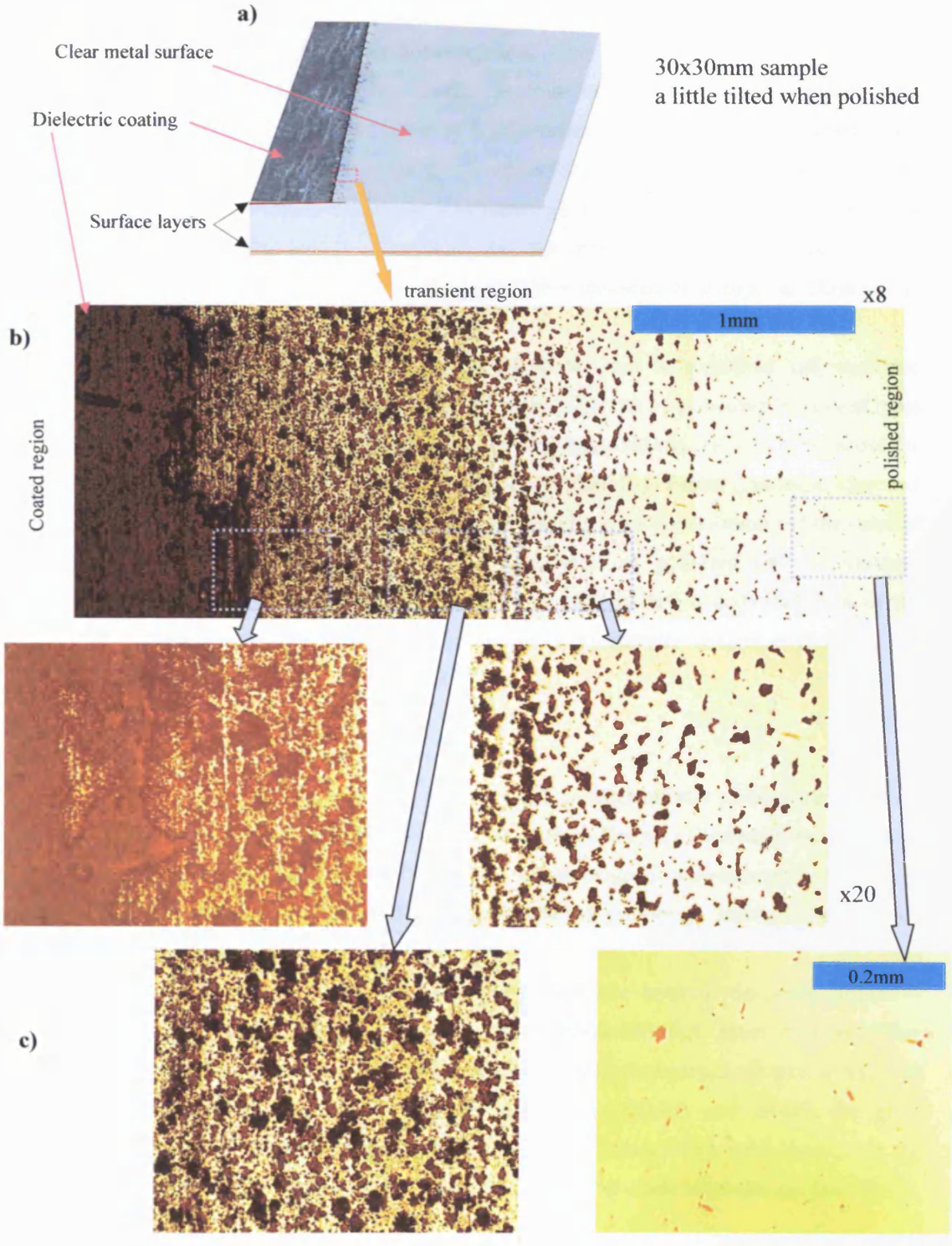

Fig.6.5 Observation of GO steel surface microstructures, using 30x30mm x 0.27mm thick sample with the surface plane tilted at small angle with respect to the polishing direction.

6.3.5 Reflectivity and surface roughness

A perfectly flat, defect-free smooth surface will reflect incident light uniformly and efficiently i.e. it is highly reflective. An unpolished surface when observed under a microscope may have scratch lines criss-crossing at all angles. These surface imperfections cause incident light to be reflected in different directions and hence the surface appears to be less reflective. In cross-section, at high magnification, the surface would appear like a mountain landscape, as illustrated in figure 6.6a.

The depth and density of the scratches can be measured and expressed quantitatively in terms of **surface roughness**. This can be measured by several types of instruments which are often based on sliding a diamond-tipped stylus across the surface to be measured (profilometer). As a surface is polished, it becomes smoother and more reflective. The number and depth of the scratches decrease and the value of surface roughness decreases. Thus, the process of polishing can be measured quantitatively [2]. Measuring the size of the defects and overall roughness of the surface can provide some indication on how to quantify domain wall pining and surface tension force, T, in equation 2.3.

6.3.6 Chemical etching

When soft material with high ductility is mechanically polished some surface flow occurs. This smearing of the metal surface leading to indistinct boundaries of adjacent grains and causes a corruption of the magnetic microstructure. Etching of metal surfaces after polishing is almost always performed during metallographic preparation.

Etching is the process whereby a very thin layer of the metal surface is dissolved and removed chemically (or electro-chemically). Since different phase components of metal together with the metal grain boundaries all etch at different rates, etching visually differentiates the phases present and reveals the grain boundaries. Nital solution (2% HNO_3 in ethanol) was used for steel samples, as the best etchant for ferrous alloys. Possible etchants for other materials are described in [2], [9].

6.3.7 Electrolytic polishing

Electrolytic polishing can be used instead of mechanical polishing for some metallic samples. The best results were achieved on samples with small grains such us non-oriented steel. The principles of electrolytic polishing are as follows:

The sample to be polished is connected as the anode in a electrolytic cell. A viscous jell layer on the surface is produced by the reaction between the metal and the electrolyte. This layer has a greater electrical resistance than the rest of the solution.

In cross-section, at high magnification, the surface would appear like a mountain landscape (with "hills" and ridges), as illustrated in figure 6.6a. The resistance at a peak A, represented by the distance A-B, will be lower than at depression C, represented by the distance C-D, because the film is thinner at A-B. The current at A will be much higher than at C, causing metal to dissolve faster at A than at C, and producing smoother surface.

The jell layer appears only under certain conditions which can be identified by the VA plot in figure 6.6b. This curve depicts anode current density as a function of cell voltage. The formation of a viscous layer starts in area B – C, with area C – D being best for polishing. Before and after this optimum condition the smooth jelly layer does not exists and pitting of the surface takes place instead.

The electrolytic polishing in contrast to the mechanical polishing does not introduce any stresses into the material. More details about electrolytic polishing can be found in [2] and [10].

6.3.8 ZnS coating for enhanced MO domain observation

The physical principle of contrast improvement was described in Chapter 4. This section is focused on the technique of deposition of the coating. As was mentioned, it is necessary to deposit 64 nm coating with even thickness across all observed surface regardless of the sample material.

Evaporation was performed in an Edwards model 4 vacuum chamber. A tantalum boat containing zinc sulphide in the form of powder was subjected to currents of up to 90 Amps to supply the necessary heating.

Before a sample was placed in the evaporation unit it was cleaned ultrasonically in carbon tetrachloride (or alternatively, boiled separately in solutions of acetone, ethanol and isopropanol for 5 minutes) and dried in a jet of nitrogen gas.

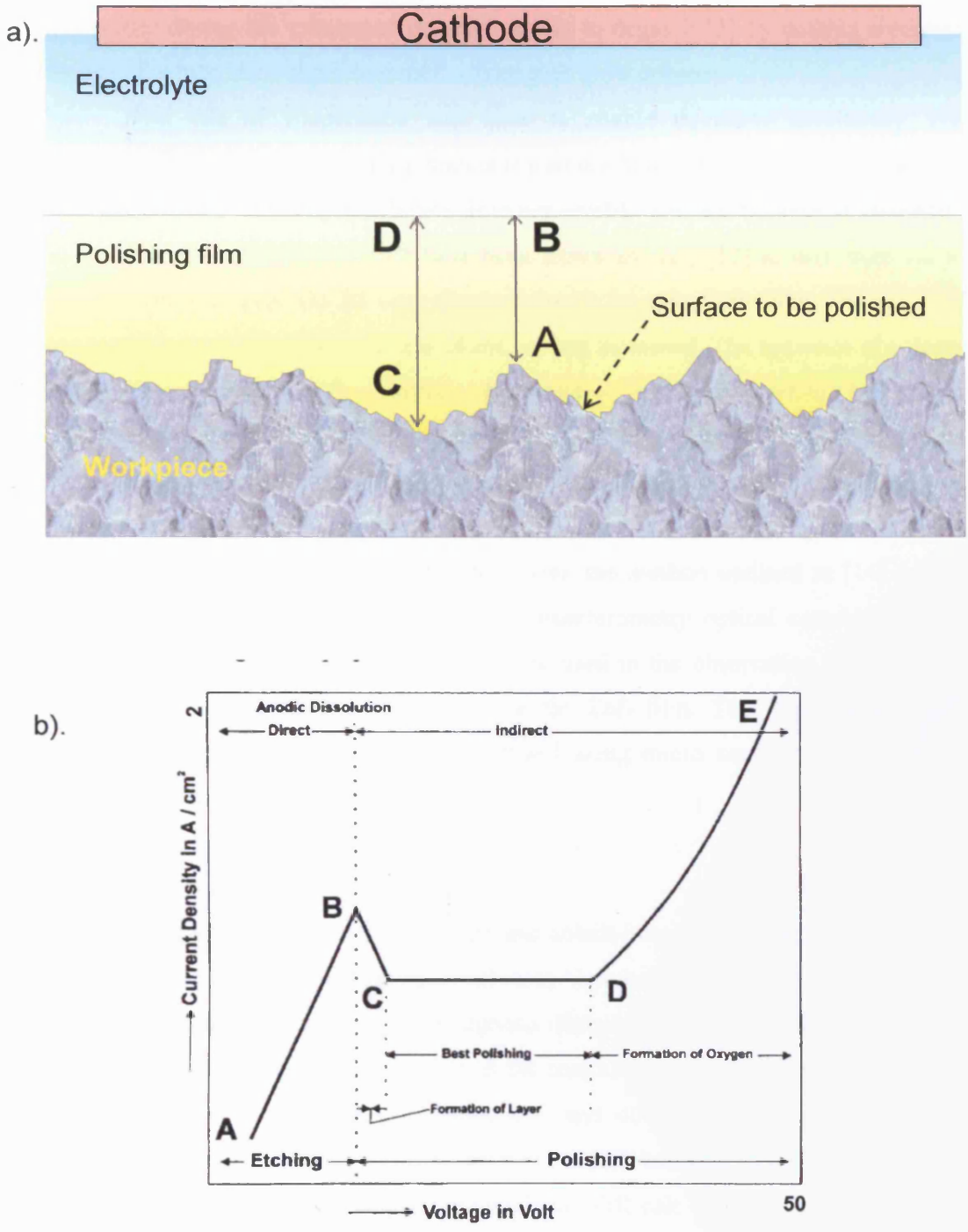

Fig.6.6 Mechanism of electrolytic polishing (a) and VA graph of electrolytic cell (b). Reprinted from [1].

The sample was held horizontally 20 cm above the boat and the evaporation was done at a pressure of less than 10^{-4} torr. When fresh powder was used it was necessary, during the process of pumping down, to degas it [5] by passing a current through the boat for a short time until a faint pink glow appears.

The rate of evaporation was slow to enable thickness monitoring. For thickness measurement a vibrating thickness monitor MAXTEK TM-100 was used. The results achieved using this device were not reliable, perhaps because of variability in the ZnS optical indexes which have been shown in [12], [13] to vary from 2.2 to 2.35. In practice good results were obtained merely by eye observation. The colour of the sample changed as the thickness of the coating increased. The sequence of colours was yellow – pink – red - purple - dark blue - light blue - white. The colour corresponding to the optimum thickness is blue for 45° angle of illumination, pink – for perpendicular illumination. If the coating was too thick it could be removed by a dilute solution of HCl.

For more precise coating in future work the method outlined in [14] can be used. The thickness is measured with the interferometry optical control until the reflectivity for the wavelength intended to be used in the observation is minimised, providing a precise optical path length in the ZnS film. The 'three wavelength' method described in [14] may be modernised using micro controlled spectrometer connected to a PC.

6.3.9 Preparation of other materials

Sample preparation of nickel-iron and cobalt-iron alloys is almost identical to the method described above for electrical steel. Care had to be taken with handling of amorphous materials and ferrites. Amorphous ribbons and wires are difficult to handle during a polishing procedure, in addition the annealing temperature must not exceed recrystallisation point (usually between 300 and 400 °C). Etching of these thin samples had to be done very carefully so as not to etch holes.

Ferrite samples and powder materials are difficult to polish because pull-out defects frequently occur. In addition these samples can fall apart when annealing is done incorrectly by using inappropriate temperature gradients or excessive heating and/or cooling rates.

The following procedures were found to be useful to many of the materials studied in this work.

- The fine polishing in one direction align all scratches parallel to each-other, it make some improvement on optical resolution, CCD array will not see scratches when they aligned with sensor lines, and FFT filtration, when images are processed, is sufficient if defects are periodic.
- Etching with picric acid can reveal the orientation of individual grains in a polycrystalline sample.

6.4 Image capturing part of the system

The purpose of the optical part of the system is achieved when a sufficiently bright image is projected on to the image sensor input window. From this point further success of the observation is measured by the performance of the image capturing system.

Understanding the physical principles of the imager operation and ability to adjust the parameters of the imaging system plays a crucial role in successful image recording. It is also important to understand the physical principles and uncertainties for correct processing and analysis of recorded the images.

Traditionally the image acquisition part of the system consists of a shutter, the image sensor, the image storage unit and the triggering circuit. The image sensor is a major unit which converts the light projection image into data. Two cameras are used in the system. A Deltapix Infinity X camera with a maximum resolution of up to 21 Megapixels and frame capture rate of 60fps was used for still imaging and slow dynamic domain observations. A second camera, a Lambert Instruments HCC-1000, was used for high-speed image acquisition, with a light intensifier in front of the image sensor array. In both cameras a CMOS photodiode array is used as an image sensor. The following sections describe the structure and performance of the single photodiode cell followed by a description of the readout architecture of the whole array.

6.4.1 The **efficiency of a single CMOS photodiode**

The sensor array consists of photodiode (or photogate) elements operating in an integrating mode. The photodiode integrates the light level by collecting photogenerated electrons. Figure 6.7a presents an equivalent circuit of the single cell with on-pixel amplifier, figure 6.7b presents a geometry of the cell. The illuminated photodiode charges a 'photocapacitor' formed from the effective junction capacitance. [15]. As the photogenerated electrons are collected, the potential across the depletion layer of the diode increases (or decreases, in discharge mode). The increase of potential across the diode is proportional to incoming light irradiance and integration time. After reading the charge, each photosite is reset to its zero state in preparation for the next light integration period.

The effect is governed by the defining characteristic of a capacitor: $Q = C\ V_c$ where Q is the charge of the capacitor, C is its capacitance, and V is the voltage across the capacitor. On the other hand $Q = \eta\ I\ A_j\ t$ where η is efficiency of electron generation, I – light intensity, A_j – area of the diode, t – time of integration. The voltage on a capacitor of a designated size when it is exposed to the light equals $V_c = \eta\ I\ A_j\ t\ /C$. The voltage is more easily measurable and is used in practice.

The effective capacitance C_j of the junction is a function of the depth and the junction area: $C_j = 1.05\ A_j/\ z_d$ (in turn $z_d = 0.53\ \sqrt{}\ V_{bias}/\rho$). Because detector noise increases with increasing capacitance (by a factor of approximately kTC, where T is a temperature and k is the Boltzmann's constant), the choice of cell area is always a compromise between sensitivity, resolution and efficiency. The sensing area has to be as large as possible, but this increases junction capacitance (and lowers IC S/N ratio). Increased C_j also decreases speed of readout. More information on the photodiodes and photogates can be found in [15] and [16].

CMOS technology allows a local readout amplifier to be added to each pixel making it an Active Pixel Sensor (ASP). This allows the conversion of the charge to voltage to happen at the pixel avoiding any distortions on guide terminals. Moreover the presence of the amplifier allows offset/gain correction specifically for each pixel.

Typical values for a CMOS camera are as follows

Typical time of exposure: 10 to 30 ms

Sensor saturation: 80000 electrons for 10 μm x 10 μm square pixel.

Sensitivity: 255 counts at 50 LUX and 20 ms exposure.

a.

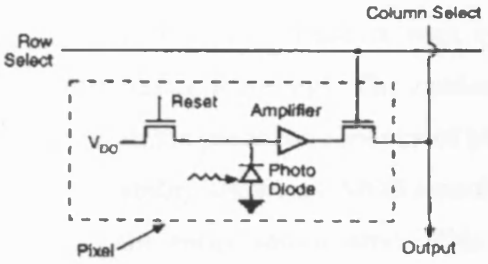

Copied from [16]

b.

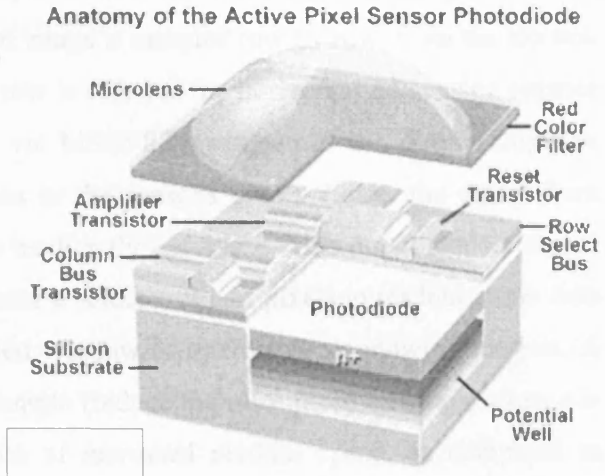

Courtesy Eastman Kodak Co.

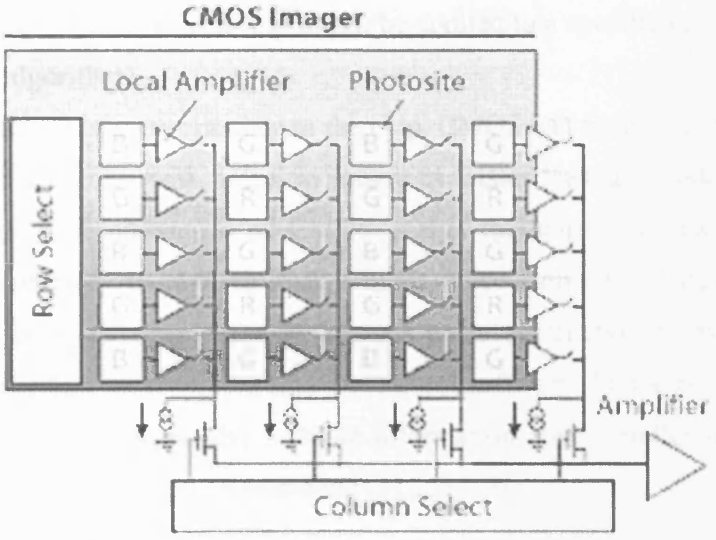

Courtesy Eastman Kodak Co.

Fig. 6.7 Active pixel equivalent circuit (a), geometry (b) and read out architecture of the color RGB array (c) arranged in Bayer's mosaic pattern.

6.4.2 Architecture and readout of CMOS array

A common raster scanning readout in a CMOS and CCD image sensor is depicted in figure 6.7c. The integrated image is sampled row by row, from the top row to the bottom row. When a specific row is selected the horizontal addressing register sequentially connects each column via MOSFET switches to the output amplifier (raster scanning). The random access to the sensor's pixels allows the signal from single pixels or columns of pixels to be directly addressed. This direct random access ability allows a CMOS sensor to choose a select group of pixels to readout rather than the entire sensor array. This is called window-of-interest or windowing readout. A CMOS sensor can intelligently subsample (reduce the resolution) an image when it is captured. It also offers the potential of increased readout speed, as compared to CCD's, which must offload all its charge through a single horizontal shift register.

In addition to amplification within the pixel site, amplifying circuitry may be placed elsewhere along the CMOS signal chain. This provides different, multiple gain stages throughout the sensor. Amplifiers can apply global gain to increase sensitivity in low light situations. Or selective gain can be applied to a specific colour to assist in white balance algorithms.

By adding this extra circuitry to the chip, CMOS has traditionally experienced a great deal of difficulty with noise, including transistor leakage, diode leakage, and residual charge. One advantage of CMOS is that the sensor can have subtractive elements on the chip, to remove dark current noise from the charge before it is offloaded. In both cameras the dark current noise subtraction is available via a calibration procedure incorporated into the control software. Full specification of the cameras is provided in Appendix 3. More information about intelligent readout and on-chip image processing can be found in [17] and [18].

6.4.3 Fast image acquisition

In this project the fast frame sampling is the most important feature of the camera. There are three factors that limit the frame acquisition speed while maintaining acceptable dynamic range and resolution.

- The first problem is the limited operating frequency of the horizontal switches and the AD converter. In the case of the HCC-1000 camera the operating frequency is 500MHz and this sets the physical limit for stable electronic

operation. This "maximum frequency of pixel readout" results in a maximum frame rate of 461 frames per second (fps) for the full resolution of 1024 x 1024 pixels (plus 11 blind lines). The maximum frame rate can be extended at the expense of resolution as explained in Appendix 3.

- The second problem is the speed of the upload interface. Mainly because of a limitation of the USB interface the Infinity X camera cannot upload more than 60 frames per second at 640x480 pixel resolution. In the HCC-1000 camera this problem is resolved with the use of the buffer memory of 512 Mb, which is able to record the sequence of images at the full speed and upload them later via an RS-644 interface to the PC hard drive. Obviously, the size of the buffer memory limits the duration of an image sequence.
- Finally, the light sensitivity of the image sensor must be sufficient for recording an image during the time of exposure at a given light intensity. The time of exposure cannot be longer then the period of the image readout.

Having adequate light levels is always a concern for imaging system designers [15]. It is critical for applications involving high-speed events. Often the domain viewing area has little light, which might be sufficient enough for static observation. Alternatively, the light may be adequate but the task involves motion for which the shutter time is too short to provide adequate exposure levels. The basic constraint on most high-speed imaging systems is that of achieving stop-action within the resolution of the smallest point to image. Because of the short exposures, stop-motion imaging requires either a high-senstivity sensor that can yield a usable image under low light conditions, or a higher output lighting system, or both. For example [15, p620], consider the inspection of 0.2 mm defects on a belt moving at 5 m/s would require 20 kW of light power to be used with conventional CCD camera.

The problem of high levels of continuous lighting is that localised heating may damage the object being imaged. Strobelighting can reduce the heating effect but replacing continuous lighting with strobe lighting introduces other problems such as light variability and accurate synchronisation with the electronic shutter of the CMOS sensor. In some cases when the observed domain motion is repeatable it is possible to use an integration-averaging readout procedure such as time-delay integration (TDI) or frame averaging integration which is detailed in section 6.5.

When no predictable motion is observed and options for increasing lighting levels are limited or dangerous, array cameras can utilise image intensifiers.

6.4.4 Image intensifier

Image intensifiers are used whenever the light intensity is too low to achieve sufficient brightness contrast for a standard camera system, or the desired exposure times are too short to acquire enough light for sufficient contrast. Modern image intensifiers (see figure 6.8) have an input photocathode followed by a micro-channel plate electron multiplier [19] and a phosphorescent output screen. The photocathode in the latest generation of these devices has a higher quantum efficiency (up to 50 %) at the blue-green end of the spectrum. The gain of the micro-channel plate is adjustable over a wide range. In the case of the HCC-1000 camera, maximum gain is 11000 i.e. a detected photon at the input leads to a pulse of 11000 photons from the output phosphor screen. Resolution of an intensified camera depends on both the intensifier and the CMOS array, but is usually limited by the intensifier micro-channel plate geometry to about 75 % of that of the CMOS array alone. In the HCC-1000 camera the CMOS array has 1024x1024 pixels but the guarantied resolution of the device is 510 TV lines [20]. The size of the intensifier often is bigger than the CMOS array, so that they are coupled with fibre-optic tap (see figure 6.8 and Appendix 3).

Image intensifiers have a reduced intrascene dynamic range compared to slow-scan CCD or CMOS cameras and it is difficult to obtain more than a 256-fold intensity range (8 bits) from an intensified camera [21]. An intensifier's gain may be rapidly and reproducibly changed to accommodate variations in scene brightness thereby increasing the interscene dynamic range. It can be done with specific gain-adaptive software. In this work we did not develop any software for gain-adaptation, but used software with manual gain control provided with the camera.

In addition to outstanding light sensitivity the second advantage of intensified camera is a gating function. By applying a negative voltage pulse between the microchannel plate (MCP) and the gating electrode, the camera can be open for a short time. In this case gating can be used as a high-speed shutter. When selecting a small gate-open time, high-speed events can be captured without blurring. In the HCC-1000 camera the desired gate-open time can be selected beginning from 40 ns and can be synchronised with external equipment (delay-pulse generator) or with frame sampling of the camera (see FEN signal in camera hardware specification [20]).

More about fast event imaging and timing performance of intensified cameras can be found in [22]. The application of intensified cameras for fast domain imaging is also demonstrated in [23].

Thermal noise from the photocathode as well as electron multiplication noise from the MPC reduce signal to noise ratio in an intensified camera to below that of the usual CCD or CMOS camera. The contribution of these components to the noise created by the statistical nature of the photon flux depends on the gain of the device and the temperature of the photocathode. Generally, a reduction of the gain of the intensification stage is employed to limit the noise although intensified CCD cameras are used with a cooled photocathode [23]. The complication in the intensifier imaging is that the noise is multiplicative, and is difficult to suppress by common image processing software. Because of that the noise must be minimised at the early stage of image acquisition. Measures and recommendations for noise minimisation can be found in [19] and [22].

6.4.5 Shutter in the imaging system

As long as the electronic image sensor's "Gate in" signal works as an electronic shutter there is no need to use any mechanical shutter. Nevertheless high intensity light can accidentally enter the system and damage the intensifier. To prevent this from happening the mirror assembly always shadows the intensifier before the light turns on, it also serves as an emergency shutter.

Electronic shuttering in CMOS image sensors requires the addition of one or more transistors to each pixel, a somewhat unpractical approach considering the already compromised fill factor in most devices (figure 6.7b). This is the case for most area-scan image sensors. Many manufacturers have implemented a non-uniform **rolling** shutter solution that exposes sequential rows in the array at different time intervals utilising a minimum of in-pixel transistors. Although rolling shutter mechanisms operate well for still images, they can produce motion blur leading to distorted images at high frame rates. To solve this problem, engineers have crafted **uniform synchronous** shutter designs that expose the entire array at one time.

In the Infinity-X camera the rolling shutter is used and distortion of moving images does occur. This problem does not exists in the HCC-1000 camera with its uniform synchronous shutter.

6.5 Triggering, clocking and synchronisation of imaging and magnetising parts of the system

For quantitative analysis of the recorded images it is necessary to know precise time of its capture, for this reason the camera must be synchronised with a magnetising system. Figure 6.9a shows an example of real time imaging at 50 Hz with synchronisation to the magnetising field by measuring the current in the coils. Every sequence of 36 frames starts every cycle at the moment when the applied field passes through zero (on rise halve cycle). The starting moment can be shifted to any point on the cycle by the variable delay generator (see figure 6.2 and figure 6.3).

Apart from the magnetising field, the synchronisation can also be taken from the magnetic induction in the sample by measuring the output voltage from the flux meter. The choice of synchronisation method is considered by the experimental conditions, sample size and magnetisation amplitude. Synchronisation from the current is usually the most precise.

Figure 6.9b shows a sequence of pulses in a typical stroboscopic Kerr microscope. The stroboscopic imaging of fast events has been known for decades [24] and is used when the camera's readout speed is too slow to upload the image before a new event occurs. In most cases triggering of the light pulses is simpler and more precise than the shuttering of the camera. This is why previous researchers [24], [25], [26] used pulse lasers, stroboscopic lamps and chopper wheels. When the frequency of light pulses is slightly higher than the frequency of magnetisation it is possible to see slowly varying images.

Another aspect of the stroboscopic method is an ability of image accumulation and averaging [26]. When the brightness of the single exposure is not sufficient to develop good contrast, it is useful to expose the sensor to the same scene in the next cycle or even over many consecutive cycles. This method was used in early experiments with photographic film cameras as illustrated in figure 6.9b mode 2, when the shutter of the camera is open over a number of cycles and light is flashing at the same time on each cycle. With multiple exposures there is a multiplicative increase in sensitivity equal to the number of integrated frames. The increased sensitivity means that for the same exposure levels, much less lighting is required, and this is accomplished with increasing of signal to noise ratio.

Apart from simple frame integration-averaging more sophisticated read out algorithms are possible. Time-delay integration (TDI) readout procedure [23],

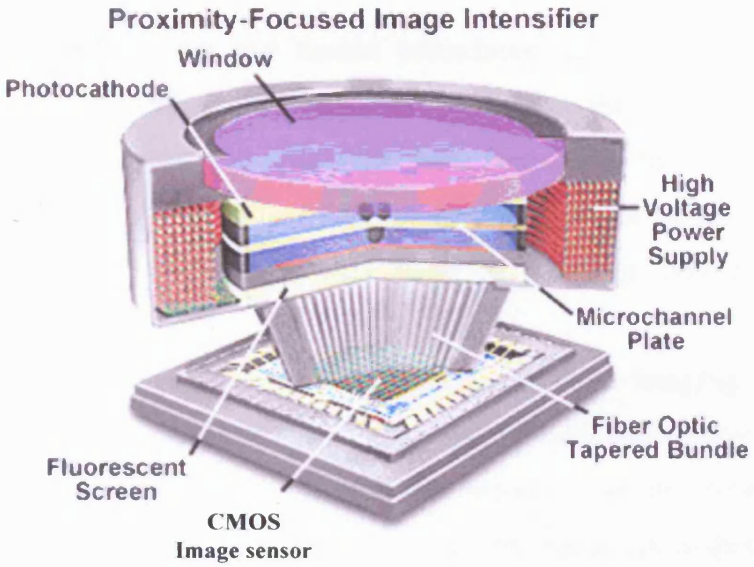

Fig. 6.8 Proximity focused image intensifier with MCP and fibre-optic tap coupling. Modified from [21]

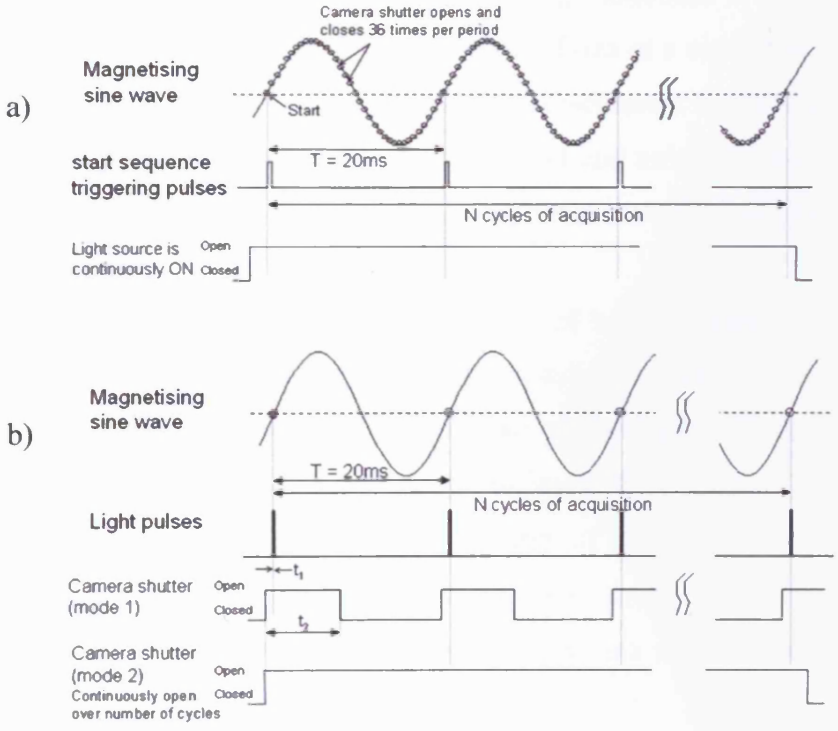

Fig. 6.9 Timing event for real time (a) and stroboscopic (b) image capture

multiple-add-subtraction and fractal procedures* [27] were used successfully to suppress a fluctuation of the light source and build up the contrast.

The only constraint placed on these methods is that the speed of the target must be known precisely (for TDI), or motion must be periodically repetitive (for frame averaging), and the motion must be precisely synchronised with sensor clocking.

The HCC-1000 camera can perform real-time imaging as demonstrated in figure 6.9a. The integration-averaging, multiple-add-subtraction and other image processing procedures for contrast enhancement can be done after images are recorded. The system is able to record real time images at magnetisation frequencies up to 200 Hz (garnet sample, which has high Kerr contrast), above this frequency the system can work in a stroboscopic mode.

6.6 Image processing for domain visualisation

Image capturing is completed when the image sequence is stored on the hard drive in the form of numbered image files or in the form of a video file. The recorded raw image often is a superposition of a weak Kerr-contrast domain image, surface imperfections and other "non-magnetic" background and noise. Techniques of digital image processing are used to extract the Kerr-contrast image preserving true domain boundary positions.

The digital monochrome image is a matrix of 8-bit integers, which represents 256 grey levels. Digital colour image usually comprises three matrixes of integer, each matrix represents colour component (RGB) of the image. Thus images can be treated and manipulated as matrices using a broad range of software.

The digital image processing is a large part of computer science and applied mathematics the details on fundamental theory and methods can be found in the relevant literature [28], [29]. This chapter covers only the most useful techniques for domain image enhancement in the project.

The following image and video processing software were used:

- Popular image editing programs, such as Adobe Photoshop version 7.0.1 and

* TDI, multiple-add-subtraction and fractal procedures are readout methods with immediate processing and uploading of the result of the calculations.

Paint Shop Pro version 7 were used for processing of single images and finding the most suitable for enhancing particular kind of images. Adobe Photoshop also was used for batch processing of numbered sequences of files.

- LabView 7 with IMAQ toolbox was the main program for specific operations with large sequences of image files. This software has a broad range of functions with a possibility of manual control of any parameter. IMAQ toolbox also has a ready to use functions for edge detection and pattern recognition which appears to be very useful for automatic domain wall detection. The disadvantage of LabView is its complexity for performing routine operations.
- Matlab version 13 with image processing toolbox can be applied to solve any image processing operation but was not used much because it did not support many file formats, also it require complex code writing which is much less flexible than LabView.
- Delphi programming language was used before LabView 7 became available. It is even less convenient than Matlab, nevertheless it allows low level programming which is particularly useful in some cases.
- Adobe Premier 6.5 and Animation Shop 3 were used for processing movie files and disassembling of movie files to the separate frames for subsequent processing in other programs. It was also used for assembling a video file from the processed images.

Each of these programs was effective for certain tasks so each was used accordingly. In the description of image processing procedure (sections 6.6.1 – 6.6.7) the application of software packages is highlighted. The general strategy of image processing is described at the end of this chapter.

6.6.1 Single point operations

Single point operations are image processing operations which are applied to individual pixels rather than large arrays. The process can be described with the mapping function.

$$\mathbf{O}_{i,j} = \mathbf{M}(\mathbf{I}_{i,j})$$

where $\mathbf{I}_{i,j}$ represents the input image pixel at coordinate location $(\mathbf{i},\mathbf{j})$, $\mathbf{O}_{i,j}$ is the output image pixel having the same coordinates, and $\mathbf{M}$ is a linear mapping function. Some

simple point operations such as brightness correction and thresholding (clipping) are illustrated in figures 6.10 and 6.11.

Possible implementation of the brightness correction in the software packages is as follow:

- In LabView: with IMAQ BCGLookup.VI
- In Matlab: with *imadjust* function
- In Photoshop: Main menu → Image → Adjust → Brightnes/Contrast
- In Delphi language via pixel by pixel arithmetic in the loop addressed by i and j, by the script:

```
for i := 0 to w do
    for j := 0 to h do
      O[i,j] := I[i,j] + b;
     End;
End;
```

Possible implementation of the thresholding in the software packages is as follow:

- In LabView: with IMAQ MultiThreshold.VI
- In Matlab: with code script like $OutIm = InIm > T$
- In Photoshop: Main menu → Image → Adjust → Threshold (binary only)
- In Delphi language by the script:

```
for i := 0 to w do
    for j := 0 to h do
    if I[i,j] < T  then O[i,j] := 0
                   else O[i,j] := I[i,j];
   End;
End;
```

Other useful single-pixel procedures that routinely were included in most image processing packages, are contrast stretching, histogram equalisation, gamma-correction and posterisation [28], [30].

Single point operations allow improving images which are not heavily degraded. Unfortunately, magneto-optic domain images have a significant level of noise and artefacts which arise from the optical and capture systems. To improve such images more sophisticated image processing is presented in the following sections.

a).

Mapping equation

$$O_{i,j} = I_{i,j} + b$$

Where b is a brightness increment

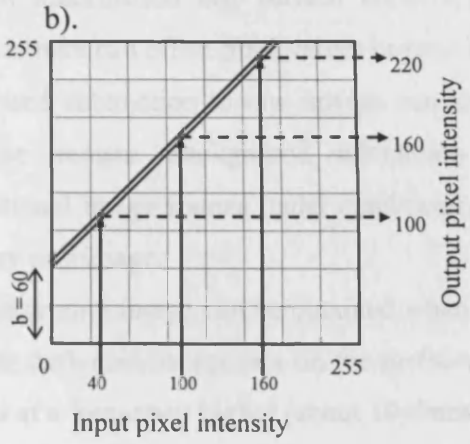

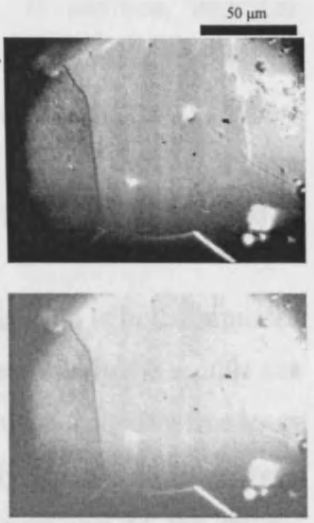

Fig. 6.10 Brightness correction operation (a) increases the intensity of each pixel for a constant value "b". However, (b) the saturating is possible when $I_{i,j}$ + b exceeds 256. (c) example of brightness correction of a domain image of non oriented steel.

a).

Mapping equation

$$O_{i,j} = \begin{cases} 0, & \text{if } I_{i,j} < T \\ I_{i,j}, & \text{if } I_{i,j} \geq T \end{cases}$$

Where T is a threshold value

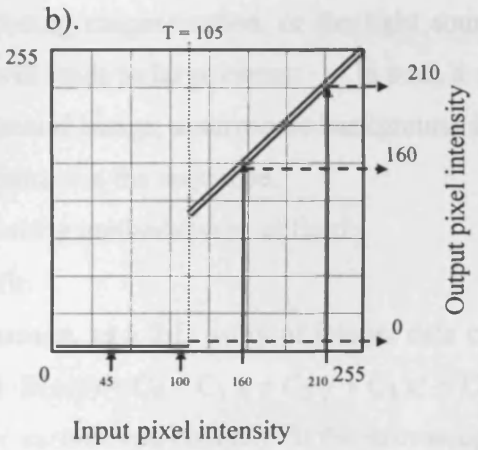

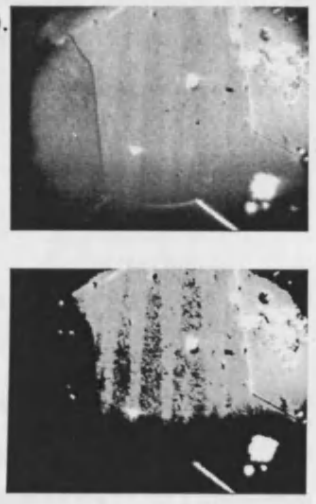

Fig. 6.11 Threshold operation (a) was used for segmentation light and dark regions. Example of application (b) on the domain image of non oriented steel (c).

6.6.2 Background subtraction technique

Raw images acquired from a microscope, usually have a background gradient caused by uneven illumination and surface imperfections. In addition, improper adjustment of the camera can offset pixel values beyond their true photometric values. Applying background subtraction to raw images can improve the magnetic contrast contained in these images. Background subtraction techniques usually require collection of additional image frames under conditions similar to those employed to capture the primary raw image.

Such a background image can be obtained when the sample is in the saturated state when a single dark domain appears on the surface. Alternatively the sample can be AC magnetised at a frequency higher (about 10 times) than the sampling frequency of the camera. In this case magnetic images are effectively averaged over several periods. The similar effect can be achieved by digital averaging of the images recorded over a number of periods.

Figure 6.12 demonstrates the dramatic improvement of a magneto-optic image achieved by the subtraction of the domain images in the demagnetised and saturated states. Subtraction was accomplished with offset bias (+100) to avoid clipping to "0" when the result of subtraction becomes negative. Subtraction was followed by contrast stretching.

For successful background subtraction it is necessary to have high optical, mechanical and thermal stability of the microscope system. Otherwise, when the sample moves during magnetisation, or the light source exhibits random flickering, the subtraction will leads to large errors. In such a case when it was not feasible to capture a background image, a surrogate background image was produced artificially for each of the frames in the sequence.

The following methods were utilised:

1. Surface fit:

The grey-scale image, as a 2-D array of integer data can be interpolated by a surface function such as $B(x,y) = C_0 + C_1 x + C_2 y + C_3 x^2 + C_4 y^2 + C_5 x y$

Such a parabolic surface can coarsely fit the microscope image usually darker on one side than on the other or lighter in the centre than at the edges of the image.

Using a few reference points in the original image a Least Square Fit (LSF) algorithm [29], [31] gives the best fit function by selecting appropriate $C_0,\ldots C_5$ coefficients. This artificial background then can be subtracted from the specimen image. The LSF

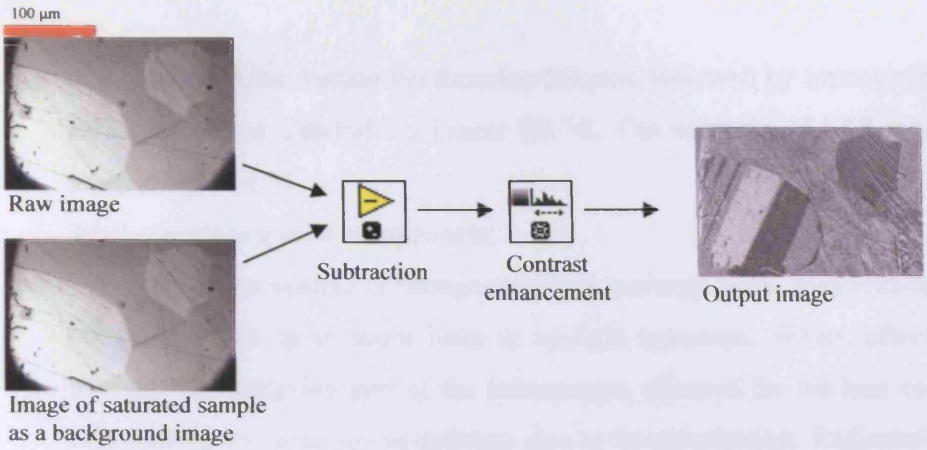

Fig. 6.12 Image of the saturated state is used as a background for image subtraction. Example of non oriented steel

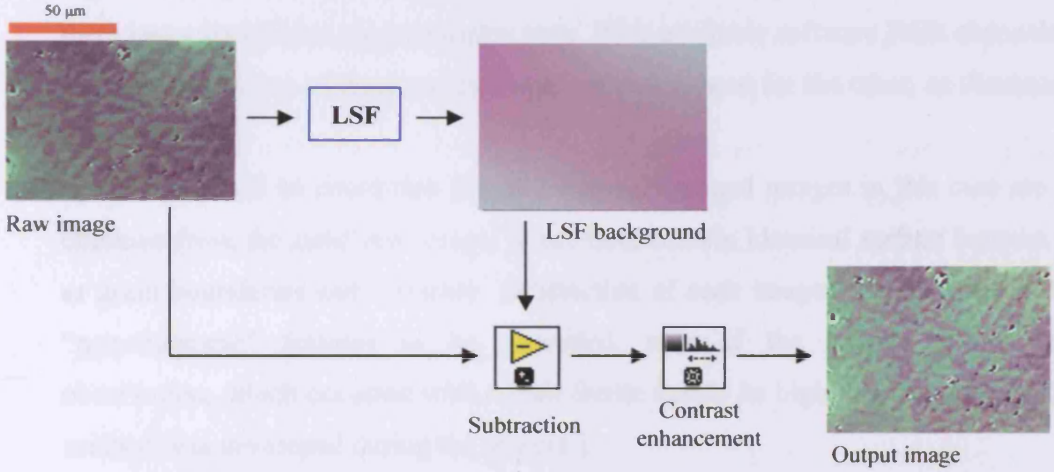

Fig. 6.13 Subtraction of artificial background produced with LSF surface function fit. Example of cobalt ferrite.

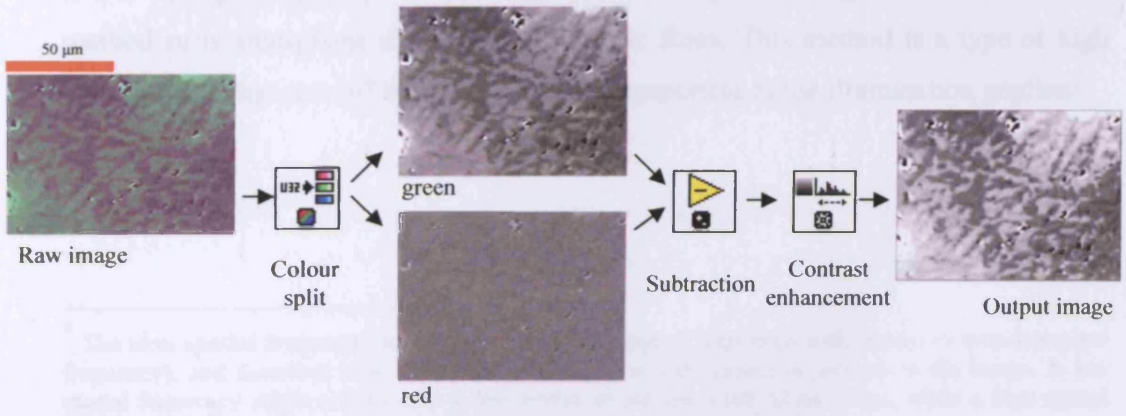

Fig. 6.14 Subtraction of artificial background produced with colour split. Example of cobalt ferrite.

is available in the Matlab via function Blkproc followed by imresize(bg,...'bicubic'). In LabView via General LS Linear Fit VI. The example of LSF application can be seen in figure 6.13

2. Split to colour components:

When a sample is illuminated by a mercury lamp, magneto-optic modulation occurs with all three major lines in its light spectrum. When reflected light passes through the analysing part of the microscope, adjusted for the best contrast, only one line undergoes intensity-modulation due to its polarisation. Reflected light attributed to other lines in the spectrum, also passes through the analyser, but the intensity modulation is much smaller. This is why raw images are greenish or bluish in colour.

Calibrating the Infinity X camera to balanced colour gain (white balance) in an acquired image all RGB components have the same average intensity, but only one of them has a significant magneto-optic term. With available software RGB channels can be split up and one of them can be used as a background for the other, as illustrated in figure 6.14.

It should be noted that the MO and background images in this case are both obtained from the same raw image, hence both contain identical surface features such as grain boundaries and scratches. Subtraction of such images enables most of these "non-magnetic" features to be cancelled, even if the sample moves during observation, which occurred with cobalt ferrite due to its high magnetostriction. [The method was developed during the project.]

3. A simple, but sometimes most effective, method of background subtraction is a deep blur of the raw image. Figure 8.10 presents images obtained by subtraction of blurred images of themselves. It works well when domains are small and the surface is free of high frequency* defects such as scratches, dust and grain boundaries. The method suits amorphous ribbons and magnetic films. This method is a type of high pass filtering that cuts off the low frequency component of the illumination gradient.

* The term **spatial frequency** is analogous to the concept of frequency with respect to time (temporal frequency), and describes how rapidly a signal changes with respect to position in the image. A low spatial frequency might exhibit only a few cycles across the width of an image, while a high spatial frequency often displays numerous cycles in the same linear dimensions.

Realisation of background subtraction:

Having the original raw image and the image of its background (real or artificial) the subtraction can be performed in one of the packages list below. However not all of them can do automatic batch processing of the image sequences.

- Adobe Photoshop: Image/Calculations/Subtraction interactive dialogue.
- Paint Shop Pro: Image/Arythmetic/ Subtraction.
- LabView: with IMAQ Image Subtraction virtual instrument.
- Matlab: with simple script such us OutIm = RawIm – Bkgr;
- Delphi: with point by point subtraction OutIm[i,j] := RawIm[i,j] – Bkgr[i,j] ;

It should be noted that simple subtraction adds the noise components of raw and background images. To prevent this occurring, the images must be filtered prior to subtraction.

In the cases when the magnetic contrast is very weak and noise level is higher than the magnetic contrast, the subtraction and noise removal should be combined in one procedure. Such procedures are not available in commercial software packages, so it was developed within this project. Delphi language was used to perform low-level programming. Image noise removal techniques are described in the next section.

6.6.3 Smoothing convolution filtering

Image processing with spatial convolution utilises multipixel operations, in which the integer value of each output pixel is altered by contributions from a number of adjoining input pixel values. These operations involve multiplication of a selected set of pixels from the original image with a corresponding array of weighting coefficients in the form of a **convolution kernel** or **convolution mask** [30].

The operation begins when the convolution kernel is overlaid on the original image in such a manner that the centre pixel of the mask is matched with the single pixel location to be convolved from the input image. This pixel is referred to as the **target pixel**.

Next, each pixel integer value in the original (often termed the **source**) image is multiplied by the corresponding value in the overlying mask (Figure 6.15). These products are summed and divided by the number of pixels and the greyscale value of the target pixel in the destination image is replaced by the sum of all the products, ending the operation. The convolution kernel is then translocated to the next pixel in

a).

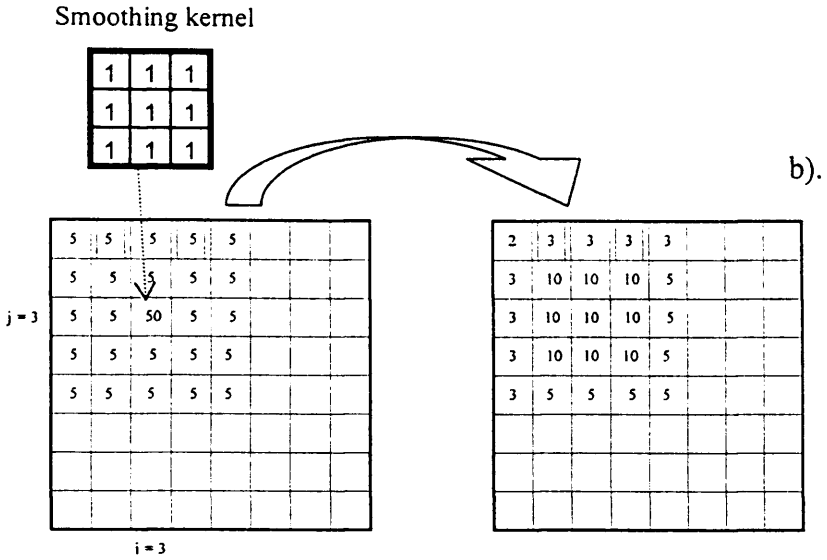

c).

```
O[i,j]:= (Im[i,j]+ Im[i -1,j]+ Im[i,j-1]+ Im[i+1,j]+ Im[i,j+1]+
          Im[i-1,j-1]+ Im[i-1,j+1]+ Im[i+1,j-1]+ Im[i+1,j+1])/9
```

Fig. 6.15 Spatial averaging filter with 3 x 3 convolution kernel (a), result of application to the pixel with large amplitude on uniform background at coordinates 3,3 (b). Equation that uses in Delphi program (c).

the source image, which becomes the target pixel in the destination image, until every pixel in the original image has been targeted by the kernel.

Specialized convolution kernels, often termed **smoothing filters**, are very useful in reducing random noise in digital images. A typical smoothing convolution filter is illustrated in Figure 6.15a, and is essentially a unity matrix.

When an image is convolved with unity kernel, the grey value of each pixel is replaced by the average intensity of its eight nearest neighbours and itself. Random noise in digital images is manifested by spurious pixels having unusually high or low intensity values. If the grey value of any pixel overlaid by the convolution kernel is dramatically different than that of its neighbours, the averaging effect of the filter will tend to reduce the effect of the noise by distributing it among all of the neighbouring pixels. Smoothing convolution kernels act as **low-pass** filters to suppress the contribution of high spatial frequencies in the image.

However, other "real" image features that are desirable, such as object boundaries and fine structural details, may also be suppressed by the spatial averaging. Consequently, application of a smoothing convolution kernel will often have the undesirable effect of blurring an input image. Furthermore, the larger the kernel (5 x 5, 7 x 7, and 9 x 9), the more severe this blurring effect will be. For most applications, the size and form of the smoothing kernel must be carefully chosen to optimize the trade-off between noise reduction and image degradation.

Alternative forms of noise reduction filters that preserve the image features are Gaussian filter [30], Median and Morphological enhancement [28], Winner filter and Wavelet transformation methods [28] and [32].

6.6.4 Median Convolution Filters

Median kernels are applied in a manner that is different from standard smoothing or sharpening kernels. Although the median filter employs a kernel that is translated from pixel to pixel, there is no convolution matrix applied in the typical fashion. At each successive pixel location, the pixels under scrutiny by the convolution kernel are ordered in rank according to intensity magnitude. A median value is then determined for all of the pixels covered by the kernel, and that value is assigned to the central pixel location in the output image.

Median filters are useful for removing random intensity spikes that often occur in digital images captured in the microscope. Pixels contributing to the spike are

replaced with the median value of the corresponding member pixels selected by the kernel overlay, which produces a more uniform appearance in the processed image. Background regions that contain infrequent intensity spikes are rendered in a uniform manner by median filter kernels. In addition, because the median kernel preserves edges, fine specimen detail, and boundaries, it is often employed for processing images having high contrast [30].

Smoothing filters are good tools for making simple cosmetic improvements to images that are eroded by additive noise. The additive noise is common in the conventional image sensors such as Infinity X camera, so that the images from this camera were successfully improved by the smoothing tools of available commercial software.

Although in the intensified camera a strong multiplicative noise [32] occurs. The filtration of multiplicative noise is much more complicated and requires non linear image processing techniques. Normally, the noise-removal technique requires prior knowledge of the noise statistics and a feasible noise model. This is why there is no universal commercial image processing tool available. Unlike the filters for additive noise, the filters for multiplicative noise must be custom developed. In [19], [33] and [34] some attempts of noise modelling in the image intensifiers are demonstrated.

Complexity of the filter development went beyond the aim of this project, so the noise minimisation was achieved with alternative methods. The first aim was to adjust conditions of the experiment to achieve minimal noise. The images were qualified as acceptable if after application of a median filter and subtraction the domain boundaries were resolvable. The limited degradation of the images features was corrected with morphological techniques. In some cases image integration was very useful for noise suppression.

6.6.5 Morphological image enhancement

Morphological operators [30] within a kernel, usually sized 3 x 3, sets the pixel value in the output image according to a set operator employed. The set operator changes a value of the pixel in the kernel centre according to the original values and geometry of the neighbouring pixels within a kernel.

The simplest examples can be demonstrated on the binary images for which the set operators can be represented via logical operators (intersection, union, inclusion, complement). An example is shown in figure 6.16. If at least one pixel is equal to "1" within 3 x 3 square kernel in the origin image, then the central pixel is set to"1" in the output image. Such an operation, called dilation, is one basic morphology operation, the other being erosion. As can be seen, the effect of dilation on a binary image is to gradually enlarge the boundaries of regions of foreground pixels (i.e. white pixels). Thus areas of foreground pixels grow in size while holes within those regions become smaller.

Erosion – is an opposite operation. It sets a pixel to "0" if at least one of its neighbouring pixels is equal "0" in the original image (within 3 x 3 square kernel). The effect of erosion on a binary image is shown in figure 6.17. It shrinks areas of foreground and eliminates single-standing white pixels, effectively 'tidying up' the resultant image.

Dilation and erosion are two basic operators from which many other morphologic operators can be derived. For example, the closing operator shown in figure 6.18 is in fact dilation followed by erosion. It is able to close gaps in the broken boundary.

Morphological operators can also be applied to grey-level images, e.g. to reduce noise or to brighten the image. IMAQ Morphology VI was used in this work to enhance the grey-level images. The theory of morphological processing of the grey-level images can be found in [28].

6.6.6 Image integration and averaging

Because a digital image is a matrix of integers, operations such as the **summation** or **integration** of images can readily be conducted in the PC. If the original images were digitized with 8-bit resolution, the storage region, or **digital frame memory**, which holds the accumulated images, must have sufficient capacity to accommodate a sum that exceeds 8 bits. If it is assumed that a few pixels in an 8-bit

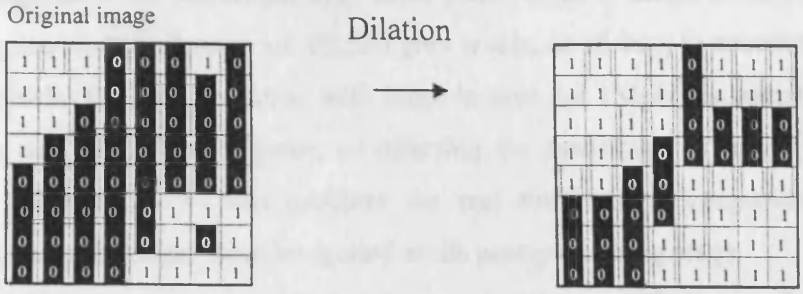

Fig. 6.16 Dilation of the binary image enlarges the boundaries of regions of foreground pixels (white or ones) and close holes.

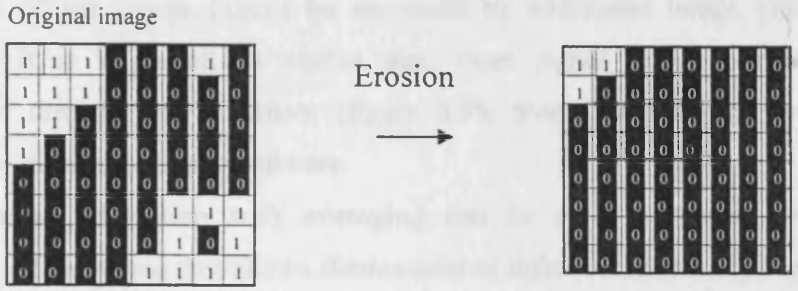

Fig. 6.17 Erosion of the binary image

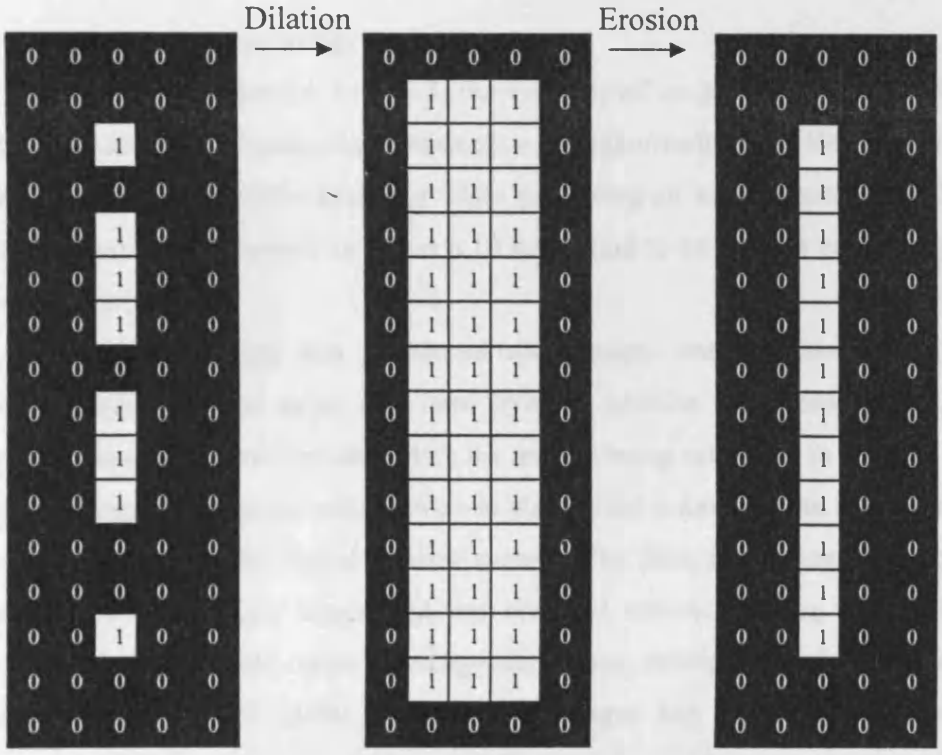

Fig. 6.18 Closing operator applied to the binary image of a broken boundary. Closing is used to close gaps produced by the errors on the early stages of image processing such as subtraction, thresholding, noise clipping.

digital image have the maximum grey-level value of 255, then summation of 256 frames require storage capacity of 65,536 grey levels, or 16 bits, to accommodate the brightest pixels. Such an operation with large images (of 1Mpix) is computationally demanding and halts the computer, so effecting the synchrony of image download from the camera. Due to this problem the real time image integration was not developed, instead images were integrated at the post-processing stage.

Image integration using digital image processing techniques often enables visualisation of a faint object that is barely detectable above the camera noise. Integration may be of the particular value in low-light-level imaging when the brightness of the image cannot be increased by additional image intensification. However, it is important to realize that, from signal to noise considerations, integration directly on the sensor (figure 6.9b, mode 2) is always preferable to integration in the processing software.

Trivial integration with averaging can be easily upgraded to the more sophisticated technique that allows fluctuations of light source and severe noise levels to be overcome. An example of such a multiple-add-subtraction technique is presented in [27].

6.6.7 General strategy for image processing.

As shown in sections 6.6.2 – 6.6.5, the visibility of magnetic domains can be improved dramatically by background subtraction and other techniques. However it is important to preserve scientific accuracy while improving an image's visibility. The sequence of operations proposed in figure 6.19 was found to be best for processing a series of domain images.

All image processing was performed after images were acquired from the microscope, catalogued and saved to a hard drive. In addition to the raw images, a **background image** also was recorded with the sample being saturated. In addition to a background image, it was sometimes wise to also record a **dark frame** to establish the dark noise level of the digital camera system. The dark frame used the same exposure as the original raw image, but was obtained without opening the camera shutter. As with the flat-field frame or background image, multiple dark frames could be collected and averaged. After the necessary images had been gathered (raw, background, and dark), image processing operations were carried out.

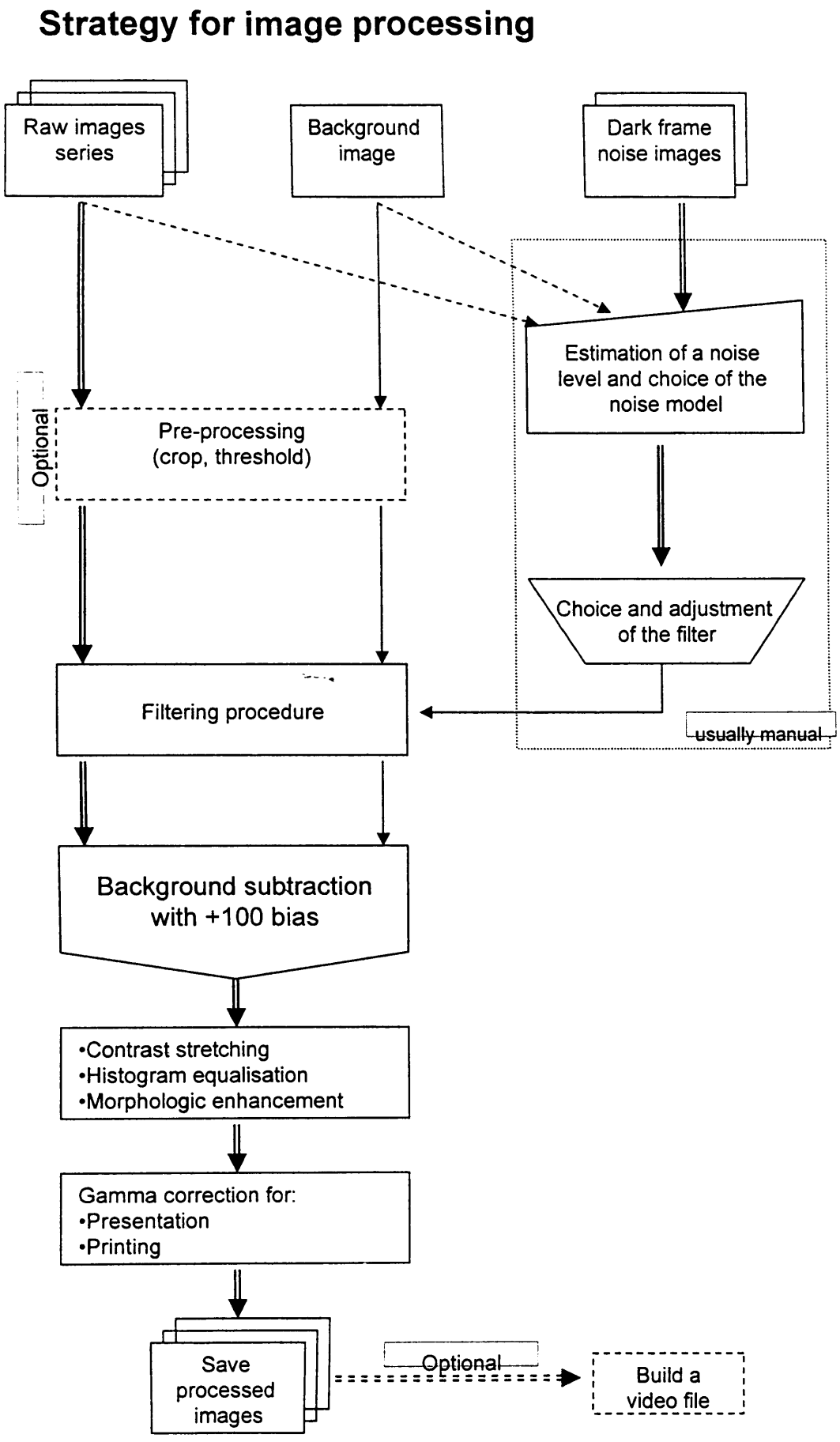

Fig. 6.19 General strategy for image processing

As a first step, it was often necessary to trim the edges of the raw image in order to save disk space and make the following operations faster. This optional step is called 'pre-processing'.

If the image was highly degraded by the noise, as images from the intensified camera often are, it was necessary to reduce the noise with application of one of the filtering techniques prior to subtraction.

The next step in image processing was to remove brightness fluctuations (due to uneven background illumination). For the majority of digital images, simple background subtraction was sufficient and produced corrected images that had even brightness values across the image. After background subtraction had been applied to the image, the next step is to restore brightness and contrast levels. Histogram stretching and sliding operations have performed satisfactory adjustments to the image. Morphologic operations are sometimes useful to rehabilitate the effect of errors (rounding during subtraction of the noisy images) and produce an overall clear up of the image.

Finally, the "gamma correction operation" was used to enable exponential scaling for the purpose of simultaneously displaying both bright and dark features of the image in the target application. This operation was specified for a computer monitor or for a printer.

Implementation:

Because of the large number of images obtained in the experiments, it was necessary to develop the software for automatic processing of numbered series of image files. It was successfully completed first in Delphi and then in LabView. LabView Block diagrams of developed programs are presented in Appendix 4.1 and fragments of Delphi code in Appendix 4.3. All these programs were able to open the first marked file, perform a pre-defined set of operations and then save the result in the new file. Three last characters of the file name must form a number from 000 to 999. In this case the program is able to process 1000 images at once.

The noise filtering method was normally selected "manually" by examining the noise statistics. The parameters of the filters were selected by trial-and-error using a Photoshop editing program using one or more images from the sequence. As soon as the best filtering method was found, it was implemented in the LabView program enabling its automatic application on the large sequence of images.

A filtering procedure prior to subtraction, reduces noise, but at the same time reduces the contrast of the image. When the MO contrast is already small, the filtering can result in loss of information. To prevent this happening the subtraction was combined with smoothing filtering in one procedure using Delphi language.
The key fragment of the code script in this procedure is shown in Appendix 4.3 **(Procedure Sub_Aver3).**

The same could be done in LabView but its realisation could be too complex. After the sequence of images has been processed, the domain boundaries could normally be clearly seen.

6.7 Domain wall recognition and automatic measurement of its motion.

In the past the manual measurements of the domain wall positions was made using a ruler [35]. Today there is an opportunity to employ the rapidly growing science of Machine Vision [21] for the automatic measurement and shape recognition. Probably a first attempt of machine vision application for domain image analysing is presented in this work. The objective of automatic measurement was time saving when the large sequence of images is measured.

If the observed domain wall is straight and remains so during motion, it is possible to find its precise position with respect to some reference point. If the position and the moment of time when each image was taken is known, then the instantaneous speed of a wall can be measured as a difference of wall positions in "n" and "n - 1" devided by time between consecutive frames Δt.

The block diagram of the program developed in LabView 7 is presented in Appendix 4.4. The key element of the program is an "IMAQ edge find" module. It locates the intersection points between a set of parallel search lines and the edge of an object (see figure 6.20a). The intersection points are determined by their contrast, width, and steepness. A best-fit line is calculated through the points found. The program returns the coordinates of the edge found as well as its straightness. The coordinates of the best-fit line are stored and the program opens the next image in the sequence. After a cycle ends, all coordinates and calculated speed of domain walls are stored in ASCII.txt file. This file can be imported to any other software for analysing and presentation. For example it can be opened in Excel, see graphs in figure 6.20b.

Conversion of position in pixels to millimetres is always uniquely defined by the width of the field of view W divided over width of the image in pixels N and

a).

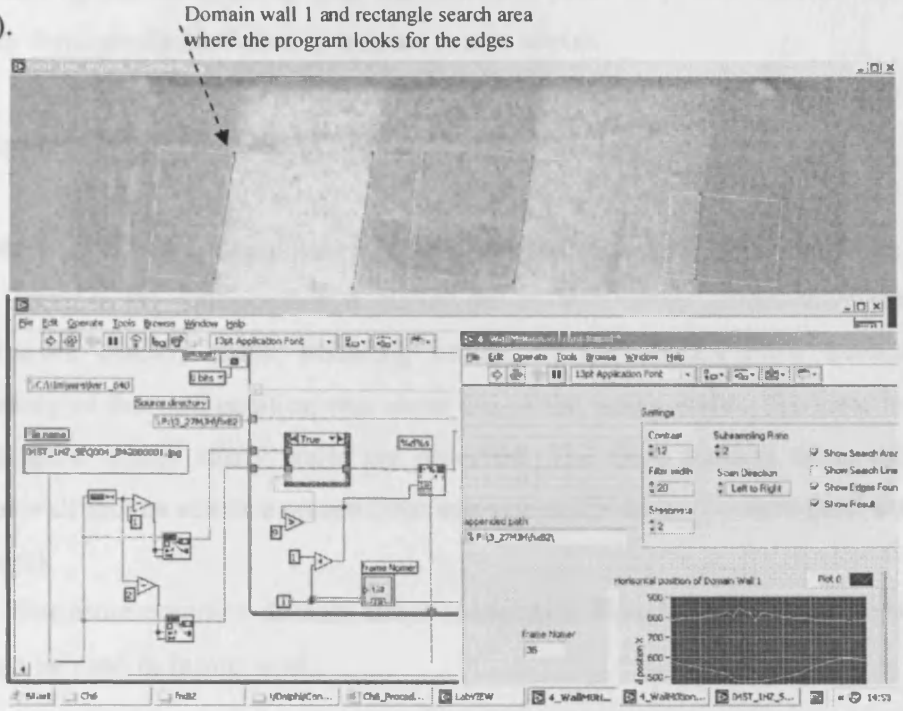

b).

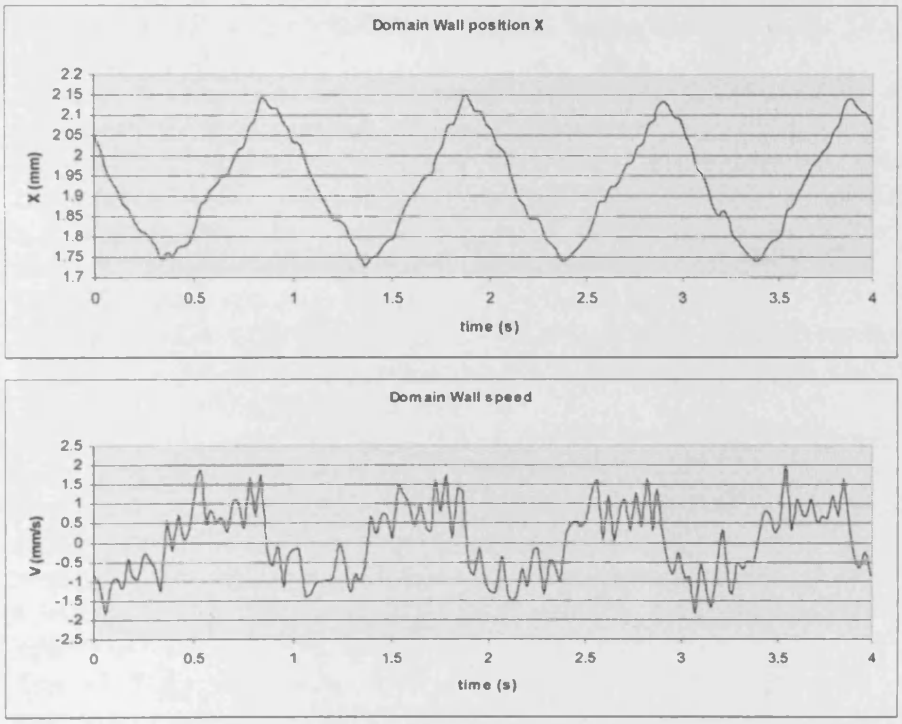

Fig.6.20 Example of application of edge recognition software to the images of bar-like domains of grain oriented steel (a), obtained plot of the first domain wall position and speed over four magnetising cycles (b).

multiplied by the distance X_n from the reference point in pixels. Conversion of the velocity from pixels per frame to mm/sec is also trivial:

Wall speed (mm/sec) $= ((X_n - X_{n-1}) * W/N) / \Delta t$

In figure 6.20 $W = 8.6$ mm, pixels horizontal $N = 1024$, and $\Delta t = 0.028$ s (for 36.5fps)

Error in the wall position is mainly due to defocusing. Additionally, when the wall moves quickly some smearing occurs. In the demonstrated example the uncertainty of the wall position was about 1% of the image width. The error in speed is high here, where many walls are observed. The error reduces when only one domain wall moves across a screen from one side to the other (because pixel sampling increases).

For more complex domain shape recognition Hough Transformation methods [28] can be used in future work.

6.7 References of chapter 6

1. Bjerregaard L., Metalog guide, Struers, Denmark (2000).
2. Lyman T., Metals Handbook vol.8, Metals Park, Ohio (1973).
3. Folks L, Street R, Warburton G. and Woodward R.C., A sphere forming and polishing machine, Meas. Sci. Technol. 5 (1994).
4. Samuels L.E., Metallographic polishing by mechanical methods, fourth edition, (1986).
5. Derebasi N., Effect of tension and surface properties on magnetic domains and power loss in amorphous ribbons, Thesis (Ph.D.) – University of Wales, (1994).
6. Fortunati S., Grain oriented electrical steels: Status and trends, Workshop Metallurgy and Magnetism Proceedings, 7, (2004).
7. Weidenfeller B., Rieheman W., Domain refinement and domain wall activation of surface treated Fe-Si sheets, J. Magn. Magn. Mat., 160, p136, (1996).
8. Europe Patents: EP 390160, EP 398114, EP 394694
9. Rudzki G.J., Surface finishing systems : metal and non-metal finishing handbook-guide, (1982).
10. Metallography: Principles and practice/ George F. Vander Voort, (1999).
11. Flewitt P.E.J., Wild R.K., Microstructural characterisation of metals and alloys. The Institute of Metals, London, (1986).
12. Durrani S.M.A, Al-Shukri A.M., Iob A., Khawaja E.E., Optical contrast of zinc sulfide films determined from transmittance measurements. Thin Solid Films 379, p199, (2000).
13. Khawaja E., Tomlin S.G., The optical constants of thin evaporated films of cadmium and zinc sulphides, J. Phys. D: Appl. Phys., 8, (1975).
14. Beckley P., Porter C.H., A three wavelength photometer for controlled deposition of Kerr magneto-optic enhancement films, J. Phys. E: Sci. Instrum., 2, 3, p449, (1969).
15. Burke M., Image acquisition, London: Chapman & Hall, (1996).
16. Bass M., Handbook of optics, Vol. 3, McGraw-Hill (2001)
17. Coulomb J., Swan M. and Wang C., Variable resolution CMOS current mode active pixel sensor, IEEE International Symposium on Circuits and Systems 2000, p II-2932000, Geneva, (2000).
18. Infinity X camera datasheet and DeltaVu techniques, available online www.deltapix.com
19. Morgan S., E., Ulich B.,L., Elkins W.,P., DeWeert, M.,J., Intensified CCD (ICCD) dynamic range and noise performance, SPIE, 3173, Ultrahigh and high-speed photography and image-based motion measurement, (1997).
20. HI-CAM, gated intensified high speed camera datasheet, available online http://www.lambert-instruments.nl/fs_pr_highspeed.cfm
21. Spring K.R., Davidson M.W., Electronic imaging detectors, optical microscopy primer, available online at http://micro.magnet.fsu.edu/primer
22. Jagutzki O., Barnstedt J., Spillmann U., Schmidt-Böcking H., Fast-position and time-sensitive readout of image intensifiers for single-photon detection, Proc. SPIE, (1999), available online www.hsb.uni-frankfurt.de

CHAPTER 7 OBSERVATION OF BAR DOMAINS IN COMMERCIAL GRAIN-ORIENTED ELECTRICAL STEEL

7.1 Introduction

Dynamic domain wall motion was observed on the surface of commercial grain-oriented 3 % Si Fe sheet. This chapter covers sample selection and preparation prior to domain observation followed by related power loss measurement and domain wall observation. The superior spatial and time resolution of the system was utilized for real-time observation of the domain dynamics during magnetisation at 0.5, 1, 5, 25, 50 and 75 Hz. Analysis is focused on the non-repeatable wall motion and refinement of the domain structure.

7.2 Sample selection and preparation

High permeability samples of 27MJH commercial grade and conventional samples of 27M4 and 35M4 grades were selected because of their anticipated regular bar like domain structure. An Epstein strip of each material was selected and cut into 3 cm squares, designated 1 to 7, as shown in figure 7.1a for domain observation. The surface coating of each sample was removed by hydrochloric acid as described in section 6.3. Samples were then polished, annealed and coated with ZnS.

A precision, 0.5 mm diameter drill bit was used with a high speed drilling machine to make the holes for localised search coils in sample No. 3 of 27MJH. While drilling the holes the sample was held horizontally and supported from below by a glass slide. This procedure was not expected to induce significant strain in the material but as a precautionary measure each sample was annealed at 800 ^{o}C after drilling.

A 7 turn search coil (B1 in figure 7.2) was wound around the sample perpendicular to the rolling direction and 5 mm away from the sample edge. It was used to measure the total flux density and to check uniformity of induction along the sample in the direction of magnetisation. A five turn search coil (B2 in figure 7.2) was wound through the two holes made at a grain boundary so that it enclosed the grain. The search coil wire was threaded through the holes and the leads twisted tightly together. A 4 mm thick sponge was used to keep the leads away from the sample. The holes were sealed with wax thus preventing movement of the search coil. The sample width and distance between the holes through which coil B2 was wound were measured with a travelling microscope and found to be 30.04 mm and 6.20 mm respectively.

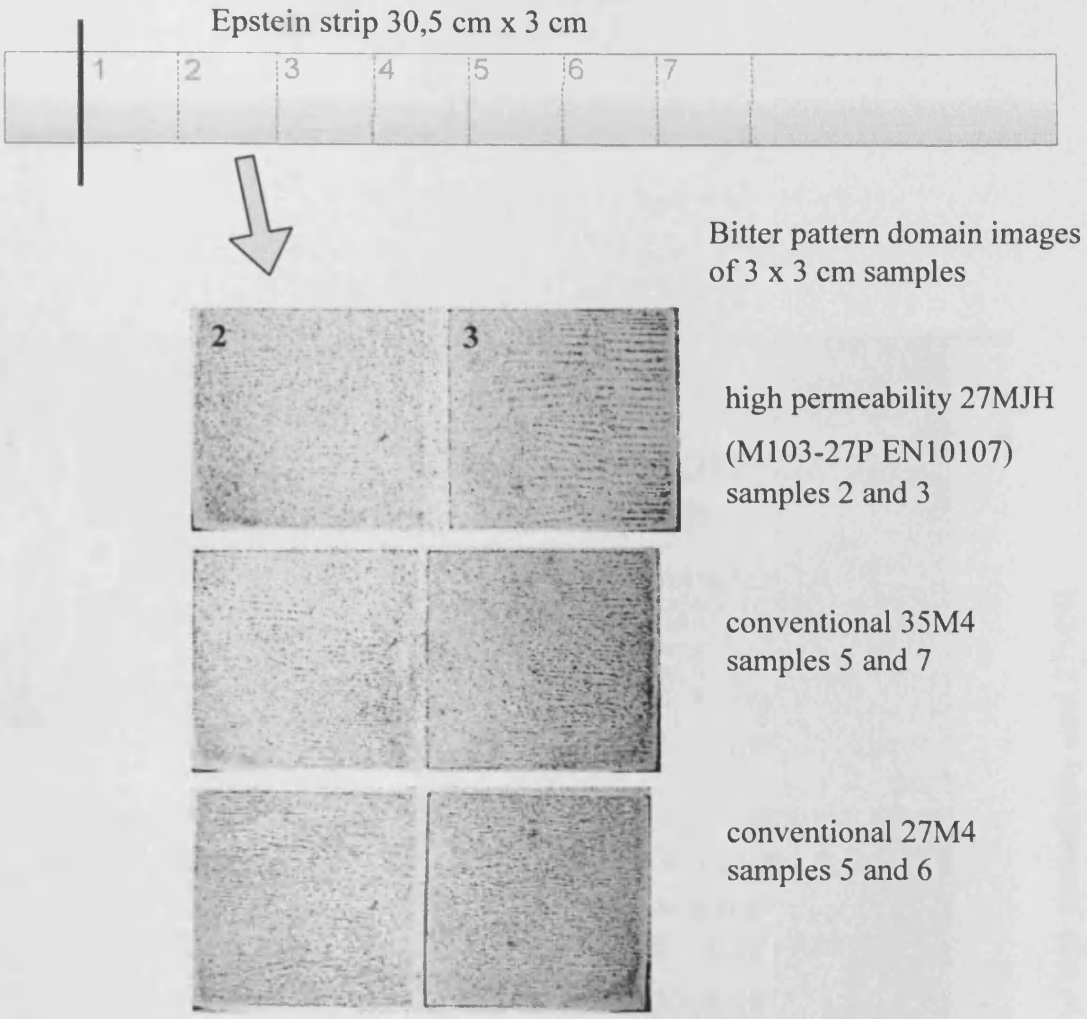

Fig. 7.1 Samples selection and preparation for domain observation.
Photographs of samples and Bitter images of static domain patterns in samples.

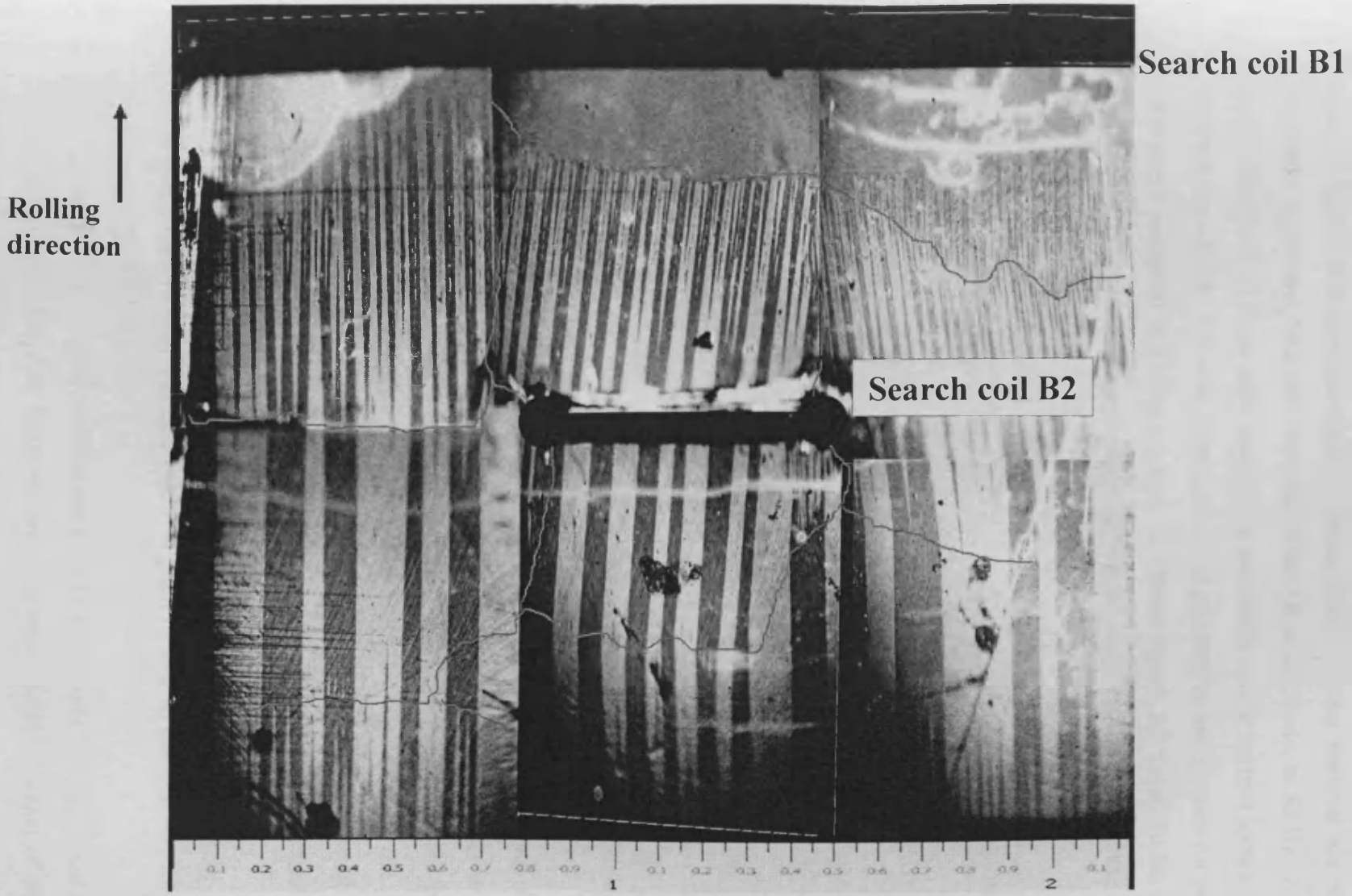

Fig. 7.2 Area of view on sample No 3 of high permeability steel 27MJH with a search coil around studied grain in the centre of the sample. Present domain pattern obtained after cyclic demagnetisation at 500 Hz

7.3 Power loss measurement

The results of the power loss measurement on bundles of 24 strips of each material tested in a standard Epstein frame before coating removal are shown in Appendix 2.2. Power loss was measured from 1.0 to 1.7 Tesla, at 50 Hz. The single strip Soken tester [1] was used to measure the power loss at various locations in the selected strips before and after coating removal and cutting into squares for polishing. Results are presented in Tables 7.1 and 7.2. Power loss at 1.0 Tesla, 50 Hz was also measured after cyclic demagnetisation at 500 Hz and was found to be the same as prior to demagnetisation.

Sample		Actual Thickness(mm)	Power loss (W/kg) ±0.05W/kg		
			1T	1.5 T	1.7 T
27MJH	2	0.27	0.25	0.60	0.85
	3		0.30	0.65	0.85
27M4	5	0.27	0.30	0.70	0.95
	6		0.30	0.75	0.95
35M4	5	0.35	0.35	0.80	1.00
	7		0.35	0.80	1.10
30MOH	7	0.3	0.30	0.70	0.90

Table 7.1 Power loss of coated samples measured at 1.0, 1.5 and 1.7 Tesla using the Soken tester.

Sample		Actual Thickness(mm)	Power loss (W/kg)±0.05W/kg		
			1T	1.5 T	1.7 T
27MJH	2	0.25	0.30	0.65	0.90
	3		0.30	0.70	0.90
27M4	5	0.25	0.35	0.75	0.95
	6		0.40	0.75	0.95
35M4	5	0.34	0.40	0.80	1.05
	7		0.40	0.85	1.15
30MOH	7	0.28			

Table 7.2 Power loss of uncoated samples at 1.0, 1.5 and 1.7 Tesla.

Results from only one or two samples are presented because the others were not suitable for domain observation since they were either etched too deeply or became bent due to unavoidable non-uniform coating removal. In general, losses increased due to coating removal however some caution should be applied since the increases were similar in magnitude to the specified accuracy of the Soken tester (i.e.± 0.05 W/kg). It should be noted that the average loss measured at 1.5 T in the Epstein frame was 0.69 W/kg, which relates to losses in the strips, see Appendix 2.2.

After surface preparation regular bar-like domains were found in the high permeability steel (27MJH) sample No. 3. A grain located in the centre of this sample was selected for study.

Also, two samples of conventional GO steel were selected. Static and dynamic domain images together with Electron Back Scattered (EBSD) images of crystalline orientations are presented in section 8.3.

7.4 Flux and field measurement

The flux was measured with a Lake Shore 480 flux meter and the applied field was measured with an H-coil, placed on the bottom surface of the sample. However, the sensitivity of the H-coil (148 turns, 20 mm x 0.2 mm, 14 mm long) was not high enough to measure the field at low amplitude. To overcome this problem, the proportionality between field and current in the windings was measured at high amplitude for sinusoidal and triangular waveforms at magnetising frequencies 0.5, 1.0, 5.0, 25, 50 and 75 Hz. These coefficients of proportionality were used to find the field strength from the applied current, assuming a linear dependence of H on I.

Simultaneous measurement from search coils B1 and B2 revealed the flux distribution was not uniform across the width of the sample. This is due to grain-to-grain variation of the flux distribution, which additionally was frequency and amplitude dependent. It therefore appears that the flux transfer characteristics of a particular grain are determined both by its own orientation and the orientation of its neighbouring grains. Similar behaviour of flux was reported by previous researchers [2], [3]. Hence a well-oriented grain amongst badly oriented grains will carry a much larger flux than its neighbours. This will also lead to an increase in the power loss.

7.5 Domain observation results

The experimental system described in Chapter 6 was used to record a series of images. The wall displacement and speed of individual walls within a grain were measured using software described in section 6.7. The flux density within matched grain was measured by the Lakeshore 480 flux meter. The integrated signal from the flux meter together with a magnetising field waveform were displayed and recorded using an Agilent 54624 oscilloscope. It was found that the domain wall motion was stable and repetitive only for peak flux densities below 0.4 T. Above this flux density the wall motion ceased to be stable. Some walls began to move in a *jerky* fashion and would merge at higher flux densities. Increasing the flux density further above 0.8 T resulted in unstable domain patterns. New domains were often nucleated at the grain boundary. For a given sheet thickness d, the primary geometric parameter is the domain density ratio $r = d / p$, where p = a + b (see figure 2.9, Chapter 2) and is the mean spacing of the major domains.

Domain wall positions and speed measured over several cycles of magnetisation were used for analysis of:

1. The nucleation of new domains.
2. The repetition of domain wall motion from cycle to cycle, (at a magnetisation rate below the limit of 0.8 T at 25 Hz and 1 T at 0.5 Hz).

7.5.1 Nucleation of new domains with increasing magnetisation rate

It is commonly observed that the domain density ratio r obtained in the cyclically demagnetised state generally increases with the frequency at which the cyclic demagnetisation was carried out. As noted in Chapter 2, the number of domain walls tends to increase with increasing frequency and is roughly proportionally to $\sqrt{f}$, (or $r(f) \sim \sqrt{f_{demagn}}$). Also, the number of walls increases roughly in proportion to the amplitude of the applied field, $r(H) \sim H_{peak}$. An example of such "domain refinement" or "domain wall multiplication" is presented in figure 7.3. These static images where taken after the alternating 50 Hz (b) and 500 Hz (c) field of peak value 200 A/m was abruptly switched off*. The domain pattern of the sample demagnetised at 0.5 Hz (figure 7.3a) is shown for comparison.

The objective of the observation was to illustrate the nucleation process and reversal process of domains collapse. Three experiments were carried out as described in the next sections. Prior to each experiment the sample was demagnetised at 0.5 Hz from saturation along the rolling direction.

7.5.2 Refinement with increasing frequency

With the induction amplitude constant at 0.7 T (or 0.9 T) the frequency was increased from 0.5 to 100 Hz. The camera was synchronised with the B2 signal, enabling capture of an image at any time on the magnetising cycle. A portion of the grain with only two original domain walls was observed.

Beginning from 0.5 Hz and up to 24 Hz, two oscillating domain walls appeared in the area of view. At 24 Hz a few additional narrow spike domains were nucleating for a short time as shown in figure 7.4. This brief appearance of new domains occurs at the middle of the slope of the magnetisation curve, while at the

* The images present the maximum number of walls obtained after several on/off repetitions. The magnetisation is not necessarily the same for these images.

Static images after magnetisation at

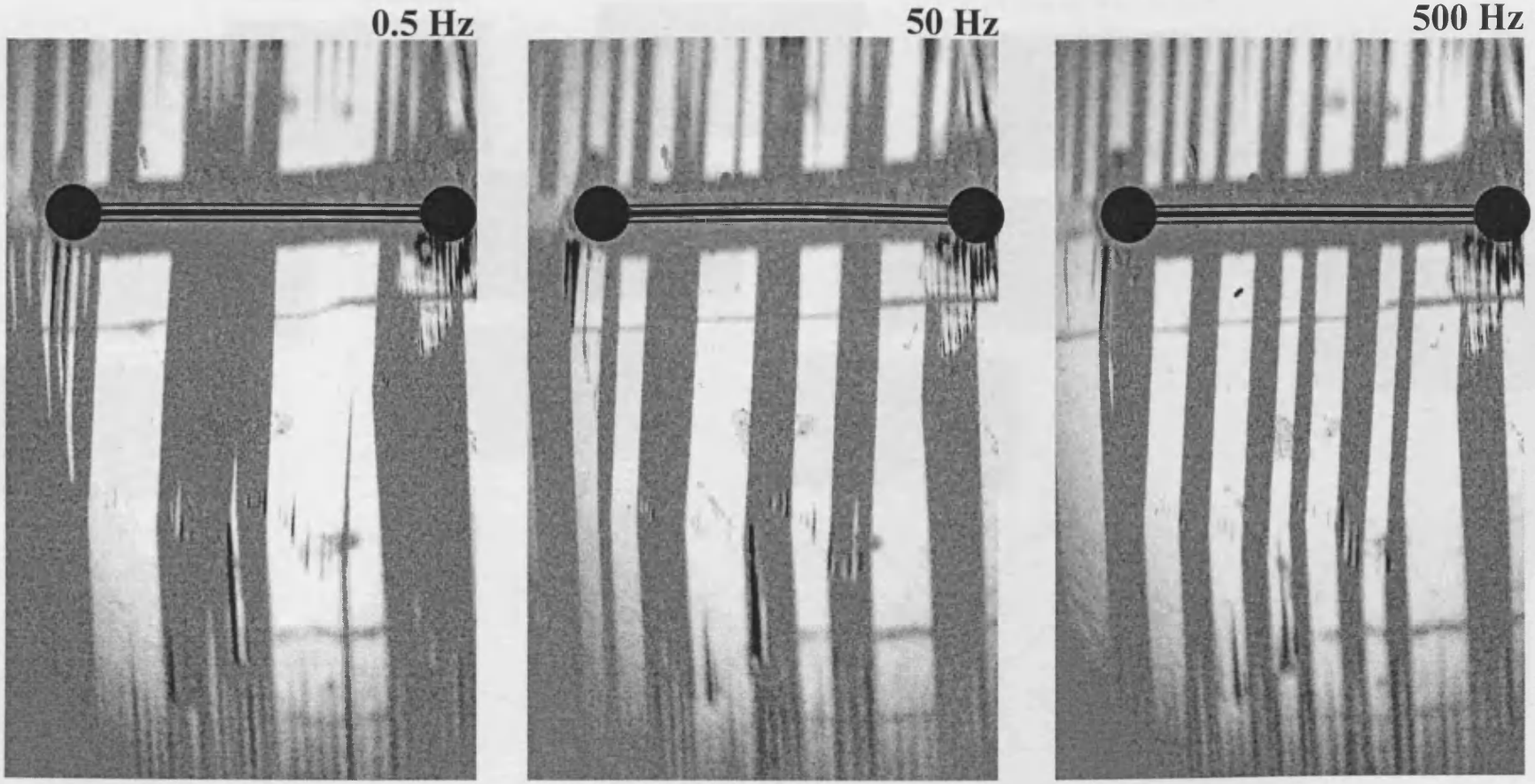

a). 4 Walls after cyclical demagnetisation at 0.5 Hz

b). 5 to 8 walls at 50 Hz

c). 9 to 13 walls at 500 Hz

Fig. 7.3 Nucleation of the new domain walls with increasing frequency.
Background subtraction and contrast correction were used for image enhancement.

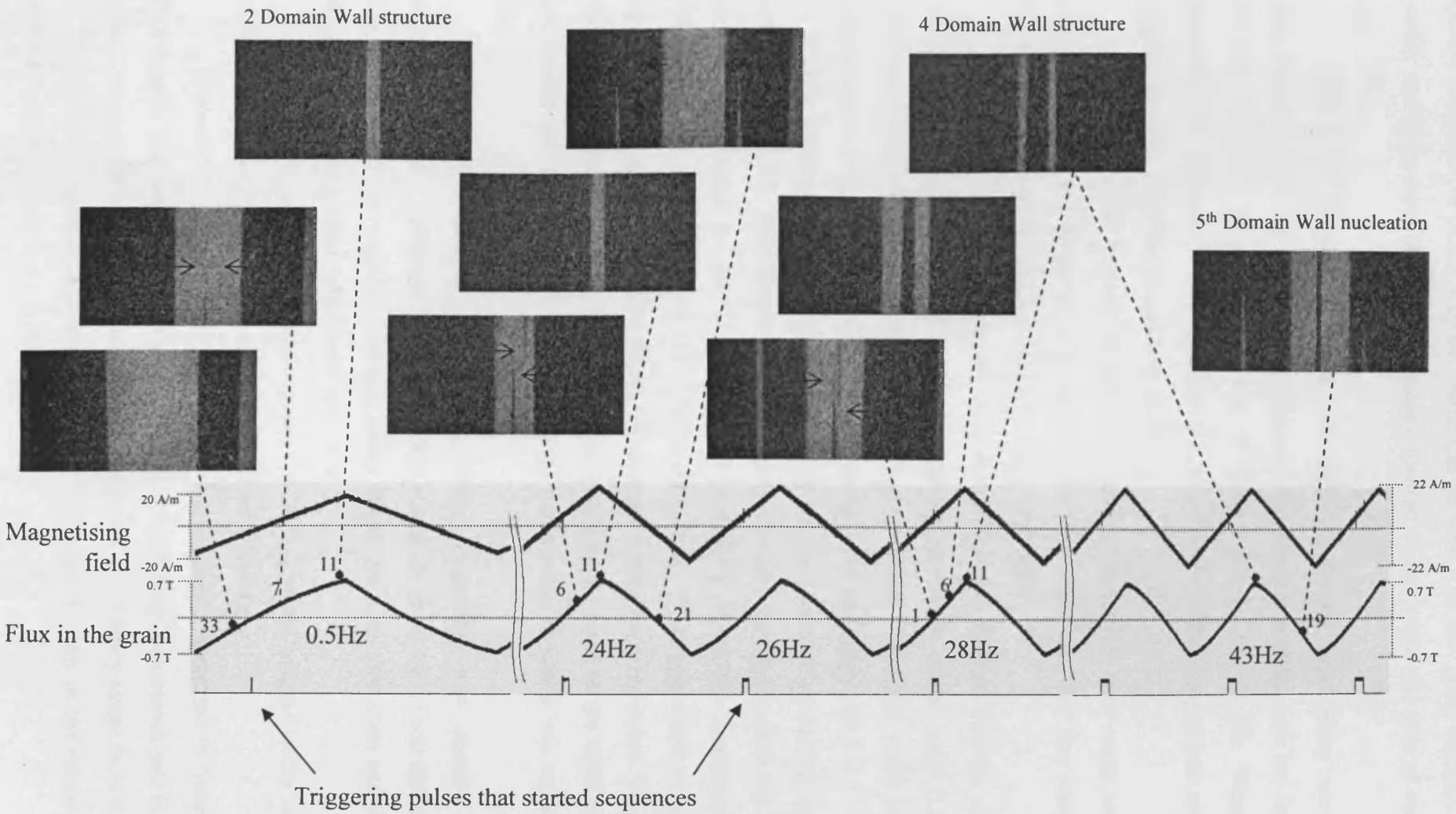

Fig. 7.4 Nucleation of new domain walls with increasing frequency. The number of each image is count from the first one at the triggering pulse. The time period between images in the sequences was 1/36th of the magnetisation period, t_{exp} was 1ms.

positive and negative peaks only two walls can be seen. The new spike domains were usually springing from the grain boundary situated 2 mm below the area of view in figure 7.4.

With further increase of the magnetising frequency the "brief spikes" met each other forming a new bar-like domain. Although the formation of the new bar domain was not consistent from cycle-to-cycle at frequencies below 28 Hz. When the frequency was reduced to less than 24 Hz, the new domains disappeared and the original two wall structure reappeared.

With a gradual increase of frequency above 28 Hz the new walls became persistent and did not disappear after the frequency was reduced, they also remained after the amplitude of the applied field was reduced to zero.

The new four-wall structure was observed with further increase of the frequency as shown in figure 7.5. The oscillating amplitude of the walls (i.e. the maximum displacement) became correspondingly smaller. This may result in loss reduction according to the theory outlined in section 2.6.4 and Appendix 5.

The frequency was increased slowly up to the point of nucleating another domain wall (DW). This happened in the range from 40 to 43 Hz, with the same "instability" as seen for the 2DW → 4DW transition. After the frequency was increased above 44 Hz, a new 5 DW system was created which persisted, even after the frequency was reduced below 40 Hz but this new system was not stable. When the frequency was reduced below 30 Hz the domain pattern reverted to the 4DW system (see dashed line in figure 7.5). It also was not stable when the field was reduced to zero.

With further increase of the magnetising frequency, new domain walls nucleated gradually. Although some of the new structures were stable and did remain after reduction of the magnetization rate, many others were not persistent and tended to return to the last known "persistent" structure.

When this experiment was repeated at 0.9 T peak magnetisation similar nucleation of new domains happened, but at a lower frequency.

Extension of the above effect over the whole grain is presented in figure 7.6. Wall density was measured at the moments when the flux through search coil B2 was zero. Three values of peak induction were used over a frequency range from 0.5 Hz to 75 Hz. Domain dynamics within the grain can also be seen in the movie files 1Hz054T.avi ... 75Hz07T.avi on the CD.

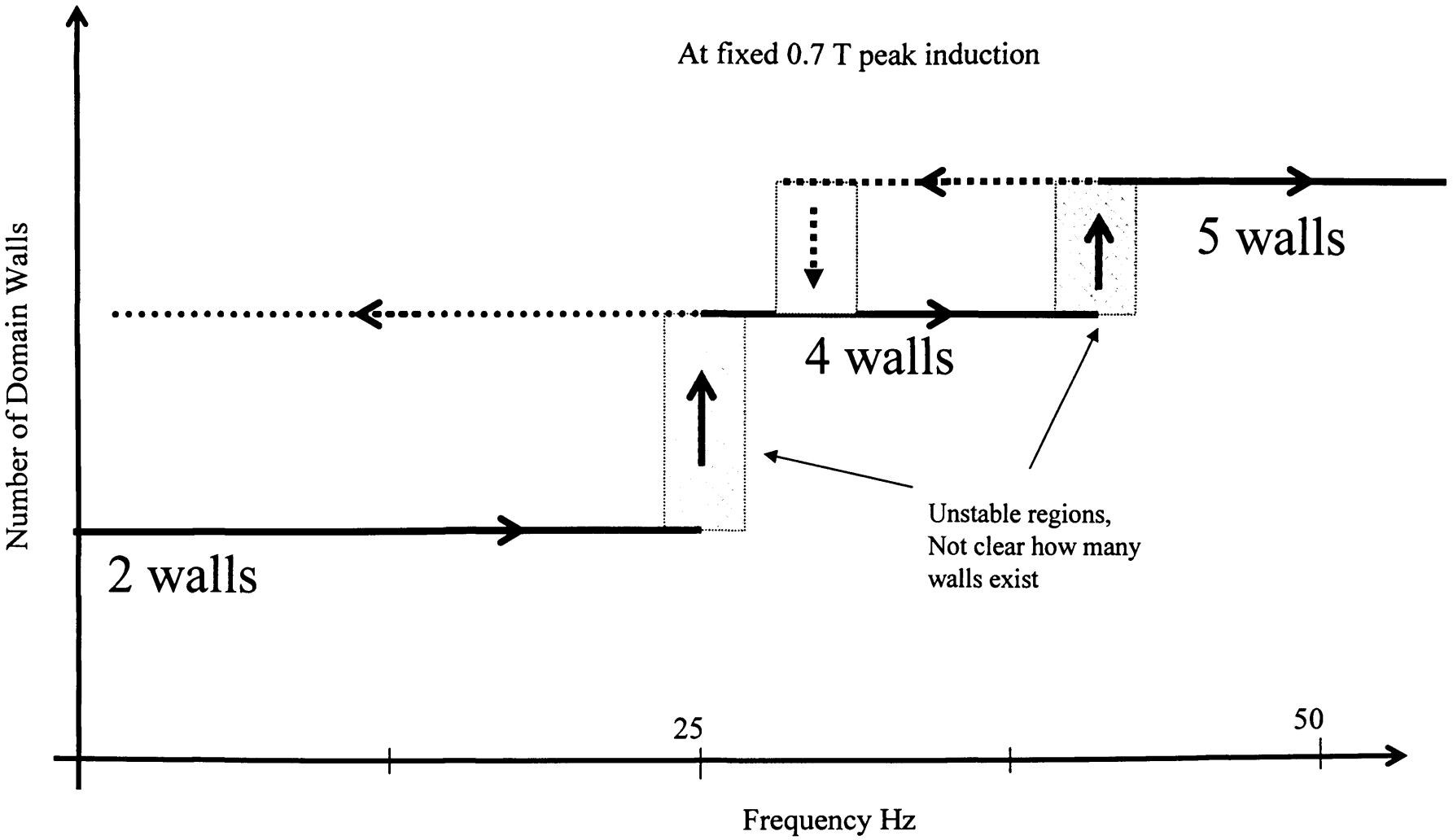

Fig 7.5 Change of number of the domain walls in the area of view with increasing frequency.

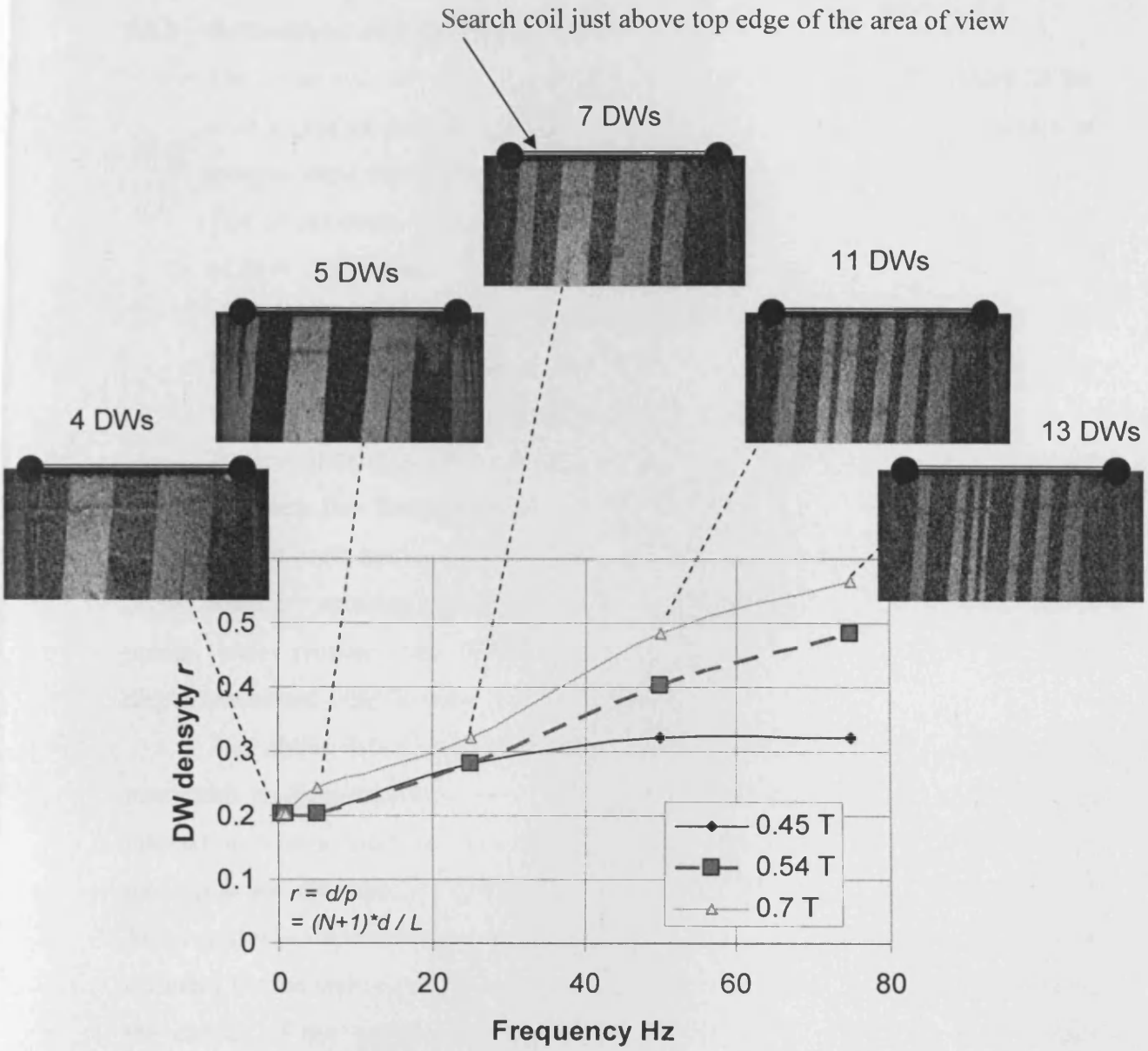

Fig 7.6 Domain wall density *r* in the grain vs. frequency for three peak induction values with corresponding images for 0.7 Tesla acquired at the moment when $B_2 = 0$ T.

7.5.3 Refinement with increasing amplitude

The same area of view was observed at fixed frequencies of 0.5 and 25 Hz with a gradual increase of alternating induction from 0 to 1.5 T. A series of images were recorded, with synchronisation with the B2 search coil signal. The observations were made at times separated from each other by increments of $\Delta t = T/36$, where T is the period of the magnetisation cycle in seconds. Four cycles of magnetisation with 36 frames per cycle were recorded at each frequency. The positions of bar-like domain walls and their speeds were measured using the software described in section 6.7.

Typical plots of surface wall displacement versus time are shown in figure 7.7 for various peak flux densities under a triangular applied field. At 0.5 Hz, beginning from low amplitude and up to 0.4 T, the motion of two domain walls was smooth and linear, roughly repeating the wave shape of the applied field. This may indicate a planar wall profile. The linear proportionality between applied field, wall displacement and bulk flux density exists for this case

Just above 0.4 T, the displacement plot of DW2 ceases to be linear at its maximum, as illustrated in figure 7.7 (second column). The jump may occur due to an interaction with a local pinning site. It also can be seen that the motion of a wall moving in one direction is not the mirror image of the motion in the reverse direction. This result was expected since the effect of pinning point upon the wall is likely to be different for the wall moving in opposite directions. Beginning from these conditions, the motion of the walls is not linearly proportional to applied field. With further increase of applied field amplitude, pinning occurs more often on both walls, see figure 7.7 (third column). Finally walls merge at about 1.0 T peak.

When the same experiment was carried out at 25 Hz the wall motion was similar but the amplitude of oscillation was slightly lower for the same flux condition. Also sharp edges of a plot became somewhat rounded. This can be explained by the effects of eddy current damping fields. In addition the previous unpinning jumps became less distinctive, because the walls are already moving at high velocity which produces high eddy currents and any additional increase of velocity becomes limited by eddy current force exerted opposite to the direction of wall propagation (see theory in 2.6.3).

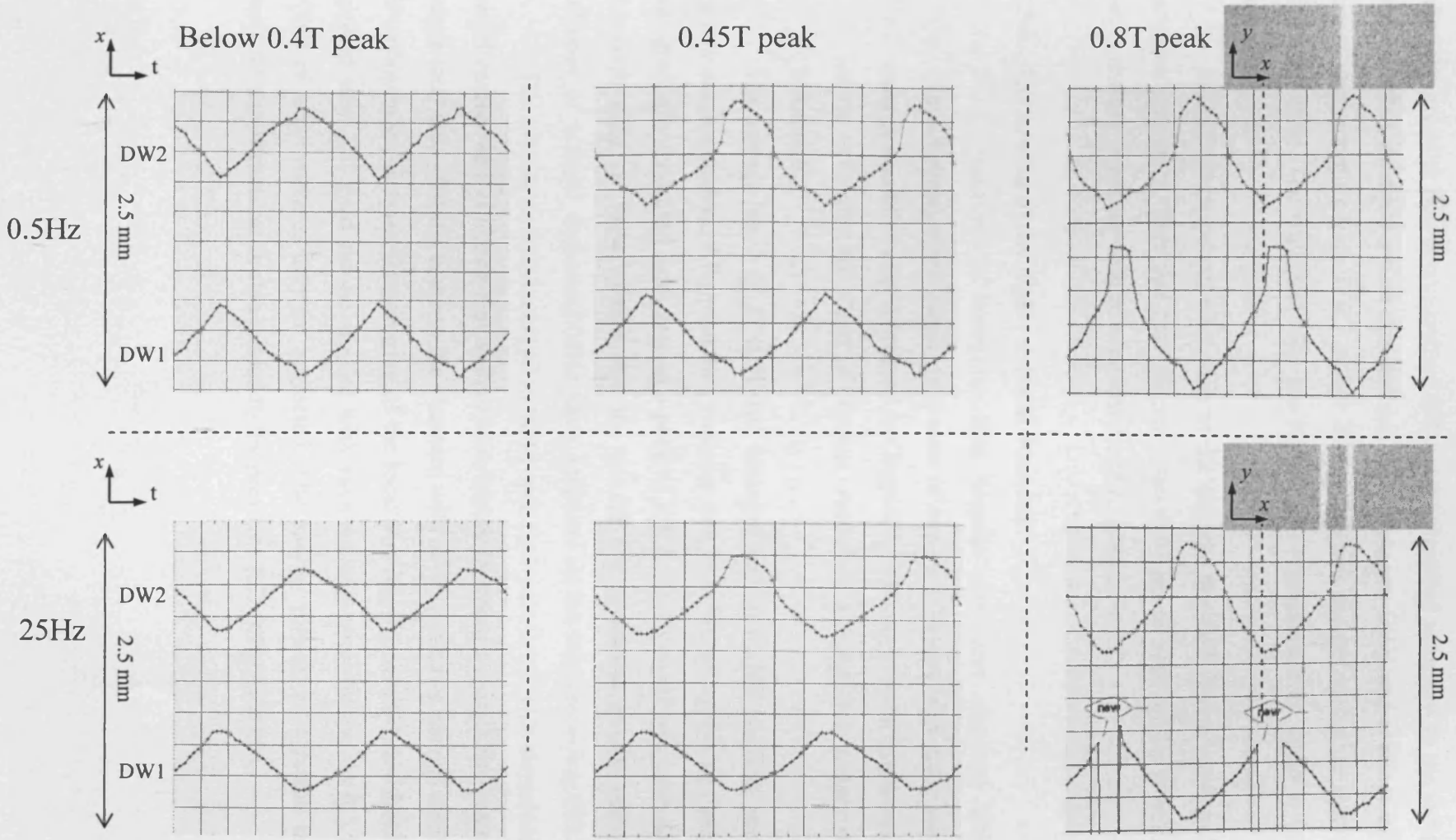

Fig. 7.7 Domain walls 1 and 2 displacement plots under different conditions of magnetisation. Images illustrate domain wall positions just before domains merge at about 0.8 T peak induction.

This eddy current damping is a reason for the emergence of the new domains when the growing flux is constrained to be accommodated somehow in the sample. In the presented example a new domain nucleates between DW1 and DW2 at 0.7 T. It grows until merging with DW1 at 0.8 T. All domains merge on further increase of flux amplitude. The wall positions are highly non repeatable from cycle to cycle at this point.

Despite the apparent saturation at the surface, the bulk domain system is still far from saturation. This fact may indicate that the domain wall profile is not planar but is skewed in reality with bowing effects as illustrated in [4].

7.5.4 Collapsing of the highly refined domains

It is important to recognise that domain structures obtained after AC demagnetisation are usually in a state of non-equilibrium with static minimum energy conditions (as discussed in Chapter 1). Owing to local hysteresis, these static structures are a sort of "frozen" record of the dynamic history of their formation.

The sample No. 3 of 27MJH was demagnetisation at 500 Hz first, providing narrow domain pattern. After that the generator was switched to 0.5 Hz and amplitude was gradually increased from zero to a peak of 1.5 T. The process was recorded with the wide field of view system and the results are presented in the movie file: collapse_of_refined_domains@05Hz_incr_Ampl.avi on the accompanying CD.

The narrow domains merged to build up a new pattern of wide domains. It can be interpreted as a structure that accumulates higher hysteresis energy associated with larger total area of walls come to the structure with lower potential energy where only few domain walls exist. Overcoming of the local pinning (hysteresis) threshold by an applied semi DC field can be studied with such domain observation. At 0.5 Hz the effect of eddy currents may be neglected. The energy difference between the two static domain structures is also related to the previous AC energy balance.

7.6 Repeatability of the individual wall motion

Existing theoretical models of domain wall dynamics and related power loss assume that the wall position is repeatable under stable magnetising conditions (see [4] and section 2.6.3). In reality non repeatable wall motion frequently occurs in soft magnetic materials [9], [10]. It has only become possible to study this phenomenon with development of real time imaging. Some early examples of non-repeatability are presented in Appendix 1. However, here the phenomenon of non repeatability is studied in more depth with the sample No. 3 of 27MJH.

Using the same procedure as described in section 7.4.3 a series of images was recorded over 12 cycles of magnetisation with 36 frames per cycle, applying 0.5 and 25 Hz trianglar field waveforms. Observations were made at 0.5 Hz for 0.4 T and 0.51 T peak flux density values. At 25 Hz flux densities of 0.4 T, 0.51 T, and 0.70 T were used, the latter being when nucleation of new domain occurs. The observations were then repeated at 0.51 T with the new nucleated domain pattern (this is the second persistent pattern in figure 7.5). The positions of walls 1 and 2 were measured with the same software as before and the instantaneous speed of each wall was calculated. The results are presented in figures 7.8 –7.11. Small differences in the walls' cycle-to-cycle positions can be observed in these plots.

The uncertainty in a domain wall position was assessed from the standard deviation of the position for each instance which was superimposed as an error bar on the plot of average positions, in figures 7.12 – 7.15. These show that the non repeatability varies from point to point. Usually, higher non repeatability is observed when a wall passes a large pinning site. Minimum, maximum and average standard deviations were compared. It was generally noticed that:

- The non repeatability increases with amplitude and reaches its maximum when the new domain nucleates. After the new domain became stable the amount of non repeatability drops.
- The differences in minimum and maximum standard deviations is greatest at low frequency. There are very stable and very unstable points at 0.5 Hz, in contrast, at 25 Hz all points are unstable with a few having a little higher instability.

Correlation of eddy currents between neighbouring walls is likely to be a reason for such collective wall behaviour. At low frequency the eddy currents are localised in

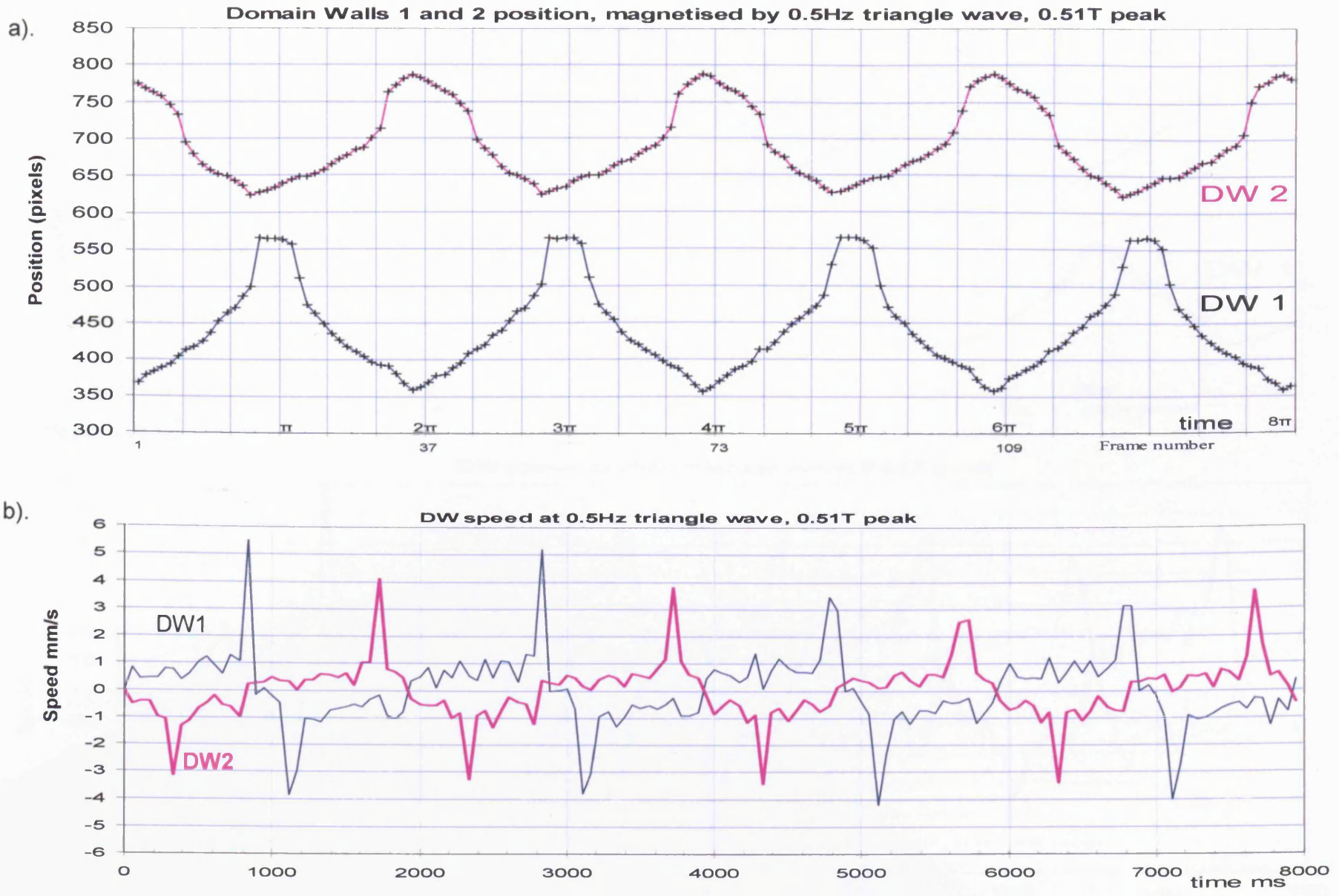

Fig. 7.8 Domain walls 1 and 2 displacement (a) and speed (b) over 4 cycles at 0.5Hz, 0.51T peak induction

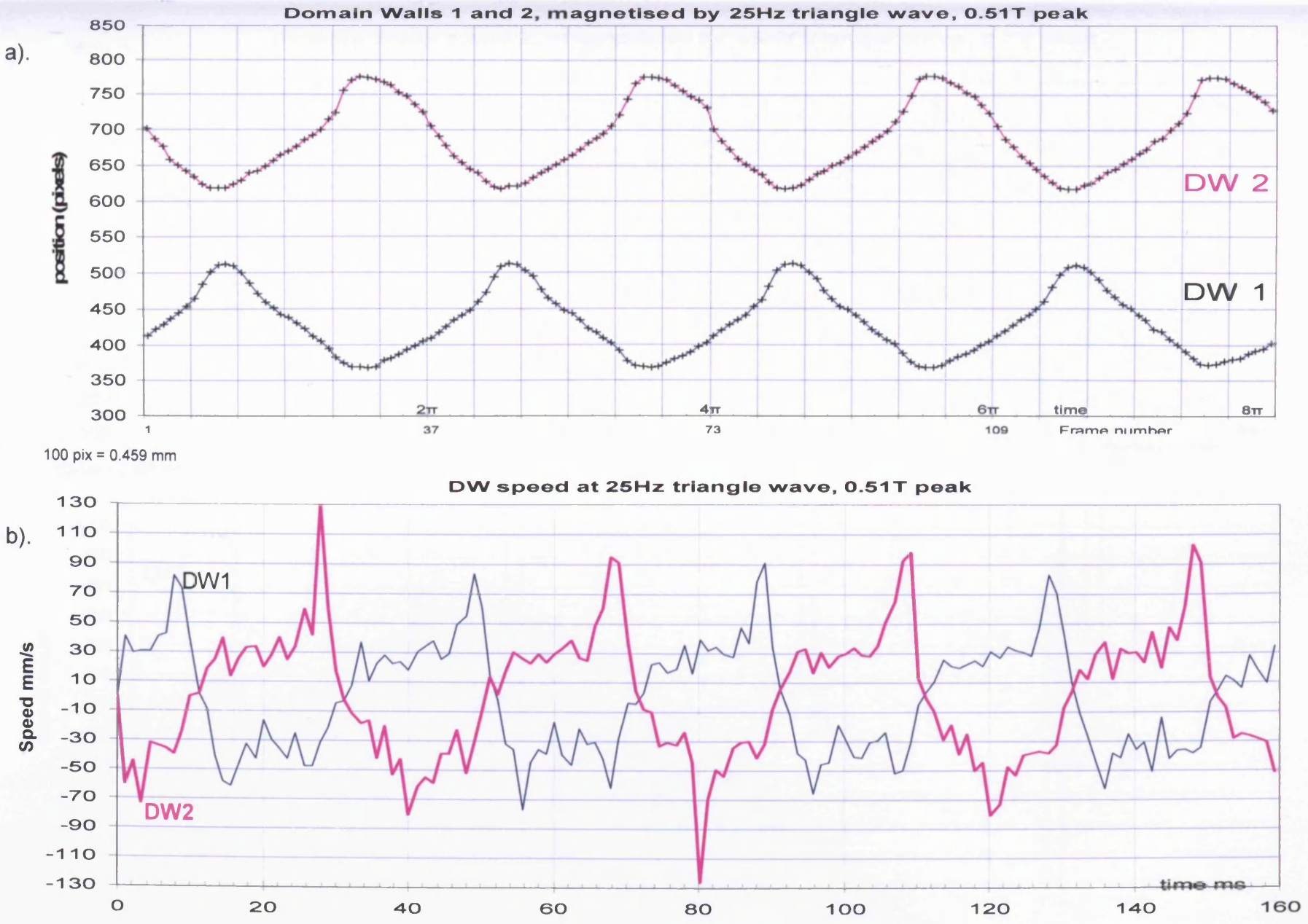

Fig. 7.9 Domain walls 1 and 2 displacement (a) and speed (b) over 4 cycles at 25Hz, 0.51T peak induction

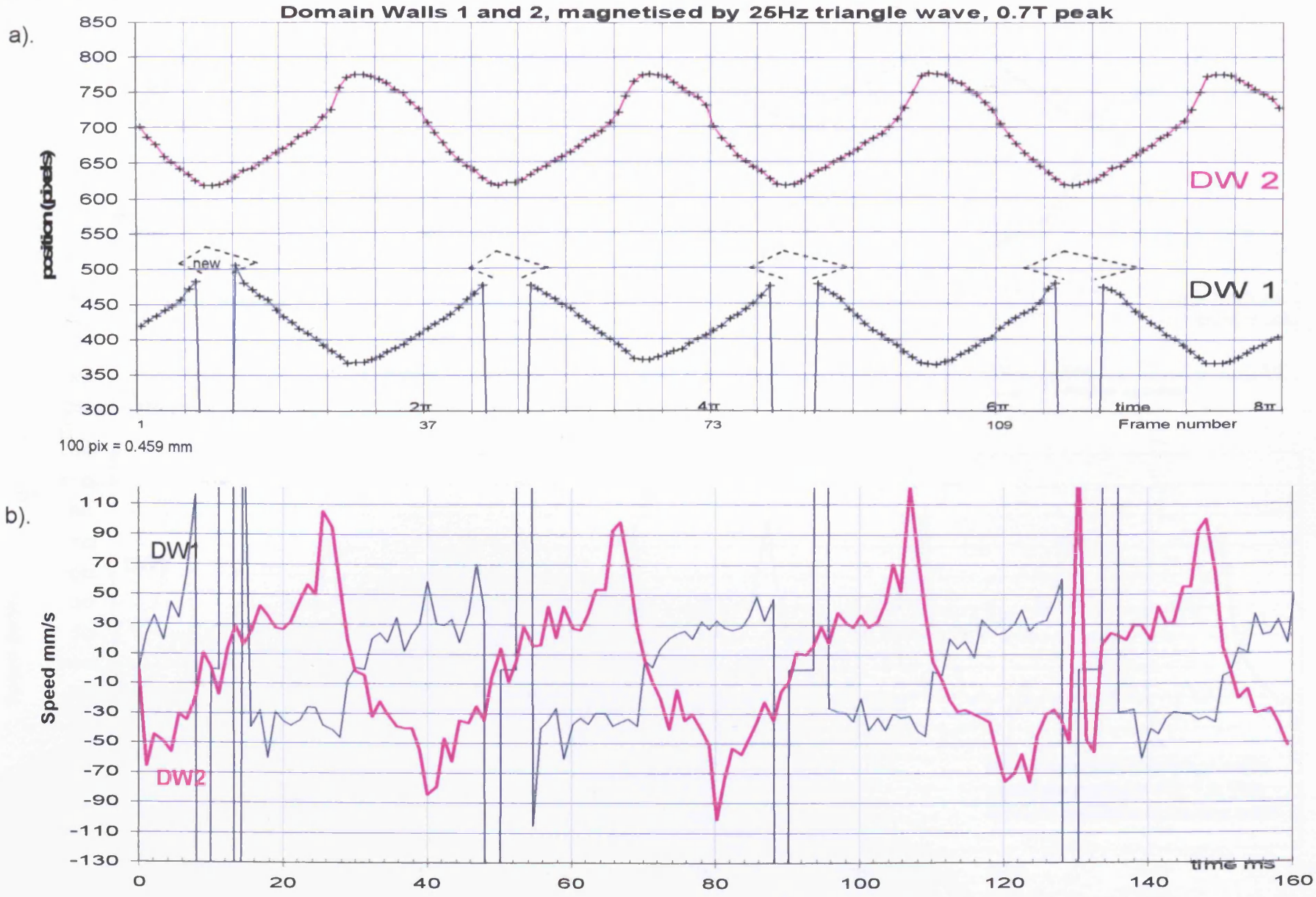

Fig. 7.10 Domain walls 1 and 2 displacement (a) and speed (b) over 4 cycles at 25Hz, 0.7T peak induction. New spike domain briefly nucleates and DW1 merges with this domain for a short time (schematic drawing).

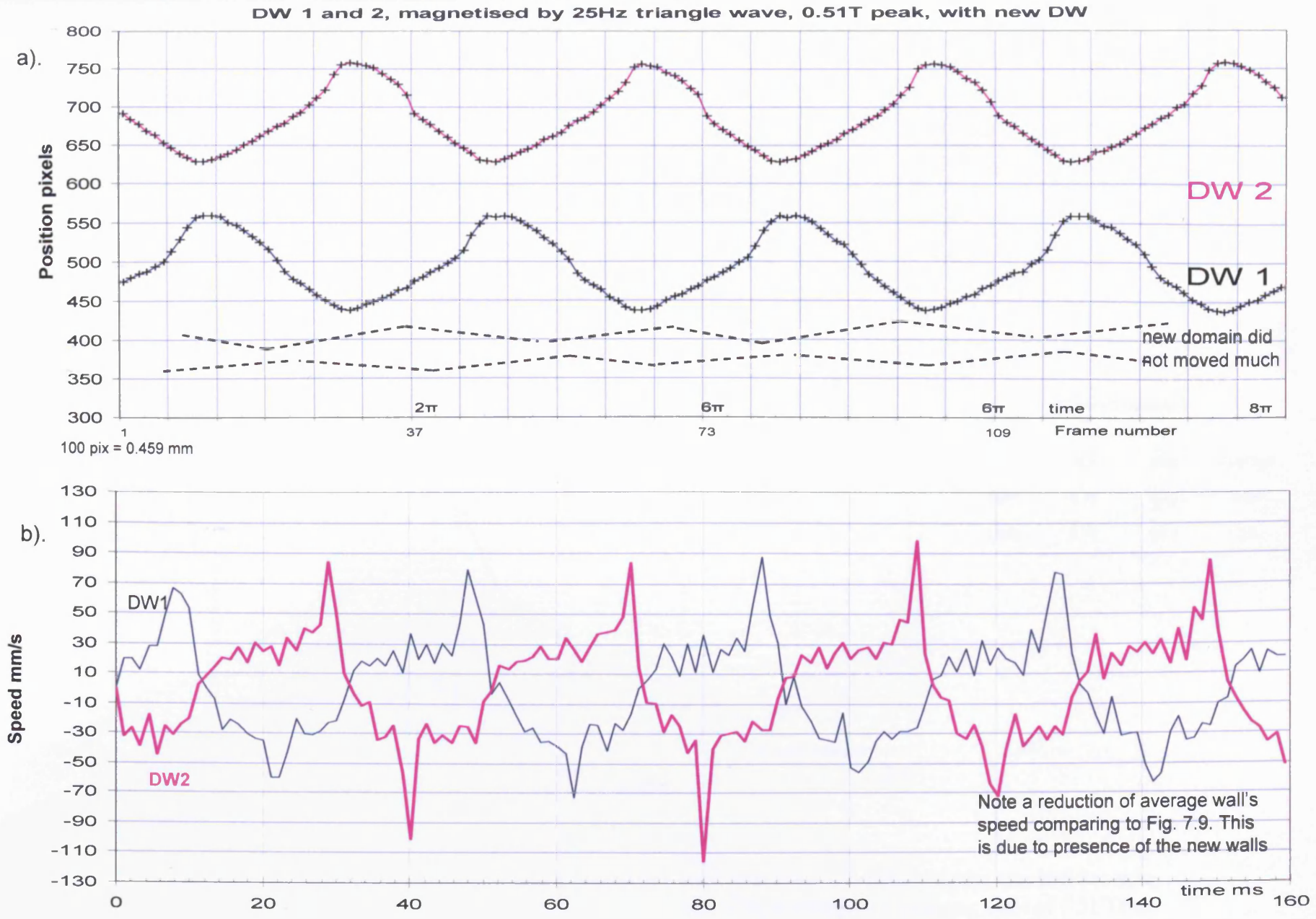

Fig. 7.11 Domain walls 1 and 2 displacement (a) and speed (b) over 4 cycles at 25Hz, 0.51T peak induction with new stable domain pattern. Newly domain is presented schematically.

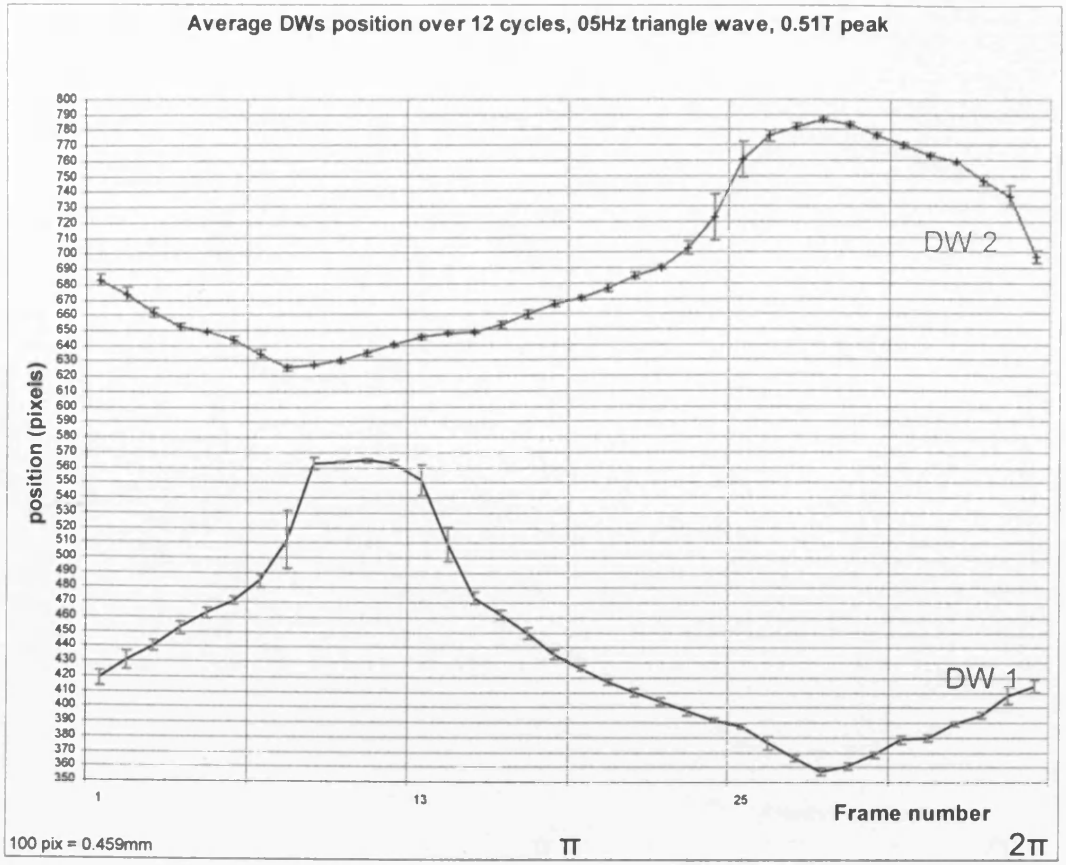

Standard deviation

	Min	Max	Average
DW1	0.18	19.2	3.84
DW2	0.75	14.9	2.3

Fig. 7.12 Average domain walls position over 12 cycles with error bars indicating the standard deviation of the wall position at each point of the magnetising cycle, 0.5Hz. A triangle magnetising wave of 0.51 Tesla peak induction in the observed grain.

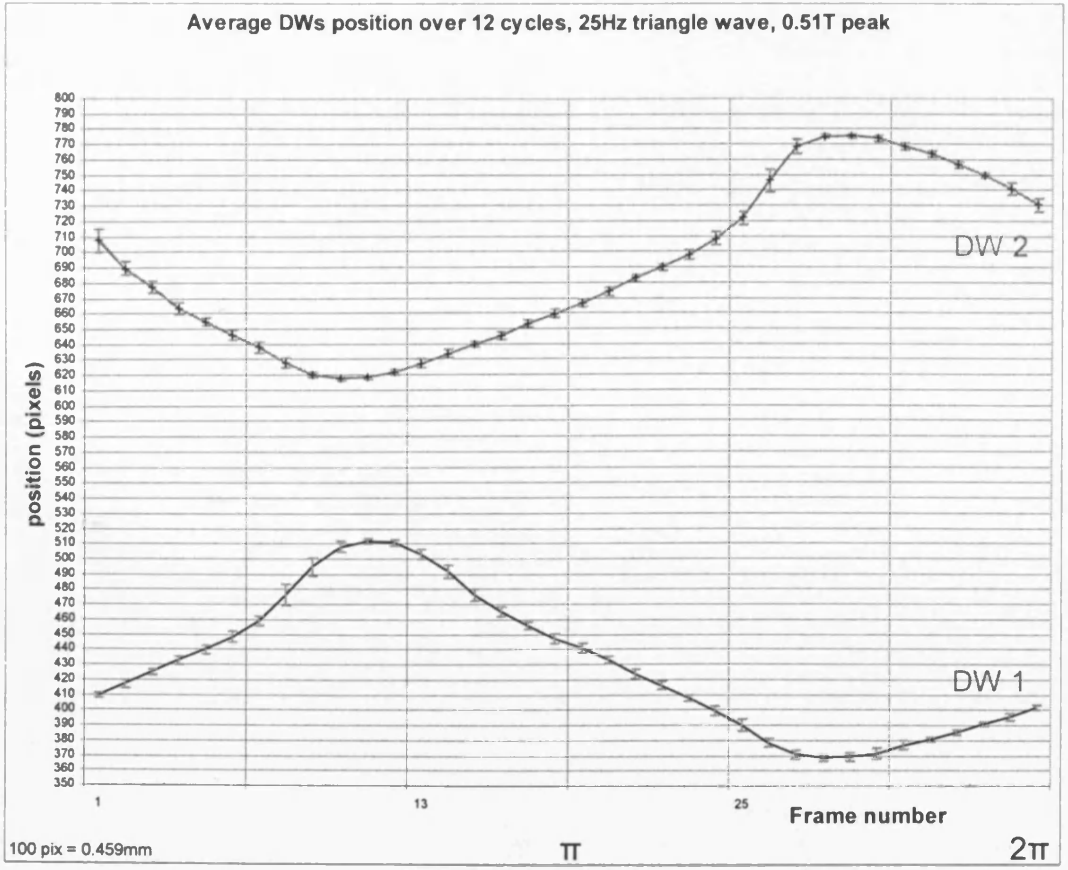

	Standard deviation		
	Min	Max	Average
DW1	1.43	7.4	2.9
DW2	0.94	7.54	2.94

Fig. 7.13 Average domain walls position over 12 cycles with error bars indicating the standard deviation of the wall position at each point of the magnetising cycle, 25Hz. A triangle magnetising wave of 0.51 Tesla peak induction in the observed grain.

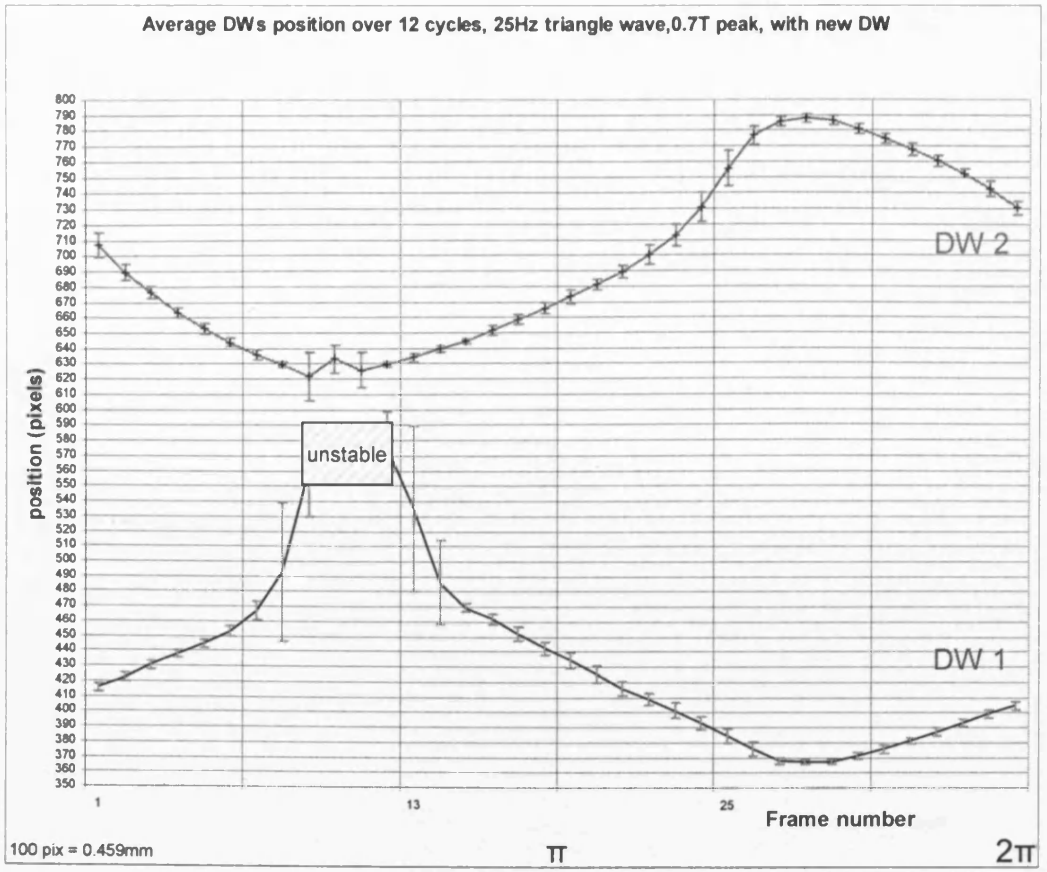

	Standard deviation		
	Min	Max	Average
DW1	1.59	54.6	8.34
DW2	1.44	15.9	4.8

Fig. 7.14 Average domain walls position over 12 cycles with error bars indicating the standard deviation of the wall position at each point of the magnetising cycle, 25Hz. A triangle magnetising wave of 0.7 Tesla peak induction in the observed grain. The top of DW1 plot is merged with brief spike domains, unstable data from this area is voided in the statistics.

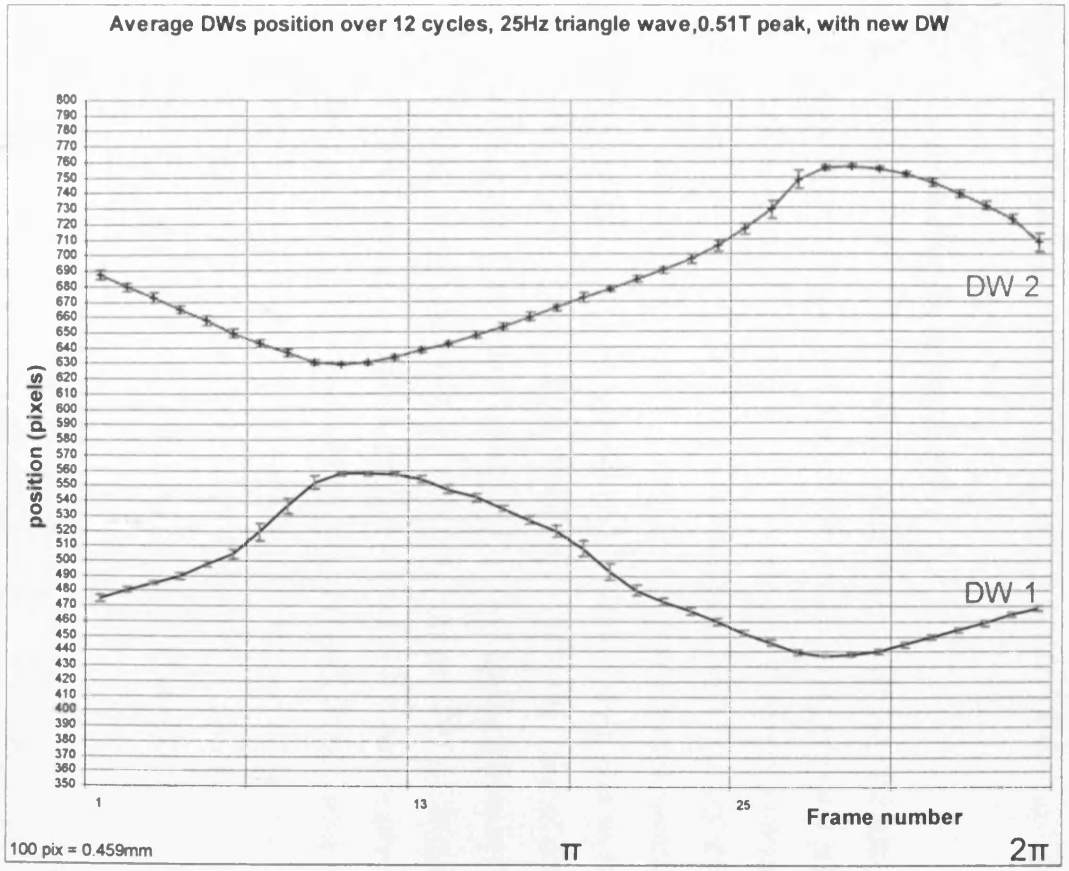

	Standard deviation		
	Min	Max	Average
DW1	0.69	5.84	2.42
DW2	0.47	5.87	2.66

Fig. 7.15 Average domain walls position over 12 cycles with error bars indicating the standard deviation of the wall position at each point of the magnetising cycle, 0.5Hz. The triangle magnetising wave of 0.51 Tesla again, after the new domain nucleated (four domain walls structure exists in the area of view)

the vicinity of individual walls and there is no correlation. Walls are independent of each other and interact only with local pinning points. At higher frequency the eddy currents correlate with each other as explained in section 2.6.4, so that the pinning of one wall affects the motion of neighbouring walls.

The values of instantaneous domain wall speeds over 12 cycles are presented in !04T_05Hz.xls ... !051TnewDW_25Hz.xls files on the CD. This data can be used to find relevant power loss using equation 2.12. For instance, the average power loss contribution due to DW1 and DW2 at 25 Hz and 0.51 T peak induction will drop by 23% after nucleation of another domain. The total average power loss has therefore been effectively redistributed over DW1, DW2 and the new domain. This sum of losses on each wall can be higher or equal, or even lower than the losses on original two walls. But unfortunately the wall speeds and power losses on the new domain couldn't be measured precisely due to very small displacements of the new walls.

7.7 Uncertainties in experiments:

1. Figures 7.8 – 7.11 show equivalent wall movements for discrete time measurements and although some detail of the intricate wall motion has been lost the general character of the movement has been retained.
2. Accuracy of the position measurement is limited mainly due to the focusing of the system. It is approximately 5 pixels, which corresponds to 0.03mm in the experiments reported in section 7.5 (this corresponds to 0.7% of the field of view or 3.5% of the domain wall spacing in the case of four walls). Note this error comparing to the 'error bars' at most stable points in figures 7.12 – 7.15.
3. Timing error comprises a typical random 10 μs triggering error of the comparator and a camera sampling error. The camera sampling error emerges from the difference between the actual magnetising frequency and a number of sampling periods that the camera makes during one cycle. This error can be effectively reduced below 10 μs by accurate adjustment of the frequency and sampling parameters. Together, the total timing error is ±20 μs or 2% at 1.1 ms sampling period.
4. Domain wall speed is calculated from the formula $(x_2 - x_1)/(t_2 - t_1)$ (7.1) hence the maximum speed error is ±11% (2 * 3.5% + 2 * 2%).

7.8 Discussion and conclusions of domain observations in high permeability GO steel

From investigation of domain dynamics it is concluded:

1. The observed domain wall refinement with frequency is broadly in agreement with previous observations [2], [3], [8] and theory in [4], [5]. Shilling [6] suggested that as f is increases, and the field required to drive the existing walls increases, new walls nucleate progressively as the field exceeds the local nucleation thresholds. In this investigation the nucleation of new domains in the given grain occurs above a certain *magnetisation rate*, dM/dt, which for a triangular wave is approximately a linear function of the frequency and the amplitude of the applied field, i.e. $dM/dt \sim f\cdot(H_{peak} - H_{coercivity})$. At 0.7 T amplitude of alternating induction the new domains begin to nucleate above the *critical frequency* what for majority of grains lies between 10 and 40 Hz.

2. Spike domains were found to nucleate at grain boundaries. When the applied field or frequency was increased further, the spike domains coalesce to form a new bar-like domain. The nucleation of new domains can be correlated to instances when the existing domain walls are already moving at maximum speeds, i.e. maximum rate of change of magnetisation.

3. The spike domains are unstable and always disappear when the magnetisation rate is reduced. However, if two spikes have merged into a new bar-like domain, the resulting domain can be stable and remain even after the field is switched off.

4. A sideways movement of the domain pattern as a whole, such as reported in [8], was not observed. Instead, the nucleated domains became mobile and other domains did not disappear while the magnetisation conditions remained the same. New domains could disappear when the magnetisation rate is reduced. It was often observed that the frequency at which a domain disappears is lower than the frequency at which it has previously nucleated (at fixed amplitude of M).

5. The surface position of the walls at the peaks of the magnetising cycle (such as in movie 25Hz07T.avi) showed that surface saturation is reached on the positive peak at 0.8 T while on the negative peak the surface is only about 80% saturated. Such an *asymmetry* was observed previously [4], [5], [8] and is attributed to the skewed profile of the walls in the (110)[001] textured steel.

6. It was generally noticed that the non repeatability of domain wall motion increases with amplitude and reaches its maximum when the new domain nucleates in

the observed grain. After the new domain became stable the amount of non repeatability drops.

7. The amount of non repeatability of domain wall displacement at each point on the magnetisation cycle is more uniform at higher frequency (25, 50, 75 Hz) whereas at 1 Hz some points on the cycle are much more non repeatable than others. Such a distribution of non repeatability is attributed to the eddy-current correlation between walls at higher frequencies, and the absence of correlation at low frequency.

8. The non repeatability is always high at the pinning points.

9. The non repeatability, discontinuous nucleation and collapse of domains may describe the proximate cause of other discontinuous phenomena such as Barkhausen noise. A comprehensive and quantitative model has not been developed yet. There are "energy minimisation static" and "minimum entropy dynamic" models [4], [7]. The dynamic model is in broad agreement with the observed $r(f) \sim \sqrt{f}$ trend at higher frequencies, but the transition to this from a state of minimum energy at the low frequency limit is unresolved. Hopefully some useful information for developing a new theoretical model is extracted from experiments such as those presented in sections 7.4 and 7.5.

10. In a theoretical study, Bishop [4] assumed that at any frequency f the system seeks to minimise its average energy over the magnetisation cycle. This requires the time scale for the domain density r to reach equilibrium to be longer than the period of the magnetising cycle. This justifies at least one component of non repeatability. Moreover, when the minimisation of dynamic energy gives more than one solution for a given condition, such as in the observed region of instability in figure 7.5, the system randomly jumps from one possible pattern to another causing a high degree of non repeatability.

11. The maximum possible power loss occurs when the instantaneous speeds of the walls are maximal. Assuming the maximum possible speed equals to the average speed plus the speed increase due to the wall position non repeatability, the maximum possible relative increase in power loss during one cycle of magnetisation due to the non repeatability can be calculated as

$$1-\frac{E_{\max speed}}{E_{average}}=1-\frac{\sum_i (V_i+\Delta V_i)^2}{\sum_i V_i^2}=1-\frac{\sum_i \left((|x_i-x_{i-1}|+|Stdev_i-Stdev_{i-1}|)/\Delta t\right)^2}{\sum_i \left(|x_i-x_{i-1}|/\Delta t\right)^2} \qquad (7.2)$$

where V_i is the average instantaneous speeds of a given domain wall at i instance, ΔV_i is the speed increase, x_i is the average position at i instance, $Stdev_i$ is the standard deviation of the wall position from the x_i. The calculations for DW1 in files !051T_05Hz.xls, !051T_25Hz.xls and !051TnewDW_25Hz demonstrates that increase in power loss due to the non repeatability can be as high as 33% at 0.51 T, 0.5 Hz and 17% at 0.51 T, 25 Hz. (We understand, in reality, that this has very low probability to happen during one cycle.)

12. It was demonstrated in figure 7.5 that under certain magnetisation conditions different domain patterns can exist in the grain. For example at 10 Hz both 2DW and 4DW systems are possible, depending on the "magnetic history" of the sample. The 4DW system is more power efficient than 2DW system, as confirmed by calculations in Appendix 5.1, hence it is useful to modify the "magnetic history" to produce narrower domains.

13. Under triangular time varying magnetisation M, were dM/dt is a rectangular function of time, observed individual wall velocities were non-rectangular functions of time, often increasing and decreasing several times during magnetisation cycle.

14. The eddy current loss on individual walls is determined by the integral of the wall velocity squared per cycle, so that the uniform wall motion with constant speed would be the most energy efficient. This leads to the conclusion that manufacturers should produce material without pinning defects. Also the material should have a smooth surface, smooth grain boundaries, equal grain size to make the domain spacing the same in the neighbouring grains and ideal orientation of grains to make bar domains extending over many grains without kinks.

15. The conclusions presented in this chapter are based on quantitative measurements of the domains within single crystal grain in sample No. 3 of 27MJH steel. It should be clear that exact values of domain wall speeds, non-repeatability and instances of nucleation of the new domains are local values and cannot be generalised for domains in other samples. The qualitative generalisation can be made only on the tendency of domain pattern to refine with increasing magnetisation rate and on the dependence of the non-repeatability of domain wall motion on magnetisation conditions, while the behaviour of domain walls such as in section 7.5.2 should be studied further on a large number of samples to confirm its general validity.

7.9 References of chapter 7

1. Larsen A.M.R., Blotzer R.J., Lauer B.A., and Anderson J.P., Magnetic testing methods for motor lamination steels, Proceedings of the 12th Conference on Properties and Applications of Magnetic Materials, Chicago, Illinois (1993).
2. Beckley P., Basic properties of grain oriented electro-technical steels, Final report EUR 8270 EN, British Steel Corporation, (1983).
3. Khanlou A., Static and dynamic domain observations studying the effect of adhesive on G.O. 3% SiFe domain structures, Report in Wolfson Centre. (1996).
4. Bishop J.E.L., Pfutzner H., Domain wall bowing and dynamic domain width in grain oriented SiFe, IEEE Trans. Magn., 30, 1, p46, (1994).
5. Pfutzner H., Bishop J.E.L., Physical mechanism of domain spacing in highly grain oriented silicon iron, Proc. 2nd Int. Symp. Phys. Magn. Mater., Beijing, p152, (1992).
6. Shilling J.W., Domain structures in 3% Si-Fe single crystals with orientations near (110)[001], IEEE Trans. Magn., vol. MAG-9, p351, (1973).
7. Pry R.H. and Bean C.P., Calculation of the energy loss in magnetic sheet materials using a domain model, J. Appl. Phys., 29, p532, (1958).
8. Morgan J.V.S., Losses in 3.25 per cent grain-oriented silicon-iron, PhD. Thesis, University of Wales College Cardiff (1980).
9. Flohrer S., Schäfer R., McCord J., Roth S., Schultz L., Herzer G., Magnetization loss and domain refinement in nanocrystalline tape wound cores, Acta Materialia 54, p3253, (2006).
10. Moses A.J., Williams P.I., Hoshtanar O.A., Real time dynamic domain observation in bulk materials, J. Magn. Magn. Mat., 304, p150, (2006).

CHAPTER 8 THE CAPABILITY OF THE KERR MICROSCOPE SYSTEM FOR IMAGING DOMAINS IN A RANGE OF DIFFERENT MAGNETIC MATERIALS

8.1 Introduction

In this chapter some typical examples of domain structures in various materials are presented. The main aim of this chapter is to show the system's capability and versatility for observing domains under various magnetising conditions. Possible applications of the system are summarized in table 8.1 at the end of this chapter.

8.2 Domain observations of non-oriented electrical steel

It is expected that surface oxidation which occurs during the manufacturing process of steel, affects its magnetic properties [1], [2]. The aim of the domain observation was to find the effect of oxidation on domain dynamics and hence the magnetic properties.

Three samples of 0.5 mm thick 3% silicon non-oriented steel supplied by Cogent Power Ltd were cut into 14 mm x 6 mm rectangles. One edge of each sample was mechanically polished followed by etching with 3% Nital solution. Samples 1 and 2 were etched for 2 minutes and sample 3 for 20 sec. After this they were stress relief annealed in a vacuum at 810 $^{\circ}$ C for 2 hours. A clear surface was obtained on sample 3, so it was selected for examination. It was magnetised with a 400 turns coil wound around a C-yoke (with 10 cm magnetic path length, see figure 8.1a. An 18 turn search coil was wound around the sample and connected to a LakeShore 480 fluxmeter for flux density measurement.

The magnetising system could develop 1.54 T DC induction (with 0.2 A in the winding), and the peak induction in AC mode was 1.43 T (at 0.14 A peak, at 0.5 Hz). The sample could not be saturated, so observation was carried out on a minor B-H loop as shown in figure 8.1b.

The NEOARK BH-780-IP polarising microscope was used in longitudinal Kerr effect mode with a 20 times magnification lens. The plane of incidence was parallel to the direction of magnetisation along the rolling direction. The area of view was approximately 300 x 250 μm. In each case, six images were taken and assembled into a

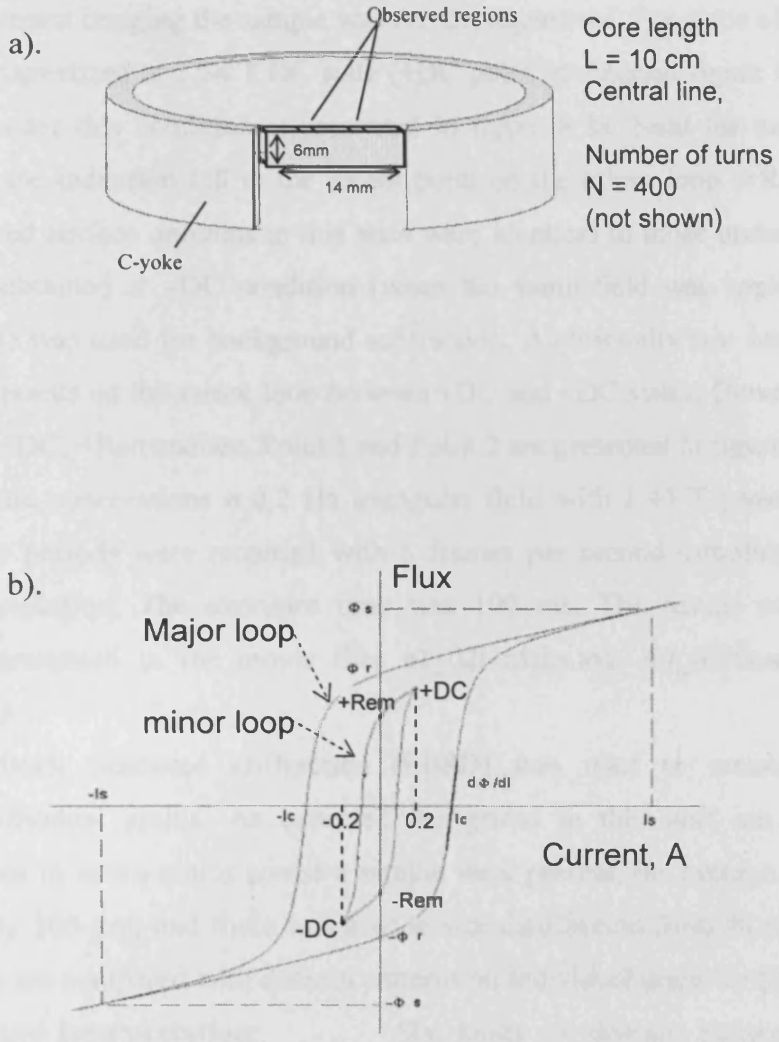

Fig. 8.1 (a) Sample mounted in the C-yoke (b), and magnetisation conditions for static imaging.

3x2 map to obtain an 0.5 mm x 0.8 mm area of view across the sample thickness. Digital subtraction and morphological filtering described in section 6.5 was used.

Prior to domain imaging the sample was AC demagnetised. For static observation the sample was magnetized at 1.54 T DC state (+DC point in diagram figure 8.1b). The image obtained under this condition is presented in figure 8.2a. Next the current was switched off and the induction fell to the +Rem point on the minor loop (+Remanence state). The observed surface domains in this state were identical to those under the +DC state. An image obtained at –DC condition (when the same field was applied in the opposite direction) was used for background subtraction. Additionally two images were taken at arbitrary points on the minor loop between +DC and –DC states. Domain images corresponding to +DC, +Remanence, Point 1 and Point 2 are presented in figure 8.2b.

For dynamic observations a 0.2 Hz triangular field with 1.43 T peak induction was applied. Two periods were recorded with 5 frames per second sampling rate and 800x600 pixel resolution. The exposure time was 100 ms. The results of dynamic observation are presented in the movie files a1_02Hz5fps.avi, A7_05Hz.avi on the accompanying CD.

Electron Back Scattered Diffraction (EBSD) was used to measure lattice orientation of individual grains. As expected the grains in this steel are randomly oriented. From four to seven grains across a sample were present, the average grain size was approximately 100 μm, and there was a wide size distribution from 40 to 250 μm. The EBDS results are compared with domain patterns on individual grains in figure 8.3.

Analysis and Interpretation: Six kinds of domain patterns can be observed in the image in figure 8.3. Grains are designated by nomenclature such as 1*a*, where 1 indicates the type of domain pattern and "*a*" denotes a particular grain. Domain patterns are determined mainly by the orientation of the grain lattice. In general grains with similar orientation, as confirmed by the EBSD image, had similar domain patterns (the exception to this was grain 4*d*.).

- Grains 4*a*, 4*b* and 4*c* have [100] axes parallel to the magnetising direction and (001) planes lies close to the plane of the sample surface. Because of this, these grains are saturated easier than others [3] (see figure 1.3 and figure 1.4). According to curve (i), such a grain reaches saturation and reverses to negative

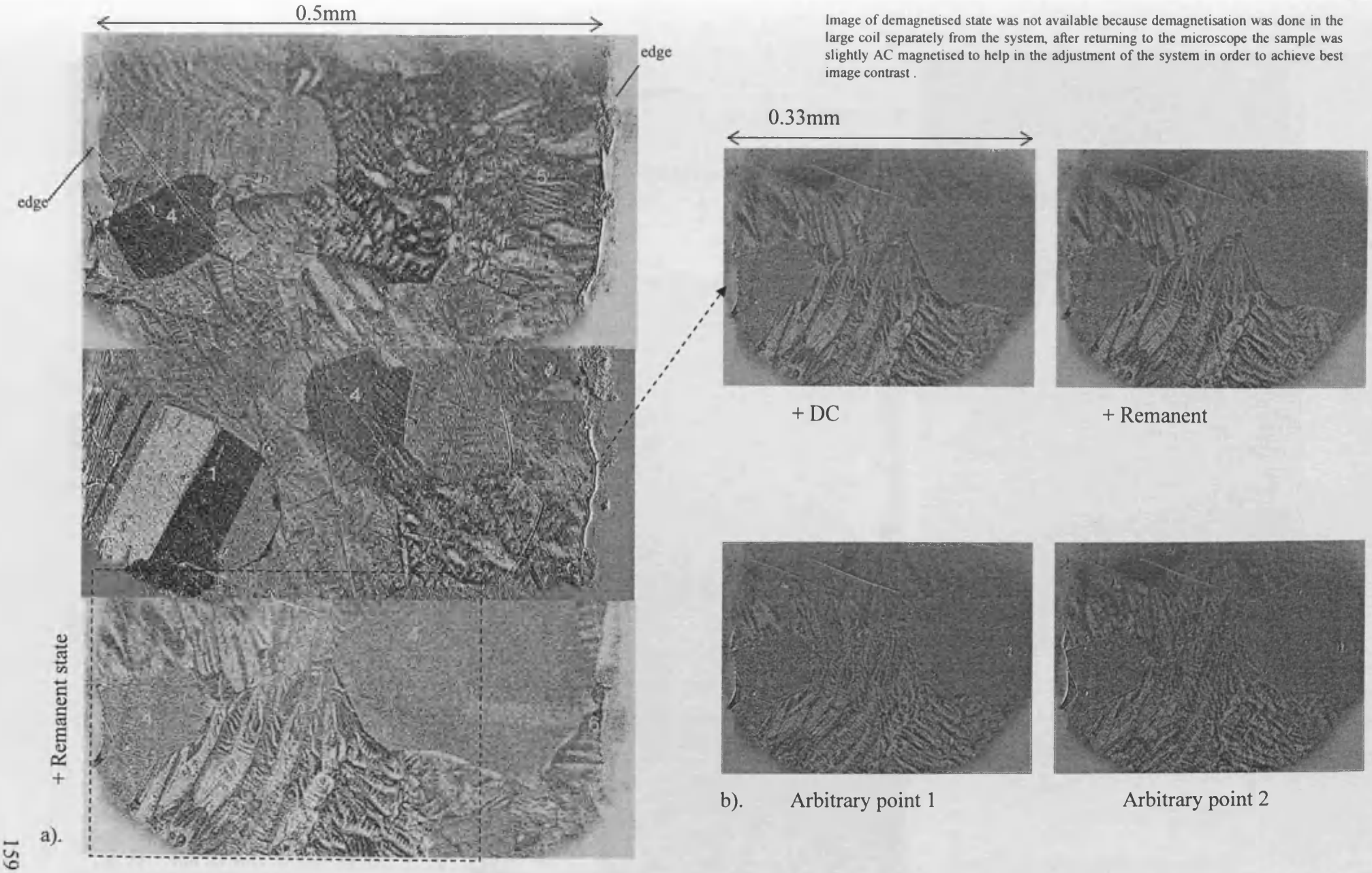

Fig. 8.2 DC images of domain structure on the edge of the non oriented steel sheet. Sample No. 3 at the marked region.

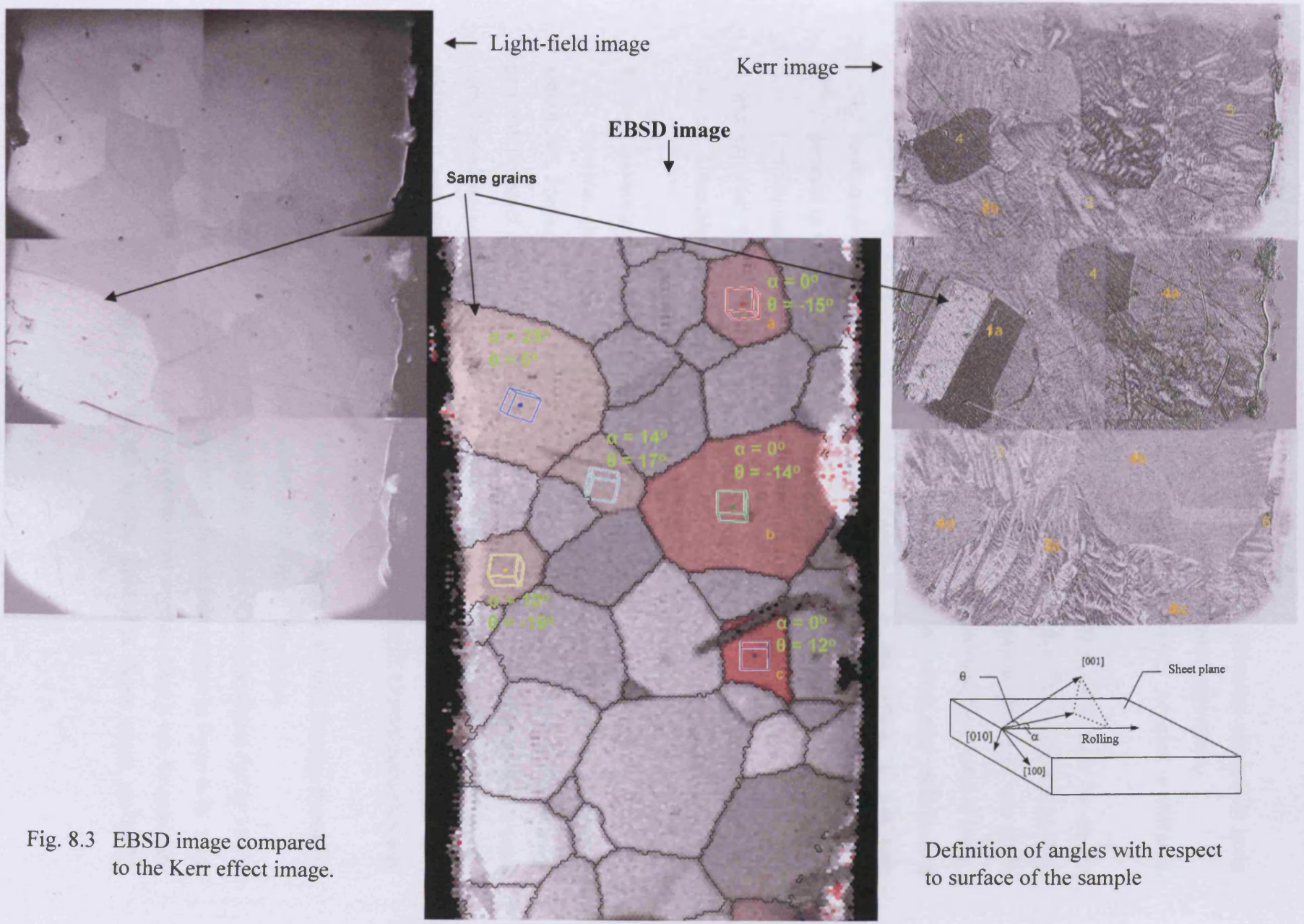

Fig. 8.3 EBSD image compared to the Kerr effect image.

Definition of angles with respect to surface of the sample

saturation rapidly. Probably this is why domain boundaries are not seen in grain 4*b*, because magnetisation goes rapidly from +saturation to -saturation.

- Domains in grain 4*d* have similar features but EBSD revealed a different orientation of the lattice.
- Bar domains are present in grain 1*a* which has its (110) plane close to the sample surface and an angle of yaw $\alpha = 25^{\circ}$. However it does not reach saturation at +DC where grains 4*a*, 4*b* and 4*c* were saturated. This is because the large yaw angle causes the field component along the [001] axis to be reduced by a factor of cos α.
- Domains in type 2 grains form "echelon patterns" [4] which may indicate that their (111) directions are almost perpendicular to the surface. It was also confirmed by dynamic observation that there was a weak response of these patterns to the applied field, which can be attributed to the curve (iii) in figure 1.4. Unfortunately there was no EBSD information regarding these grains.

It was expected that the domain dynamics should depend on the conductivity of the material. Although nothing was seen that could be attributable to surface oxidation.

8.3 Conventional grain-oriented steel

Samples of commercial grade 27M4 and 35M4 were selected as detailed in section 7.2. Preparation and examination of these samples was the same as for the high permeability steel discussed in chapter 7, but interpretation of the results was much more complicated because the grain size is much smaller and misorientation is greater. In addition it was not possible to measure the flux in individual grains because the search coils could not be made sufficiently small using the available drill. Overall induction was measured using a search coil wound across sample.

Static domain observations are presented in figure 8.4b and domain dynamics during magnetisation can be seen in file 35M4_0.2HzTriang_5fpsR.avi.

As can be seen from figure 8.4a, a large degree of misorientation (of up to 9°) exists in these samples which is confirmed also by the domain images in figure 8.4b. As a consequence of misorientation the bar domains are not regular. Also it can be seen that well oriented grains respond faster to the applied field than those which are badly

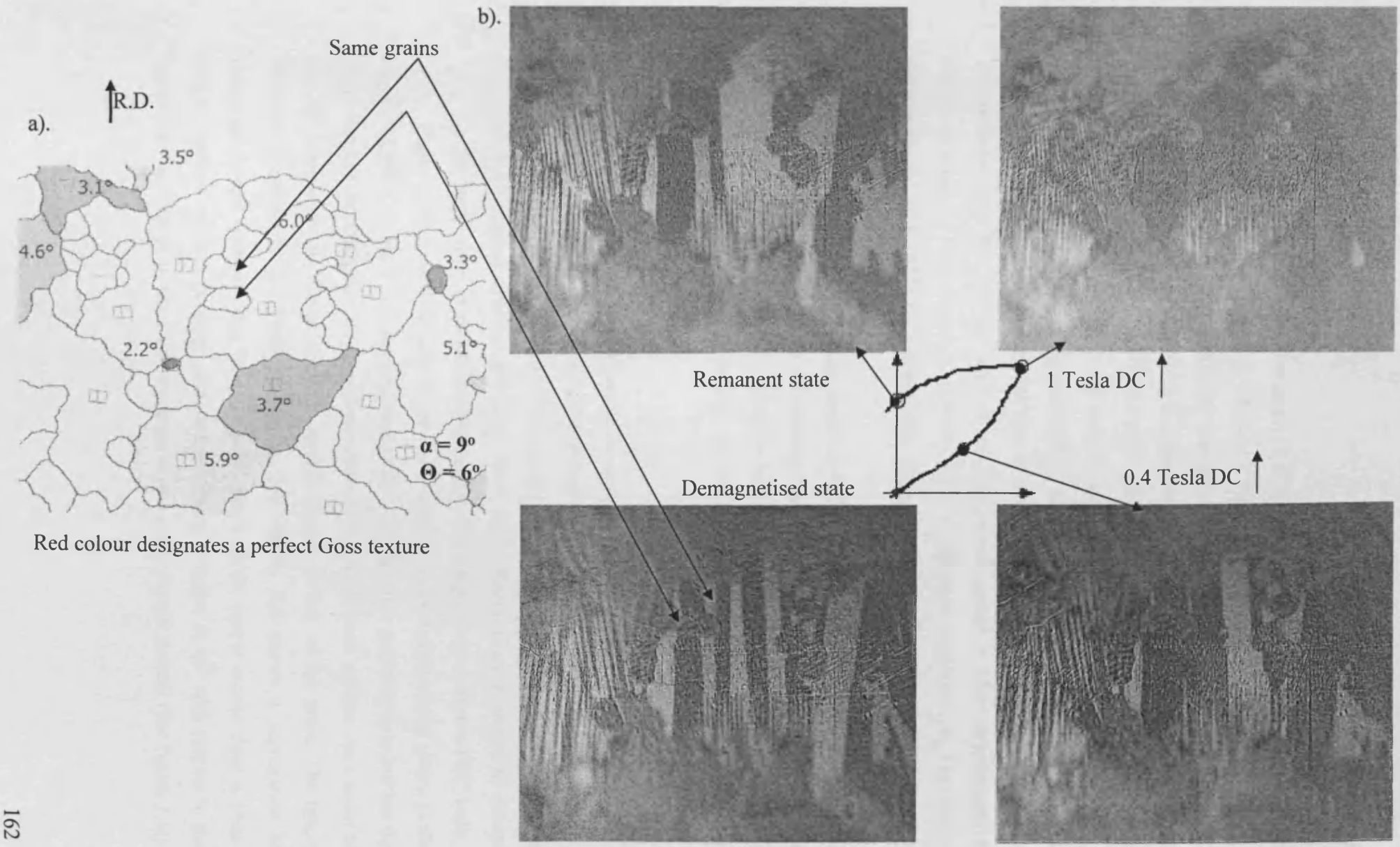

Fig. 8.4 EBSD image (a) and domain patterns (b) of the sample No 5 of conventional 35M4 GO steel

oriented. Figure 8.4 shows that the grain in the centre reaches saturation (at least at the surface) when the bulk induction is still only 1 Tesla.

It was observed by Khanlou [5] that grains with (110) planes lying at an angle to the surface of the sheet (tilt angle) have lower surface flux density levels compared to the total flux density in the sample. Grains oriented away from the rolling direction but still in the same plane as the surface of the sample (yaw angle) were not so affected.

Very different surface magnetisation of neighbouring grains can be related to the large differences of their flux densities (see movie M4_7mm_wide_02Hz10fpsR.avi for 1 T peak induction). The flux in a well oriented grain surrounded by badly oriented grains can be as much as 50% higher, especially for low induction amplitude.[6] This fact is directly related to the different permeability of each grain and indirectly to the differences in power loss in each grain.

Despite well-observed large domains the quantitative analysis of such irregular patterns is complicated. There is no suitable theoretical model that can be used in this case. Interaction of domain walls with grain boundaries and intergranular bar domains is especially difficult to model. Because of the lack of theory, conventional steel was studied only qualitatively here.

8.4 Further domain observations on electrical steel

8.4.1 Lancet combs switching in tilted grains of high permeability steel

There are a number of domain phenomena which can be related to bulk properties such as magnetostriction and Barkhausen noise. Barkhausen noise can be related to the 'switching' of lancet comb structures with large number of non-180° walls.

Figure 8.5 presents images of bar like domains in two neighbouring grains in the sample of 30MOH high permeability steel. The upper grain is perfectly oriented but the lower one has its [001] axis slightly tilted with respect to the sheet surface. As a result of this tilt misorientation, lancet domains appear on the surface of the grain. The lancet domain formation is discussed in section 2.3. Figure 8.5 shows a segregation of individual lancet domains into lancet combs. Each of the lancet combs have a plate-shaped internal domain structure with magnetisation oriented at 45° with respect to the sample surface (close to the [110] diagonal of the cubic crystal lattice) (see figure 2.4f).

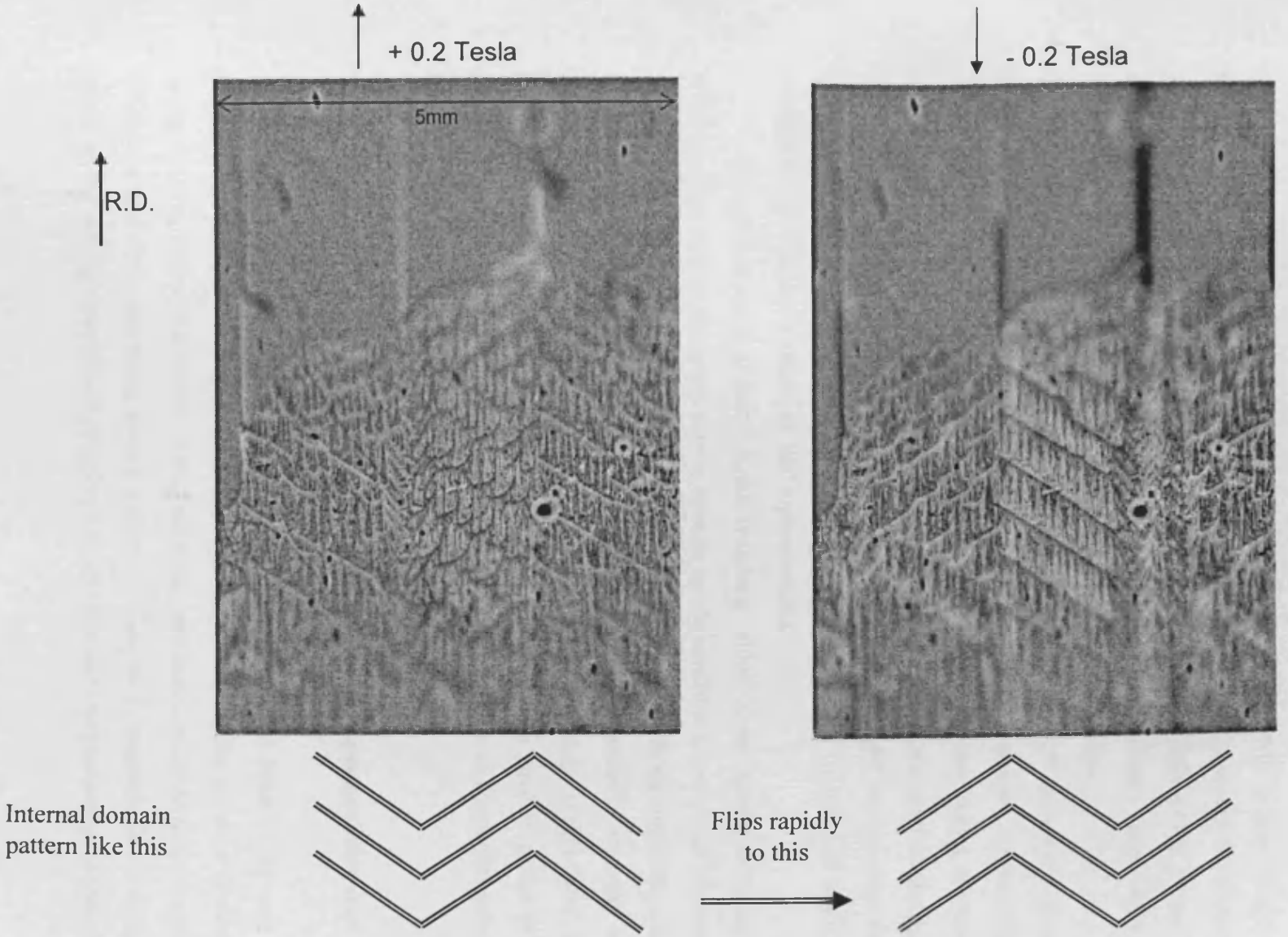

Fig. 8.5 Lancet combs switching when field is applied along the rolling direction

Such lancet combs have been observed previously and the phenomenon of reorientation of the lancet combs in an applied transverse field was reported by Hubert in [7].

In the present experiment it was found that reorientation of combs takes place not only with an altering transverse field component but also with a pure longitudinal (parallel to the R.D.) applied field. Moreover the value of the external field required to swap the orientation is small as can be seen from the small displacement of the basic domain walls in the upper grain. The process of reorientation seems to occur by a rapid jump from [1 1 1] oriented combs to ones oriented at [1 -1 1] direction.

The magnetoelastic energy is associated with internal "90°" domains. Taking into account the large number of such domains in the lower grain, it can be supposed that the magnetoelastic energy component is quite significant in this grain. During reorientation of lancet combs one large internal domain disintegrates and at the next moment a new lancet comb assembles with new internal domains oriented at 90° to the previous one, probably generating magnetostrictive pulses. The generation of such pulses needs to be confirmed by localised acoustic or EM measurements.

The phenomenon of lancet comb switching which occurs almost simultaneously within a large area of the grain can be seen in movie combSwitch.avi. This phenomenon was not just local but was observed in other misoriented grains in this and other samples. It is interesting that the "simultaneous switching" of large volumes is observed only in the high permeability steel with large grains, - the materials which have higher magnetostriction compared to that of conventional steel with smaller grains [8], [9]. However, research is required to confirm the assumed increase of magnetostriction as a result of lancet combs switching.

8.4.2 Dynamics of regular bar-like domain arrays in high permeability steel when a field is applied at 45 degree to the rolling direction

Samples, 3 cm x 3 cm square, of high permeability steel 30MOH [8] were cut at 45° to their rolling direction. As a result, a regular array of bar like domains was oriented along the diagonal of the sample. Using the same preparation procedures as described in Chapter 6 and the magnetising system reported in Chapter 7, magnetic flux was induced at 45° to the rolling direction. In practical applications such magnetisation conditions can

occur in the corners and T joints of transformer cores and can be responsible for additional losses [10].

Figure 8.6 shows a few instantaneous images from dynamic observations, carried out using a 0.5 Hz triangular excitation waveform, presented in file @45deg_to_RD_05Hz.avi.. As a triangular field waveform was applied, bar domain walls moved slowly at first (first image in figure 8.6) and then the domain pattern rapidly transformed into closure domains (second image in figure 8.6) leading to rapid surface saturation. The domain motion, when the field reverses, follows a similar pattern. Narrow spike domains on the surface nucleate, grow and then merge to form large bar-like domains. Boundaries of large bar domain walls move slowly until they split on the negative half-cycle of magnetisation.

Similar domains have been observed previously using stroboscopic imaging [11]. The phenomenon of non repeatability can be studied using a real time system (similar to that described in section 7.5) to help in understanding the nature of losses.

8.4.3 Dynamics of bar-like domain arrays when a grain oriented sample is subjected to bending stress.

Ideal bar domains can be distorted due to many factors, including deformation of the sheet. The high permeability sample described in section 7.4.2 was subjected to a force of 0.1 N perpendicular to the surface in the centre of the sample as illustrated in figure 8.7a. A little bending caused by the force was sufficient to change the anisotropy in the surface layer resulting in a change of easy axis of magnetisation. Because of this the bar domains transformed to the closure domains perpendicular to the rolling direction (the second image in figure 8.7a). After the load was released the stress-induced anisotropy disappeared and domains return to the original bar-like array (see the fourth image in figure 8.7a or movie StressPoint.avi). However, in some locations residual stresses remained.

Figure 8.7b shows some features of domain dynamics in the post-bent sample over a different area of view. In the static condition the domains exist with straight walls (first image). With application of a 0.5 Hz field, the walls move to stressed surface regions resulting in the formation of closure domains as in the third image in figure 8.7b.

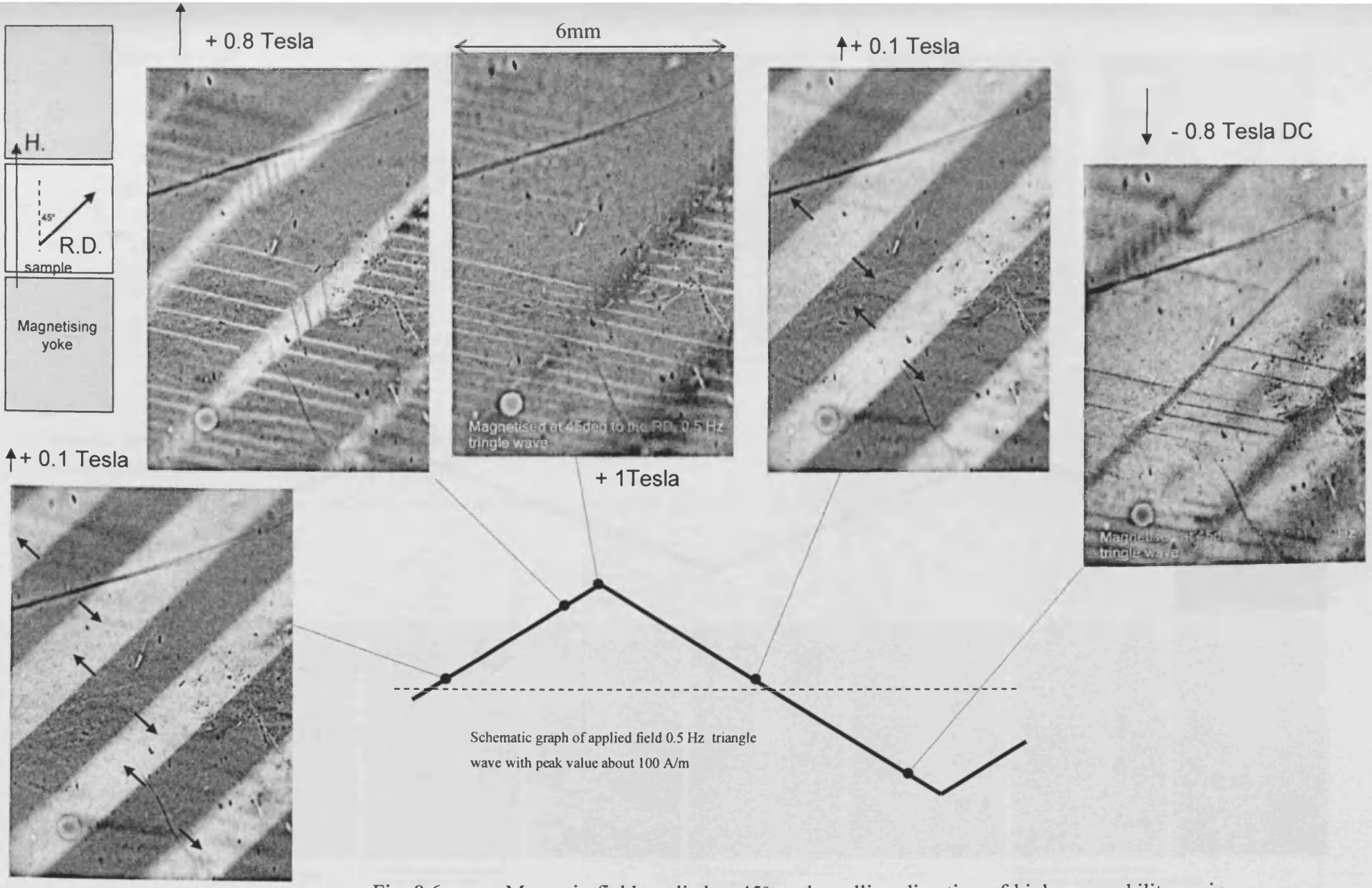

Fig. 8.6 Magnetic field applied at 45°to the rolling direction of high permeability grain oriented steel (30MOH grade). Arrows show direction of domain wall motion.

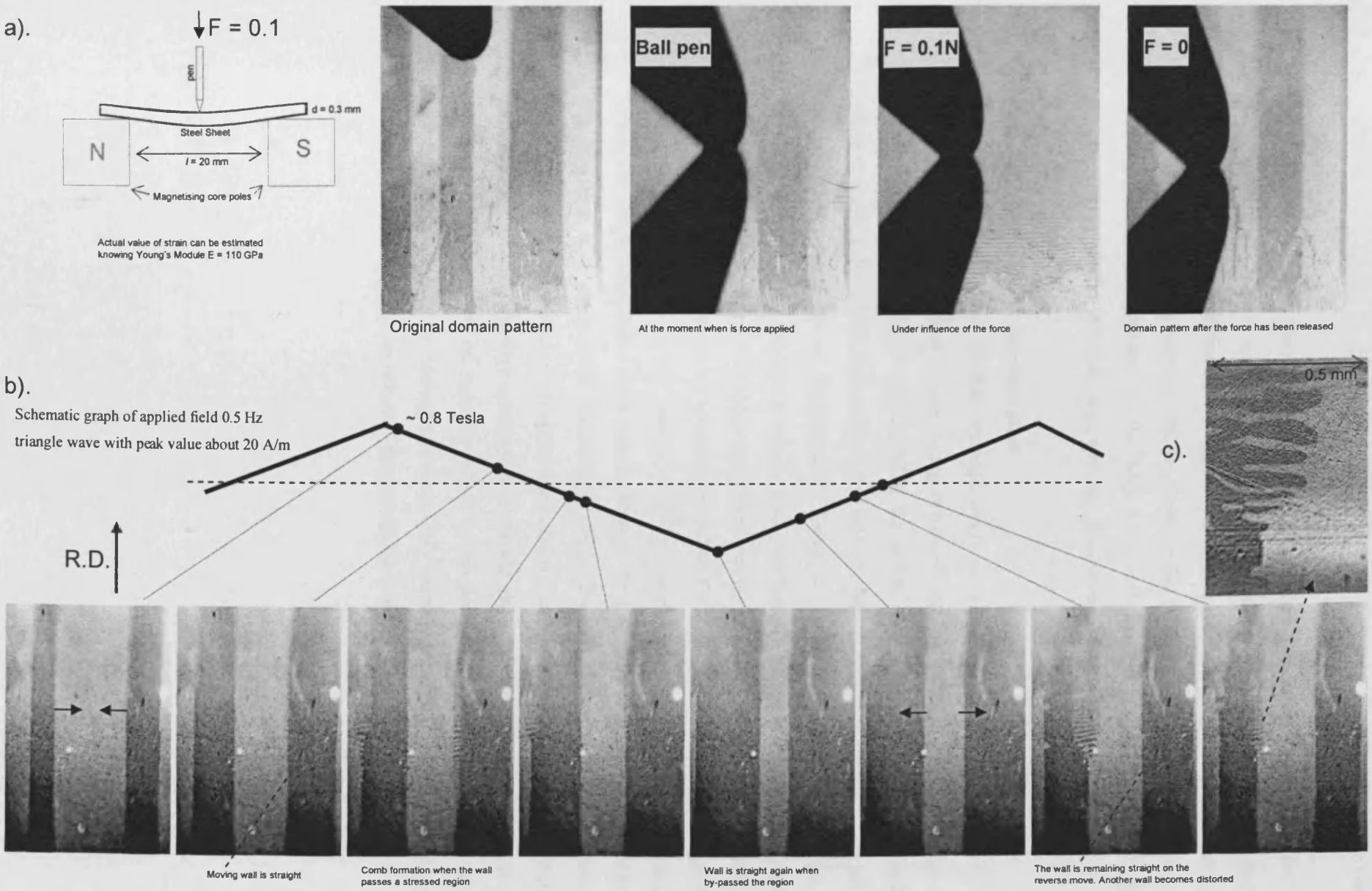

Fig. 8.7 a). Appearance of transverse domains on application of bend stress. b). Magnetisation reversal of the bar pattern with residual strains on the surface. c). Magnified view of comb pattern at the region with compressive strains.

After passing this area the domain walls become straight again. On reversing the field the stripe domains appear in a different location at another wall boundary (image 7, also see in movie StrSurf_02Hz5fpsR.avi). This phenomenon may be attributed to the combined effect of localised eddy currents and the skew profile of the basic 180° domain walls.

Domain observations in the bent sheet will help in the understanding of the processes in transformer cores with stressed laminations.

8.5 Cube textured oriented steel

Cube textured or double oriented steel – is a material whose grains are oriented with [001] directions close to the rolling direction and [010] directions close to the sheet transverse direction [12]. It has potential for use in motor cores and other applications when a rotating magnetic induction vector occurs. Square samples 3 cm x 3 cm and 0.5 mm thick were prepared as discussed in Chapter 6. Using the Neoark microscope with 45° attachment and 5x objective lens a chequered domain pattern as shown in figure 8.8 was observed in a sample immediately after annealing at 800 °C. When a small amplitude oscillating magnetic field was applied parallel to the rolling direction the domain walls oscillated as indicated by the arrows (also see movie cubex_640_0_25Hz_10fps3.avi). When the amplitude of the field was increased, the pattern changed to an irregular bar-like structure with some areas containing fir-tree domains. After the field was switched off the domains remained as irregular bars and did not return to the original chequered pattern even after cyclic demagnetisation at 50 Hz along various directions. This may be evidence of some form of memory effect which persists in the ferromagnetic domain structure even after cyclic demagnetisation. Only thermal treatment above the Curie point will return the sample to its original magnetostatic configuration.

8.6 Cobalt-iron alloys

In aeronautic applications, where weight saving is important, FeCo alloys are used in the cores instead of electrical steel [13]. FeCo alloys have a unique combination of magnetic properties including highest saturation magnetisation, high permeability, acceptable losses and a high Curie temperature. The latter make them exclusive materials for use in generators mounted co-axially inside gas turbine engines. Materials scientists are aiming to develop new materials which can operate at 500°C [14].

Samples, 3 cm x 3 cm of commercial grade Rotealloy 8 and Hyperco 50HS (both $Fe_{49}Co_{49}V_2$ composition) were selected for domain observation in order to test the performance of the system. They were cut, polished and annealed as detailed in section 6.2. The results in figure 8.9 (and movie CoFe_Rottoalloy_7mm_wide_02Hz10fps.avi) show well resolvable domains with an average width of 0.4 mm. The shape of domains is quite unusual for a crystalline material because curved walls are common for materials with weak anisotropy such as some amorphous ribbon. In observed FeCo alloy weak anisotropy can occur due to the manufacturing process (rapid quenching or alike). Another unexpected observation was that the grain boundaries were not visible. A similar domain structure was observed in Hyperco 50HS samples. Because of the large domains the low-magnification set-up (section 4.2) could be used with its relatively long working distance (5 – 10 cm) making possible future observation of domains on the surface of samples at temperatures up to 500°C. The good image contrast also makes high-speed dynamic observations possible using an intensified camera.

8.7 Amorphous ribbons

As-cast commercial 2605SC ($Fe_{81}B_{13.5}Si_{3.5}C_2$) amorphous ribbon was observed under high magnification (50x objective lens) using the longitudinal Kerr effect mode. Various domain patterns that exist in the sample are illustrated in figure 8.10a. The curved walls of the large domains appear to be the most mobile hence representing the major flux change during magnetisation in an external field. Dynamic observation of one such wall was carried out using the method described in section 7.4 and examples of the domains are shown in figure 8.10b to illustrate the non repeatable cycle-to-cycle motion of the wall (see movie Ribbon_nonrep_c3c10c15c16stop.avi with a stop-highlighting of

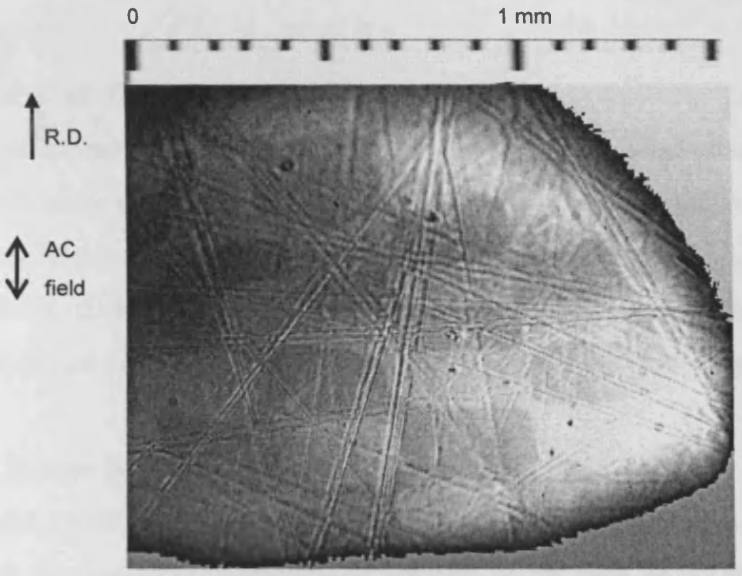

Fig. 8.8 Chess-board pattern in annealed double-oriented electrical steel at B = 0 and directions of oscillation of domain walls in applied AC field, $B_{peak} \sim 0.1T$

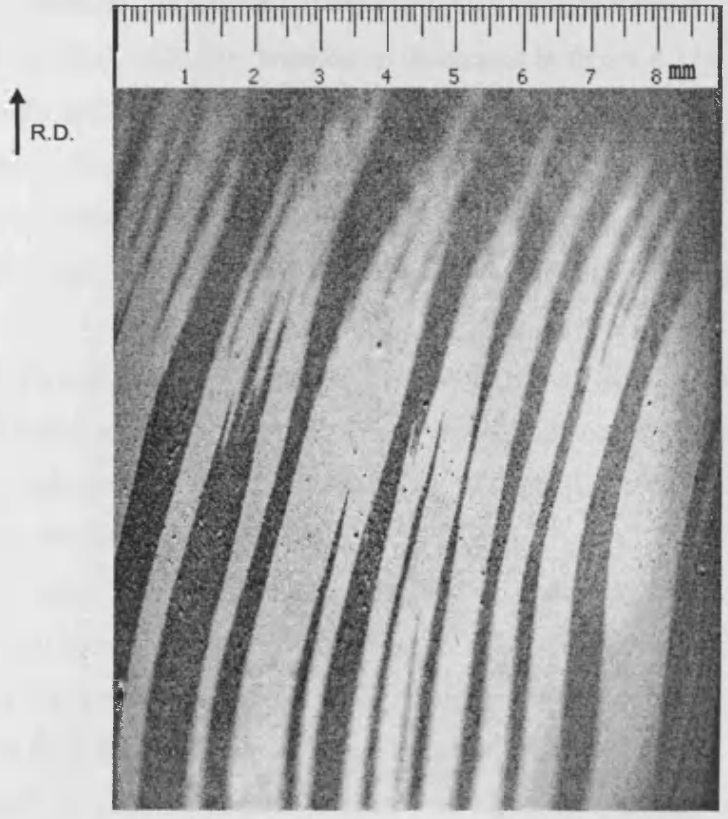

Fig. 8.9 Domain structure of Rotealloy 8 sample at arbitrary magnetisation conditions.

the wall position at the same time on the different cycles). In general, the non repeatability was higher that in GO steel [15]. Although a quantitative analysis of these domains is much more complex because of its irregularity and the variation of thickness roughly between 18 μm and 28 μm and conductivity of amorphous ribbon [16].

Refinement of the domains with increasing frequency of magnetisation was also noticed. The observed domain structures were similar to those reported by Flohrer at [17].

8.8 Cobalt ferrite (Co $Fe_{1.7}$ $Mn_{0.3}$ O_4)

Mn-doped cobalt ferrite is a novel high-magnetostrictive material which promises to be applicable for actuators and sensors because of its high permeability [18], [19]. Developers are now aiming to make cobalt ferrite with much higher permeability than terfenol [20].

A polycrystalline cylindrical ferrite sample, 11 mm in diameter and 9 mm long with an average grain size of 50 μm was prepared. The surface was mechanically polished as described in section 6.3. The sample was magnetised by the U-yoke, described in section 6.2.1, with iron brackets as illustrated in figure 8.11a.

Two domain patterns were distinguished. Figure 8.11a (and movie 320blb2.avi) presents domains with irregular 'blob' formation (denoted as pattern A) which is sensitive to the magnetisation field. A 2000 A/m peak value sinusoidal field at 0.5 Hz was applied. The 'blob' domains are seen to be pinned to surface defects and grain boundaries.

Figure 8.11b and movie 800str2.avi show another area of the sample where three grains contain stripe-like domain patterns. These domains (denoted as pattern B) are less sensitive to the magnetisation field. It is obvious that they are not affected by surface defects as much as the domains in pattern A.

Generally, when the sample was magnetised with the highest possible field, the majority of grains were observed to have some domain activity. Approximately (visually) 50% of them revealed pattern B, 25% revealed a more complex structure with large blobs, small branching domains or a superimposed A and B pattern. The other 25% did not show any domain wall activity but some changed intensity without distinct domain wall movement. The cause of invisible walls could be that the domain features

were smaller than the microscope resolution limit of 1 μm. Alternatively the grains may be in a single domain state which rotates with the applied magnetic field.

Visually, the changes in magnetisation patterns A and B are repeatable from cycle to cycle and they seem to be independent of frequency as is expected in low conductive material (below 1 kHz). Due to a small size of domains, only qualitative analysis is possible. For instance, coercivity, initial permeability and saturating field can be found from the observations [21].

During the domain observation occasional cracks were found in the sample which changed width by 2 μm during magnetisation reversal, see movie crack.avi. The opening and closing of the crack is attributed to the high magnetostriction of the sample. Knowing the diameter of the sample, the magnetostrictive constant can be found as diameter to crack width ratio, equals 1.8×10^{-4}. This value is comparable with magnetostrictive constant reported previously in [18], [19] being in the range of 10^{-4}.

8.9 Magnetic films

Vacuum deposited magnetic films usually have smooth surfaces eliminating the need for any surface preparation. Magnetic films can be produced with specific structures which can be easily modeled or simulated. In combination with simplicity of domain observation, magnetic films are often used as etalon samples for fundamental magnetic science [7]. In addition some films with weak anisotropy have very wide walls between domains (up to 3μm [7]). It is possible to study an internal structure of the domain walls with Kerr microscope.

Figure 8.12 illustrates two examples of domains in magnetic films. Figure 8.12a shows the domains in a 10 μm thick Fe-based film with in-plane anisotropy (deposited onto a glass substrate by vacuum evaporation). Figure 8.12b and movie GarnetSat1024.avi present typical maze domains in a film with perpendicular anisotropy (yttrium-iron garnet film of composition $Y_{2.35}Bi_{0.65}Fe_5O_{12}$, 2.62 μm thick, epitaxially grown on a garnet substrate). The domain wall width in these magnetic films was in the range of tenths of nanometers, so it was not possible to resolve anything inside the walls.

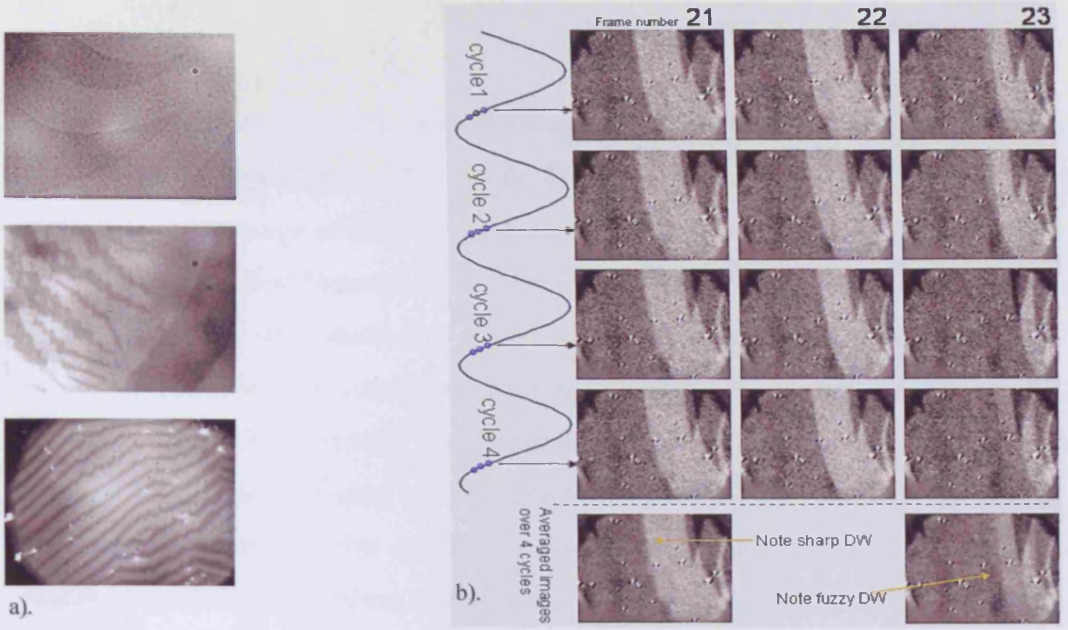

Fig. 8.10 a). Various patterns in 2605SC amorphous ribbon at arbitrary B value.
b). Non repeatable wall motion in 2605SC amorphous ribbon.

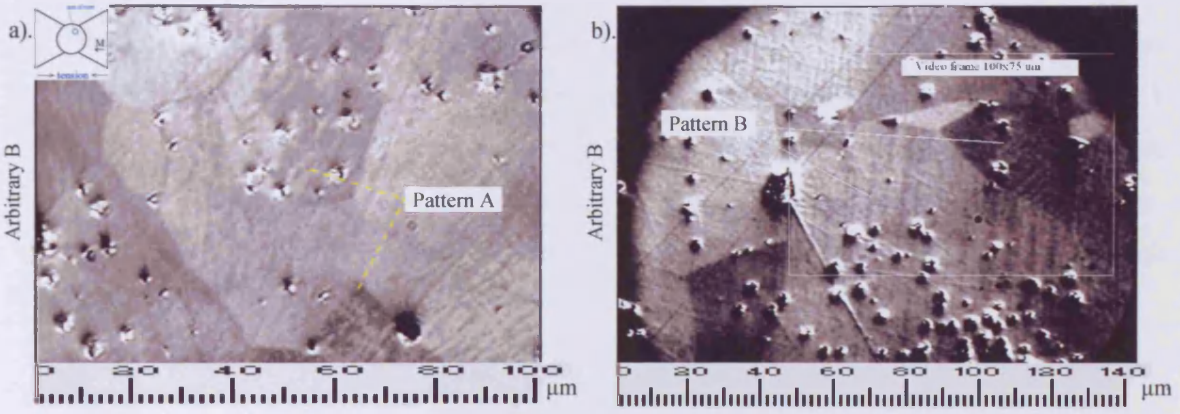

Fig. 8.11 Domain patterns in the Co $Fe_{1.7}$ $Mn_{0.3}$ O_4 cobalt ferrite at arbitrary B.

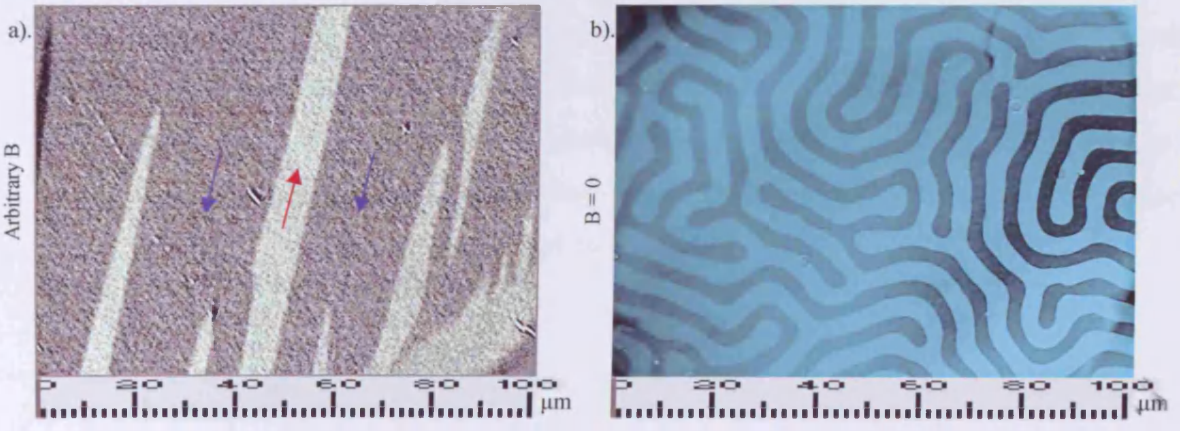

Fig. 8.12 Domain patterns in the thin films with in-plane (a) and perpendicular (b) easy axis of magnetisation.

8.10 General conclusions on domain viewing in various materials

The examples given illustrate the capability of the system for imaging domains in materials with a range of different structures. This is summarised in table 8.1.

The superior features of the optical equipment (including high light intensity, prism polarisers and strain-free long working distance lenses) make it possible to overcome unfavourable conditions such as distorted surfaces (in ribbons and wires) or poor reflectivity (in ferrites). The achieved good optical contrast makes it possible to perform high-speed imaging with an intensified camera. The Lambert Instrument HCC-1000 camera offers precise synchronisation with the magnetising system which in turn makes it possible to achieve quantitative real time imaging such as that described in Chapter 7.

Values of $\mathbf{t_{exp}}$ in table 8.1 are given for the continuous light source supplied with the system. $\mathbf{t_{exp}}$ can be much shorter when a pulsed light source is used. The Chadwick Helmuth pulsed light source (see section 5.8) can produce 0.1 ms light pulses with about 300 W light power. This makes it possible to perform stroboscopic observations at 1.8 kHz magnetisation with external gating of the intensifier at $\mathbf{t_{exp}} \approx 0.05$ ms. Further increase in observation speed and contrast of images may be achieved if, for instance, a pulsed laser is used as a light source, but the maximum frame rate cannot be extended above 1825 fps.

Quantitative analysis of the observed images requires a comprehensive theoretical model of the structure and automatic wall recognition software outlined in sections 6.7, which (although not strictly required) saves much time and can be more precise compared to manual measurement.

For many examples presented, quantitative domain theory is not available. In such cases the observation of the domains can show only the overall surface magnetisation. Analysing the domain images and magnetisation conditions make it possible to estimate coercivity and saturation fields. Also easy directions of magnetisation can be determined from a domain's response to fields applied at different angles.

	Field required, A/m		Magnetising system used:	Typical size of features		Optical arrangement			Imaging	
	To start motion, ~H_{coer}	To Saturate surface		Grains μm	Domains width μm	mode	Objective	Field of view μm	Shortest * t_{exp} ms	Fastest frame rate fps
GO steel	7-20	100	Electromagnet Helmhotz coils	0.5 – 20 mm	0.1 – 5 mm	In-plane	X20 X5 at 45 deg Low Magn	280 (1..3x1.7mm) 4mm-18mm	2 0.5 0.5	461 1825 1825
NO steel	30-50	300	Electromagnet Helmhotz coils	10-70	1-50	In-plane /polar	X50 X20	140 280	20 20	50 50
Cubex oriented		250	Electromagnet Helmhotz coils	0.1-1	0.1-2 mm & fir-trees	In-plane	X50 X20 X5 at 45 deg Low Magn	140 280 (1..3x1.7mm) 4mm-18mm	20 20 2 2	50 50 461 461
Co Fe alloys μ-metals	20-140	1000	Electromagnet	10-70	1-50	In-plane	X50 X20 X5 at 45 deg Low Magn	140 280 (1..3x1.7mm) 4mm-18mm	10 20 0.5 0.5	100 50 1825 1825
Amorphous ribbon	5-8		Electromagnet Helmhotz coils		5 μm -2 mm	In-plane /polar	X50 X20 X5 at 45 deg	140 280 (1..3x1.7mm)	2 5 0.5	461 200 1825
Wire	5-10		Helmhotz coils current through		5 μm – 0.2 mm	In-plane	X50 X20	140 280	50 50	20 20
Ferrites	100	10000	Electromagnet	10 – 50	2 – 30 μm	In-plane /polar	X50 X20 X5	140 280 1..3mm	20 20 20	50 50 50
Films with in-plane anisotropy	From 10		Electromagnet Helmhotz coils current through		2 μm – 5 mm	In-plane /polar	X50 X20 X5 at 45 deg	140 280 (1..3x1.7mm)	2 20 2	461 50 461
Films with perpendicular vector	From 10	200	Helmholtz coils Perpendicular coil		2-20 μm	polar	X50 X20 X5	140 280 1..3mm	0.5 0.5 0.5	1825 1825 1825

Table 8.1

* Values of t_{exp} are given for the continuous light source supplied with the system. t_{exp} can be much shorter when pulse light source is used, but the maximum frame rate cannot be extended above 1825 fps.

8.11 References of chapter 8

1. Yoon G. G., Park K. M., Moon S. P., Kweon D. J. and Heo N. H., Surface Oxidation and Magnetic Induction in Thin-Gauged 3 % Si-Fe, Journal of the Korean Physical Society, 43, 6, p1067, (2003).
2. Geiger A.L., Surface oxidation of non-oriented silicon-aluminum electrical steels during annealing, J. Appl. Phys., 49, 3, p2040, (1978).
3. Jiles D., Introduction to magnetism and magnetic materials, Chapman and Hall (1991).
4. Schafer R., Schinnerling S. Bulk domain analysis in FeSi-crystals, J. Magn. Magn. Mater., 215-216, p140, (2000).
5. Khanlou A., Static and dynamic domain observations studying the effect of adhesive on G.O. 3%SiFe domain structures, Report in Wolfson Centre. (1996).
6. Beckley P., Basic properties of grain oriented electro-technical steels, Report EUR 8270 EN, British Steel Corporation, (1983).
7. Hubert A. and Schafer R., Magnetic domains, Springer (1998).
8. Beckley P., Electrical steels: a handbook for producers and users, European Electrical Steels, (2000).
9. Moses A.J., Electrical steels: past, present and future developments, IEE Proc., 137, Pt. A, 5, p233, (1990).
10. Moses A.J., Prediction of core losses of three phase transformers from estimation of the components contributing to the building factor, J. Magn. Magn. Mater., 254-255, p615, (2003).
11. Dragoshanskiy, Y..N,. Zaykova, V.A., Tiunov, V.F., Phys. Met. Metal, 39, p61, (1975).
12. United States Patent 5370748, Process for manufacturing double oriented electrical steel sheet having high magnetic flux density, (1994).
13. Sourmail T., Near equiatomic FeCo alloys. Constitution, mechanical and magnetic properties. Progress in Material Science 50, p816, (2005).
14. Godfrey S., Development in fibre-reinforced soft magnetic metal-matrix composite materials, UK Magnetic Society Seminar, (2006).
15. Moses A.J., Williams P.I., Hoshtanar O.A., A Novel Instrument for Real Time Dynamic Domain Observation in Bulk and Micromagnetic Materials, IEEE Trans. Magn, 41, 10, p3736, (2005).
16. Maricic A., Minic D.M., Zak T., Influence of the Changes of Free Electron Density on Electrical and Magnetic Properties of the Co70Fe5Si10B15 Amorphous Alloy, Science of Sintering, 36, p197, (2004).

17. Flohrer S., Schafer R., McCord J., Roth S. and Schultz L., Dynamic magnetization process in nanocrystalline tape wound cores, Vortrag am Instituto Elettrotecnico Nazionale Galileo Ferraris, Turin, Italien, 2.5.05 (2005).

18. Melikhov Y., Snyder J.E., Jiles D.C., Ring A.P., Paulsen J.A., Lo C.C.H, Dennis K.W., Temperature dependence of magnetic anisotropy in Mn-substituted cobalt ferrite, J. Appl. Phys., 99, p08R102, (2006).

19. Paulsen J., A., Lo C. C. H., Jiles D.C., Study of the Curie temperature of cobalt ferrite based composites for stress sensor applications, IEEE Trans. Magn, 39, 5, p3316, (2003).

20. Gibbs M.R.J., Modern Trends in Magnetostriction: Study and Application, Kluwer, (2001).Engdahl G., Mayergoyz I.D., Handbook of Giant Magnetostrictive Materials, Academic Press, New-York, (2000).

22. Globus A., Influence des dimensions des parois sur la permabilite initiale, C.R. Acad. Sci., 255, p1709, (1962).

CHAPTER 9 EXAMINATION OF ELECTRICAL STEEL USING A MAGNETIC INDICATOR FILM

9.1 Principle of operation

A magnetic indicator film is a thin layer of soft magnetic material deposited onto a transparent substrate. Sometimes an additional reflective layer is incorporated to achieve greater light sensitivity (see figure 9.1a). Such a magnetic film utilizes the Faraday effect to map stray magnetic fields above a surface. Some successful results have been previously achieved on superconductors [1], hard magnetic materials [2], magnetic records and magnetic security prints [3] and in NDT applications [4]. Also, indication films have been used for fast dynamic domain observation on microdevices such as recording heads [5] with nanoseconds time resolution. The last example demonstrates that the technique might be applicable for observing moving domains in electrical steels. Moreover, the technique can be sensitive enough to observe a stray field at some distance above the surface of a sample. [6]. This provides a possibility of seeing moving domains under the coating of grain-oriented steel without any surface preparation so the true domains structure in commercial GO steel sheets can be observed. The second advantage of the technique is that rare earth magnetic films have high magneto-optic rotation (12000 deg/cm) and is transparent, therefore, contrast of images should be much higher than in steel (which has a value of ~50000 deg/cm, but the light penetration depth is only 20 nm). Accordingly, the images can be obtained with much higher contrast and the recording frame rate can be extended.

9.2 Domain observation with indicating film

A 2.62 μm thick perpendicular-anisotropy yttrium-iron garnet film of composition $Y_{2.35}Bi_{0.65}Fe_5O_{12}$, on a 250 μm thick garnet substrate was used. It was epitaxially grown by Scientific Research Company "Carat" Lviv, Ukraine and donated by its director Dr. M. Syvorotka. The film was coated with a reflecting layer of 10nm Cr + 70nm Au as shown in figure 9.1a.

The microscope described in chapter 5 was used in polar mode with the x5 lens. When the indicator was not in contact with a steel sample, the reflected Double Faraday effect revealed high contrast maze domains with an average width of 14 μm. This width was consistent across the whole surface as shown in figure 9.1c. When a field was applied perpendicular to the surface, the domains change in width as

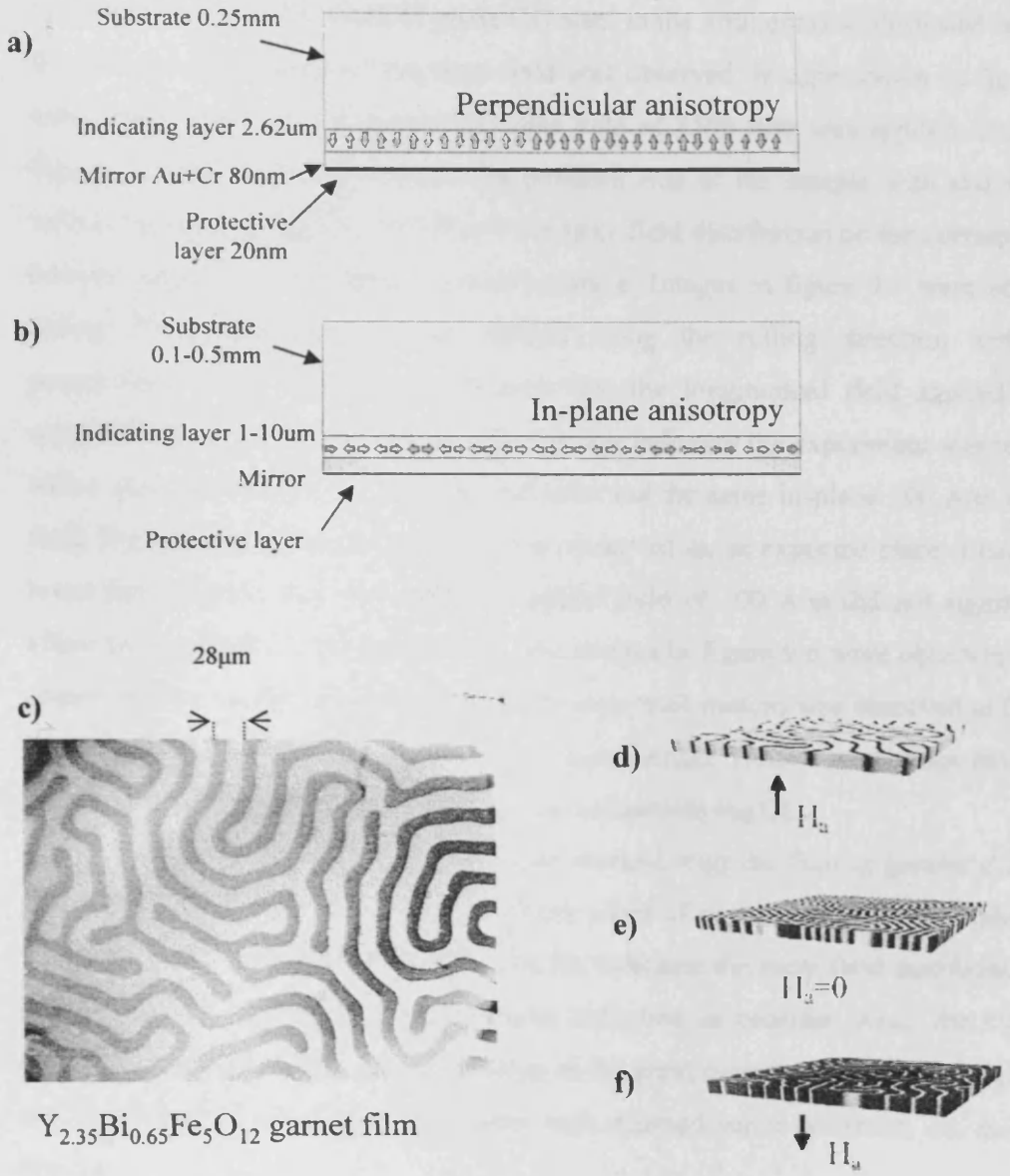

Fig.9.1 Indicator film with (a) perpendicular and (b) in-plane anisotropy. (c) Typical maze domain structure in the films with perpendicular anisotropy and (d, e, f) its reaction to applied perpendicular field.

illustrated in figures 9.1 d, e, f. All domain boundaries disappear when the film reaches its saturation at H = 3800 A/m, this field value was measured with a Hall probe and an F.W. Bell 9950 gaussmeter. The indicator was placed on the upper surface of a sample of 30MOH grade GO steel in the arrangement illustrated in figure 9.2 and the distribution of the stray field was observed. Images shown in figure 9.3 were observed when a perpendicular bias field of 3500 A/m was applied. Images in figures 9.4 a,b were observed on the polished side of the sample with and without indicating film, and figure 9.4c shows the stray field distribution on the corresponding bottom, unprepared (phosphate coated) surface. Images in figure 9.5 were observed during DC magnetising of the sample along the rolling direction without a perpendicular bias. In order to confirm that the longitudinal field applied to the sample does not have a significant effect on the indicator the experiment was repeated with a sheet of aluminum under the indicator and the same in-plane 100 A/m applied field. No modulation in the indicator was observed in, as expected since it has much lower permeability than the steel (an applied field of 100 A/m did not significantly affect the indicator domain structure). The images in figure 9.6 were observed on the coated surface of the same sample. The domain wall motion was observed at 0.5 and 50 Hz at 0.20, 0.25 and 0.60 Tesla peak magnetisation. These observations have been recorded as movie files and included on the accompanying CD.

The indicating film technique also worked with the film at greater distances above the sample surface. When a 10 thick sheet of paper was placed in addition to ~10 μm coating between the sample and the indicator the stray field distribution was still observable although there was some reduction in contrast. Also, the indicator showed very clear images of flux leakage at the grain boundary when the sample was AC magnetised. No domains were seen with doubled paper thickness, i.e. at 20 μm distance.

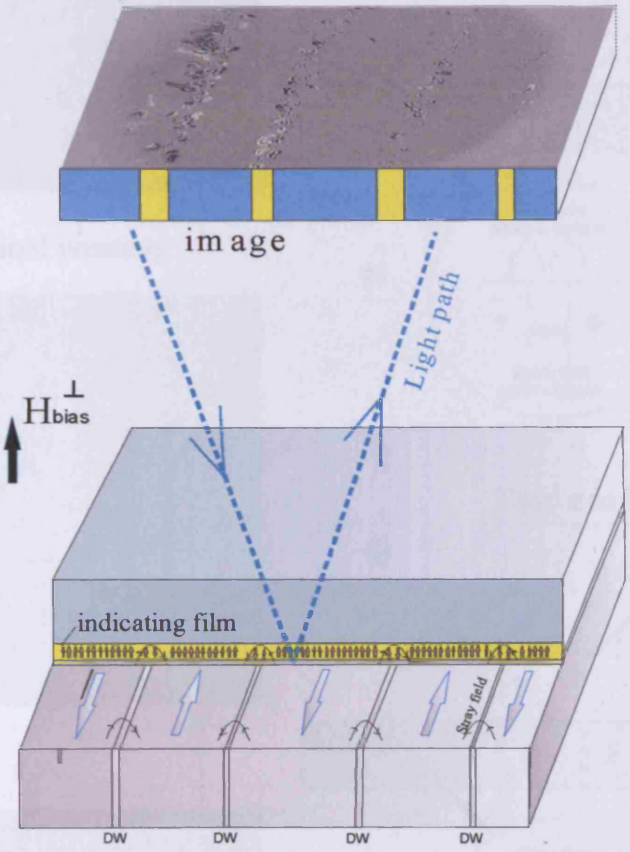

Sample of grain oriented steel with bar domains

Fig. 9.2 The arrangement used to observe stray field above a sample of grain oriented steel.

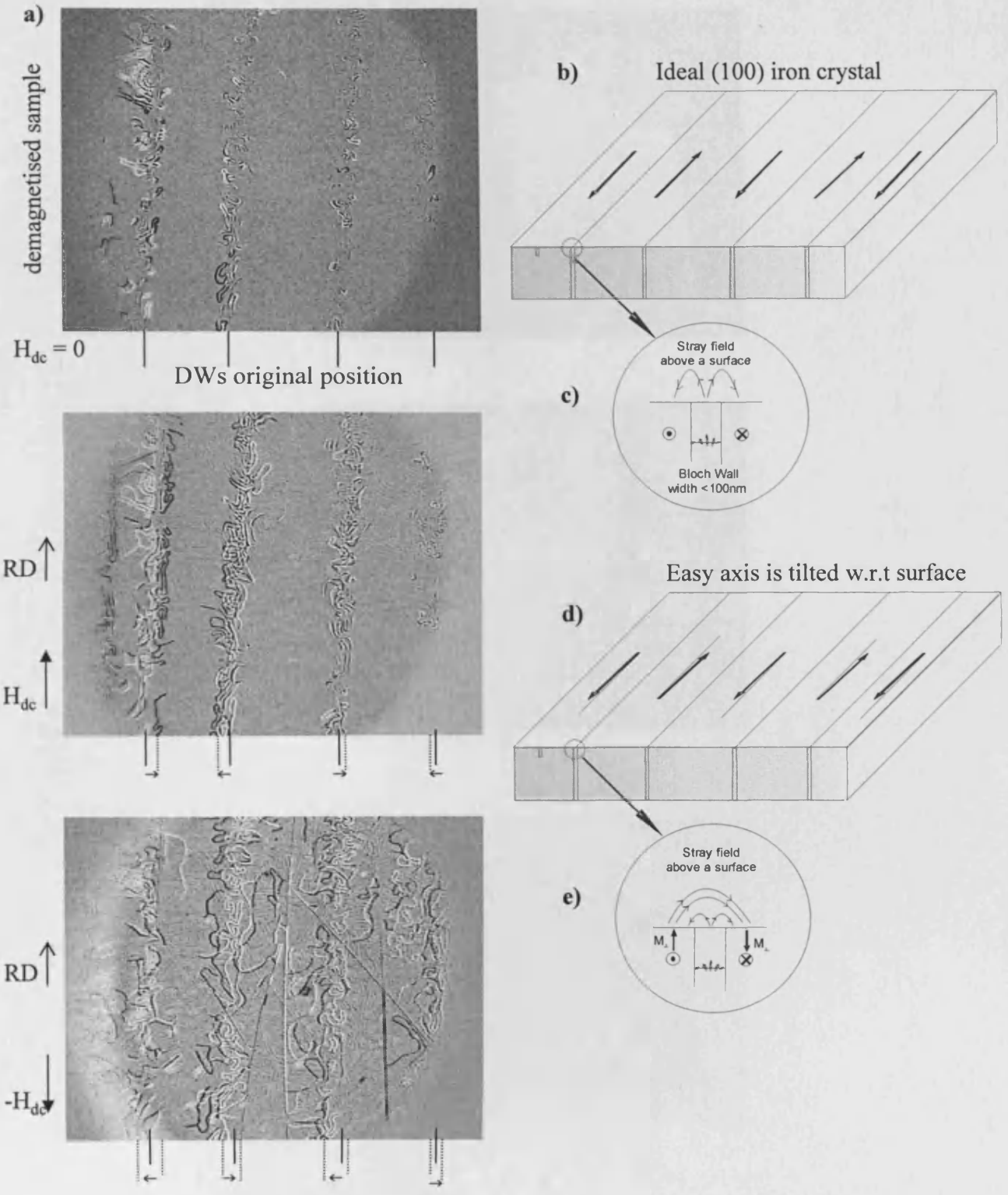

Fig.9.3 (a) Observation of bar domains with perpendicular biased indicating film. Magnetisation vector (b) and stray field (c) above a sample in ideally oriented and (d, e) misoriented grains of Goss-textured steel.

a).

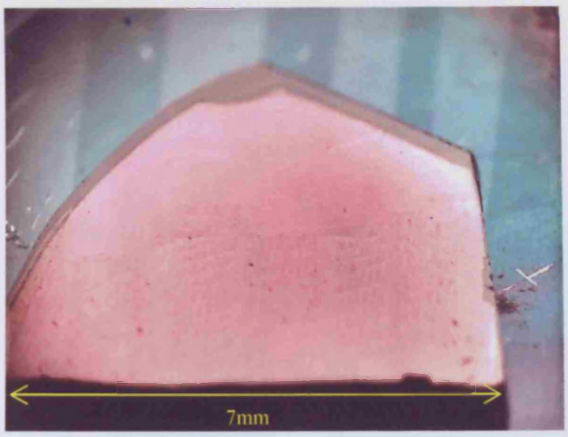

Indicating film is On

b).

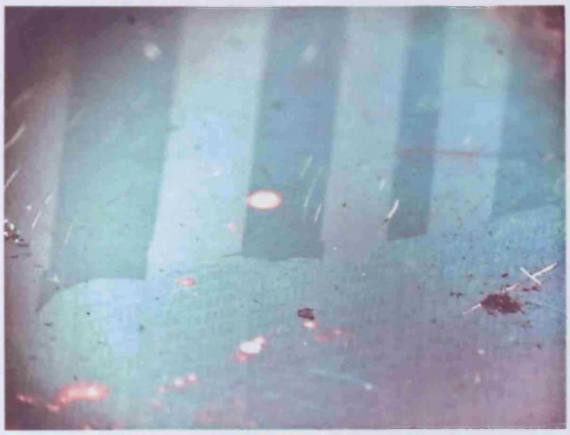

Indicating film is Off

c).

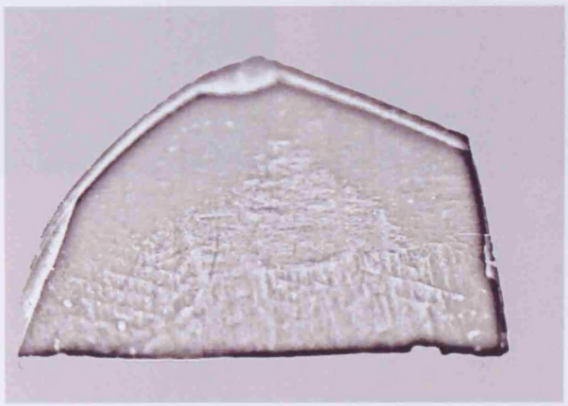

Fig.9.4 (a) Observation of domains in the GO sample with the non-biased indication film. (b) Direct Kerr image of the domains in the same area. (c). Image of the coated surface of the sample in the same are.

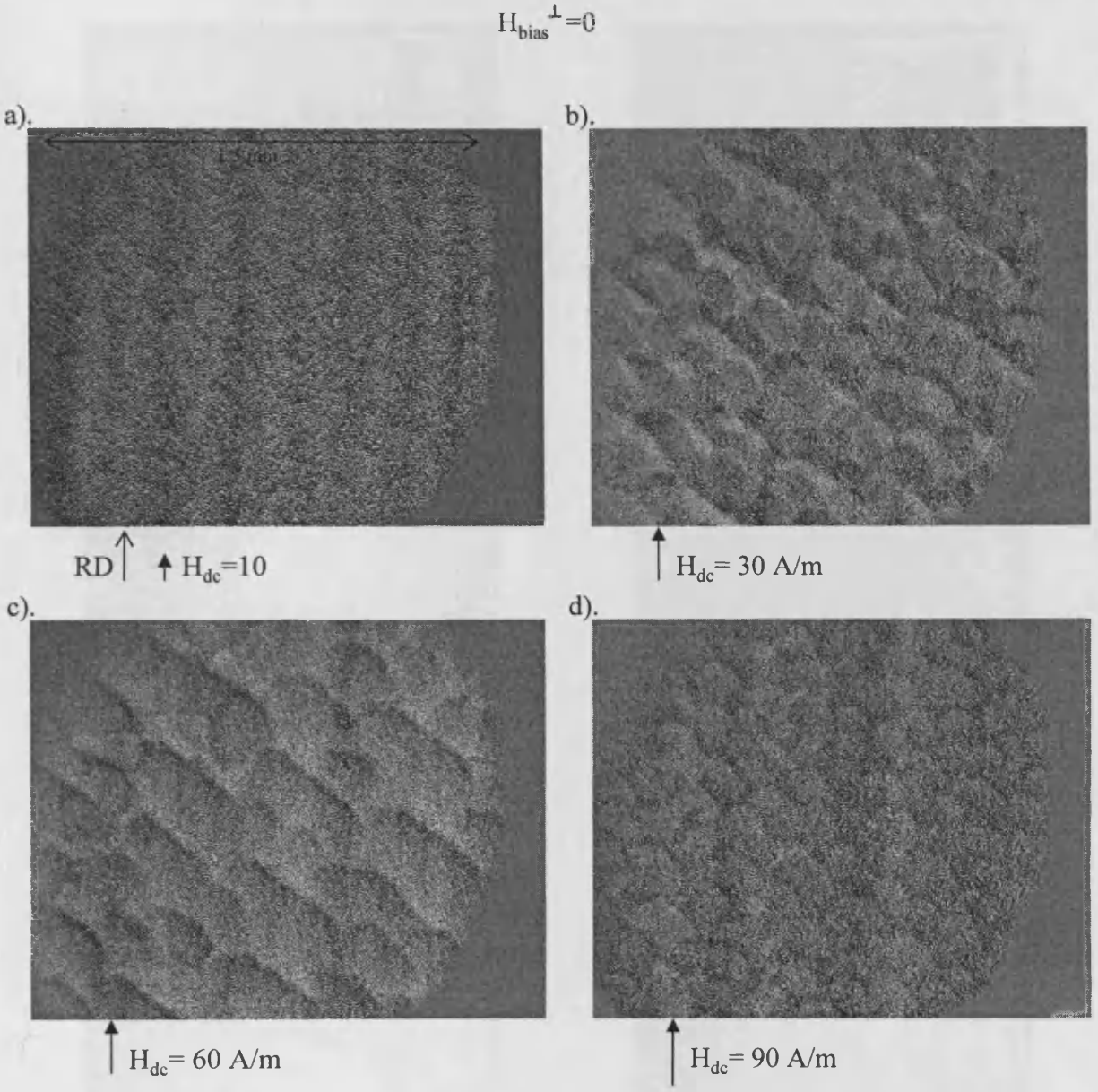

Fig.9.5 Observation of domains in the GO sample with the non-biased indication film. With DC field applied to the sample along the rolling direction, of (a) 10 A/m, (b) 30 A/m, (c) 60 A/m and (d) 90 A/m.

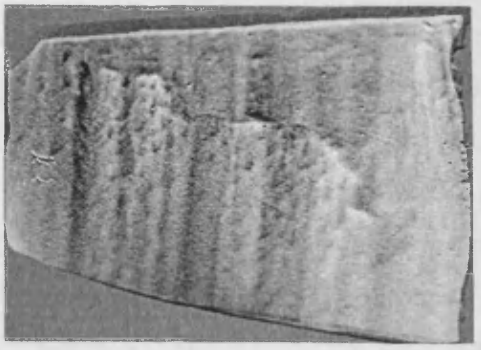

Demagnetised

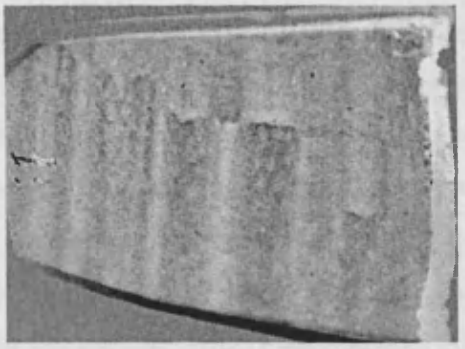

At magnetisation 0.8 T along RD

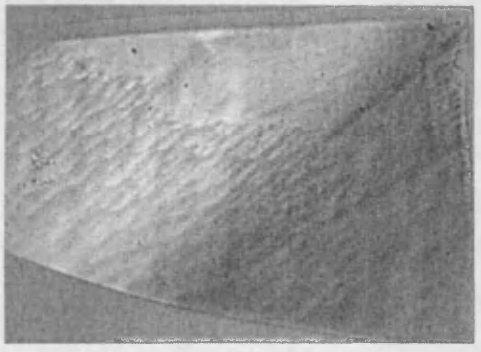

At magnetisation 1.6 T along RD

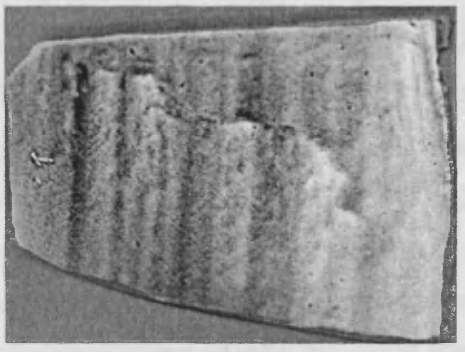

Remanent state

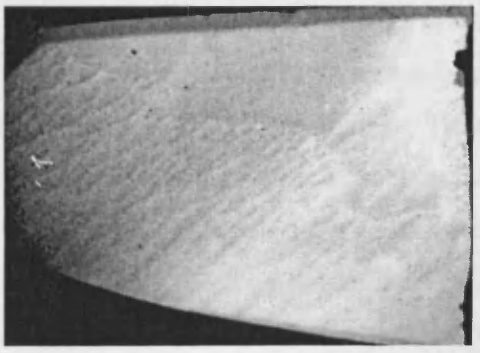

At magnetisation -1.6 T along RD

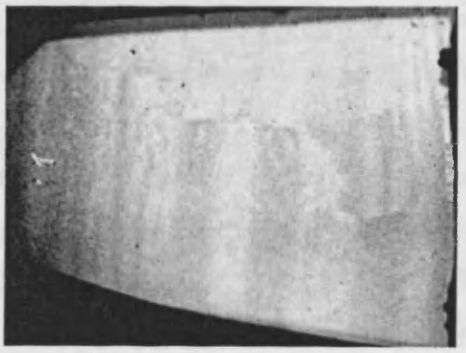

Negative remanent state

Fig.9.6 Domain imaging of the coated, unprepared sample of high permeability GO steel with indicating film.

9.3 Discussion and conclusions

A change in direction of the magnetisation in a Bloch Wall takes place gradually over many atomic planes, as illustrated in figure 9.3c. At the centre of the Bloch Wall the magnetisation vector is perpendicular to the surface of the sample hence it produces a stray field at the sample surface. The width of walls in GO steel is ~ 40 nm (or 160 atomic layers) [7], hence a field from such narrow regions does not extend far and is unlikely to affect the indicator located a few micrometers above the surface. In addition the size of the region is far below the limits of optical resolution. Nevertheless, domain-like pictures of the stray field above the sample are observed, which is confirmed by the Kerr image shown in figures 9.3a, 9.4a. This is due to the fact that even in high permeability GO steel, grains are slightly misoriented with respect to the surface. Even so, when the easy axis is at an angle of 1° from the plane of the surface (figure 9.3d), the perpendicular component of magnetisation vector $M_{\perp} = M_s \sin(1^{\circ})$ is 35 mT, which is a enough to produce stray field. Moreover $M_{\perp}$ components are antiparallel in the neighbouring bar domains, consequently a flux closing stray field above the surface extends over a much longer distance than in the case of an ideally (100) oriented sample, as shown in figure 9.3e. The observed image of a demagnetised sample figures 9.3a is comparable with those images obtained by scanning using a MR sensor [8]. They have bar-like shadows with fuzzy boundaries. Images in figure 9.3a were taken with a superimposed perpendicular bias field that highlights locations where stray field opposing to the bias field. Motion of 180° walls stimulated by applying a small field (0.1 Hz, 8 A/m peak) along the rolling direction of the sample was observed by the movement of a *decoration* on the indicator film which followed the position of the walls on the surface of the sample. However because of the indicator's own hysteresis, the *decoration* due to previous stray fields did not vanished completely. Thus a moving wall leaves a trace at previous points along its path as shown in the second and third images in figure 9.3a. Such traces can be erased by applying a higher bias field for a short time. This results in the image becoming clear again like the first image in figure 9.3a. Dynamic motion of the walls can be recorded continuously with "reset" pulses applied prior to every image acquisition.

As illustrated in section 2.3, lancet closure domains are very common in commercial steel samples. The lancet domains in the sample of 30MOH steel described in section 8.4.1 are clearly visible using the indicating film as shown in

figure 9.4a. The domains visualised with the indicating film are very similar to those visualised with the normal Kerr method, as shown in figure 9.4b. On the coated side of the sample, in the same area, a similar image was observed, figure 9.4c, but it is blurred because of the increased distance due to the presence of the ~10 μm coating. Also some non-uniform features were superimposed on the image, most likely from the surface roughness (under the coating). A boundary between the grains is also visible due to the grain-to-grain flux leakage.

Dynamic observations with the indicating film during magnetisation along the rolling direction (without perpendicular bias) have revealed some differences in the magnetisation reversal processes in the coated and uncoated samples. In the uncoated sample, the wide bar-like domain walls moved across the sample as demonstrated in section 7.5. However the domains in the coated sample remained as parallel bars only at low flux density (below 0.8 T). At higher flux density the regular bar domains become eroded by supplementary structures as shown in figure 9.5 b, c, d, figure 9.6 and the movie file 'Coated_Barrs_02Hz_with_Suplems2.avi'.

Such unusual patterns were observed both at 10Hz and under DC magnetisation, hence they are not an eddy current effect. This unusual kind of pattern was observed consistently in a number of 30MOH, 27MJH and 27M4 samples.

A possible explanation of these patterns may be the existence of uncompensated strains in the sheet from the top to bottom coatings and the effect of surface roughness on the emergence of the flux closure structures, but more research is necessary to confirm this.

The images shown in this chapter demonstrate the unique capabilities of the magnetic indicator to visualise the domains under a coating of unprepared grain-oriented electrical steel. Although the indicating film used here was not specified for use with electrical steel, the obtained images are of printable quality. With the development of indicators specifically for domain observation in steel the quality of the images and capability of the method can be improved.

9.4 References of chapter 9

1. Gaevski M.E., Galperin Y.M., Karmachenko S.F., Magneto-optical study of magnetic-flux penetration into a current-carrying high-temperature-superconductor strip, Physical Review B, 59, 14, p9655, (1999).
2. Grechishkin R., Goosev M., Ilyashenko S.E., High-resolution sensitive magneto-optic ferrite-garnet films with planar anisotropy, J Magn. Magn. Mater, 157/158, p305, (1996).
3. Trouilloud P.L., Patek B., Argyle B.E., Methods for wide-field Kerr imaging of small magnetic devices, IEEE Trans. Magn, 30, 6, p4494, (1994).
4. Lee J., Lee H., Shoji T., Minkov D., Application of Magneto-optical Method for Inspection of the Internal Surface of a Tube, NDT.net, 4, 8, (1999).
5. Elezzabi A.Y., Freeman M.R., Ultrafast Magneto-optic sampling of picosecond current pulses, Appl. Phys. Lett., 68, 25, p3547, (1996).
6. Lee J.G., Govorkov S.A., Arrott A.S., Iron whisker domain patterns imaged by garnet films, J. Appl. Phys. 79, 8, p6051, (1996).
7. Jiles D., Magnetism and Magnetic Materials, Chapman and Hall, New York (1991).
8. So M.H., Nicholson P.I., Meydan T., Moses A.J., Magnetic domain imaging in coated silicon-iron using magnetoresistive sensors, IEEE Trans. Magn, 31, p3372, (1995).
9. Schäfer H, Calculation of the surface stray field and the demagnetizing field of a g.o. SiFe sheet caused by a misoriented grain, Phys. Scr. 39, p531, (1989).

APPENDIX 1 PUBLISHED PAPERS

A Novel Instrument for Real-Time Dynamic Domain Observation in Bulk and Micromagnetic Materials

Anthony J. Moses, Paul I. Williams, and Oleksandr A. Hoshtanar

Wolfson Centre for Magnetics Technology, Cardiff School of Engineering, Cardiff, CF24 3AA, U.K.

Dynamic domain observations have been made using a high-magnification Kerr microscope in combination with a high-speed light-intensified CMOS camera. Results have demonstrated nonrepeatable domain wall motion in electrical steel and amorphous ribbon at 1- and 50-Hz magnetizing frequencies.

Index Terms—**Amorphous ribbon, electrical steel, magnetic domains, magneto-optic Kerr microscopy.**

I. Introduction

OBSERVATION of domains on the surface of soft magnetic materials magnetized under ac conditions have usually been carried out by stroboscopic Kerr magneto-optic methods previously [1], [2]. Such studies have helped establish the effect of magnetizing frequency, sample thickness, grain size, etc., on losses in electrical steels and other soft magnetic alloys. This in turn has helped material producers identify means of reducing losses which, in electrical steels in particular, have a major environmental impact [3].

Losses are conveniently analyzed into hysteresis, classical eddy current, and excess loss components. The excess loss is believed to be partially due to nonrepeatable domain wall motion from cycle to cycle or to nonuniform wall mobility from grain to grain. In conventional stroboscopic methods wall position is effectively averaged over a large number of magnetizing cycles, so these effects, if they occur, cannot be detected.

This paper outlines the design and specification of a Kerr magneto-optic system which can be used to observe instantaneous positions of domain walls in a wide range of soft magnetic materials magnetized at power frequencies. Examples of its use to observe dynamic wall motion in electrical steel and amorphous ribbon are shown to illustrate the versatility of the system.

II. Experimental

A. High-Magnification Dynamic Domain Observation System

Fig. 1 shows a schematic diagram of the measurement system. A high-pressure mercury lamp is the light source in a Neoark BH-780-IP polarizing microscope. Glan Thomson prisms with a 5×10^{-4} extinction ratio and ultra long working distance objective lens with ×50 magnification enables high-resolution (1 μm) and high-contrast observations on various samples. Depending on the mode of operation and the material being studied, parallel or perpendicularly magnetized surface domains can be observed. An additional wide field attachment has been added

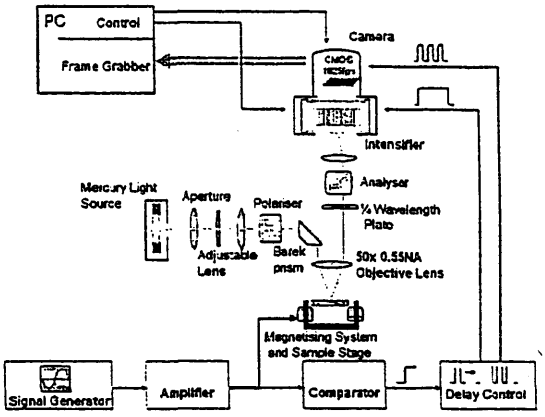

Fig. 1. High-magnification observation system.

which enables observation with lower magnification lenses (i.e., ×5 objectives). In this case the sample is oriented at a 45° angle relative to the incident light which is in turn reflected back into the objective lens via a mirror. The field of view with this setup is approximately 1.2 mm × 1.7 mm. Images are recorded using a high-speed intensified camera (HICAM) with low light sensitivity (646 μA/Lm) and high-speed image grabbing (1825 fps). This enables dynamic observation of domain wall motion to be recorded at frequencies up to 50 Hz. The electronic system consists of a function generator, an amplifier that provides a current for the magnetizing coils, and a comparator that generates a step signal at the moment when the current in the coil passes through zero from negative to positive current. The step signal is used as a reference for the delay generator which generates triggering pulses for the camera and intensifier. The variable time of delay may be controlled in the range 0–100 ms for both independent triggering channels. The error in triggering at 50 Hz was less than ±10 μs. One-megapixel resolution images are possible, which is sufficient for precise wall position measurement. Onboard camera memory of 512 MB is able to store multiple sequences of images with different settings triggered at different times. Time of exposure, frame rate, number of images in the series, and resolution of the camera as well as the gain of the

Digital Object Identifier 10.1109/TMAG.2005.854924

0018-9464/$20.00 © 2005 IEEE

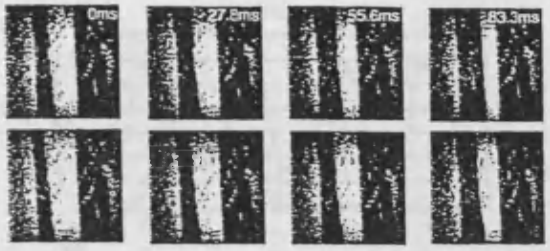

Fig. 2. Comparison of images (1.2 mm × 1.7 mm) captured at identical points on two consecutive magnetizing cycles (1 Hz) for GO steel.

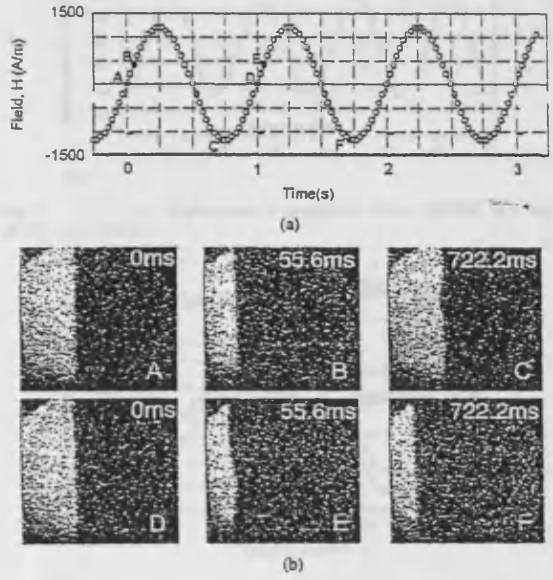

Fig. 3. (a) Magnetizing waveform showing the moment of image capture. (b) Comparison of images (140 μm × 140 μm) captured at identical points on two consecutive magnetizing cycles (1 Hz) for GO steel.

intensifier are set externally by personal computer control software. Image processing for contrast enhancement was carried out on raw images using background subtraction techniques followed by histogram equalization. In the case of 50-Hz images, additional morphological processing (filtering) was also used.

B. Examples of Domain Observation

A sequence of images captured at 1-Hz magnetization is shown in Fig. 2. The top sequence of images is from one cycle and the bottom sequence from the following cycle. From the images, it is clear that there is some variation between the sequences with regards to domain width and wall position. It should be noted that because of the geometrical setup the image is foreshortened in the vertical direction. Therefore, the field of view is actually rectangular rather than square as shown in Fig. 2.

Fig. 3 shows the movement of a single 180° wall in a 140 μm × 140 μm region of the same commercial 3.2% Goss oriented (GO) silicon steel featured in Fig. 2. Prior to testing,

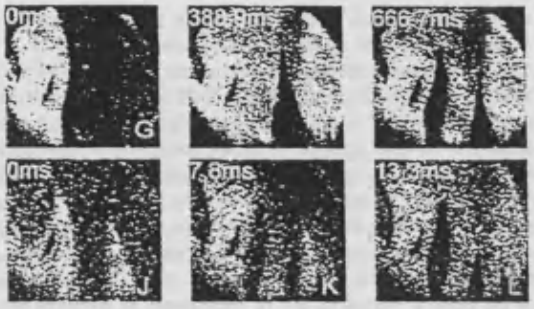

Fig. 4. Images captured at 1 Hz (G, H, I) and 50 Hz (J, K, L) for amorphous ribbon. Capture times are given in milliseconds, and area of view is 140 μm × 140 μm.

the insulating coating had been removed and the surface mechanically polished and annealed. In this case, magnetization was at 1 Hz by a sinusoidal external field with peak value H_p = 1200 A/m. The camera was triggered every cycle at the moment when the magnetizing current was zero, recording a series of 36 images with an exposure time equal to 4 ms and a sample period of 27.8 ms. Fig. 3(a) shows where each image was captured on the magnetizing cycle including images labeled A, B, C, D, E, and F which are shown in Fig. 3(b). Images A, B, and C show the wall position at different times in one cycle, and D, E, and F are the corresponding wall positions at the same times in the next cycle. The images show wall curvature occurring at different points in different cycles and also different wall positions at the same time in different cycles indicating that domain wall velocity and anomalous loss will vary from cycle to cycle.

A large amount of data has been obtained very rapidly, and Fig. 3(b) simply illustrates the typical nonuniform motion. Such phenomena were also visible at 50 Hz although not to such an extent. In this case an exposure time of 1.1 ms was used (18 frames/cycle). From such observations wall velocity or acceleration can be calculated locally for more detailed studies, which will be reported later.

Fig. 4 shows a sequence of images taken from 2605SC amorphous ribbon at three different points on the magnetizing cycle from a region (area 1) measuring 140 μm × 140 μm. The ribbon was magnetized at 1 Hz (G, H, I) and 50 Hz (J, K, L). To improve image contrast the surface was coated with a ZnS layer. The following describes wall motion in two areas of view. In area 1, quite different structures are observed at equivalent times in each cycle, and it varies greatly with frequency as shown. Again, the purpose here is to illustrate that these phenomena do occur and that they can be observed using the technique. As with the silicon steel the nonrepeatability was lower at high frequency, but a detailed analysis is necessary to confirm how general this observation is.

For quantitative analysis, we selected a second region [shown as an insert in Fig. 6(a)] containing the boundary of two wide domains and magnetized the sample at a low field (H_p = 200 A/m). Oscillation of the domain wall was observed. Using similar methodology reported by Mivehchi *et al.* [4], the position (x) of the domain wall was measured at two points on

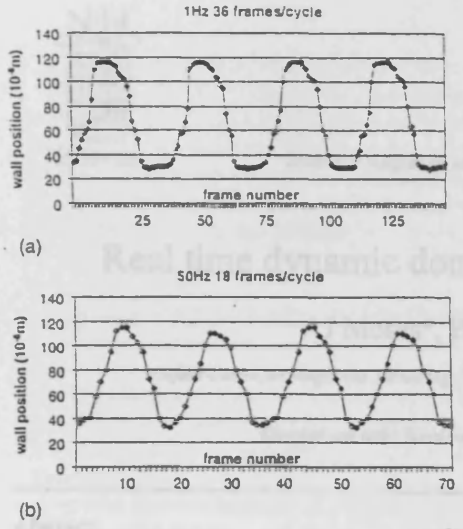

Fig. 5. Domain wall displacement in amorphous ribbon (2605SC) at 1- and 50-Hz magnetization.

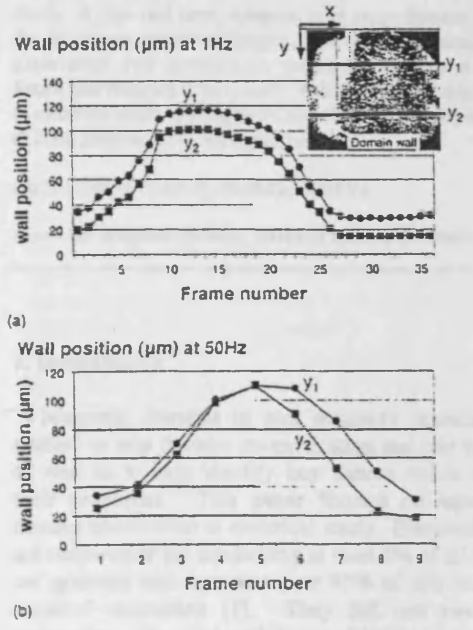

Fig. 6. Domain wall position in amorphous ribbon (2605SC) at 1- and 50-Hz magnetization.

the wall where it intersected with two parallel paths designated y_1 and y_2 as illustrated in Fig. 6(a) (insert). These coordinates were measured at 1- and 50-Hz magnetization for four consecutive cycles. The position of the wall (x) measured along y_1 at various points on the magnetizing cycle is presented in Fig. 5. Close inspection reveals variations in wall displacement from cycle to cycle confirming a degree of nonrepeatable wall motion at both 1 and 50 Hz. In Fig. 6, a plot of x along y_1 and y_2 is shown for a single magnetizing cycle. Two measurements were chosen in order to obtain an average value of wall position. Fig. 6(a) represents the motion of a straight wall which is inclined at an angle relative to its direction of motion at 1-Hz magnetization. The antisymmetrical shape of the profile is due to nonuniform domain wall velocity. The reason for this has yet to be established. By contrast at 50 Hz, domain wall bowing was observed as represented by the difference in plots for y_1 and y_2 in Fig. 6(b).

To determine a measure of the uncertainty in the domain wall position, values were taken for x along y_1 and y_2 at $H = 0$ over 16 cycles. The mean value was calculated followed by the standard deviation. In the case for $H = 0$, the average domain wall position was 26.9 μm (std.dev. = 1.6) at 1 Hz and 27.7 μm (std.dev. = 1.4) at 50 Hz. The standard deviation at 50 Hz is smaller confirming that nonrepeatability is lower at the higher frequency.

III. Conclusion

The initial results presented here illustrate some of the capabilities of the new instrument for successfully imaging domains up to 50-Hz magnetization. Observation of dynamic domain wall motion in real time has been demonstrated at 1 and 50 Hz in electrical steel and amorphous ribbon. Nonrepeatability is greatest at 1 Hz in both materials indicating a general underlying mechanism is responsible. Further work is needed to clarify the degree of nonrepeatability by observing other domain structures in the same materials as well as other materials not used in this study.

Acknowledgment

This work was supported by the Engineering and Physical Sciences Research Council under Grants GR/M86248/01 and GR/R10493/01.

References

[1] A. Hubert and R. Schäfer, *Magnetic Domains—The Analysis of Magnetic Microstructures*. Berlin, Germany: Springer-Verlag, 1998, p. 44.

[2] M. H. Kryder, P. V. Koeppe, and F. H. Liu, "Kerr effect imaging of dynamic processes in magnetic recording heads," *IEEE Trans. Magn.*, vol. 26, no. 6, pp. 2995–3000, Nov. 1990.

[3] T. Moses, "Opportunities for exploitation of magnetic materials in an energy conscious world," *Interdisciplinary Sci. Rev.*, vol. 27, no. 2, pp. 100–113, 2002.

[4] E. Mivehchi, D. H. Horrocks, H. Iranmanesh, and P. Beckley, "Domain wall speed measurement of Si-Fe samples at 50 Hz magnetization from dynamic SEM images," *J. Magn. Magn. Mater.*, vol. 133, pp. 405–408, 1994.

Manuscript received February 4, 2005.

APPENDIX 1 PUBLISHED PAPERS

ELSEVIER

Journal of Magnetism and Magnetic Materials 304 2 (2006) 130--242

Real time dynamic domain observation in bulk materials

AJ Moses*, PI Williams, OA Hoshtanar

Wolfson Centre for Magnetics Technology, Cardiff University, The Parade, Cardiff, CF24 3AA, Wales, UK

Elsevier use only: Received date here; revised date here; accepted date here

Abstract

The paper briefly reviews the development of domain observation techniques used to study basic properties of electrical steels. A new real time, dynamic high magnification domain observation technique is presented as an example of a state of the art system capable of imaging non-repetitive domain wall motion at power frequencies. Advantages of real time domain observation over stroboscopic magneto-optic studies are presented and the need for real time observations in developing future loss theories is proposed. Possible relationships between Barkhausen noise, hysteresis and non repetitive wall motion in electrical steels are suggested and finally examples of non-repetitive wall motion in other magnetic materials are illustrated.
© 2006 Elsevier B.V. All rights reserved

PACS: 75.60.-d; 75.60.Ch; 75.50.Bb; 42.30.Va

Keywords: Magnetic domains; Electrical steel, Eddy currents loss; Hysteresis loss; Barkhausen noise

1. Introduction

Magnetic domains in soft magnetic materials are studied to help develop magnetisation and loss theories as well as to help identify key factors which control their properties. This paper focuses on aspects of domain observation in electrical steels. Electrical steels are responsible for consuming at least 5% of all energy we generate and represent over 97% of soft magnetic material production [1]. They fall into two main categories: the first and larger family are the non-oriented steels which have a random grain orientation and hence a complex domain structure [2], the second smaller but equally important family are the grain, or Goss oriented steels whose domain structure is more easily observed and understood because of its large grain [001](110) strong texture [3]. Both materials are produced in coated strip form in a 0.1mm to 1.0 mm thickness range.

The first visualisation of domains was reported in the 1930s using a magnetic powder method to observe structures on the surface of single crystals of steel [4][5]. Such powder techniques were useful for characterising static domain structures occurring in steels from which an understanding of loss and magnetisation processes began to develop. The technique is limited to static or very low frequency observation [6] on sample surfaces but some prediction

* Corresponding author Prof. AJ. Moses . Tel.: +44 2920 876854; fax: +44 2920 876729
E-mail address: Mosesaj@cf.ac.uk

of sub-surface structures could be made [7].

The application of the Kerr-magneto-optic (KMO) effect [8] to surface domain observations offered the opportunity for accurate static imaging although there is a need for careful surface preparation [9]. Such early work confirmed the existence of domain structures predicted by Landau and Lifshitz.

2. Dynamic Domain Observations on Electrical Steels

The KMO effect was used widely in the late 1960s and 1970s for dynamic imaging of domain structures on the surface of grain-oriented electrical steels, [10][11][12][13][14][15][16]. The dynamic observations are carried out by triggering the time of a light pulse to illuminate the polished sample-surface at the same point in time over a series of magnetisation cycles to produce an apparent static image. By varying the trigger angle a slowly moving image of the change in the domain structure which occurs at power frequency is obtained. Studies of domain wall motion, wall spacing, bowing, nucleation, etc. helped identify the role of features such as grain size and texture on losses, particularly the anomalous loss. Optimum lamination thickness for given magnetising conditions could be identified [16] as well as mechanisms responsible for stress dependence of magnetic properties [17]. This type of knowledge helped manufacturers reduce losses of grain-oriented steels by some 40% over a 20 year period.

The stroboscopic KMO studies also indicated that domain wall motion was not always repeatable from cycle to cycle [15]. Domain wall pinning was observed and the importance of the reduction of domain wall spacing with increasing frequency was highlighted. Anomalous loss in particular was related to the irregular pinning process occurring in a given wall during the magnetising cycle [4][15]. Although it was recognized that the phenomenon of anomalous loss was not understood, it was suspected that the variation of the number of mobile walls participating in magnetisation reversal, which varied with factors such as peak flux density and magnetising frequency [13], was an important parameter. Much of the emphasis of the work at the time was on obtaining evidence to help develop and verify domain models such as the Pry and Bean theory [18] from which eddy current loss could be predicted. Such observation and models pointed towards local eddy current loss being proportional to the square of domain wall velocity. Although such stroboscopic studies have made immense contributions to our understanding of domain processes, it will be seen later that the non repeatability of wall motion from cycle to cycle, which is not seen stroboscopically may be an important factor in loss mechanisms. Also the need for surface preparation is a major drawback for KMO studies since it is a destructive process which undoubtedly affects the domain structure. Furthermore it is know that surface roughness itself increases domain wall bowing during a.c. magnetisation causing additional eddy current loss which can be explained in terms of a drag force on wall motion [19]. The coating removal has been found unnecessary in some cases such as for example when the KMO effect has been exploited on untreated amorphous ribbon making use of advanced CCD imaging which could perhaps one day be applied to non-oriented steel [20].

Another possible future method would be to observe dynamic motion through a coating by scanning the surface field with an array of magnetoresistive field sensors [21]. Smaller sensors, higher resolutions and faster signal processing may lead to such a method replacing KMO techniques for real time power frequency observations.

A direct method of detecting domain structures beneath the coating is by use of a stroboscopically controlled, high voltage scanning electron microscope (SEM) [22][23]. Observations have been made at up to 5kHz in thin gauge electrical steel [24] and more recently more advanced image processing has been applied to obtain high quality stroboscopic images under the phosphate coating of conventional grain-oriented steel. SEM studies do highlight the importance of the coating in surface pinning due to roughness or near surface inclusions particularly at high frequency [25].

3. Other Imaging Methods

Magnetic Force microscopy (MFM) imaging of static domains on electrical steel is feasible and some studies have been carried out but with little reported correlation, if any, with domains observed by other

methods. At present the method cannot be applied to coated grain-oriented steel since the coating is too thick for the MFM tip to detect wall positions clearly from the steel surface field. However the very high resolution of the MFM might be put to good advantage in relating surface field profiles at nanoscale dimensions to surface domain features and the effects of surface topology which cannot be resolved at the normal level of KMO observations. This may also give insight into hysteresis phenomena at this level.

A major challenge is to observe sub surface domain structures in electrical steels. This is necessary to understand the complex magnetization processes which occur in non-oriented steel which have small grain size (around 10μm to 100μm) and proportionately smaller domains. KMO methods have been used to carry out static surface observations and anticipated complex structures are observed [26] but dynamic observations are more difficult. In the Kerr effect the light effectively penetrates to a depth of around 20 nm so it is a surface effect in its reflection mode. X-Ray and neutron methods can be used to observe static positions of domain walls but the sub surface structures are complex and difficult to interpret.

An interesting indirect method of sub surface observation is based on the precipitation of particle platelets along magnetisation directions in certain high silicon steels [27]. Observation of the precipitated particle distribution by successively etching away layers of the surface leads to good interpretation of what type of static structures are possibly present below the surface of normal electrical steels [28].

An earlier method based on sweep field techniques can be used to deduce the effect of internal wall motion which in turn can be related to the inclusion content and also show hysteretic effects dependent on non repetitive internal wall motion particularly at low frequency [29].

It is perhaps worth noting here that the early work of Barkhausen [30] indicated that magnetisation proceeds as a succession of discrete jumps which can be interpreted as random, frequency independent pinning of walls but which now is claimed to be comprised of two components, the second of which is believed to be frequency dependant and might be correlated with macroscopic irregularity in domain wall motion [13].

Some of the important features of the methods which can be applied to domain observations in electrical steels are shown in table 1. These and other techniques are reviewed more thoroughly elsewhere [2][31] but the purpose of this paper is to show the importance of having the capability to carry out real time, power frequency, domain observation in electrical steel as opposed to the stroboscopic methods which have been used effectively to form the basis for our present understanding of losses.

	Bitter	Field Sensing	KMO	SEM
Need for surface preparation	No/Yes	No	Yes	No
Need for coating removal	No/Yes	No	Yes	No
Sub surface observation	No	No	No	No
Convenience	High	Medium	Low/Medium	Low
Capital Cost	Low	Medium	Medium/High	High
Resolution	Low 1μm	Medium μm	Medium 0.1 μm	Medium 0.5 μm
Typical Field of View	Up to several cm^2	Around $1cm^2$		
Dynamic operation (Strobe)	No	Possibly	Yes	Yes
Dynamic operation (real time)	No	Not Yet	Yes	No

Table 1. Comparison of features of domain observation techniques applied to electrical steels.

4. Real Time Domain Observations

Stroboscopic methods have always indicated that in many cases non repeatable wall motion occurs which is difficult to quantify. Real time observations have been made previously on grain oriented steel at power frequency (50Hz) using a Kerr microscope together with high speed stroboscopically illuminated cameras at 24-110 frames per cycle [13][15]. Such studies verified the variation of the number of walls participating in the magnetisation process depends on frequency and flux density but timing and exposure time of the photographs was perhaps not very accurate so measurement of non repeatability was difficult or impossible in most cases.

Figure 1 shows a real time domain observation

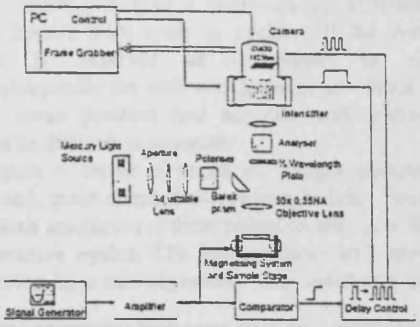

Figure 1. Real time imaging Kerr microscope.

system recently developed with the objective of quantifying surface structures in regions 1.2mm x 1.7mm and 140µm x 140µm with optical resolutions of 2µm and 0.5µm respectively. A high pressure mercury lamp is switched on continuously and a Neoark BH-780-IP polarising microscope is used. Depending on the mode of operation, parallel or perpendicular surface domains can be studied [32]. Images are recorded using a high speed intensified camera (HICAM) and frame grabber capturing up to 1825 frames per second (36 frames per cycle at 50Hz). Figure 2a shows the normal operating sequence at 50Hz. Figure 2b shows a sequence of pulses in a typical stroboscopic KMO

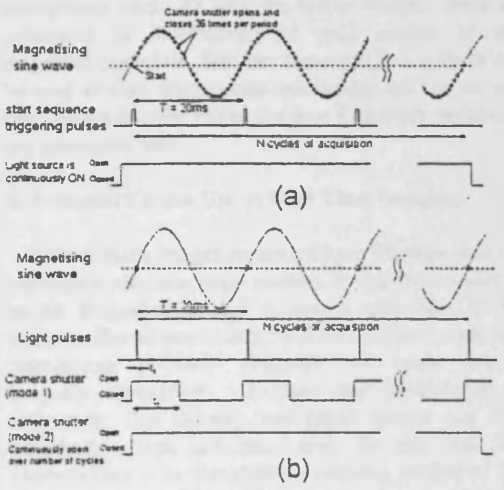

Figure 2. Timing event sequence for real time (a) and stroboscopic (b) image capture at 50Hz.

system assuming a light pulse of typically 0.1ms duration. Using the real time system at 50Hz an image is captured in 0.5ms or 2.5% of the cycle time. In the strobed system the image is captured in the same 0.1ms period of successive cycles and averaged over many cycles. If the wall motion is non-repeatable from cycle to cycle images obtained using the strobed KMO system will be blurred, distorted or simply not visible. Stroboscopic high energy pulsed (1ns) laser systems have been used in studies on other materials where the light intensity of each pulse is sufficiently high for capturing real time images [33].

5. Stroboscopic Errors due to Non Repetitive Wall Motion

Figure 3 shows a sequence of instantaneous domain images observed on the surface of an iron-based amorphous ribbon at the same time in 4 successive cycles when magnetized at 5Hz using the system shown in Figure 1. Small differences in wall positions can be observed and measured to determine variations in instantaneous wall velocity which gives an indication

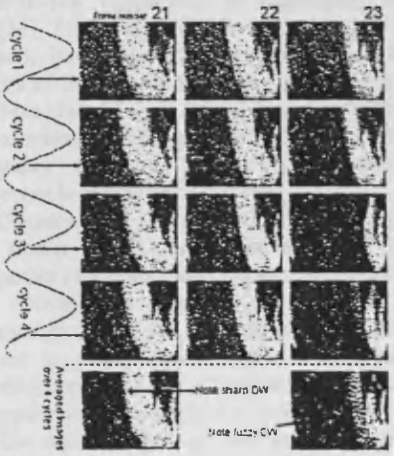

Figure 3. Domain images observed on amorphous ribbon at 5kH magnetisation.

of local losses. The results of averaging these images as would occur in a stroboscopic system are also shown in Figure 3 for this particular time in the cycle. At first sight this does appear very similar but close analysis

will show that the wall varies in position by around 20μm which will give a wall velocity difference of about 2mm/s from cycle to cycle. If the averaged image is observed as it would be viewed stroboscopically the wall would appear to wobble about some mean position and accurate wall positioning would be difficult to measure.

Figure 4 shows a series of images obtained on decoated, grain oriented silicon iron at 1Hz. Here wall positions are shown at three points on the cycle for two consecutive cycles. The images show wall curvature occurring in a non repeatable way indicating domain

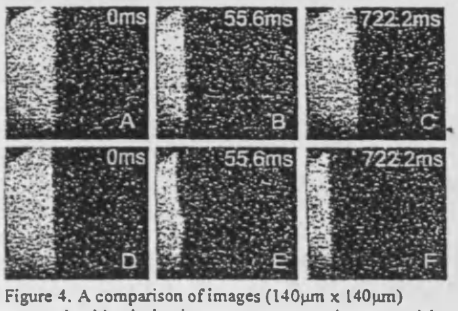

Figure 4. A comparison of images (140μm x 140μm) captured at identical points on two consecutive magnetising cycles (1Hz) for GO steel

wall velocity and anomalous loss will vary from cycle to cycle. Figure 5 is an example of domain wall propagation along a 120μm diameter cobalt-based amorphous wire. As with the earlier images, these are presented as illustrations of wall motion in soft magnetic materials. Similar non-repetitive effects can be seen at high frequencies but images are not so well reproduced in print hence the low frequency sequences are presented here.

6. Potential Future Use of Real Time Imaging

The domain images presented here illustrate that non repeatable domain wall motion frequently occurs at power frequency in soft magnetic materials. It had been confirmed previously by KMO methods that such phenomena probably occurred but could not be properly quantified. Further the dependence on frequency, flux density and other factors has been observed. One important area for the real time observations is to complement ongoing studies of loss mechanisms and loss prediction which need to be

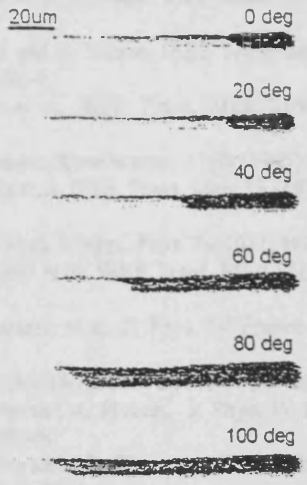

Figure 5. Progression of a domain wall boundary on the surface of a cobalt-based amorphous wire for different points on the magnetisation cycle.

improved to cope with more exacting user demands.

It has long been inferred that hysteresis loss per cycle is not independent of magnetizing frequency [34][35]. Previously excess or anomalous loss has been linked to Barkhausen noise [36]. More recently power spectra of Barkhausen noise in grain oriented material has been claimed to be related to total loss [37]. More recently again, Barkhausen noise has been found to be frequency dependent and closely related to the hysteresis loss per cycle [38][39].

Theoretical modeling based on the assumption that the excess loss is solely dependent on hysteresis properties of materials has formed a creditable platform for several loss models [40]. Such modeling approaches based on magnetic viscosity phenomena appear to contain parameters which appear to be material dependent and more closely related to physical magnetisation phenomena than many others [41].

The implementation of these studies is that there are closer relationships between Barkhausen noise, anomalous loss and hysteresis processes which might be discovered with the aid of real time domain studies. This may give us a new understanding and representation of losses in electrical steels which in turn might act as a platform for predicting methods of developing new generations of low loss materials

APPENDIX 1 PUBLISHED PAPERS

which can cope with the anticipated increasingly demanding needs of users in the next decades.

7. Acknowledgements

The authors are grateful for Grant GR/M 86248 under the EPSRC/OST JIF scheme which enables the domain observation system to be developed. We are also grateful to the EPSRC for Platform grant GR/R 10493 which contributed towards a studentship for OAH and for grant EP/C518616 which is providing the support for ongoing dynamic domain studies.

8. References

1) A. J. Moses, Interdisciplinary Sci. Reviews, 27(2) (2002) 100-113
2) A. Hubert and R. Schafer, Magnetic Domains, (Springer-Verlag, Berlin, 1998)
3) A.J. Moses, IEE Proc. 137A, (1990) 2333-45
4) F. Bitter, Phys. Rev. 38 (1931) 1903-5
5) L. Hamos, and P.A. Thiessen, Z. Physik 71 (1932) 442
6) R.M. Bozorth, J. Phys. Rad. 12 (1951) 308
7) H. Williams et al, Physical Rev. 75(1) (1949) 155-178
8) J. Kerr, Phil Mag. 5(3) (1877) 321-43
9) C.A. Fowler and E.M Fryer, Phys. Rev. 86 (1952) 426
10) T. Nozawa et al, IEEE Trans. Mag. 32(2) (1996) 572-89
11) J.W. Shilling and G.W. Houze, IEEE Trans. Mag. 10(2) (1974) 195-223
12) C. Boon and J.Robey, Proc. IEE 115 (1968) 1535-40
13) T. Haller and J. Kamer, J. Appl. Phys. 41 (1970) 1034-5
14) Y. Shur et al, Phys. Met. Met. 29 (1970) 770
15) G.W. Houze, J. Appl. Phys. 38(3) (1967) 1089-96
16) K.J. Overshott, IEEE Trans. Mag. 12(6) (1976) 840-5
17) L.J. Dijkstra and U.M. Martius, Rev. Mod. Phys. 25(1) (1953) 146-50
18) R.H. Pry and C.P. Bean, J. Appl. Phys. 29 (1958) 532-3
19) A. Honda et al. J. Magn. Mag. Mater. 112 (1992) 20-22
20) A. Honda and K. Shirae, IEEE Trans. Mag. 17(3) (1981) 3096-8
21) M.H. So et al, IEEE Trans. Mag. 31(6) (1995) 3370-2
22) T. Yamamoto, Kotaibutsuri, 11(9) (1975) 513
23) B. Fukuda et al, IEEE Trans. Mag. 13 (1977) 1499-1
24) K.I. Arai et al, J. Appl. Phys. 70(10) (1991) 6256-8
25) E. Mivehchi et al, IEEE Trans. Mag. 26(5) (1990) 1975-7
26) R. Kaczmarek et al, J. Phys. IV France 8 (1998) 311-4
27) S. Libovicky, Phys. Stat. Sol. A 12 (1972) 539
28) R. Schafer and A. Hubert, J. Phys. IV France, 8, (1998), 283-90
29) P. Beckley and J.E. Thompson, IEE Proc. 117(11) (1970) 2194-2200
30) H. Barkhausen, Phys. Z. 20 (1919) 401-3
31) R. Carey and E.D. Isaac, Magnetic Domains and Techniques for their Observation, (Academic Press, New York, 1966)
32) A.J. Moses et al, IEEE Trans. Mag. (2005) accepted for publication
33) M.H. Kryder, P.V. Koeppe and F.H. Liu, IEEE Trans. Mag. 26(6) (1990) 2995-3000
34) D.J. Seagle and S.H. Charap, J. Appl. Phys. 53 (1982) 8299
35) F. Brailsford and R. Fogg, IEE Proc. 111 (1964) 1463
36) J.E.L. Bishop, J. Magn. Mag. Mater. 49 (1985) 241-9.
37) H. Birsan et al, IEEE Trans. Mag. 32(2) (1996) 527-34
38) A.J. Moses et al, Stahleisen (2004) 215-219
39) A.J. Moses and W.A. Pluta, Stahleisen, (2004) 451-6
40) I.D. Mayergoyz and C. Serpico, IEEE Trans. Mag. 36 (2000) 3192-4
41) S.E. Zirka et al, IEE Proc-Sci. Meas. Technol. 149(5) (2003) 218-21

APPENDIX 2.1 PROPERTIES OF ELECTRICAL STEEL USED FOR STUDIES .

Data were taken from Cogent website. © http://www.orb.gb.com/

Unisil Grade		Thickness	Specific total loss at frequency of 50 Hz				B at H=800 A/m, 50 Hz
IEC	EN		Guaranteed max		Typical		
60404-8-7	10107		B=1,5T	B=1,7T	B=1,5T	B=1,7T	Typical
		mm	W/Kg	W/Kg	W/Kg	W/Kg	T
.							
Unisil-H							
M90-23P5	M90-23P#*	0.23	-	0.90	0.62	0.88	1.90
M100-23P5	M100-23P	0.23	-	1.00	0.66	0.92	1.91
	M95-27P#*	0.27	-	0.95	0.68	0.92	1.90
M103-27P5	**M103-27P**	0.27	-	1.03	0.71	0.97	1.93
M105-30P5	M105-30P	0.30	-	1.05	0.77	1.02	1.93
M111-30P5	**M111-30P**	0.30	-	1.11	0.80	1.08	1.93
M117-30P5	M117-30P	0.30	-	1.17	0.84	1.14	1.92
.							
Unisil							
M120-23S5	M120-23S	0.23	0.77	1.20	0.72	1.09	1.83
M127-23S5	M080-23N	0.23	0.80	1.27	0.76	1.15	1.83
M130-27S5	M130-27S	0.27	0.85	1.30	0.77	1.12	1.83
M140-27S5	**M089-27N**	0.27	0.89	1.40	0.83	1.21	1.83
M140-30S5	M140-30S	0.30	0.92	1.40	0.84	1.21	1.83
M150-30S5	M097-30N	0.30	0.97	1.50	0.91	1.31	1.83
M150-35S5	M150-35S	0.35	1.05	1.50	0.95	1.35	1.83
M165-35S5	**M111-35N**	0.35	1.11	1.65	0.99	1.42	1.83
	M175-50N*	0.50	1.75	-	1.35	1.92	1.82

Where M103-27P5 is 27MJH, M111-30P5 is 30MOH, M140-27S5 is 27M4,
and M165-35S5 is 35M4, definitions used in tables 7.1 and 7.2 and in the following test data

APPENDIX 2.2

POWER LOSS OF GO STEEL MEASURED WITH EPSTEIN FRAME

Power loss was measurement on bundles of 24 strips of each material. After the testing in a standard Epstein frame one strip of each material was selected for the domain observation. This data were provided by Dr P. Marketos.

27MJH

m=435.54g
d=7650kg/m^3
24 Epstein strips

Hp (A/m)	Bp (T)	Power loss (W/kg)	Apparent Power (VA/kg)	Permeability
2.928	0.1	0.0042	0.0061	27192
5.241	0.2	0.0158	0.0219	30366
7.250	0.3	0.0344	0.0457	32925
8.990	0.4	0.0592	0.0757	35413
10.57	0.4995	0.0894	0.1112	37601
12.03	0.5997	0.125	0.1519	39679
13.36	0.6993	0.1657	0.1973	41656
14.63	0.7993	0.2114	0.2473	43492
15.79	0.8993	0.2622	0.302	45321
16.85	0.9991	0.3182	0.3613	47185
17.87	1.0991	0.3799	0.4262	48936
18.78	1.1995	0.4469	0.4967	50817
19.76	1.2994	0.5208	0.5756	52340
20.66	1.3997	0.601	0.664	53909
22.05	1.4997	0.6892	0.7685	54132
26.12	1.5999	0.7883	0.9052	48750
37.41	1.6997	0.9114	1.1338	36153
78.54	1.8001	1.1151	1.7858	18288
404.4	1.9001	1.522	6.6354	3739

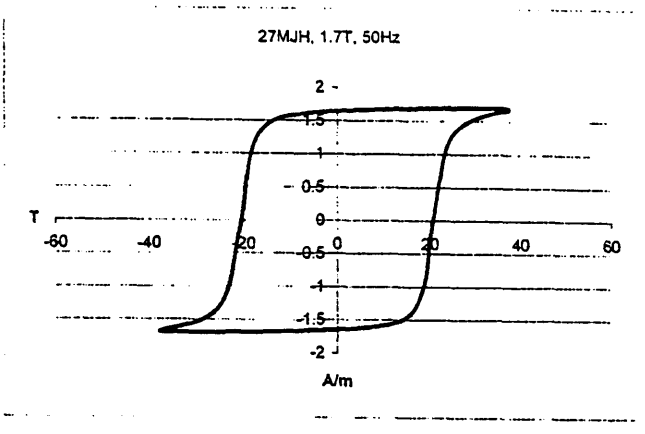

30MJH

m=477 84g
d=7650kg/m^3
24 Epstein strips

Hp (A/m)	Bp (T)	ver loss (W	ent Power (	ermeability
3.227	0.1	0.0047	0.0068	24655
5.718	0.2001	0.0177	0.024	27849
7.844	0.2999	0.0383	0.0496	30430
9.753	0.3999	0.0654	0.0822	32631
11.50	0.4996	0.0985	0.1207	34579
13.02	0.5997	0.1374	0.1651	36651
14.51	0.6996	0.1817	0.2145	38360
15.89	0.7996	0.2315	0.2691	40051
17.13	0.8995	0.2869	0.3289	41791
18.29	0.9997	0.3473	0.3936	43503
19.40	1.0996	0.4143	0.4648	45115
20.44	1.1993	0.4873	0.5429	46688
21.45	1.2995	0.5673	0.6298	48208
22.56	1.3994	0.6534	0.7281	49356
24.87	1.5001	0.749	0.8473	48000
30.70	1.5996	0.8572	1.0083	41459
46.34	1.6998	0.9936	1.2978	29192
106.5	1.8002	1.2255	2.2265	13454
539.5	1.8999	1.642	8.9852	2802

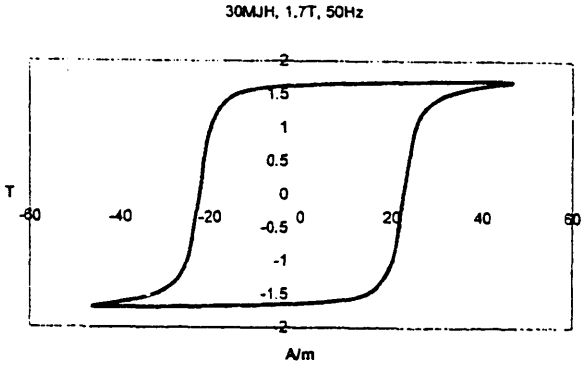

APPENDIX 2.2

POWER LOSS OF GO STEEL MEASURED WITH EPSTEIN FRAME

Power loss was measurement on bundles of 24 strips of each material. After the testing in a standard Epstein frame one strip of each material was selected for the domain observation. This data were provided by Dr P. Marketos.

27MJH

m=435.54g
d=7650kg/m^3
24 Epstein strips

Hp (A/m)	Bp (T)	Power loss (W/kg)	Apparent Power (VA/kg)	Permeability
2.928	0.1	0.0042	0.0061	27192
5.241	0.2	0.0158	0.0219	30366
7.250	0.3	0.0344	0.0457	32925
8.990	0.4	0.0592	0.0757	35413
10.57	0.4995	0.0894	0.1112	37601
12.03	0.5997	0.125	0.1519	39679
13.36	0.6993	0.1657	0.1973	41656
14.63	0.7993	0.2114	0.2473	43492
15.79	0.8993	0.2622	0.302	45321
16.85	0.9991	0.3182	0.3613	47185
17.87	1.0991	0.3799	0.4262	48936
18.78	1.1995	0.4469	0.4967	50817
19.76	1.2994	0.5208	0.5756	52340
20.66	1.3997	0.601	0.664	53909
22.05	1.4997	0.6892	0.7685	54132
26.12	1.5999	0.7883	0.9052	48750
37.41	1.6997	0.9114	1.1338	36153
78.54	1.8001	1.1151	1.7858	18268
404.4	1.9001	1.522	6.6354	3739

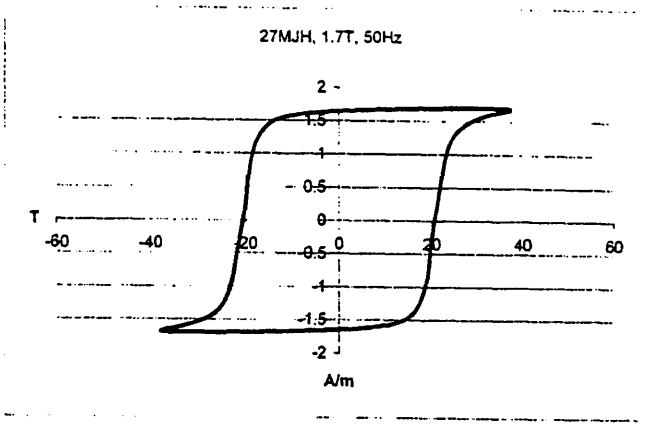

30MJH

m=477.84g
d=7650kg/m^3
24 Epstein strips

Hp (A/m)	Bp (T)	ver loss (W	ant Power (	ermeability
3.227	0.1	0.0047	0.0068	24655
5.718	0.2001	0.0177	0.024	27849
7.844	0.2999	0.0383	0.0496	30430
9.753	0.3999	0.0654	0.0822	32631
11.50	0.4996	0.0985	0.1207	34579
13.02	0.5997	0.1374	0.1651	36651
14.51	0.6996	0.1817	0.2145	38360
15.89	0.7996	0.2315	0.2691	40051
17.13	0.8995	0.2869	0.3289	41791
18.29	0.9997	0.3473	0.3936	43503
19.40	1.0996	0.4143	0.4648	45115
20.44	1.1993	0.4873	0.5429	46688
21.45	1.2995	0.5673	0.6298	48208
22.56	1.3994	0.6534	0.7281	49356
24.87	1.5001	0.749	0.8473	48000
30.70	1.5996	0.8572	1.0083	41459
46.34	1.6998	0.9936	1.2978	29192
106.5	1.8002	1.2255	2.2265	13454
539.5	1.8999	1.642	8.9852	2802

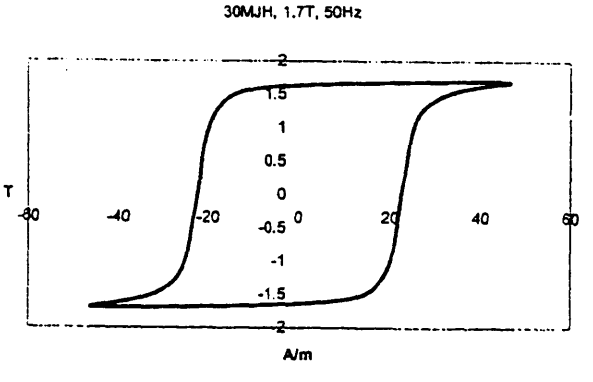

27M3

m=425.69g
d=7650kg/m^3
24 Epstein strips

the same as 27M4

Hp (A/m)	Bp (T)	Power loss (W/kg)	Apparent Power (VA/kg)	Permeability
3.718	0.1	0.0044	0.0078	21411
6.121	0.1999	0.0165	0.0258	25984
8.180	0.2998	0.0354	0.0518	29170
10.04	0.4002	0.0608	0.0849	31726
11.74	0.4996	0.0925	0.1243	33858
13.40	0.5998	0.1312	0.1702	35629
14.75	0.6996	0.1763	0.2221	37731
16.21	0.7996	0.2286	0.281	39245
17.68	0.8997	0.2878	0.3476	40507
19.02	0.9997	0.3533	0.4223	41818
20.69	1.0995	0.4262	0.509	42280
23.38	1.1998	0.5064	0.6114	40844
28.01	1.3006	0.5969	0.7414	36952
35.90	1.3998	0.699	0.9184	31027
51.46	1.5003	0.8234	1.2066	23199
87.05	1.6001	0.9923	1.7985	14629
199.0	1.7002	1.2659	3.584	6800
659.8	1.7995	1.6842	11.4802	2170

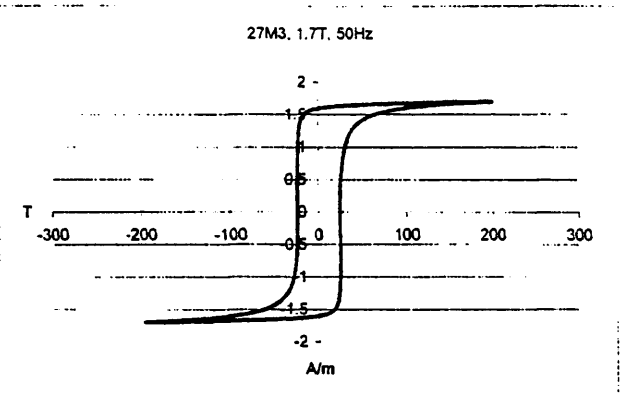

35M4

m=565.84g
d=7650kg/m^3
24 Epstein strips

Hp (A/m)	Bp (T)	Power loss (W/kg)	Apparent Power (VA/kg)	Permeability
3.843	0.1	0.0057	0.0081	20710
6.553	0.2	0.021	0.0275	24292
8.884	0.3	0.0447	0.0561	26873
11.02	0.3997	0.076	0.0927	28854
13.03	0.4996	0.1147	0.1367	30522
14.74	0.5994	0.1603	0.1877	32354
16.58	0 6995	0.2134	0.2461	33578
18.18	0 7995	0.2738	0.3115	34992
19.71	0.8995	0.3417	0.3845	36312
21.20	0.9993	0.4173	0.4656	37515
22.51	1.0993	0.5005	0.5559	38862
23.82	1.1996	0.5923	0.6589	40072
25.56	1.2998	0.6928	0.7785	40470
30.16	1.3996	0.8053	0.9284	36932
39.49	1.4998	0.9344	1.139	30227
61.15	1.5999	1.0937	1.5168	20820
130.8	1.6999	1.3179	2.5835	10345
457.9	1.7996	1.6556	7.9329	3127
1699	1.8987	2.0156	31.3434	889

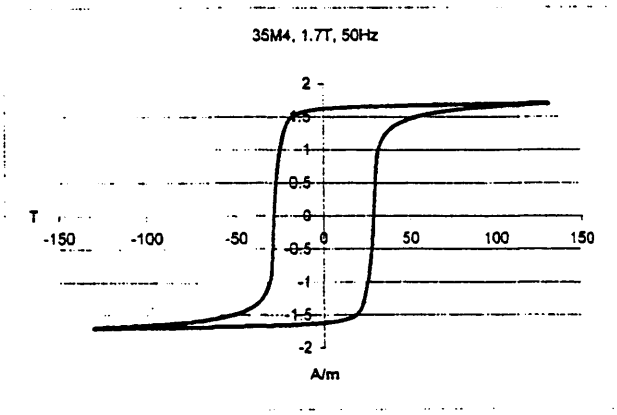

APPENDIX 3 CAMERA SPECIFICATIONS

1. DeltaPix™ Infinity X high-resolution CMOS camera
   © DeltaPix, www.deltapix.com

2. Lambert-Instruments HI-CAM, Gated Intensified High Speed Camera
   © www.lambert-instruments.com

HI-CAM is combined of Lambert-Instruments Image Intensifier and VDS Vosskühler HCC-1000 high-speed camera.

Preliminary

DeltaPix

Infinity X

Digital camera for microscopes
USB 2.0
Windows 2000 / XP

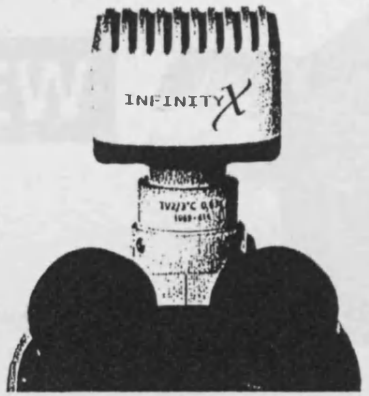

21 Million Pixels and Streaming Video

The Infinity X™ is designed to satisfy the unique and varried demands of digital microscopy. It offers exceptional fast streaming video at an incredibly high-resolution on the computer monitor as well as outstanding resolutions on still images.

The impressive performance and revolutionary resolution of the Infinity X is achieved by combining state-of-the-art sensor design with innovative engineering skills.

A ground-breaking resolution of up to 21 million pixels in precise colour puts the Infinity X in a class all by its own. By integrating DeltaVu™, a highly successful, patent pending technology invented by DeltaPix, these incredible resolutions are achieved.

DeltaVu
DeltaVu™ is a revolutionary new technology designed to dramatically increase the image resolution of a digital camera. The Infinity X has a 1.3 million pixels sensor with Red, Green and Blue colour filters placed in standard Bayer pattern.

Through a process of combining precise position information of the sensor, and capturing additional images, by moving the sensor only fractions of the length of a pixel, the DeltaVu technology allows calculation of finer details than the size of a pixel.

This process also includes the same detailed reproduction at all pixel locations in each of the three colour planes, Red, Green or Blue. The result is an impressive image file, where 63 million pixels have captured the information, 21 million pixels for each of the 3 colours (precise colour).

Easy-to-use
The Infinity X is a small and compact digital camera with a standard C-mount interface for flexible attachment to microscopes.

Installation of the electronic connection is also very simple by connecting a single standard USB 2.0 cable between the camera and the computer. The Infinity X uses the USB 2.0 cable for power, control information and the transmission of data. The very low power consumption of the Infinity X has made it possible only to use a single cable.

Fast video
The use of the 480 Mbit/s high-speed architecture of the USB 2.0 standard has allowed the Infinity X to deliver fast streaming colour video in high-resolution on the monitor of the connected computer.

With a rate of 60 frames per second the microscopy image appears on the monitor without delay. The fast live image makes the process of focusing and interactively optimizing the image very easy.

Features:

- Outstanding performance of a small and compact digital camera for microscopy with extremely high-resolution and exceptional fast live images
- Ideal camera for documentation and analyses for an exceptionally wide-ranging spectrum of applications
- Streaming live video on computer monitor through the high-speed USB 2.0 bus at 480 Mbits/s
- Fast streaming colour video images in high resolution with 60 fps at 640 x 480 pixels resolution
- Selectable video resolution in 4 steps from 1,280 x 1,024 pixels
- Perfect image and colour quality with the finest detail
- Resolution up to the extreme of 21 million pixels in precise colour
- Selectable resolution between 1.3 and 5.2, 12 and 21 million pixels in DeltaVu colour
- Automatic and manual exposure and sensitivity control
- Superior anti-blooming (overexposure) behaviour
- Easy to connect through a single standard USB 2.0 cable to a computer
- Easy and flexible daily use with dynamic insertion and removal of the camera to PC and notebook through standard USB 2.0 high-speed interface
- Small compact microscopy camera with optical C-mount for easy attachment to a microscope
- Silent operation without noisy fan due to very low power consumption
- Intuitive user interface with powerful and easy-to-use image capture and processing functions
- Standard TWAIN driver for integration to 3rd party imaging application and software

Preliminary

Infinity X specifications:

Imager

Effective size:	1/2" format 6.7 mm x 5.3 mm
Colour filter:	Red, Green, and Blue in Bayer pattern
Effective pixels:	1,280 x 1,024 pixels (1.3 million)
Pixel size:	5.2 x 5.2 microns
Dynamic range:	>60 dB
Dark current noise:	20 electrons/pixel/ second
Exposure time:	0.1 milliseconds to 6 seconds
Exposure sensitivity:	Adjustable from 1 times to 3.7 times
Exposure mode:	Automatic, manual or converging
Colour balance:	Automatic, manual or spot white balance
Shutter:	Electronic rolling shutter with streaming video and single frame capture mode

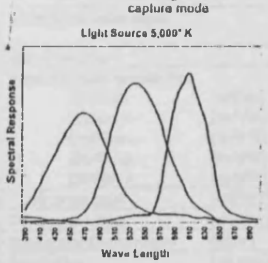

Digital video

Resolution:	1,280 x 1,024 pixels 15 frames per second
	1,024 x 768 pixels 24 frames per second
	800 x 600 pixels 37 frames per second
	640 x 480 pixels 60 frames per second

Digital still image

Single exposure:	1,280 x 1,024 pixels (1.3 million pixels) 24 bit RGB: 3.8 MB 30 bit RGB: 7.6 MB
Multiple exposures:	2,560 x 2,048 pixels (5.2 million real pixels) 24 bit RGB: 15 MB 30 bit RGB: 30 MB
	3,840 x 3,072 pixels (11.8 million real pixels) 24 bit RGB: 34 MB 30 bit RGB: 68 MB
	5,120 x 4,096 pixels (21.0 million real pixels) 24 bit RGB: 60 MB 30 bit RGB: 120 MB

Data format & compression

Digital output:	24 bit uncompressed TIFF-RGB (8 bits per colour)
	30 bit uncompressed TIFF-RGB (10 bits per colour)
	24 bit loss-less compressed JPEG2000 (8 bits per colour)
	24 bit compressed JPEG (8 bits per colour)

Computer connection

Data interface:	480 Mb/s high-speed USB 2.0 architecture
Cable:	Standard USB 2.0 cable with series "B" connector
Power:	Direct powered from the USB 2.0 bus
Application interface:	Intuitive, easy-to-use user application
Application support:	TWAIN driver for integration to 3rd party imaging applications

Operational requirements

Temperature:	0° C to +40° C
Humidity:	15 to 80 % RH (non-condensing)

Physical data

Optical mount:	Standard C-mount
Compliance:	CE, FCC Class B
Housing:	Aluminium with cooling fins
Height:	54 mm
Width:	70 mm
Depth:	98 mm
Weight:	425 g

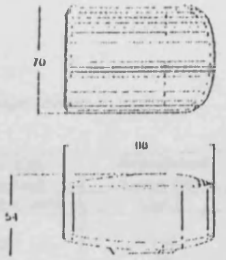

Minimum computer platform
Pentium III,1.3 GHz or similar
256 MB RAM
5 GB free harddisk space
USB 2.0 Port
Windows XP, Windows 2000

Product includes:
- Infinity X digital camera for USB 2.0
- CD-ROM with standard user application
- TWAIN driver
- Documentation
- USB 2.0 cable (2.0 m)

Specifications and products are subject to change without any notice or obligation on part of DeltaPix ApS. January 2004
DeltaPix, Infinity X and DeltaVu are trademarks of DeltaPix ApS. All other brands or product names are registered trademarks of their respective holder. © 2004 DeltaPix ApS

DeltaPix

DeltaPix
CAT Science Park
Frederiksborgvej 399
DK-4000 Roskilde
Denmark
Tel: +45 46 76 02 05
Fax: +45 46 32 19 19

HI-CAM

GATED INTENSIFIED HIGH SPEED CAMERA

NEW

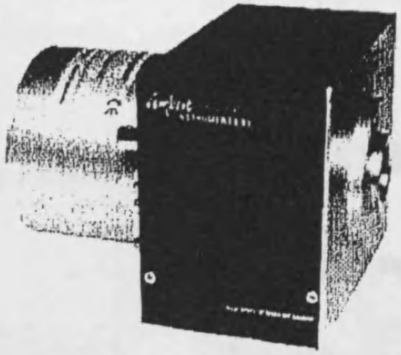

The perfect tool for your demanding high speed low light level imaging applications

The **HI-CAM** is a high-speed intensified camera, based on the VDS Vosskühler HCC-1000, offering the unique combination of high speed and sensitivity down to single photon level.

To achieve this the **HI-CAM** is equipped with a high gain, high output brightness, dual stage image intensifier fibre-optically coupled to the CMOS sensor. The first stage is a second generation image intensifier that is available in many different configurations. Depending on the specific application a model can be selected for spectral sensitivity, gain, linearity, gating and other specific requirements. As a second stage a first generation image intensifier is used to enhance the maximum output brightness to the level needed to utilise the whole dynamic range of the CMOS sensor. Both intensifiers have special fast phosphor screens to avoid smear effects.

The **HI-CAM** is capable of taking images at a maximum rate of 1825 (optional 6832) frames per second. The images are stored in the buffer memory (512MB or 1GByte)) of the camera and directly available for playback before optional transfer to the harddisk. A continuous rate of approx. 30 frames per second is available for set-up and focusing.

The camera and intensifier settings are fully software controlled via an RS-232 interface while the images are transferred to the computer via a digital frame-grabber.

Lambert INSTRUMENTS
PERFECTION IN IMAGE DETECTION

I N F O R M A T I O N

Specifications:

- 1024x1024 square pixels
- 12µm pixel size on the input
- 12 x 12 mm image area on the input
- C-mount input
- Speed:
  - 462 frames per second at 1024 x 1024 pixels
  - 923 frames per second at 1024 x 512 pixels
  - 1825 frames per second at 1024 x 256 pixels
  - *Optional:*
  - 1820 frames per second at 256 x 256 pixels
  - 3570 frames per second at 256 x 128 pixels
  - 6832 frames per second at 256 x 64 pixels
- Internal image buffer 512MB or 1GByte
- Sensitivity down to single photon level
- Resolution 500 TV-lines
- Fast shutter (gating) down to 60ns
  - *optional* down to 5ns
- 8-bit digital image data output up to 30 fps
- Matrix SDIG framegrabber
- Triggering:
  - Input trigger for starting a sequence
  - strobe output trigger per frame
- *Optional* Fire Wire output (IEEE-1394)
- Camera and intensifier control via two RS232 interfaces
- Extensive software package for image acquisition, image viewing and image storage

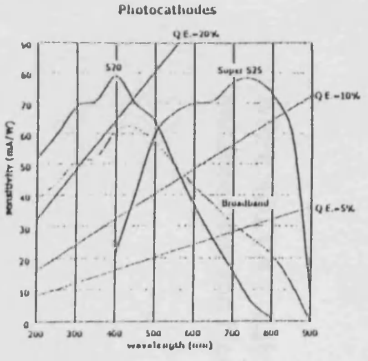

Available Intensifiers:

Photocathode type		S20 (typical data)	Super S25 (typical data)	Broadband (typical data)
Input window		Quartz*	Glass or fibre-optic	Quartz
Photocathode sensitivity:				
@2850K	(µA/lm)	150	700	250
@200nm	(mA/W)	45	0	30
@400nm	(mA/W)	65	15	48
@600nm	(mA/W)	25	65	25
@800nm	(mA/W)	0	65	12
Luminance gain	($cd/m^2/lx$)	6000	10000	8000
Dark count rate	($cts/sec/cm^2$)	1500	50000	20000
Equivalent background	(µlux)	0,05	0,15	0,10
Resolution	(lp/mm)	27	27	27

*Fibre-optic is also possible but cuts off sensitivity below 400nm

Remark: please call for special options like fast gating and special image intensifiers

Dimensions and weight:

Camera:
Size : see graph
Weight : +/- 3,5kg

Power supply:
Size : 50 x 85x 155
Weight : 0,5kg

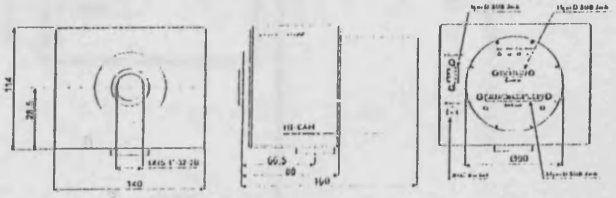

Lambert INSTRUMENTS
PERFECTION IN IMAGE DETECTION

Turfweg 4, 9313 TH Leutingewolde, The Netherlands, Tel: +31 50 501 8461, Fax +31 50 501 0034
E-mail: info@lambert-instruments.com, Web: http://www.lambert-instruments.com

APPENDIX 4.1 LabView block diagram of the program for morphologic enhancement and block diagram of the subVI used in the main program.

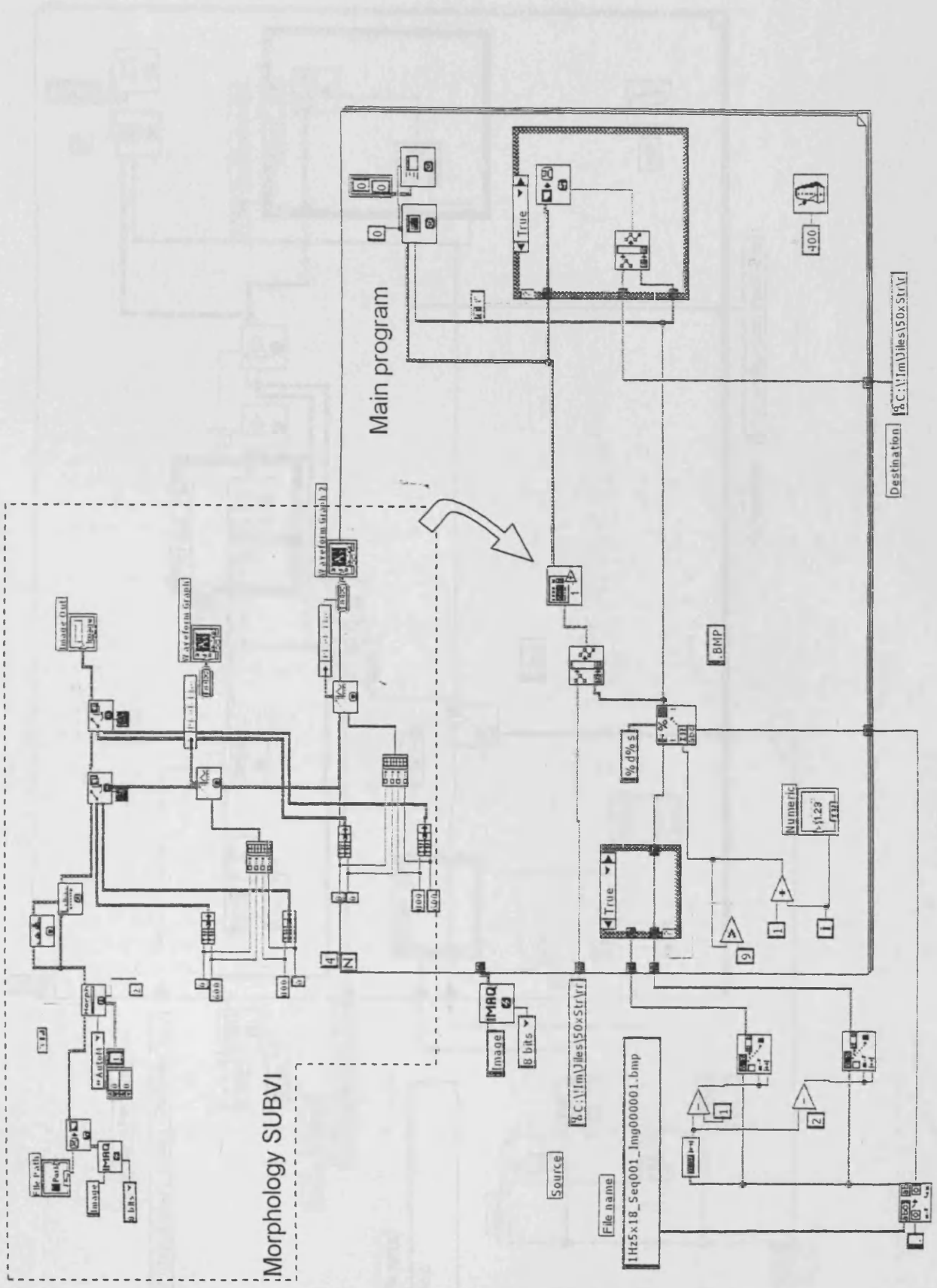

APPENDIX 4.2 LabView block diagram of the program for background subtraction of a series of the numbered images

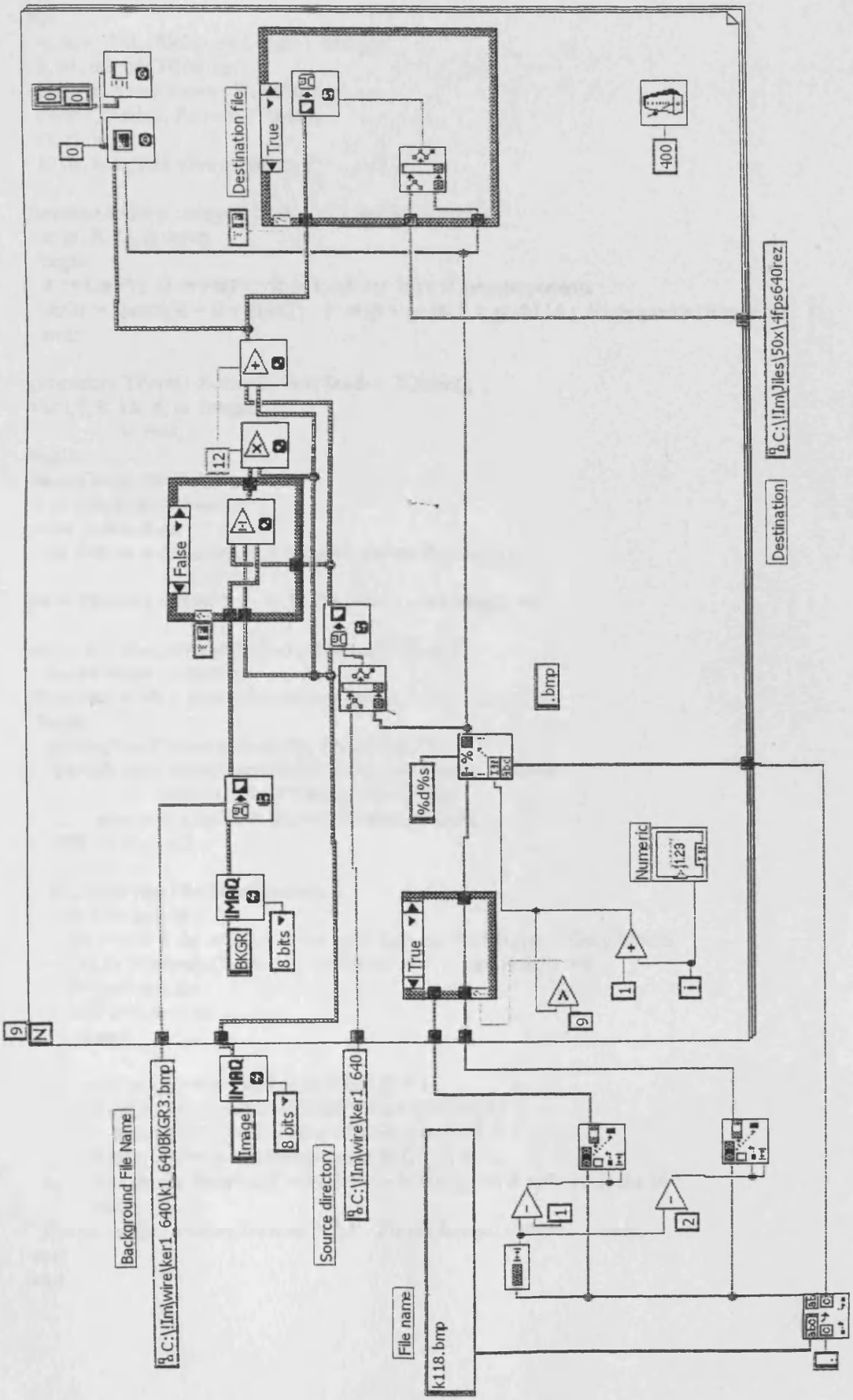

APPENDIX 4.3 DELPHI SCRIPT

1. Brightness and contrast enhancing program, able to process a numbered sequence of image files. Trivial script is omitted.

```
var
 w, h, s, FNL{fileName Length} :integer;
 b, b1, b2, b4: TBitmap;
 FName, NewFName : ShortString;
 Form1, Form3, Form4: TForm1;
 t1, t2 :byte;
 b1Gr, bGr, Rez :GrayMatrix;

function toGr( p :integer):byte;    // Load RGB pixel
var gr, R, G, B :byte;
 begin
 R := Lo(P) ;  G := Hi(P) ;  B := Lo(P shr 16) ;  // get components
  toGr := trunc((R + G + B)/3) ;   {  := gr + gr shl 8 + gr shl 16 ;  // composite Grey pixel   }
 end;

procedure TForm1.Button2Click(Sender: TObject);
var i, j, k, kk, d, m :integer;
          x :real;
begin
 m := SpinEdit6.Value ;
 x := SpinEdit3.Value/10 ;
 {for j:=0 to h do
  for i:=0 to w do  bGr[i,j] := toGr(b1.canvas.Pixels[i,j]) ;   }

b4 := TBitmap.Create ;     b4.Width :=w  ;     b4.Height :=h  ;

 kk := StrToInt(FName[FNL-5]+FName[FNL-4]);
   NewFName :=FName;
 for k:=kk to kk + SpinEdit1.value - 1 do
 begin
   delete(NewFName,FNL-5,2);  FNL:=FNL-2;
   if k<10  then begin insert(IntToStr(k),NewFName,FNL-3);
                 insert('0',NewFName,FNL-3); end
         else insert(IntToStr(k),NewFName,FNL-3);
   FNL := FNL + 2 ;

   b1.LoadFromFile(NewFName);
    for i:=0 to w do
     for j:=0 to h do  bGr[i,j] := toGr(b1.Canvas.Pixels[i,j]);  // Gray Matrix
      b4 := TBitmap.Create ;     b4.Width :=w  ;     b4.Height :=h  ;
     for j:=0 to h do
      for i:=0 to w do
       begin

        if bGr[i,j] <= m - m/x then bGr[i,j] := 1;
        if (bGr[i,j]> m-m/x)and(bGr[i,j]<m+ (256-m)/x)
           then b1Gr[i,j]:= trunc(m + (bGr[i,j]-m)*x ) ;
        if bGr[i,j] >= m+ (256-m)/x then b1Gr[i,j] := t2;
         b4.Canvas.Pixels[i,j] := b1Gr[i,j] +b1Gr[i,j] shl 8 +b1Gr[i,j] shl 16 ;
        end;
  Form2.Image1.Picture.Bitmap := b4 ;  Form2.Image1.refresh;     beep;
end;
end;
```

2. Subtracting-Averaging program with various kernels.
(Im[i,j] is an input image, BkGr[i,j] – background image and
b4.Canvas.Pixels[i,j] is an output image, t1 and t2 are bottom and top thresholds respectively.)

```
type
 Hist = array[0..255,1..3]of int64;
 GrayMatrix =array[0..800,0..600]of byte;        {  sise !!  }

var
 w, h, s, FNL{file Name Length} :integer;
 b, b1, b2, b4: TBitmap;
 FName, NewFName, SaveN : ShortString;
 Form1, Form3, Form4: TForm1;
 t1, t2 :byte;
 b1Gr, bGr, Rez :GrayMatrix;
implementation

function getR( P: integer ): byte;
 begin
  getR := Lo(P) ;
 end;
function getG( P: integer ): byte;
 begin
  getG := Hi(P) ;
 end;

function getB( P: integer ): byte;
 begin
  getB := Lo(P shr 16) ;
 end;

function PComp( R, G, B :byte):integer;      // pixel composition
  begin
   PComp := R + G shl 8 + B shl 16 ;
  end;

function GrayComp( R, G, B :byte):integer;   // compos to Gray scale
var gr :byte;
  begin
   gr := trunc((R + G + B)/3) ;
   GrayComp := gr + gr shl 8 + gr shl 16 ;
  end;

function PixAdd( P1, P2 :integer):integer;
var Rs, Gs, Bs, GrayS :byte;
 begin
  Rs := getR(P1) + getR(P2) ;
  Gs := getG(P1) + getG(P2) ;
  Bs := getB(P1) + getB(P2) ;
  if Form1.CheckBox1.Checked = True then PixAdd := GrayComp(Rs,Gs,Bs)
                    else PixAdd := PComp(Rs,Gs,Bs) ;
 end;
```

```
function Subst( P1, P2 :integer):integer;
 var Rs, Gs, Bs :byte;
 begin
 if (getR(P1) - getR(P2))>=4 then  Rs :=(getR(P1) - getR(P2))
                    else Rs :=0   ;
 if (getG(P1) - getG(P2))>=0 then Gs :=(getG(P1) - getG(P2))
                    else Gs :=0   ;
 if (getB(P1) - getB(P2))>=0 then Bs := getB(P1) - getB(P2)
                    else Bs :=0 ;
  if Rs*Form1.SpinEdit1.Value <256 then Rs := Rs*Form1.SpinEdit1.Value
                          else Rs := 255 ;
  if Gs*Form1.SpinEdit1.Value <256 then Gs := Gs*Form1.SpinEdit1.Value
                          else Gs := 255 ;
  if Bs*Form1.SpinEdit1.Value <256 then Bs := Bs*Form1.SpinEdit1.Value
                          else Bs := 255 ;


 if Form1.CheckBox1.Checked = True then Subst := GrayComp(Rs,Gs,Bs)
                    else Subst := PComp(Rs,Gs,Bs) ;
 end;


function SUB( P1, P2:integer):integer;
 var  r,g,b,r1,g1,b1, Rs, Gs, Bs  :byte;
 begin
 r := getR(P1);  g := getG(P1);   b := getB(P1);
 rs := getR(P2);  gs := getG(P2);   bs := getB(P2);

 if (r-rs)>=t1 then  R1 :=r - rs   else R1 :=0   ;
 if (g-gs)>=t1 then G1 := g - gs   else G1 :=0   ;
 if (b-bs)>=t1 then B1 := b - bs   else B1 :=0 ;
  if R1*Form1.SpinEdit3.Value <t2 then R1 := R1*Form1.SpinEdit1.Value
                          else R1 := t2 ;
  if G1*Form1.SpinEdit3.Value <t2 then G1 := G1*Form1.SpinEdit1.Value
                          else G1 := t2 ;
  if B1*Form1.SpinEdit3.Value <t2 then B1 := B1*Form1.SpinEdit1.Value
                          else B1 := t2 ;
  SUB := GrayComp(R1,G1,B1) ;
 end;

 function SubBytes(P1, P2:byte):Byte;
  Var P3 :byte;
  begin
    t1 :=Form1.SpinEdit4.Value;  t2 :=Form1.SpinEdit5.Value;
    if (P1 - P2)>=t1 then  P3 :=P1 - P2   else P3 :=0   ;
     if P3*Form1.SpinEdit3.Value +P2 <t2 then P3 := P3*Form1.SpinEdit1.Value +P2
                          else P3 := t2 ;
    SubBytes := P3;
  end;

 function toGr( p :integer):byte;     // Load RGB pixel
 var gr, R, G, B :byte;
  begin
  R := Lo(P) ;  G := Hi(P) ;  B := Lo(P shr 16) ;  // get komponents
   toGr := trunc((R + G + B)/3) ;
  {  := gr + gr shl 8 + gr shl 16 ;  // composit Grey pixel    }
  end;
```

```
Procedure Sub_Aver2(Im,BkGr :GrayMatrix);  { cross + 3x3 }
var i,j,dif, ImPixel :integer;
   p, R,G,B:byte;
 begin
  for i:=0 to w-1 do
   for j:=0 to h-1 do begin
    dif := (Im[i,j]+ Im[i-1,j]+ Im[i,j-1]+ Im[i+1,j]+ Im[i,j+1]
        -( BkGr[i,j]+ BkGr[i-1,j]+ BkGr[i,j-1]+ BkGr[i+1,j]+ BkGr[i,j+1] ));

    if dif< t1*5
     then p := 1
     else
      if trunc(dif * Form1.SpinEdit3.Value/5) + Im[i,j] >= t2
       then p := t2 - Im[i,j]
       else
        p := trunc(dif * Form1.SpinEdit3.Value/5) ;
     if Form1.CheckBox1.Checked = true then R := p ;
     if Form1.CheckBox2.Checked = true then G := p ;
     if Form1.CheckBox3.Checked = true then B := p ;
     If Form1.CheckBox4.Checked = True then  ImPixel := Im[i,j] else ImPixel :=0;
    b4.Canvas.Pixels[i,j] := R+ ImPixel  + (G+ImPixel ) shl 8 + (B+ImPixel ) shl 16 ;
    end;
  end;
//=============================================

Procedure Sub_Aver3(Im,BkGr :GrayMatrix);  { Rectangle 3x3 }
var i,j,dif, ImPixel :integer;
   p, R,G,B:byte;
 begin
  for i:=0 to w-1 do
   for j:=0 to h-1 do begin
    dif := (Im[i,j]+ Im[i-1,j]+ Im[i,j-1]+ Im[i+1,j]+ Im[i,j+1]+
          Im[i-1,j-1]+ Im[i-1,j+1]+ Im[i+1,j-1]+ Im[i+1,j+1]
        -( BkGr[i,j]+ BkGr[i-1,j]+ BkGr[i,j-1]+ BkGr[i+1,j]+ BkGr[i,j+1]
           +BkGr[i-1,j-1]+ BkGr[i-1,j+1]+ BkGr[i+1,j-1]+ BkGr[i+1,j+1] ));
    if dif< t1*9
     then p := 1
     else
      if trunc(dif * Form1.SpinEdit3.Value/9) + Im[i,j] >= t2
       then p := t2 - Im[i,j]
       else  p := trunc(dif * Form1.SpinEdit3.Value/9) ;
     if Form1.CheckBox1.Checked = true then R := p ;
     if Form1.CheckBox2.Checked = true then G := p ;
     if Form1.CheckBox3.Checked = true then B := p ;
     If Form1.CheckBox4.Checked = True then  ImPixel := Im[i,j] else ImPixel :=0;
    b4.Canvas.Pixels[i,j] := R+ ImPixel  + (G+ImPixel ) shl 8 + (B+ImPixel ) shl 16 ;
    end;
  end;
//=============================================
Procedure Sub_Aver4(Im,BkGr :GrayMatrix);  { cross X 3x3 }
var i,j,dif, ImPixel :integer;
   p, R,G,B:byte;
 begin
  for i:=0 to w-1 do
   for j:=0 to h-1 do begin
    dif := (Im[i,j]+ Im[i-1,j-1]+ Im[i-1,j+1]+ Im[i+1,j-1]+ Im[i+1,j+1]
        -( BkGr[i,j]+BkGr[i-1,j-1]+ BkGr[i-1,j+1]+ BkGr[i+1,j-1]+ BkGr[i+1,j+1] ));

    if dif< t1*5
     then p := 1
```

```
    else
     if trunc(dif * Form1.SpinEdit3.Value/5) + Im[i,j] >= t2
      then p := t2 - Im[i,j]
      else
       p := trunc(dif * Form1.SpinEdit3.Value/5) ;
    if Form1.CheckBox1.Checked = true then R := p ;
    if Form1.CheckBox2.Checked = true then G := p ;
    if Form1.CheckBox3.Checked = true then B := p ;
    If Form1.CheckBox4.Checked = True then  ImPixel := Im[i,j] else ImPixel :=0;
   b4.Canvas.Pixels[i,j] := R+ ImPixel  + (G+ImPixel ) shl 8 + (B+ImPixel ) shl 16 ;
   end;
 end;
//=======================================
...
//---------------------------------
Procedure Sub_Aver7(Im,BkGr :GrayMatrix);   { Diag \3 }
var i,j,dif, ImPixel :integer;
   p, R,G,B:byte;
 begin
   for i:=0 to w-1 do
    for j:=0 to h-1 do begin
     dif := (Im[i,j]+Im[i-1,j-1]+ Im[i+1,j+1]
         -( BkGr[i,j] +BkGr[i-1,j-1]+ BkGr[i+1,j+1] ));
     if dif< t1*3
      then p := 1
      else
       if trunc(dif * Form1.SpinEdit3.Value/3) + Im[i,j] >= t2
        then p := t2 - Im[i,j]
        else  p := trunc(dif * Form1.SpinEdit3.Value/3) ;
     if Form1.CheckBox1.Checked = true then R := p ;
     if Form1.CheckBox2.Checked = true then G := p ;
     if Form1.CheckBox3.Checked = true then B := p ;
     If Form1.CheckBox4.Checked = True then  ImPixel := Im[i,j] else ImPixel :=0;
    b4.Canvas.Pixels[i,j] := R+ ImPixel  + (G+ImPixel ) shl 8 + (B+ImPixel ) shl 16 ;
    end;
 end;
//---------------------------------

procedure TForm1.Button1Click(Sender: TObject);   // 1st File of sequence
 var i,j :integer;

begin
   b1 := TBitmap.Create;
  OpenPictureDialog1.Title := 'Open First Image of Sequence';
  if OpenPictureDialog1.Execute then
    try
    b1.LoadFromFile(OpenPictureDialog1.FileName);
    finally
    end;   FName := OpenPictureDialog1.FileName ; FNL := length(FName);
     Form2.Visible := true;
     Form2.Enabled := true;
     Form2.Width := w * SpinEdit2.Value +5;   Form2.Height := h * SpinEdit2.Value +5 ;
     Form2.Caption := 'First Image of Sequence '+ FName ;
     Form2.Image1.Width :=w * SpinEdit2.Value; Form2.Image1.Height :=h * SpinEdit2.Value;
     Form2.Image1.Picture.Bitmap := b1 ;  Form2.Image1.refresh;
    { Form2.canvas.draw(0,0,b1);} beep;
 end;
```

```
procedure TForm1.Button2Click(Sender: TObject); //main cycle
var ss : ShortString;
   cc : char;
   p3, p4 :byte;
   i, j, x, k ,kk :integer;
label 1;
begin   if FNL=0 then begin
        ShowMessage('1st Image or Back Ground hasn''t been opened!');
        goto 1; end;
  b1 := TBitmap.Create;

  for i:=0 to w do
   for j:=0 to h do  bGr[i,j] := toGr(b.Canvas.Pixels[i,j]) ; //backgr matrix

 b4 := TBitmap.Create;    b4.Width := w;   b4.Height := h ;

  kk := StrToInt(FName[FNL-5]+FName[FNL-4]);
   NewFName :=FName;
 for k:=kk to kk + SpinEdit1.value - 1 do
 begin
   delete(NewFName,FNL-5,2);  FNL:=FNL-2;
   if k<10  then begin insert(IntToStr(k),NewFName,FNL-3);
                 insert('0',NewFName,FNL-3); end
         else insert(IntToStr(k),NewFName,FNL-3);
   FNL := FNL + 2 ;

   b1.LoadFromFile(NewFName);
 for i:=0 to w do
  for j:=0 to h do  b1Gr[i,j] := toGr(b1.Canvas.Pixels[i,j]);  // Gray Matrix
 //=============================================================
  if RadioButton1.Checked = true then Add(b1Gr,bGr);
  if RadioButton2.Checked = true then Sub_Aver2(b1Gr,bGr);
  if RadioButton3.Checked = true then Sub_Aver3(b1Gr,bGr);
  if RadioButton4.Checked = true then Sub_Aver4(b1Gr,bGr);
  if RadioButton5.Checked = true then Sub_Aver5(b1Gr,bGr);
  if RadioButton6.Checked = true then Sub_Aver6(b1Gr,bGr);
  if RadioButton7.Checked = true then Sub_Aver7(b1Gr,bGr);
  if RadioButton8.Checked = true then Sub_Aver8(b1Gr,bGr);
  if RadioButton9.Checked = true then Sub_Aver9(b1Gr,bGr);
   //=============================================================
     Form2.Caption := '( Im'+IntToStr(k - kk)+' - BackGR ) x '+IntToStr(Form1.SpinEdit3.Value)+' +
Im'+IntToStr(k - kk) ;
     Form2.Image1.Picture.Bitmap := b4 ;  Form2.Image1.refresh;  beep;
     if CheckBox5.Checked = true then b4.SaveToFile(SaveN + IntToStr(k)+ '.bmp');
  end;
1:end;


end.
```

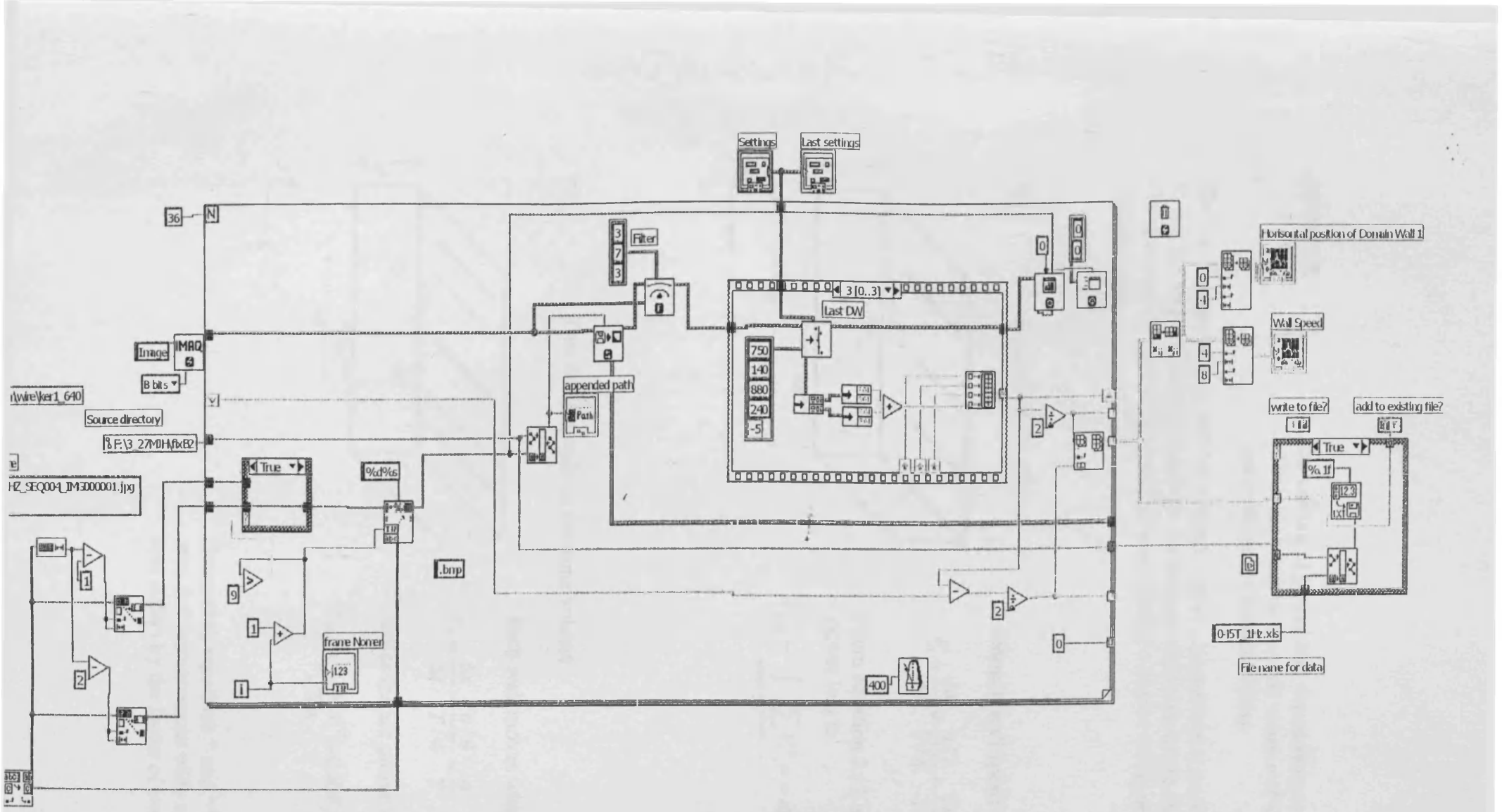

APPENDIX 4.4 LabView block diagram of the program for domain wall position measurement

APPENDIX 5.1 **Estimation of power loss dependence on the number of domain walls in the unit volume of ideal GO steel under B-controlled conditions.**

The unit volume of steel with ideal Block walls is magnetised at a constant rate so that the magnetisation grows from the demagnetised state to the saturated state. The process can be considered as take place during a quarter of the period T of a triangle wave.

a). Single domain wall

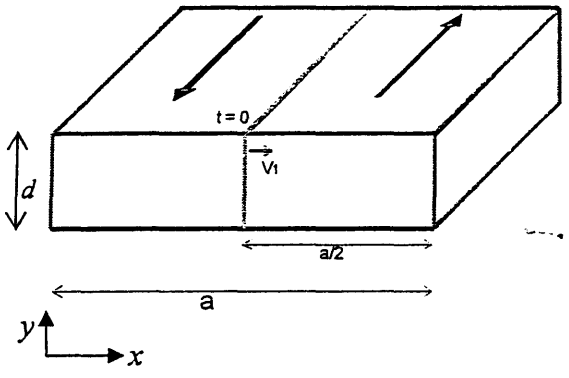

Domain wall speed

$$V_1 = \frac{\Delta x}{\Delta t} = \frac{a/2}{T/4} = \frac{2a}{T}$$

From equation 2.12 instantaneous power loss is

$$P_{T/4} \sim \int_{volum} \sum_{n\_walls} V_i^2 = = dbV_1^2 = db\frac{4a^2}{T^2}$$

*

b). Two domain walls in the same volume

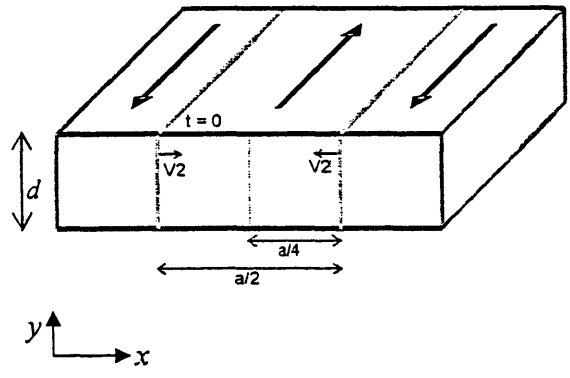

Each wall moves with speed

$$V_2 = \frac{\Delta x}{\Delta t} = \frac{a/4}{T/4} = \frac{a}{T}$$

Hence instant power loss

$$P_{T/4} \sim \int \sum_{n\_walls} V_i^2 = 2dbV_2^2 = db \cdot 2\frac{a^2}{T^2}$$

**

Comparing equations * and ** it can be seen that instantaneous eddy current power loss differs by the factor of two.

APPENDIX 5.2 **Theoretical comparing of eddy current power loss of pinned and non-pinned domain wall**

According to equation 2.12 local instantaneous eddy current loss are proportional to the squared domain wall velocity $P_{inst} \sim v_{inst}^2$ than for discrete time power loss on single wall

$P_{total} = \sum P_{inst} \sim \sum_i v_i^2$ where vi is wall velocity at i instance

1. In an ideal material without pinning sites for a rising half of triangular cycle that lasting 3 s.

$$P_{total} \sim \sum_i v_i^2 = 3\left(\frac{\Delta x}{\Delta t}\right)^2 \overset{\Delta t = 1}{=} 3(\Delta x)^2$$

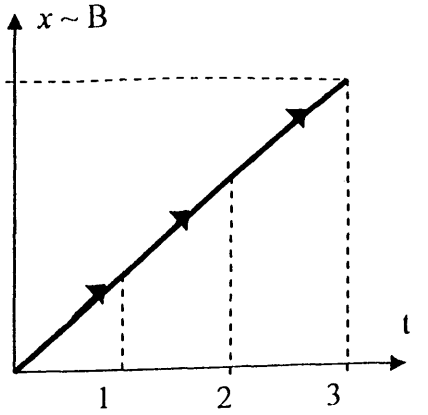

2. If instead a travelling wall meets single point pinning site where it resting for 1 second, than under ΔB constrained to be the same than

$$P_{total} \sim \sum_i v_i^2 = \left(\frac{\Delta x}{\Delta t}\right)^2 + 0 + \left(\frac{2\Delta x}{\Delta t}\right)^2 = 5(\Delta x)^2$$

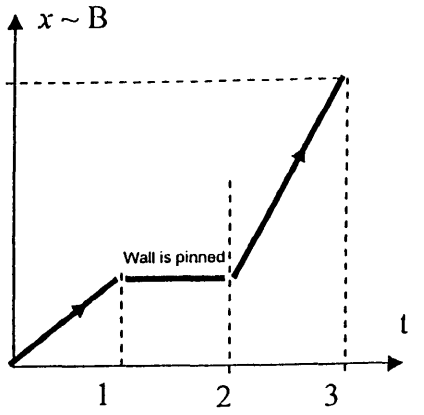

Power loss has raised for 2/3 comparing to the smooth DW motion

The same wall at ΔH constrained to be the same

$$P_{total} \sim \sum_i v_i^2 = \left(\frac{\Delta x}{\Delta t}\right)^2 + 0 + \left(\frac{\Delta x}{\Delta t}\right)^2 = 2(\Delta x)^2$$

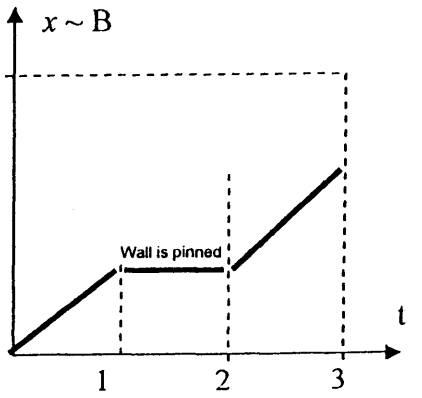

Power loss has dropped for 1/3 together with dropped transfer efficiency, ΔB what can be referred to reduced permeability due to the presence of the defect